

**RARE EARTH NANOPARTICLES: BUILDING THERANOSTIC AGENTS  
FROM THE GROUND UP**

Par  
Artiom Skripka

Thèse présentée pour l'obtention du grade de Philosophiae Doctor (Ph.D.)  
en sciences de Énergie et Matériaux

**Jury d'évaluation**

Président du jury et  
examineur interne

Prof. Emanuele Orgiu  
Institute National de la Recherche  
Scientifique

Examineur externe

Prof. Tomislav Friščić  
Department of Chemistry  
McGill University

Examineur externe

Prof. Muralee Murugesu  
Department of Chemistry and  
Biomolecular Sciences  
University of Ottawa

Directeur de recherche

Prof. Fiorenzo Vetrone

## REMERCIEMENTS

---

“Who’s better than you?” was among the first things that I heard and learned from my supervisor, Prof. Fiorenzo Vetrone, upon joining his group. This mantra of sorts together with his unwavering support and utter enthusiasm for science guided me throughout my whole PhD – giving me freedom and encouragement to strive for ever greater accomplishments and relish the academia in the process. It is hard to put in words the gratitude that I feel towards him, as there is nothing less than being forever thankful for having him as my PhD supervisor. I thank him for being flexible with my whims to pursue different research lines, and for sending me off to international conferences and short-term stays in different universities. He was always there for me to provide advice and clear my doubts when solving issues, or when struggling with getting to the set goals. Some of which literally forced us to bang our heads on the wall. I was also lucky enough to get to know him outside of the academia, having many deep and stimulating conversations, some of which took place whilst enjoying wine in Venice, cigars in the mountains of Madrid or forests of Lithuania. I thank him for helping me become the scientific scholar I am today, and for making the journey through this PhD smooth and blissful. Thank you, Fiore, for being the best boss and mentor.

I am grateful to Prof. Rafik Naccache, Prof. Eva Hemmer and Dr. Marta Quintanilla for showing me the ropes in the Vetrone Group and for lending a helping hand to their new, and at times over his head, member of the group. Without the knowledge and ideas they have imparted on me I would have had particularly hard time transitioning to the unexplored to me realms of inorganic chemistry, and un-doubtedly so would not have had the thesis I have now.

On this journey, I had a pleasure to meet many exceptional scientists whose insights and collaborative efforts lead to realization of wonderful research projects. I wholeheartedly believe that these strong connections, not only expanded my academic network, but rewarded me with peers that I can trust and whom I can rely on. I am thankful to Prof. Patrizia Canton, Prof. Adolfo Speghini, Prof. Luís D. Carlos, Prof. Dongling Ma, Prof. Marta Cerutti, Prof. Andrey Kuzmin, Prof. Daniel Jaque, Prof. Rute Ferreira, Prof. Louis Cuccia, Prof. Jose Marques-Hueso, Prof. Jinyang Liang and the members of their respective groups whom I had a pleasure to get to work with. I am grateful to become scientific and personal friends with Dr. Fan Yang, Dr. Paolo Cortelletti and Dr. Giacomo Lucchini. I deeply appreciate the help of Prof. Carlos D. S. Brites and Callum M. S. Jones for being patient with me during my stays in Aveiro and Edinburgh, respectively; for helping me with measurements, data analysis, and for the scientific discussions

I could have with you. I am also grateful to my very first supervisor Prof. Ričardas Rotomskis and wonderful members of his group, whom I have the honor to call my friends – Dr. Vitalijus Karabanovas, Greta Jarockytė, Dominyka Dapkutė and Evelina Voronovič. We got a chance to work and to spend time together again, which have led to accomplishing many scientific goals, and I believe there is still more to come. Ačiū.

Looking inwards, there is likely not a single person that passed through the Vetrone Group that did not in one way or another provided support to me during these years. To all of you, I would like to say thank you, and I hope you know how much I appreciate the chance to meet you and work with you. My deepest gratitude goes towards Dr. Cheng Ting, who would be there to argue (courteously) with me, no matter how confident I was in my ideas, and who was willing to comply with my stubbornness. I am thankful to Dr. Marija Matulionytė for always being there for me science- and non-science-wise, for all the chats we had during our coffee and tea breaks. Dr. Lucas Vasquez-Besteiro, thank you for broadening my horizons outside the scope of my PhD, for the great discussions we had on philosophy, ethics, religion, arts and culture; and for helping me switch to a more virtuous, I hope, way of living. Dr. Alma Ramos, Dr. Yue Huang, Dr. Joe Gerald Jesu Raj, Dr. Chun Liu, Dr. Isabel Gessner, Dr. Chanchal Hazra, Alexandre Morinvil, Vivienne Tam and many others, thank you.

There are few people that hold a special place in my heart. My dearest colleagues and friends Dr. Riccardo Marin, Dr. Antonio Benayas and Dr. Daniele Benetti. Guys, there is nothing I can say that you do not already know. We have been through quite a lot together, the ups, the downs, the joyous and totally frustrating moments. The support and competitiveness you have given me, and relentless pursuit to move forward, never being complacent, are the pillars on which we helped to build each other and which will continue to drive us onwards.

I would like to also thank all the people at INRS with whom I had the opportunity to interact and who definitely made my time at INRS-EMT worthwhile and memorable. Ahlem, Luca, Fabrizio, Gianluca, Denis, and many others. I thank the Italian gang of INRS for excellent coffee, particularly one “coffee-maniac”, my roomy Giacomo.

A big thank you to my friends who are scattered all around the world, as luck would have it, but who, regardless of that, have helped me by sharing their own PhD experiences and by taking my mind away from academia once in a while. Thank you Aistė, Kike, Johannes, Disa, Rūta, Saulius.

Finally, I would like to express the appreciation to my family. I wholeheartedly thank my mother Valentina Skripka, father Valerij Skripka, and my brother Nikita Skripka who have supported me throughout this journey in every way they knew how. I am indebted to them over and beyond. Also, my grandma Jekaterina Šimanel and grandpa Vitold Šimanel who have always been there for me, and who have helped to nurture my passion for science from the earliest of my days.



## RÉSUMÉ

---

L'arrivée de la nanotechnologie a révolutionné les sciences fondamentales et applicatives. En biomédecine, les concepts diagnostiques et thérapeutiques qui étaient auparavant de la science-fiction prennent graduellement vie sous forme de nanoparticules sophistiquées - mettant en œuvre la détection et le traitement des maladies. Les nanoparticules photoluminescentes, qui répondent au stimulus optique en émettant de la lumière utilisée pour l'imagerie, la détection et la thérapie, sont des agents théranostiques prometteurs, intégrant ensemble le diagnostic et la thérapie. Les nanoparticules préférées sont celles qui fonctionnent sous de longueurs d'onde proche infrarouge (NIR), qui transpercent plus profondément les tissus et ne se limitent pas à une application superficielle seule. Parmi celles-ci, les nanoparticules dopées aux terres rares, ou RENP, sous excitation NIR peuvent émettre à travers les gammes spectrales UV, visible et NIR. Grâce à la conversion ascendante des photons, les RENP ajoutent de multiples photons dans le proche infrarouge et émettent une lumière d'une énergie suffisamment élevée pour stimuler les processus thérapeutiques. De plus, l'excitation NIR est émise sous forme de lumière de longueurs d'onde encore plus grandes, ce qui est parfait pour l'imagerie et la détection des indices environnementaux, comme la température. En fait, les RENP sont d'excellents nanothermomètres, explorés pour la détection précoce des maladies et l'exécution contrôlée des thérapies basées sur la chaleur.

Cette thèse explore les RENP en tant que futures nanomédicaments théranostiques, en se concentrant sur les RENP qui émettent à travers une large gamme spectrale, UV-NIR. Des propriétés photophysiques fondamentales de différents RENP sont signalées, nécessaires pour brosser un tableau réaliste du potentiel et des pièges de ces nanostructures. En outre, les premiers RENP du genre en tant que nanothermomètres fonctionnant au-delà de 1500 nm de longueurs d'onde sont introduits, pour l'imagerie des tissus profonds et la cartographie thermique avec le contraste optique le plus élevé. Enfin, une nouvelle idée de théranostic découplé avec RENP est développée. Les théranostiques découplés impliquent l'initiation à la demande d'une thérapie ou d'un diagnostic, mais pas des deux en même temps si cela n'est pas nécessaire. Par conséquent, le trajet de ces RENP vers la zone d'intérêt pourrait être suivi sans crainte de dommages indésirables aux tissus sains, et la thérapie est lancée lorsque seule la cible est acquise. De par leur conceptualisation, ces RENP sont méticuleusement optimisés, entraînant l'évolution d'agents théranostiques découplés nouveaux et améliorés.

Mots-clés: théranostic, proche infrarouge, upconversion, nanothermométrie, terres rares.



## ABSTRACT

---

The arrival of nanotechnology has revolutionized the way we approach fundamental and applicative sciences. In the medical framework, the diagnostic and therapeutic concepts that previously existed only in the creative minds of science fiction writers, are gradually coming to life in the form of sophisticated nanoparticles – enacting disease detection and treatment. Photoluminescent nanoparticles, that respond to optical stimulus by emitting light used for imaging, sensing, and therapy are promising theranostic agents – integrating diagnostics and therapy under one roof. Preference is also given to nanoparticles that operate under electromagnetic radiation of near-infrared (NIR) wavelengths, which pierce deeper inside tissues and are not limited to superficial application alone. Among such, rare earth doped nanoparticles, or RENPs, under NIR excitation can non-strenuously emit across UV, visible and NIR spectral ranges. By means of photon upconversion, RENPs add multiple impinging NIR photons and emit light of high-enough energy to drive photochemical reactions for therapy. At the same time, downshifting process converts NIR excitation to emission of even longer wavelengths, perfect for imaging and contactless sensing of environmental cues, like temperature. In fact, RENPs are excellent nanoscale temperature sensors – nanothermometers – explored for early stage disease detection and controlled execution of heat-based therapies.

This thesis explores the RENPs as future theranostic nanomedicines starting from the very basics and moving towards new concepts in RENP synthesis, nanothermometry, and theranostics. Particularly, RENPs that simultaneously emit across a broad, UV-to-NIR, spectral range are scrutinized. Fundamental photophysical properties of different RENPs are reported, necessary to paint a realistic outlook on the potential and pitfalls of these nanostructures. Furthermore, first of their kind RENPs as nanothermometers operating beyond 1500 nm wavelengths are introduced, for deep-tissue imaging and thermal mapping with highest optical contrast. Finally, a novel idea of decoupled theranostics with RENPs is developed. Decoupled theranostics entail on-demand initiation of either therapy or diagnostics, but not both at the same time if it is not required. Consequently, the journey of such RENPs to the area of interest could be tracked without fear of undesired damage to healthy tissues, and therapy is initiated only when the target is acquired. From their conceptualization, these RENPs are meticulously optimized, resulting in the evolution of new and improved decoupled theranostic agents.

Keywords: theranostics, near-infrared, upconversion, nanothermometry, rare earth nanoparticles.



## SOMMAIRE RÉCAPITULATIF

---

### *Introduction*

*Chapitre 1.* Les objets à l'échelle nanométrique (1-100 nm), les nanoparticules (NP), ont des propriétés physiques et chimiques uniques qui font l'objet de recherches actives et de mises au point, pour être exploitées en biomédecine. Les NP ciblées pour le diagnostic, la thérapie, la détection ou l'activation de réponses physiologiques présentent un intérêt particulier.<sup>[1]</sup> En fait, il existe déjà un certain nombre de nanomédicaments disponibles sur le marché, ou en cours d'essais cliniques, qui offrent une meilleure administration des médicaments,<sup>[2]</sup> une thérapie de haute précision,<sup>[3]</sup> et une imagerie améliorée.<sup>[4]</sup>

Le point central de la recherche en science des matériaux est devenu ce qu'on appelle les PN théranostiques – des nanoplateformes multifonctionnelles équipées de moyens thérapeutiques et diagnostiques pour la médecine personnalisée.<sup>[5-7]</sup> Sur le plan diagnostique, ces PN peuvent servir d'agents de contraste pour l'imagerie (optique, magnétique, radiographique et photoacoustique) et, enrichies de la capacité thérapeutique, elles peuvent agir comme vecteurs de médicaments, médiateurs de processus chimiques ou sources de chaleur.<sup>[8]</sup> Les NP de théranostic particulièrement optiques offrent une précision laser ponctuelle dans la détection et l'éradication des maladies non invasives (c'est-à-dire le cancer).<sup>[9]</sup> Il est envisagé que les NP de théranostic photoluminescentes puissent éclairer la tumeur maligne et la traiter à distance avec des dommages réduits aux tissus sains (figure 1.1).

Par définition, les NP photoluminescents absorbent l'énergie d'excitation entrante et la réémettent à des fréquences spécifiques à chaque NP, ce qui permet de discriminer les structures d'intérêt par rapport au fond environnant. Cependant, de nombreux NP fonctionnent à des longueurs d'onde correspondant au domaine spectral ultraviolet-visible (UV-vis) où les tissus biologiques absorbent et diffusent fortement la lumière<sup>10</sup>. Dans ce cas, ni la lumière d'excitation ne peut pénétrer profondément dans le tissu, ni l'émission émergente ne peut s'échapper pour être détectée. Même si elle pouvait être détectée, la trajectoire des photons est perturbée par la diffusion au point qu'il est impossible de localiser exactement une cible. En outre, les molécules biologiques endogènes présentent une photoluminescence sous excitation UV-vis (autofluorescence tissulaire) qui peut se mélanger à l'émission de NPs situés à des longueurs d'onde similaires, ce qui compromet davantage l'imagerie.<sup>[11]</sup> Combinées, les propriétés optiques des tissus dictent la profondeur, la résolution et le contraste de l'imagerie

qui peut être obtenue, les agents photoluminescents doivent donc être adaptés sur mesure pour maximiser les informations utiles recueillies.

Une solution à bon nombre de ces problèmes consiste à passer dans la région spectrale du proche infrarouge (NIR). L'absorption des principaux composants des tissus, tels que l'hémoglobine, la mélanine, la graisse et l'eau, a tous des minima dans les fenêtres d'imagerie biologique (BW) du NIR.<sup>[12-14]</sup> Ces BW correspondent approximativement aux plages spectrales 750-950 nm (BW-I), 1000-1350 nm (BW-II), et 1500-1800 nm (BW-III), où la lumière est moins atténuée et pénètre les tissus plus profondément (figure 1.2).

Il est important de noter que l'autofluorescence est faible, voire inexistante, dans les modèles BW-II et BW-III. De plus, la diffusion de la lumière dans les tissus dépend inversement de sa longueur d'onde, ce qui signifie qu'étant donné que l'atténuation de la lumière par diffusion est réduite aux grandes longueurs d'onde, il est possible d'acquérir des images de photoluminescence à fort contraste.<sup>[15]</sup>

Le passage effectif aux longueurs d'onde de l'imagerie NIR nécessite le développement d'agents de contraste absorbant et émettant la lumière NIR. Ainsi, les molécules organiques émettant dans le NIR,<sup>[16]</sup> les points quantiques,<sup>[17]</sup> les NP des métaux nobles,<sup>[18]</sup> les NP des chalcogénures,<sup>[19,20]</sup> et les nanotubes de carbone,<sup>[21]</sup> sont tous activement recherchés comme agents de contraste dans le NIR. Il est important de noter d'emblée, cependant, que l'imagerie des tissus profonds dans le NIR implique que les images à fort contraste sont acquises à des profondeurs allant jusqu'à quelques millimètres.<sup>[22]</sup> Bien que la lumière du NIR puisse pénétrer quelques centimètres de tissu, l'imagerie à ces profondeurs avec une résolution à l'échelle du micromètre est impossible, et ne peut raisonnablement être utilisée que pour la localisation grossière de l'agent de contraste. Les méthodes de nettoyage des tissus pourraient peut-être annuler une partie de ces limitations et faire progresser l'imagerie à haute résolution à des profondeurs plus importantes,<sup>[23]</sup> tandis que les techniques endoscopiques peuvent être utilisées pour atteindre les organes internes inaccessibles à la lumière de l'extérieur.<sup>[24]</sup>

Le potentiel de l'imagerie NIR a été illustré à de nombreuses reprises, cependant, dans le cadre des nanomatériaux théranostiques, l'application de nombreux PN est limitée à la seule imagerie, et l'action thérapeutique, si elle existe, est techniquement difficile à obtenir. Les NP plasmoniques ou les points quantiques peuvent être utilisés pour la thérapie photothermique (PTT) et la thérapie photodynamique à excitation multiphotonique (PDT), respectivement,<sup>[27,28]</sup> mais dans ces cas, leurs capacités d'imagerie des tissus profonds pourraient être compromises. Par exemple, la PDT multi-photon nécessite des points quantiques avec émission de lumière

visible afin de stimuler la génération d'oxygène singulet; de plus, des installations laser pulsées coûteuses et encombrantes sont nécessaires pour l'émission multi-photon. Par conséquent, pour développer des agents théranostiques qui pourraient être utilisés aussi bien pour l'imagerie des tissus profonds que pour la thérapie, il convient d'explorer d'autres nanomatériaux photoluminescents.

Les nanoparticules dopées aux terres rares (RENP), qui, sous excitation NIR, présentent une photoluminescence dans les domaines spectraux UV-vis et NIR simultanément, constituent le cas le plus solide à ce jour de ce qui pourrait constituer une nanoplateforme théranostique multifonctionnelle entièrement optique. Ces propriétés optiques exceptionnelles des RENP sont dues aux dopants  $RE^{3+}$  et à leurs fascinantes caractéristiques spectrales. Les niveaux d'énergie des électrons 4f dans les  $RE^{3+}$ , responsables des transitions optiques, sont pratiquement insensibles à l'environnement (c'est-à-dire au type de cristal dans lequel les  $RE^{3+}$  sont dopés). Connaître les positions des niveaux d'énergie des différents  $RE^{3+}$  permet donc d'interpréter leur absorption et leur photoluminescence dans différents cristaux, car chaque  $RE^{3+}$  a sa signature unique. Les niveaux d'énergie ont été déterminés expérimentalement par Dieke et ses collègues dans le cristal de  $LaCl_3$ <sup>[29]</sup> et ont été utilisés pour construire ce que l'on appelle aujourd'hui le diagramme de Dieke (figure 1.4). Le diagramme de Dieke montre que de nombreux états excités de différents  $RE^{3+}$  prennent des positions très proches, ce qui permet un échange d'énergie entre les ions voisins lorsqu'ils sont à proximité, comme c'est le cas pour les RENP (figure 1.5). L'échange d'énergie radiative et non radiative peut se produire entre les ions  $RE^{3+}$ , mais les voies non radiatives sont plus courantes à l'échelle atomique. Dans les matériaux dopés  $RE^{3+}$ , tels que les RENP, les ions qui sont soit donneurs soit accepteurs d'énergie, sont respectivement appelés sensibilisateurs et activateurs. Lors de l'excitation des  $RE^{3+}$  par la lumière, de multiples mécanismes d'échange d'énergie peuvent se produire entre les ions sensibilisateurs et activateurs, qui finissent par entraîner une dissipation d'énergie par des processus non radiatifs et radiatifs.

La photoluminescence – la désintégration radiative – des  $RE^{3+}$  peut se produire à partir d'un état excité qui a été directement alimenté par l'absorption de la lumière, ou par le transfert d'énergie d'un sensibilisateur qui a agi comme capteur d'énergie. Il existe trois processus de photoluminescence qui sont distincts pour les matériaux dopés aux  $RE^{3+}$ . L'absorption et l'émission d'un seul photon est appelée «downshifting» (DS) et représente un scénario classique de photoluminescence décalée de Stokes ( $\lambda_{ex} > \lambda_{em}$ ). La photoluminescence anti-Stokes-shifted ( $\lambda_{ex} < \lambda_{em}$ ) se produit lorsque des photons à excitation multiple sont consommés

pour générer un photon à émission unique, ce qui est connu sous le nom d'émission à conversion ascendante «upconverting» (UC). Un processus inverse, de conversion vers le bas «downconversion», peut également être observé entre les  $RE^{3+}$ , auquel cas un seul photon absorbé est émis sous forme de multiples photons de plus faible énergie ( $\lambda_{ex} > \lambda_{em}$ ).

L'émission de UC est d'une importance remarquable pour l'aspect thérapeutique des RENP. Le premier mécanisme de conversion ascendante, basé sur l'absorption à l'état excité (ESA), a été proposé par N. Bloembergen en 1959. Dans un cas très simple, l'émission de la UC peut être obtenue par l'addition consécutive de photons entrants, d'abord par l'absorption à l'état excité (ESA), puis par des étapes consécutives d'ESA.<sup>[30]</sup> Cependant, les sections d'absorption pour l'ESA sont généralement faibles et l'addition de photons de cette manière est souvent inefficace. Dans le diagramme de Dieke, on peut trouver de nombreux états excités avec des écarts d'énergie presque identiques entre les différents ions  $RE^{3+}$ , ce qui permet de monter dans l'échelle des niveaux d'énergie d'un ion avec l'aide d'un autre. Un processus de transfert d'énergie en plusieurs étapes qui produit ainsi des émissions UC est la conversion ascendante de transfert d'énergie (ETU; figure 1.5), ou addition de photon par transferts d'énergie, dont F. Auzel a été le pionnier en 1966.<sup>[31]</sup> Dans le même temps, V.V. Ovsyankin et P. P. Feofilov, ont suggéré l'émission de UC par sensibilisation coopérative, où deux ions sensibilisateurs excités donneraient leur énergie à un ion activateur simultanément, sans étape intermédiaire de transfert d'énergie (Figure 1.5 – sensibilisation coopérative).<sup>[32]</sup> Cependant, l'UFE est plusieurs ordres de grandeur plus efficace pour générer l'émission de UC, que l'ASE ou la sensibilisation coopérative, et est donc principalement exploitée dans les RENP.<sup>[33]</sup>

Un exemple classique d'émission de UC dans les RENP est donné par la paire sensibilisateur/activateur  $Yb^{3+}/Er^{3+}$  (figure 1.6). L' $Yb^{3+}$  a un seul état excité ( $^2F_{5/2}$ ) qui se trouve au-dessus du niveau du sol ( $^2F_{7/2}$ ) par une différence d'énergie correspondant à un rayonnement de ~980 nm. Une séparation énergétique similaire peut être trouvée du niveau du sol  $^4I_{15/2}$  de  $Er^{3+}$  à son état excité  $^4I_{11/2}$ , et de celui-ci à l'état excité  $^4F_{7/2}$ . Ainsi, lorsque  $Yb^{3+}$  est excité par une lumière de 980 nm ( $^2F_{7/2} \rightarrow ^2F_{5/2}$ ), il peut transférer l'énergie d'excitation à  $Er^{3+}$  de manière progressive:  $^2F_{5/2} \rightarrow ^2F_{7/2} (Yb^{3+}):^4I_{15/2} \rightarrow ^4I_{11/2} (Er^{3+})$  et  $^2F_{5/2} \rightarrow ^2F_{7/2} (Yb^{3+}):^4I_{11/2} \rightarrow ^4F_{7/2} (Er^{3+})$ . À leur tour, les niveaux d'énergie émissive  $^2H_{11/2}$  et  $^4S_{3/2}$ , juste en dessous de l'état excité  $^4F_{7/2}$ , sont alimentés par une désintégration non radiative, ce qui donne finalement l'émission verte importante de  $Er^{3+}$ . Bien entendu, il ne s'agit là que de quelques unes des nombreuses voies d'échange possibles entre  $Er^{3+}$  et  $Yb^{3+}$  qui produisent une émission UC sur une large gamme spectrale VIS (figure 1.6), et qui sont examinées plus en détail dans les chapitres 4 et 8

de cette thèse. Simultanément à l'émission UC, l'émission DS de  $\text{Er}^{3+}$  à environ  $1.55 \mu\text{m}$  ( $^4\text{I}_{13/2} \rightarrow ^4\text{I}_{15/2}$ ) est générée à partir de la décroissance non radiative  $^4\text{I}_{11/2} \rightarrow ^4\text{I}_{13/2}$  après le premier événement de transfert d'énergie  $\text{Yb}^{3+} \rightarrow \text{Er}^{3+}$ . Cette émission est d'une importance vitale pour l'imagerie des tissus profonds avec les RENP dans le BW-III.

En plus des processus de migration et de transfert d'énergie, l'énergie d'excitation peut être partagée entre les ions  $\text{RE}^{3+}$  du même type parmi leurs niveaux d'énergie équidistants (ou presque) par relaxation croisée (figure 1.5 – relaxation croisée). La relaxation croisée est un processus non radiatif qui peut dépeupler les états excités intermédiaires de deux ions en amenant l'un à son état fondamental et l'autre à un état excité supérieur. Le même processus se produit également à l'inverse, de sorte que, selon sa "direction", la relaxation croisée peut redistribuer la population d'excitation dans les  $\text{RE}^{3+}$  en favorisant ou en éteignant l'excitation à un niveau d'énergie plus élevé.<sup>[33]</sup> Bien que l'auto-extinction par relaxation croisée soit le plus souvent observée dans les RENP fortement dopées, la relaxation croisée peut être positivement exploitée dans les structures dopées  $\text{Yb}^{3+}/\text{Tm}^{3+}$  pour favoriser l'émission d'UV bleus sous excitation NIR.<sup>[34]</sup>

Étant donné qu'un nombre quelconque de combinaisons  $\text{RE}^{3+}$  peuvent être intégrées dans les RENP, cela rend ces systèmes hôtes-invités extrêmement flexibles en termes de réglage spectral par type de dopant et de sélection de la concentration. Cependant, la photoluminescence des RENP n'est pas déterminée par ce seul facteur – la composition de l'hôte, la phase cristalline, la taille du NP et l'architecture multicouche peuvent toutes influencer la couleur et l'intensité de l'émission, et doivent être soigneusement prises en compte lors de la conception des RENP théranostiques (figure 1.7). Une analyse plus détaillée de la manière dont chacune des caractéristiques susmentionnées des RENP détermine leurs propriétés spectrales est donnée dans la section 1.3.3.

Depuis la conception des RENP, on peut dire qu'elles ont "colonisé" le paysage de la recherche biomédicale. La flexibilité modulaire des RENP permet de construire des nanoplateformes photoluminescentes adaptées à l'imagerie des tissus profonds, à l'administration, la libération et l'activation de médicaments, à la détection multimodale ou à la modulation des réponses physiologiques (figure 1.8). Alors que les RENP théranostiques sont conçues en exploitant différentes combinaisons des caractéristiques susmentionnées, ou en créant des nanostructures hybrides composées de RENP et de nanomatériaux d'une autre classe, chacun apportant ses forces respectives dans la recherche de nanomédicaments tout-en-un du futur.

Comme nous l'avons vu plus haut, l'imagerie biologique des tissus profonds nécessite des agents de contraste qui fonctionnent dans les zones biologiques situées dans la région spectrale du NIR. Heureusement, les RENP remplissent facilement ces conditions grâce à une sélection rationnelle des RE<sup>3+</sup> et de leurs combinaisons. Les longueurs d'onde d'excitation RENP les plus populaires sont 800 et 980 nm, respectivement absorbées par Nd<sup>3+</sup> et Yb<sup>3+</sup>, et se situent dans la BW-I.<sup>[74-76]</sup> Bien qu'à proprement parler la lumière de 980 nm soit en dehors de la BW-I et ait certaines ramifications pour l'excitation RENP dans les objets biologiques, comme le chauffage non désiré induit par l'absorption d'eau, cette longueur d'onde reste la plus utilisée pour la sensibilisation aux émissions. Lors de l'excitation dans le NIR, les RENP peuvent présenter une pléthore de bandes d'émission dans la gamme spectrale UV-vis-NIR par des processus d'excitation-émission de conversion ascendante et/ou descendante. Les émissions de DS des RENP s'étendent loin dans le NIR et sont également plus efficaces d'au moins un ordre de grandeur par rapport au processus de conversion ascendante.<sup>[79,80]</sup> De nombreux RE<sup>3+</sup> optiquement actifs présentent des transitions radiatives dans le NIR qui peuvent être exploitées dans l'imagerie des tissus profonds à fort contraste : Nd<sup>3+</sup> – 880, 1050, 1320 nm, Yb<sup>3+</sup> – 1000 nm, Ho<sup>3+</sup> – 1200 nm, Pr<sup>3+</sup> – 1300 nm, Er<sup>3+</sup> – 1550 nm (figure 1.9A).<sup>[80,81]</sup> Parmi ces transitions, les bandes d'émission DS de Nd<sup>3+</sup> et Er<sup>3+</sup> sont principalement utilisées pour l'imagerie car elles coïncident parfaitement avec BW-II et BW-III, respectivement. En fait, l'imagerie dans ces BW avec des RENP peut être obtenue avec une résolution spatiale et temporelle sans précédent, tandis que la chimie de surface des RENP peut être adaptée pour améliorer la circulation sanguine, l'accumulation aux sites des tumeurs et permettre une élimination rapide du corps.

Les bandes d'émission UC et DS des RENP peuvent également être utilisées pour la détection optique, soit en exploitant leur propre sensibilité innée à l'environnement, soit en coordination avec d'autres agents optiques. Dans ce dernier cas, les nanocomposites sont fabriqués lorsqu'un composant optique influence l'émission d'un autre. L'interaction entre les RENP conjugués à d'autres espèces optiques est alors conçue pour changer en présence de l'analyte. Comme les RENP sont excitées par une seule longueur d'onde d'excitation dans le NIR et qu'elles émettent sur une large gamme spectrale optique, cela permet de mettre en place des stratégies de détection multiplexée à haut débit,<sup>[70]</sup> sans interférence entre les différents composants du capteur ni fausse détection due à l'autofluorescence. De cette manière, les RENP sont recherchées et appliquées dans la détection du pH,<sup>[94]</sup> l'identification des métaux lourds et des petites molécules,<sup>[95,96]</sup> les acides nucléiques et la reconnaissance des protéines,<sup>[97]</sup> la mesure du voltage du potentiel de la membrane neuronale,<sup>[98]</sup> et les bio-essais.<sup>[99]</sup>

Les RENP pourraient également être utilisées comme biocapteurs autonomes si leur intensité d'émission et/ou leur couleur sont influencées par des indices externes, qui influent sur les taux de décroissance radiative et non radiative des états excités des RE<sup>3+</sup>. Cela peut être fait en modulant l'absorption/émission des phonons en treillis ou des modes vibratoires de l'environnement. Par exemple, le niveau d'hydratation d'un certain milieu peut être vérifié par la diminution de l'intensité d'émission des RENP, provoquée par l'extinction de l'eau.<sup>[100]</sup> Alors que la pression/force externe exercée sur les RENP peut être détectée en observant les changements dans l'émission UC des RENP induits par la contrainte externe.<sup>[101,102]</sup> En même temps, les changements thermiques au voisinage des RENP influencent leur dynamique excitation-émission et peuvent être utilisés pour la mesure de la température à l'échelle nanométrique – la nanothermométrie. Le concept de nanothermométrie et le rôle que jouent les RENP en tant que capteurs de température sont décrits plus en détail dans la section 1.5. La température est l'un des principaux paramètres par lesquels les systèmes physiques peuvent être décrits et par lesquels ils sont influencés. En biologie, la température contrôle les processus physiologiques et chimiques qui se déroulent du niveau moléculaire jusqu'au niveau du corps entier. Elle est la clé du fonctionnement et de la survie des organismes vivants. Le potentiel de la nanothermométrie optique a donc été reconnu dans de nombreux domaines de la recherche fondamentale et appliquée. Divers nanothermomètres ont été utilisés pour étudier les nanofluides, la microélectronique, les propriétés thermiques des matériaux, y compris des tissus biologiques, ou pour obtenir un ajustement contrôlé des températures absolues au cours de thérapies thermiques. En tant que nanothermomètres, les RENP occupent une place très particulière dans la détection optique de la température. Ce sont de loin les sondes thermiques les plus explorées, capables de mesurer les températures dans les cellules et les tissus grâce à leur émission de rayons ultraviolets et de rayons gamma, et elles continuent d'être perfectionnées en termes de sensibilité thermique ( $S_r$ ) et de luminosité d'émission, qui déterminent toutes deux la précision avec laquelle les températures peuvent être acquises.

Comme on peut le voir, les RENP sont des instruments de diagnostic polyvalents, mais leur boîte à outils optique est tout aussi adaptée aux tâches thérapeutiques. Ici, l'émission de rayons ultraviolets des RENP est d'une importance capitale, car des photons de haute énergie peuvent être générés sous excitation NIR *in situ* à des profondeurs de tissu inaccessibles sous irradiation directe par UV-vis. De plus, les RENP ajoutent des photons NIR en grim pant l'échelle de leurs niveaux d'énergie à longue durée de vie à des densités de puissance d'excitation relativement faibles de  $10^{-3}$ - $10^3$  W/cm<sup>2</sup>, ce qui rend leur mise en œuvre plus sûre et plus rentable dans les cliniques. Notez qu'à l'exception de quelques cas, les RENP n'ont pas d'action

thérapeutique, mais fonctionnent comme des médiateurs énergétiques. À cette fin, les progrès réalisés dans les RENP en tant qu'agents thérapeutiques jouent un rôle égal sur le front i) de l'ingénierie de RENP toujours plus efficaces en tant que donneurs d'énergie, et ii) de la mise au point de nouvelles techniques et de nouveaux médicaments qui tirent parti de l'émission de CU. L'administration contrôlée de médicaments et la TPD sont les principales voies de recherche thérapeutique avec les RENP.

Après cette brève introduction sur les propriétés optiques et les utilisations des RENP, leur vaste potentiel dans la recherche scientifique, en particulier biomédicale, est indéniable et, fait passionnant, reste encore à exploiter. Les RENP sont des structures hautement modulaires, dont la composition et l'architecture doivent être conçues de manière rationnelle pour obtenir une nanoplateforme adaptée à une tâche spécifique. Pour ce faire, des efforts multidisciplinaires de physique, de chimie et de biologie doivent être mis en commun. Dans cette thèse, les RENP théranostiques sont conçus et étudiés étape par étape, en s'appuyant sur les pratiques actuelles de recherche des RENP, en repoussant certaines limites et en réévaluant les approches théranostiques de pointe. Avec un objectif unique préservé, créer une nanoplateforme théranostique qui soit polyvalente, efficace et discrètement contrôlée par la lumière.

## *Méthodes*

*Chapitre 2.* Parmi les multiples approches de synthèse de la RENP, la décomposition thermique des précurseurs de métal-trifluoroacétate a été appliquée pour fabriquer toutes les RENP de cette thèse.<sup>[175]</sup> Cette méthode donne des RENP de haute cristallinité et de distribution de taille étroite, en même temps des architectures noyau/coque peuvent être facilement créées. Deux approches distinctes de synthèse de décomposition thermique ont été utilisées pour réaliser les RENP: i) le chauffage et/ou ii) l'injection à chaud. Le flux de travail général de la synthèse de décomposition thermique est décrit ci-dessous; les détails sur la préparation de RENP spécifiques sont donnés au début de chaque chapitre 3-10.

Dans une synthèse typique par décomposition thermique à chaud, les précurseurs de trifluoroacétate de métal sont d'abord dissous dans un mélange d'acide oléique (OA; également appelé oleylamine – OM) et de 1-octadécène (ODE) sous vide à 110 °C dans un ballon à fond rond (l'agitation magnétique est utilisée pendant toute la durée du trou de la procédure, il en va de même pour l'approche par injection à chaud). Après dissolution du précurseur et dégazage du mélange, le flacon est rempli d'argon et la température est portée à 330 °C (sauf indication contraire). En maintenant le flux d'argon, on laisse la réaction se dérouler pendant 1 heure

avant de la refroidir à température ambiante (RT). Les RENP obtenues sont ensuite collectées et lavées comme décrit ci-dessous.

La méthode d'injection à chaud implique la préparation de solutions séparées A et B, qui sont ensuite mélangées pour former des RENP. En général, la solution A est un mélange de parties paires d'OA et d'ODE qui est dégazé sous vide à 145 °C pendant au moins 30 minutes. Après le dégazage, la solution A est remplie d'argon et le flux d'argon est maintenu pour le reste de la synthèse. Séparément, la solution B contient des précurseurs de métal-trifluoroacétate dissous dans un mélange d'OA et d'ODE sous vide à 125 °C. La température de la solution A est ensuite portée à 290-315 °C (en fonction des RENP souhaitées), puis la solution B est injectée dans la solution A à l'aide d'un système pompe-seringue à un débit d'injection préréglé. Une fois l'injection terminée, la réaction est poursuivie pendant au moins 1 heure, puis elle est arrêtée par refroidissement jusqu'à la température ambiante ; éventuellement, la réaction est poursuivie en introduisant d'autres étapes d'injection afin d'obtenir des RENP à noyau/enveloppe avec les couches fonctionnelles souhaitées.

Les RENP obtenues par chauffage ou par injection à chaud sont précipitées avec de l'éthanol et collectées par centrifugation, puis les RENP sont lavées au moins deux fois par centrifugation. Enfin, les RENP sont redispersées dans un solvant organique comme l'hexane ou le chloroforme pour une caractérisation structurale et optique plus poussée ou un traitement de surface.

Les RENP telles que synthétisées sont recouvertes d'acide oléique qui ne permet leur dispersion que dans des solvants organiques. Afin de rendre les RENP dispersibles dans l'eau et d'étudier leurs propriétés photophysiques en milieu aqueux, ou de les appliquer dans des études biologiques, leur surface a été modifiée soit par élimination/échange de ligands (chapitres 3, 9, 10), soit par revêtement de phospholipides (chapitres 4-6).

La cristallinité et la phase de toutes les RENP ont été déterminées par analyse de diffraction des rayons X sur poudre (XRD). La morphologie et la distribution de taille des RENP ont été étudiées par microscopie électronique à transmission (TEM). Dans les chapitres 3, 8 et 10, la concentration molaire de dopage  $RE^{3+}$  a été déterminée par spectroscopie d'émission optique à plasma à couplage inductif (ICP-OES). Dans les chapitres 4 et 5, les spectres infrarouges de transformation de Fourier par transmission (FTIR) des RENP encapsulées dans des micelles de phospholipides ont également été enregistrés pour montrer la présence de phospholipides à leur surface.

Les spectres d'émission UC et DS des RENP ont été mesurés avec une installation optique du groupe Vetrone à l'INRS, au Canada. Le dispositif comprend deux spectromètres pour la collecte de la lumière dans les domaines spectraux 290-830 nm et 800-1700 nm. Les sources laser disponibles comprennent des diodes laser de 793, 806 et 960 nm (également appelées 980 nm d'excitation) de longueur d'onde de rayonnement et une lampe LED de 440 nm. Afin d'éliminer toute lumière parasite de la source d'excitation, un filtre passe-courte et un filtre passe-longue (LP) ont été utilisés dans le cas de l'émission UC et DS, respectivement. Les spectres de différentes dispersions colloïdales de RENP ont été recueillis en plaçant les échantillons dans le porte-cuvette à température contrôlée, ce qui a également permis de contrôler la température de l'échantillon dans la plage de 20 à 50 °C dans le cas des études de nanothermométrie.

Dans les études de modélisation de l'imagerie des tissus profonds par les RENP, les images NIR ont été acquises avec une caméra d'imagerie NIR InGaAs. La sélection de certaines bandes d'émission dans le NIR a été effectuée à l'aide de différents filtres LP.

Au chapitre 3, les spectres d'émission DS et rendement quantique de la photoluminescence (*PLQY*) des RENP ont été mesurés avec l'aide du professeur Carlos D. S. Brites de l'université d'Aveiro, au Portugal. Dans le chapitre 7, la *PLQY* des émissions UC des RENP a été mesurée avec l'aide de Callum M. S. Jones à l'Université Heriot-Watt, Edimbourg, Royaume-Uni. Au chapitre 3, les mesures de la décroissance de la photoluminescence ont été effectuées par le Dr. Inocencio R. Martín et le Dr. Antonio Benayas à l'université de La Laguna, Tenerife, Espagne. Dans les chapitres 7 et 8, des mesures de la décroissance de la photoluminescence ont été effectuées avec l'aide du Dr. Artūras Katelnikovas à l'université de Vilnius, Lituanie.

Dans le chapitre 6, toutes les expériences relatives à la génération d'oxygène singulet et les études *in vitro* ont été réalisées par le Dr Vitalijus Karabanovas et Mme Greta Jarockytė à l'Institut national du cancer, Vilnius, Lituanie.

### *Résultats et discussion*

Cette thèse s'articule autour i) de la conception rationnelle des RENP: l'ajustement et l'exploration du type de dopage RE<sup>3+</sup>, de la concentration, des architectures noyau/enveloppe, ainsi que des techniques de synthèse avancées et la présentation des propriétés photophysiques des RENP, qui sont toutes pertinentes pour leur développement et leur application réussis en biomédecine; ii) promouvoir l'intégration de la nanothermométrie NIR dans les BW-II et BW-III en tant qu'élément de base des RENP de théranostic avancé; iii)

réaliser une nouvelle approche de théranostic – le théranostic découplé – en tant que moyen d'obtenir des nanomédicaments plus sûrs dans le cadre des RENP. Par la suite, la figure 12.1 résume visuellement le contenu et les résultats de cette thèse, également présentée à la fin de ce résumé.

*Chapitre 3.* Les RENP dopées au  $\text{Nd}^{3+}$  présentent les avantages d'une excitation sans chauffage dans le BW-I autour de 800 nm, d'une émission dans le BW-I et le BW-II qui peut être utilisée pour l'imagerie des tissus profonds et la nanothermométrie, et de la possibilité d'agir comme des ions sensibilisateurs d'énergie primaire favorisant une large gamme de transitions radiatives allant de l'UV au NIR. Bien que les RENP dopées au  $\text{Nd}^{3+}$  représentent une excellente base pour la construction de RENP théranostiques multifonctionnelles, on manque d'informations quantitatives sur les performances réelles des RENP dopées au  $\text{Nd}^{3+}$  en termes de *PLQY* et de luminosité absolue. Dans cette optique, un ensemble complet de propriétés photophysiques des RENP dopées au  $\text{Nd}^{3+}$  a été examiné dans un premier temps. La concentration optimale de dopage  $\text{Nd}^{3+}$  a toujours été un point de discordance dans la communauté de recherche sur les RENP, différentes études affirmant que des niveaux de dopage  $\text{Nd}^{3+}$  très faibles ou très élevés donnent les RENP les plus brillants pour l'imagerie des tissus profonds. Il faut espérer que ce différend sera résolu. Les spectres d'émission DS, la décroissance de la photoluminescence, le *PLQY* et la luminosité des RENP  $\text{NaGdF}_4:\text{Nd}^{3+}/\text{NaGdF}_4$  ( $\text{Nd}^{3+}$ -RENP) ont ainsi été systématiquement examinés. Ces caractéristiques photophysiques des  $\text{Nd}^{3+}$ -RENP ont été étudiées en fonction du dopage au  $\text{Nd}^{3+}$  (5, 12,5 et 25 % en moles), de l'ingénierie noyau/enveloppe et des différents milieux de dispersion des RENP. Il a été constaté que des quantités de dopage  $\text{Nd}^{3+}$  plus faibles (5 % en moles), où la relaxation croisée entre les  $\text{Nd}^{3+}$  est minimale, donnent des RENP de *PLQY* plus élevées (figure 3.5). En outre, la présence d'une enveloppe de  $\text{NaGdF}_4$  optiquement inerte améliore considérablement la *PLQY* de différents  $\text{Nd}^{3+}$ -RENP, en particulier lorsqu'ils sont dispersés dans l'eau. L'eau est un désactivateur notoire des transitions radiatives des  $\text{RE}^{3+}$ , c'est pourquoi les barrières physiques, comme les coquilles inorganiques inertes, sont obligatoires pour obtenir des RENP de la plus haute luminosité. La *PLQY* la plus élevée des  $\text{Nd}^{3+}$ -RENP dispersées dans l'eau était de 8,8 %, alors que la *PLQY* des mêmes RENP dispersées dans l'hexane était de 17,4 %, ce qui indique que même en présence d'un obus inerte, la trempe par l'eau reste prédominante. Il est intéressant de noter qu'à une quantité de dopage  $\text{Nd}^{3+}$  plus élevée, la trempe des émissions de DS par relaxation croisée semble être plus importante que celle des molécules de solvant. Dans l'ensemble, les  $\text{Nd}^{3+}$ -RENP faiblement dopés (5 % en moles) étaient également les plus brillants. Bien que la différence de luminosité entre le faible et le fort dopage soit inférieure à celle entre les *PLQY*

des Nd<sup>3+</sup>-RENP comparés (figure 3.8), il est reconnu que les Nd<sup>3+</sup>-RENP faiblement dopés devraient être préférés dans les applications d'imagerie et de nanothermométrie – en évitant un échauffement indésirable et des lectures thermiques erronées.

*Chapitre 4.* Bien que les RENP dopés au Nd<sup>3+</sup> soient des agents d'imagerie NIR attrayants, leurs capacités théranostiques basées sur la lumière sont entravées par l'absence d'émission de photons à haute énergie. Pour ajouter la fonctionnalité manquante, d'autres RE<sup>3+</sup> sont généralement co-dopés en même temps que le Nd<sup>3+</sup>, ce qui permet une conversion ascendante des photons. L'exploration des RENP à conversion ascendante à base de Nd<sup>3+</sup> est née dans la tentative de minimiser l'échauffement indésirable de l'environnement aqueux par la lumière de 980 nm, absorbée par l'Yb<sup>3+</sup> dans les RENP à conversion ascendante classiques et l'eau.<sup>[75,76]</sup> En revanche, les Nd<sup>3+</sup> sont excités par la lumière d'environ 800 nm où l'absorption d'eau est minimale et où une éventuelle surchauffe d'une zone irradiée peut être évitée. En outre, la section d'absorption de Nd<sup>3+</sup> à ~800 nm (~10<sup>-19</sup> cm<sup>2</sup>) est plus grande que celle de Yb<sup>3+</sup> à ~980 nm (~10<sup>-20</sup> cm<sup>2</sup>),<sup>[187,188]</sup> ce qui suggère que Nd<sup>3+</sup> est également mieux adapté à la récolte de la lumière d'excitation. Néanmoins, l'analyse spectrale sur les différentes voies d'excitation des RENP co-dopées Nd<sup>3+</sup>/Yb<sup>3+</sup>, a été sous-représentée par rapport aux systèmes bien étudiés dopés à l'Yb<sup>3+</sup>. En outre, au départ, peu d'attention a été accordée à la manière dont ces nouvelles RENP pourraient être utilisées pour la thérapie et le diagnostic en utilisant leurs émissions de UC et de DS, respectivement. Pour mieux comprendre la photophysique des RENP à conversion ascendante (et descendante) à base de Nd<sup>3+</sup>, il faut étudier les différentes voies d'excitation et leur influence sur les caractéristiques optiques dans une large gamme d'émissions. À cette fin, des RENP à base de NaGdF<sub>4</sub>:Er<sup>3+</sup>, Ho<sup>3+</sup>, Yb<sup>3+</sup>/NaGdF<sub>4</sub>:Nd<sup>3+</sup>, Yb<sup>3+</sup>/NaGdF<sub>4</sub> ont été préparés et leur émission UC et DS a été analysée sous irradiation à 806 et 980 nm. L'excitation à 806 nm a doté les RENP de la plus grande probabilité d'excitation d'émission UC d'ordre supérieur dans les ions Er<sup>3+</sup> et Ho<sup>3+</sup> (figure 4.2). Cet effet a été attribué aux processus simultanés de l'ETU et de l'ESA sous une excitation de 806 nm. D'autres études ont également montré que la saturation des états excités est atteinte plus rapidement sous une excitation de ~800 nm, par opposition à celle de 980 nm, en raison de l'implication de la cascade de transfert d'énergie Nd<sup>3+</sup> → Yb<sup>3+</sup> → Er<sup>3+</sup>/Ho<sup>3+</sup>.<sup>[200,201]</sup> De plus, l'excitation de ces RENP multicouches avec une lumière de 806 nm, a permis d'étendre le nombre de bandes d'émission DS disponibles dans le NIR (figure 4.4). Sous une excitation à 980 nm, seules les émissions DS de Er<sup>3+</sup> et Ho<sup>3+</sup> à environ 1180 et 1550 nm respectivement ont pu être observées. Cependant, lorsqu'ils étaient excités avec une lumière de 806 nm, les RENP montraient également les bandes d'émission de Nd<sup>3+</sup> et Yb<sup>3+</sup>, couvrant presque entièrement les trois BW.

Ces RENP potentiellement théranostiques ont ensuite été transférées dans l'eau via un revêtement de phospholipides et examinées comme i) donneurs d'énergie au chlorine  $e_6$  ( $Ce_6$ ), photosensibilisateur excité utilisé dans le traitement du cancer par PDT et comme ii) agents de contraste NIR pour l'imagerie des tissus profonds. Le complexe entre les RENPs et le  $Ce_6$  pourrait se former rapidement en raison de l'intercalation du photosensibilisateur dans la partie hydrophobe du revêtement phospholipidique, ce qui rapprocherait les molécules de  $Ce_6$  de la surface des RENPs. Dans un tel complexe RENPs- $Ce_6$ , on a observé que le  $Ce_6$  était indirectement excité sous une lumière de 806 nm, ce qui suggère son utilisation potentielle en PDT sous excitation NIR (figure 4.7). De l'autre côté du spectre optique, dans le NIR, différentes émissions DS de RENP ont été recueillies après s'être propagées à travers des tissus *ex vivo* d'une épaisseur pouvant atteindre 10 mm (figure 4.8), ce qui atteste des capacités d'imagerie simultanée des tissus profonds de ces RENP.

*Chapitre 5.* La conception des RENP multicouches du chapitre précédent a encore été améliorée en introduisant une enveloppe dopée  $Yb^{3+}$  entre le noyau des RENP et l'enveloppe dopée  $Nd^{3+}$ , afin de réduire l'extinction inter-ion entre  $Nd^{3+}$  et  $Er^{3+}$  pour une émission encore plus brillante de UC et DS. Plus important encore, ces RENP à noyau/coquille/coquille  $NaGdF_4:Er^{3+}$ ,  $Ho^{3+}$ ,  $Yb^{3+}/NaGdF_4:Yb^{3+}/NaGdF_4:Nd^{3+}$ ,  $Yb^{3+}/NaGdF_4$  ont été étudiés comme les premiers nanothermomètres optiques de ce type fonctionnant dans le BW-III. La nanothermométrie a été obtenue en utilisant les bandes d'émission  $Ho^{3+}$ ,  $Nd^{3+}$  et  $Er^{3+}$  DS autour de 1180, 1340 et 1550 nm. En élevant la température de la dispersion aqueuse des RENP, on a observé que l'intensité d'émission de  $Ho^{3+}$  et  $Er^{3+}$  DS augmentait, tandis que l'intensité d'émission de  $Nd^{3+}$  DS diminuait. Cela a permis de construire deux paramètres thermométriques de rapport d'intensité de luminescence (LIR),  $\Delta(Ho^{3+}/Nd^{3+})$  et  $\Delta(Er^{3+}/Nd^{3+})$  (figure 5.3), fonctionnant respectivement dans les BW-II/II et BW-II/III. Ces nanothermomètres basés sur le RENP avaient une sensibilité thermique relative d'environ  $1 \text{ \%} \cdot \text{°C}^{-1}$ . Il est intéressant de noter que les propriétés de détection de la température dans le BW-III proviennent de l'interaction entre les états électroniques du  $RE^{3+}$  et les modes vibratoires des molécules d'eau. Lorsque la température de l'eau augmente, la liaison hydrogène entre les molécules d' $H_2O$  s'affaiblit, ce qui fait que les groupes OH vibrent à des fréquences plus élevées.<sup>[216 217]</sup> Dans le cas de  $Er^{3+}$ , l'augmentation de l'énergie vibratoire des groupes OH en fonction de la température entraîne une résonance mieux adaptée à la différence d'énergie  $^4I_{11/2} - ^4I_{13/2}$ , ce qui se traduit par une population plus importante de l'état émissif  $^4I_{13/2}$ . En outre, à mesure que la température de l'eau augmente, la première harmonique ( $\sim 6800 \text{ cm}^{-1}$ ) des modes d'étirement des groupes OH passe à des énergies plus élevées,<sup>[218]</sup> ce qui entraîne une

moindre extinction directe de l'état excité  $^4I_{13/2}$  qui donne lieu à une émission de 1550 nm. Ces observations soulignent l'importance de mesurer les propriétés de détection de la température des RENP dans l'environnement dans lequel elles sont conçues pour fonctionner. Lorsque les RENP étaient dispersées dans l'hexane, on a observé le comportement inverse de l'intensité de l'émission de  $Er^{3+}$  DS à la température (elle diminuait à mesure que la température augmentait; figure 5.5), ce qui vient montrer que si les RENP sont étudiées dans des environnements organiques ou sous forme de poudre, les mêmes changements de leur photoluminescence dus à la température ne peuvent être garantis lorsqu'elles sont transférées dans l'eau.

*Chapitre 6.* Les RENP susmentionnés sont définitivement qualifiés de nano-agents théranostiques, ils ont la capacité d'effectuer des diagnostics (imagerie et détection de la température) et des thérapies (c'est-à-dire des PDT) sous une seule excitation de longueur d'onde. Mais y a-t-il une meilleure façon d'aborder le théranostic? Il convient d'envisager des situations où le fait de déclencher une action thérapeutique pourrait être prématuré et dangereux pour le patient. En effet, la pierre angulaire du théranostic est la possibilité d'observer la nanoplateforme théranostique lorsqu'elle atteint et quand elle atteint la cible d'intérêt, et même lorsqu'elle est éliminée de l'organisme. Mais pour la plupart des agents théranostiques, cela signifie que l'observation se fait au prix d'une thérapie simultanée, qui pourrait être nuisible aux tissus sains environnants ou être dépensée avant que ces agents n'entrent en contact avec la maladie réelle. C'est dans cette optique que le concept de RENP théranostique découplé a été introduit. Ces RENP à noyau/enveloppe  $LiYF_4:Tm^{3+}$ ,  $Yb^{3+}/LiYF_4/LiYF_4:Nd^{3+}$  tirent parti de la notion d'excitation orthogonale – différentes longueurs d'onde d'excitation déclenchent différentes photoluminescences  $RE^{3+}$ . Comme auparavant, les RENP englobent ici l'émission UC et DS, respectivement utilisées pour la thérapie et le diagnostic, mais ici ces modalités ne fonctionnent pas en même temps, sauf si on le souhaite. La couche de RENP contenant du  $Nd^{3+}$  absorbe la lumière à 800 nm et émet dans le NIR (BW-I et BW-II) pour une imagerie et une nanothermométrie sans thérapie, tandis que la couche  $Yb^{3+}/Tm^{3+}$  convertit l'excitation à 980 nm en émission UV-visible qui peut déclencher une PDT à la demande. Ces deux couches sont séparées dans l'espace par une coquille intermédiaire en  $LiYF_4$ , de sorte qu'aucun échange d'énergie entre  $Nd^{3+}$  et  $Yb^{3+}$  ne pourrait exciter l'émission de  $Tm^{3+}$  UC et déclencher la thérapie au préalable (figures 6.3 et 6.4). Il est également démontré que l'hôte à base de  $Li^+$  permet de résoudre facilement la structure fine de l'émission de  $Nd^{3+}$  DS autour de 1060 nm pour être utilisée pour la nanothermométrie ratiométrique à bande unique dans le BW-II, et comment elle peut être exploitée pour tenir compte d'un éventuel échauffement induit par la lumière de 980 nm pendant l'exécution de la thérapie (figure 6.6).

Les études in vitro sur des modèles de cancer en 2D et 3D ont permis de montrer que le traitement avec ces RENP théranostiques découplées n'est effectué qu'une fois la lumière de 980 nm allumée, alors que sous une excitation de 800 nm, elles agissent comme des outils de diagnostic pur (figures 6.10 et 6.12). Les RENP théranostiques découplées ont constitué une étape importante dans le développement de la nanomédecine avancée, mais les RENP elles-mêmes doivent encore être optimisées de plusieurs points de vue. L'un d'entre eux consistait à rendre les RENP nettement plus petites, mais sans sacrifier leur luminosité.

*Chapitre 7.* Pour tenter de minimiser la taille des RENP à base de  $\text{Li}^+$ , une méthode modifiée de synthèse par décomposition thermique a été mise au point. Au départ, la taille des RENP classiques à base de  $\text{LiYF}_4:\text{Tm}^{3+}$ ,  $\text{Yb}^{3+}$  a été réduite à environ 5 nm en introduisant de grandes quantités de OM dans le mélange réactionnel (figure 7.1). Cependant, ces nanostructures se sont avérées trop faibles pour les applications thérapeutiques qui nécessiteraient des photons de haute énergie (figure 7.2). Pour améliorer les capacités d'absorption de la lumière des RENP à base de  $\text{Li}^+$  et réduire l'extinction de la photoluminescence par les défauts de surface et les modes de solvants vibratoires, la composition des RENP a été modifiée en  $\text{LiYbF}_4:\text{Tm}^{3+}/\text{LiYF}_4$  à noyau/enveloppe. Bien que la taille des RENP  $\text{LiYbF}_4:\text{Tm}^{3+}$  à noyau seul ait pu être réduite à 5 nm comme dans le cas des RENP  $\text{LiYF}_4:\text{Tm}^{3+}$ ,  $\text{Yb}^{3+}$ , on a remarqué que pendant l'étape de décorticage, la taille globale des RENP a augmenté de manière disproportionnée par rapport au matériau de décorticage ajouté (figure 7.3). Par la suite, on a découvert que les RENP  $\text{LiREF}_4$  ultra petites, synthétisées en grandes quantités de OM, en présence d'un excès d'OA, prennent une forme plus stable chimiquement, ce qui s'accompagne d'une augmentation de leur taille. Pour les RENP  $\text{LiYbF}_4$  et  $\text{LiYbF}_4:\text{Tm}^{3+}$ , cela a entraîné un changement de taille de 5 à environ 10 nm (figures 7.4 et 7.7). Plus important encore, une fois cette étape de stabilisation réalisée, le bombardement des RENP a pu être effectué avec un contrôle maximal, en faisant croître des structures multicouches de la taille et de l'épaisseur de coquille souhaitées (figure 7.9). Par la suite, de petites RENP  $\text{LiYbF}_4:\text{Tm}^{3+}/\text{LiYF}_4$ , d'une taille d'environ 20 nm, ont pu être synthétisées, qui se caractérisaient également par une émission intense d'UV autour de 340 nm. La capacité à générer des photons de haute énergie sous irradiation NIR est de la plus haute importance pour l'utilisation thérapeutique des RENP en tant que médiateurs de réactions photochimiques secondaires. Il est également intéressant de noter que ces petites RENP  $\text{LiYbF}_4:\text{Tm}^{3+}/\text{LiYF}_4$  ont généré autant, voire plus, d'émission de rayons UV que leurs homologues  $\text{LiYF}_4:\text{Tm}^{3+}/\text{Yb}^{3+}$  beaucoup plus grands (~90 nm) (figure 7.10).

Chapitre 8. Suite à ces développements, une vaste bibliothèque de RENP  $\text{LiYbF}_4:\text{RE}^{3+}/\text{LiYF}_4$  ( $\text{RE}^{3+} - \text{Tm}^{3+}, \text{Er}^{3+}, \text{Ho}^{3+}$ ) a été créée (figures 8.1, 8.2 et 8.3) et les caractéristiques photophysiques de ces RENP ont été étudiées en fonction du type de dopant et de la concentration de dopage. Le réglage des couleurs par recouvrement de ces RENP a été identifié, et les valeurs respectives des *PLQY* d'émission de UC à différentes densités de dopage et de puissance d'excitation ont été fournies. La relaxation croisée était particulièrement pertinente dans le cas des RENP  $\text{Tm}^{3+}$ . Les différents processus d'échange d'énergie parmi les  $\text{Tm}^{3+}$ , à différentes quantités de dopage, ont conduit au repeuplement des états excités et ont dicté laquelle des émissions de UC d'ordre élevé, UV ou bleue, est la plus dominante sous excitation NIR (figures 8.5 et 8.9). Dans le cas des  $\text{Er}^{3+}$ -RENP, on n'a observé qu'un léger réglage de la couleur en fonction des différentes concentrations de dopage  $\text{Er}^{3+}$ , l'émission UC rouge de l'état excité  $^4\text{F}_{9/2}$  étant la plus intense dans chaque cas. Bien qu'ils soient les moins efficaces dans la conversion ascendante des photons, les  $\text{Ho}^{3+}$ -RENPs ont un point d'inversion entre leur émission UC verte et rouge, à une densité de puissance d'excitation spécifique, au-dessus de laquelle l'émission UC devient principalement rouge. En même temps, dans les RENP fortement dopés au  $\text{Ho}^{3+}$  (5 mol%), cela conduit à une sortie de couleur presque constante indépendamment de la densité de puissance d'excitation (figure 8.15), ce qui pourrait être intéressant pour les applications d'éclairage et d'impression de sécurité. Dans l'ensemble, ces informations sont très importantes pour apprécier la capacité des petites et brillantes RENP  $\text{LiYbF}_4:\text{RE}^{3+}/\text{LiYF}_4$  à servir d'agents théranostiques grâce à leur émission UC, et la meilleure façon de régler leurs propriétés spectrales pour qu'elles correspondent à l'application prévue.

*Chapitre 9.* Du point de vue du diagnostic, la nanothermométrie à bande unique avec des RENP dopés au  $\text{Nd}^{3+}$  dans le BW-II, présentée pour la première fois au chapitre 6, a été étudiée plus en détail à l'aide des RENP  $\text{LiLuF}_4:\text{Nd}^{3+}/\text{LiLuF}_4$ . Comme mentionné précédemment, les hôtes à base de  $\text{Li}^+$ , dans lesquels les  $\text{Nd}^{3+}$  sont dopés, permettent de résoudre facilement différentes transitions radiatives des  $\text{Nd}^{3+}$ , même à la RT. Par la suite, cela a été exploité pour sélectionner avec soin les plages d'intégration des paramètres thermométriques LIR d'une sensibilité thermique et d'une précision de lecture thermique potentiellement supérieures, par rapport à l'approche nanothermométrique du chapitre 6. Parmi les cinq paramètres thermométriques identifiés (figure 9.4), la transition radiative  $\Delta_2 = I_2/I_3$  de la  $^4\text{F}_{3/2} \rightarrow ^4\text{I}_{11/2}$  autour de 1060 nm, où  $I_2$  (1050.7-1055.9 nm) et  $I_3$  (1055.9-1057.2 nm), s'est avérée la plus adaptée à la nanothermométrie par photoluminescence sans contact: il offre une sensibilité thermique relative appréciable, une incertitude de lecture à basse température et une grande répétabilité des mesures (figures 9.5 et 9.8). Ces RENP ont été étudiées plus avant à l'aide d'un modèle

tissulaire *ex vivo* (figure 9.10), ce qui a permis de fixer des limites claires quant à la possibilité d'utiliser la nanothermométrie  $\text{Nd}^{3+}$  à bande unique pour la mesure sous-cutanée des températures transitoires, une méthode utilisée pour reconnaître les tissus sains des tissus malins. Il est important de noter que la nanothermométrie à bande unique dans le NIR permet de contourner les préoccupations récemment exprimées concernant l'atténuation inégale de l'émission de DS par les tissus, dont il a été démontré qu'elle entraînait une lecture erronée de la température lorsqu'elle était appliquée de manière sous-cutanée.<sup>[171,172]</sup> Par conséquent, les nanothermomètres photoluminescents à bande unique et leurs étroites plages d'intégration spectralement adjacentes, ont le potentiel de mieux maintenir l'étalonnage thermique du NIR malgré les propriétés optiques inhomogènes des tissus.

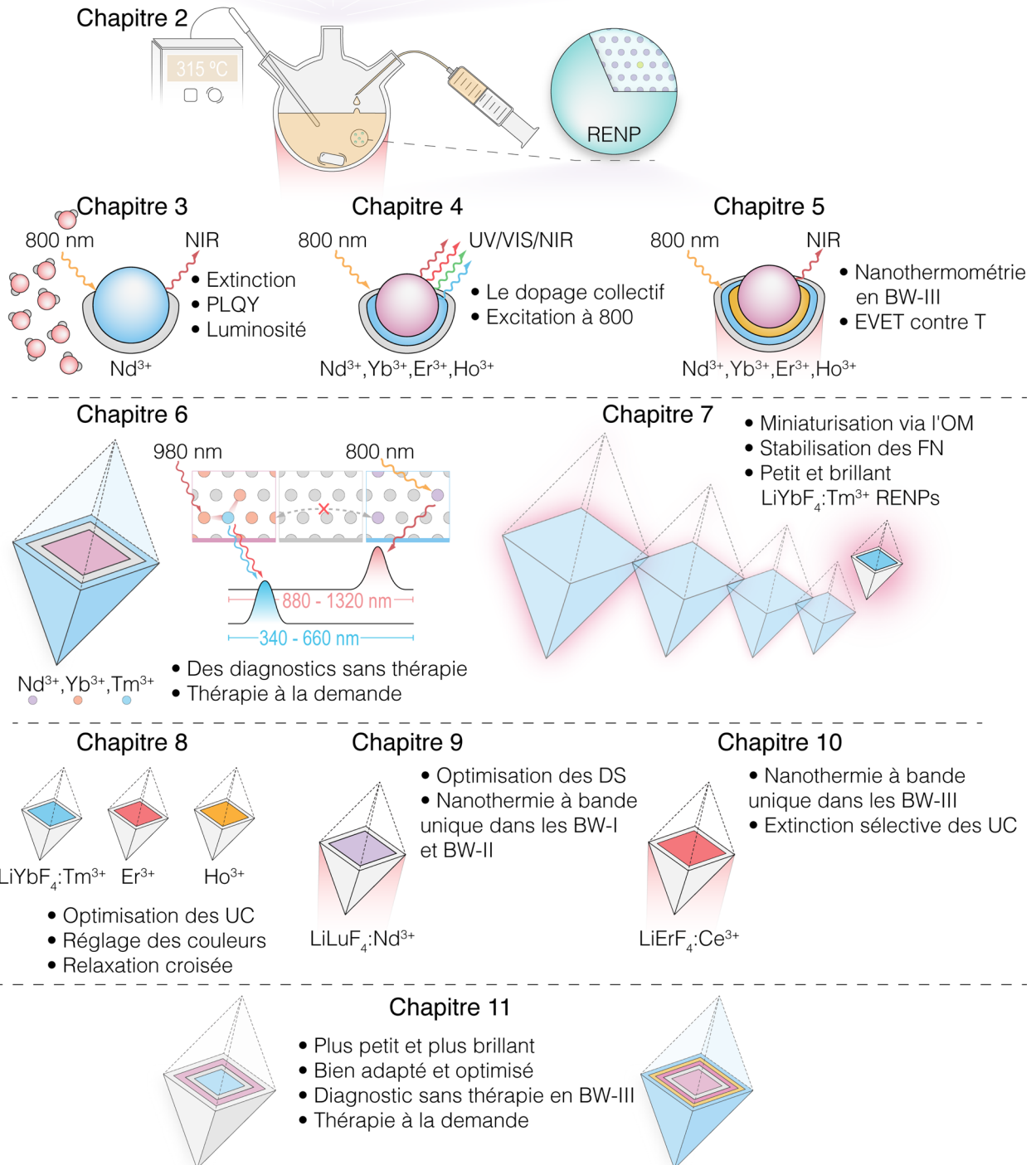
*Chapitre 10.* Néanmoins, l'avertissement de la nanothermométrie à bande unique basée sur le  $\text{Nd}^{3+}$  est qu'elle ne peut fonctionner que jusqu'au BW-II. Pour obtenir le meilleur contraste d'image et la plus grande précision dans la cartographie thermique, des nanothermomètres à bande unique doivent être fabriqués dans la BW-III. Au chapitre 10, les RENP  $\text{LiErF}_4:\text{Ce}^{3+}/\text{LiYF}_4$  ont été étudiés comme de tels nanothermomètres. Dans la bande d'émission  $\text{Er}^{3+}$  DS de l'hôte basé sur le  $\text{Li}^+$ , la résolution est également suffisante pour délimiter deux plages d'intégration pour la nanothermométrie à bande unique dans la BW-III, avec une sensibilité relative équivalente à celle des nanothermomètres à bande unique basés sur le  $\text{Nd}^{3+}$ , dont il a été question dans le chapitre précédent. Ici, le transfert d'énergie entre  $\text{Er}^{3+}$  et les modes vibratoires des molécules d'eau s'est à nouveau révélé être la clé du comportement thermique de ces nanothermomètres. En outre, le dopage au  $\text{Ce}^{3+}$  a été introduit pour éteindre délibérément l'émission UC d' $\text{Er}^{3+}$ , obtenant ainsi une émission DS sans conversion ascendante sous une excitation de 800 nm. Il convient de noter que le dopage au  $\text{Ce}^{3+}$  n'a pas eu d'effet significatif sur l'intensité de l'émission DS de ces RENP, tout en permettant d'améliorer légèrement leur sensibilité thermique relative jusqu'à  $0.45 \text{ \%}\cdot\text{°C}^{-1}$  à  $20 \text{ °C}$ . L'introduction de  $\text{Ce}^{3+}$  dans la composition des RENP  $\text{LiErF}_4/\text{LiYF}_4$  illustre la manière dont ces nanostructures pourraient être intégrées dans les RENP théranostiques découplées pour faire passer l'imagerie et la nanothermométrie sans thérapie à BW-III.

*Chapitre 11.* Enfin, de nouveaux concepts (2<sup>ème</sup> génération) de RENP théranostiques découplés sont proposés (figures 11.1 et 11.2), qui ont été conçus sur la base de l'ensemble des connaissances acquises précédemment. Grâce à de nouvelles méthodes de synthèse et à un dopage optimisé, il a été possible de concevoir des RENP théranostiques découplés beaucoup plus petits et plus brillants que leurs prédécesseurs du chapitre 6. Par exemple, des RENP

multicouches  $\text{LiLuF}_4:\text{Nd}^{3+}/\text{LiLuF}_4/\text{LiYbF}_4:\text{Er}^{3+}/\text{LiYF}_4$  ont été synthétisés avec une taille nette inférieure à 35 nm. Pourtant, malgré leur petite taille, ces RENP bénéficient de toutes les améliorations apportées aux chapitres 3, 7, 8 et 9. Ainsi, ils se caractérisent par une émission intense de  $\text{Nd}^{3+}$  DS sous une excitation de  $\sim 800$  nm et un fort signal rouge de conversion ascendante de  $\text{Er}^{3+}$ , exploitable pour la PDT uniquement lorsqu'ils sont excités avec une lumière de 980 nm. D'autres stratégies, comme la sensibilisation aux colorants, sont également envisagées pour obtenir une émission DS plus brillante et une meilleure imagerie des tissus profonds dans la BW-III avec les RENP multicouches  $\text{LiYbF}_4:\text{Er}^{3+}$ ,  $\text{Tm}^{3+}/\text{LiYF}_4/\text{LiYF}_4:\text{Er}^{3+}$ ,  $\text{Yb}^{3+}$ ,  $\text{Ce}^{3+}/\text{LiYbF}_4/\text{LiYF}_4:\text{Nd}^{3+}/\text{Yb}^{3+}$ .

Dans l'ensemble, cette thèse plaide fortement en faveur des RENP comme agents théranostiques du futur, en soulignant leurs vertus intrinsèques de conversion ascendante et descendante, et en introduisant en même temps de nouvelles façons d'aborder la conception des RENP théranostiques en général. Des recherches supplémentaires sont nécessaires pour avoir une meilleure appréciation de la photophysique et des stratégies de synthèse des RENP, car pour chaque question à laquelle on répond, il en émerge beaucoup d'autres. Les premiers pas dans la direction des RENP théranostiques ont été faits il y a plus de dix ans, et nous espérons que la recherche et les résultats obtenus contribueront à les rapprocher de leur objectif final, des bancs de science des matériaux aux laboratoires de recherche biomédicale et même aux lits des patients.

Li	Y	Chapitre 1	Les éléments de base des RENPs										F		
Na	La	Ce	Pr	Nd	Pm	Sm	Eu	Gd	Tb	Dy	Ho	Er	Tm	Yb	Lu



Petites itérations ci-dessus conduisant à des RENP théranostiques découplés de 2<sup>ème</sup> génération

**Figure 12.1. Thèse dans une coquille de noix.**  
**Représentation schématique des différents RENP étudiés dans cette thèse et points forts de ces études.**



# TABLE OF CONTENTS

---

REMERCIEMENTS .....	III
RÉSUMÉ .....	VII
ABSTRACT .....	IX
SOMMAIRE RÉCAPITULATIF .....	XI
TABLE OF CONTENTS .....	XXXI
LIST OF FIGURES .....	XXXV
LIST OF TABLES .....	XXXIX
LISTE OF ABBREVIATIONS .....	XLI
<b>1 INTRODUCTION .....</b>	<b>1</b>
1.1 NANOMEDICINE .....	1
1.2 NEAR-INFRARED EXCITATION AND EMISSION .....	2
1.3 RARE EARTH DOPED NANOPARTICLES .....	4
1.3.1 <i>Basics of RE<sup>3+</sup> spectroscopy</i> .....	4
1.3.2 <i>Photoluminescence of RENPs</i> .....	6
1.3.3 <i>Morphology and structure of RENPs</i> .....	10
1.3.4 <i>Surface modification of RENPs</i> .....	13
1.4 RENPs IN BIOMEDICINE .....	13
1.4.1 <i>Imaging</i> .....	14
1.4.2 <i>Sensing</i> .....	17
1.4.3 <i>Therapy</i> .....	18
1.4.4 <i>Modulation</i> .....	20
1.5 NANOTHERMOMETRY .....	21
1.5.1 <i>Photoluminescence nanothermometry</i> .....	21
1.5.2 <i>Characterization of nanothermometers</i> .....	25
1.5.3 <i>RENPs as nanothermometers</i> .....	27
1.5.4 <i>Practical use of nanothermometry</i> .....	29
1.5.5 <i>Challenges of nanothermometry</i> .....	32
1.6 MOTIVATION, AIMS AND OUTLINE .....	36
<b>2 MATERIALS AND METHODS .....</b>	<b>38</b>
2.1 RENP SYNTHESIS .....	38
2.1.1 <i>Materials</i> .....	38
2.1.2 <i>Preparation of precursors</i> .....	38
2.1.3 <i>Thermal decomposition</i> .....	39
2.2 SURFACE MODIFICATION .....	40
2.2.1 <i>Ligand removal/exchange</i> .....	40

2.2.2	<i>Phospholipid coating</i> .....	40
2.2.3	<i>Complex formation with Ce<sub>6</sub></i> .....	41
2.3	STRUCTURAL CHARACTERIZATION .....	41
2.4	OPTICAL CHARACTERIZATION .....	42
2.4.1	<i>Steady state spectroscopy and imaging</i> .....	42
2.4.2	<i>Photoluminescence quantum yield</i> .....	42
2.4.3	<i>Photoluminescence decay</i> .....	43
2.5	BIOMEDICAL FRAMEWORK .....	44
2.5.1	<i>Singlet oxygen evaluation</i> .....	44
2.5.2	<i>Cell culturing</i> .....	44
2.5.3	<i>In vitro studies</i> .....	45
<b>3</b>	<b>ND<sup>3+</sup>-RENPS. DOWNSHIFTING</b> .....	<b>47</b>
3.1	RENPs PREPARATION AND STRUCTURAL CHARACTERIZATION .....	48
3.2	STEADY-STATE AND TIME-RESOLVED PHOTOLUMINESCENCE .....	49
3.3	PLQY ANALYSIS .....	51
3.4	FURTHER DISCUSSION AND BRIGHTNESS .....	54
<b>4</b>	<b>ND<sup>3+</sup>-RENPS. UPCONVERSION AND DOWNSHIFTING</b> .....	<b>57</b>
4.1	RENPs PREPARATION AND STRUCTURAL CHARACTERIZATION .....	57
4.2	UC EMISSION .....	59
4.3	DS EMISSION .....	62
4.4	PROOF-OF-CONCEPT STUDIES .....	63
4.5	DISCUSSION .....	67
<b>5</b>	<b>ND<sup>3+</sup>-RENPS. NANOTHERMOMETRY IN BW-III</b> .....	<b>69</b>
5.1	RENPs PREPARATION AND CHARACTERIZATION .....	69
5.2	NIR NANOTHERMOMETRY .....	71
5.3	UNDERSTANDING THERMAL BEHAVIOR OF RENPs .....	73
5.4	DISCUSSION .....	75
<b>6</b>	<b>DECOUPLED THERANOSTICS WITH RENPs</b> .....	<b>77</b>
6.1	RENPs PREPARATION AND STRUCTURAL CHARACTERIZATION .....	78
6.2	OPTICAL CHARACTERIZATION OF RENPs .....	80
6.3	ND <sup>3+</sup> SINGLE-BAND NANOTHERMOMETRY .....	82
6.4	RENPs-CE <sub>6</sub> AND <i>IN VITRO</i> CHARACTERIZATION .....	84
6.5	ON-DEMAND THERAPY .....	87
6.6	DISCUSSION .....	88
<b>7</b>	<b>MINIATURIZATION OF LI<sup>+</sup>-BASED RENPs</b> .....	<b>90</b>
7.1	SIZE OF RENPs VS OM/OA RATIO .....	91

7.2	UNCONTROLLED SHELL GROWTH .....	94
7.3	STABILIZATION PROTOCOL .....	96
7.4	CONTROLLED SHELL GROWTH.....	100
<b>8</b>	<b>OPTIMIZING LiYbF<sub>4</sub>:RE<sup>3+</sup>/LiYF<sub>4</sub> RENPS .....</b>	<b>105</b>
8.1	RENIP PREPARATION AND STRUCTURAL CHARACTERIZATION .....	105
8.2	LiYbF <sub>4</sub> :Tm <sup>3+</sup> /LiYF <sub>4</sub> .....	108
8.3	LiYbF <sub>4</sub> :Er <sup>3+</sup> /LiYF <sub>4</sub> .....	113
8.4	LiYbF <sub>4</sub> :Ho <sup>3+</sup> /LiYF <sub>4</sub> .....	117
8.5	DISCUSSION .....	119
<b>9</b>	<b>SINGLE-BAND NANOTHERMOMETRY – Nd<sup>3+</sup> .....</b>	<b>124</b>
9.1	RENIP PREPARATION AND CHARACTERIZATION .....	125
9.2	Nd <sup>3+</sup> SINGLE-BAND NANOTHERMOMETRY .....	127
9.3	EX VIVO IMAGING AND TEMPERATURE SENSING .....	132
<b>10</b>	<b>SINGLE-BAND NANOTHERMOMETRY – Er<sup>3+</sup> .....</b>	<b>136</b>
10.1	RENIP PREPARATION AND CHARACTERIZATION .....	137
10.2	Er <sup>3+</sup> NANOTHERMOMETRY .....	141
10.3	UNDERSTANDING THERMAL BEHAVIOR OF Er <sup>3+</sup> DS EMISSION .....	143
10.4	RELIABILITY OF Er <sup>3+</sup> NANOTHERMOMETRY IN BW-III .....	146
<b>11</b>	<b>2<sup>ND</sup> GENERATION DECOUPLED THERANOSTICS RENPS .....</b>	<b>150</b>
<b>12</b>	<b>GENERAL DISCUSSION AND CONCLUSIONS.....</b>	<b>153</b>
<b>13</b>	<b>BIBLIOGRAPHY .....</b>	<b>159</b>
	<b>APPENDIX I – XRD DATA.....</b>	<b>178</b>
	<b>APPENDIX II – PLQY DATA .....</b>	<b>182</b>
	<b>APPENDIX III – FTIR DATA .....</b>	<b>183</b>
	<b>APPENDIX IV – TEMPERATURE REPEATABILITY DATA.....</b>	<b>184</b>
	<b>APPENDIX V – ADDITIONAL NIR IMAGES .....</b>	<b>187</b>
	<b>APPENDIX VI – DECONVOLUTION OF Tm<sup>3+</sup> EMISSION BAND AT 790 NM.....</b>	<b>189</b>



## LIST OF FIGURES

---

FIGURE 1.1. LIGHT BASED THERANOSTICS AND NANOMEDICINE.....	1
FIGURE 1.2. TISSUE EXTINCTION AND BIOLOGICAL IMAGING WINDOWS.....	2
FIGURE 1.3. RE <sup>3+</sup> ENERGY LEVEL SPLITTING.....	5
FIGURE 1.4. DIEKE'S DIAGRAM. ....	5
FIGURE 1.5. RENPs AND THEIR EXCITATION-EMISSION.....	6
FIGURE 1.6. YB <sup>3+</sup> /ER <sup>3+</sup> EXCITATION-EMISSION.....	8
FIGURE 1.7. RENPs' PHOTOLUMINESCENCE VS STRUCTURE.....	10
FIGURE 1.8. APPLICATION OF RENPs IN BIOMEDICINE.....	14
FIGURE 1.9. DEEP-TISSUE IMAGING WITH RENPs.....	15
FIGURE 1.10. RENPs AS ENERGY DONORS IN PDT.....	20
FIGURE 1.11. PHOTOLUMINESCENCE NANOTHERMOMETRY.....	22
FIGURE 1.12. APPLICATION OF RENPs AS NANOTHERMOMETERS.....	30
FIGURE 3.1. STRUCTURAL CHARACTERIZATION OF Nd <sup>3+</sup> -RENPs.....	49
FIGURE 3.2. PHOTOLUMINESCENCE OF Nd <sup>3+</sup> -RENPs.....	50
FIGURE 3.3. EXCITED STATE LIFETIMES OF Nd <sup>3+</sup> -RENPs.....	51
FIGURE 3.4. SPECTRUM OF BLANK NaGDF <sub>4</sub> RENPs.....	52
FIGURE 3.5. PLQY OF Nd <sup>3+</sup> -RENPs.....	52
FIGURE 3.6. PLQY OF Nd <sup>3+</sup> -RENPs INDIVIDUAL EMISSION BANDS.....	54
FIGURE 3.7. QUENCHING OF Nd <sup>3+</sup> EXCITED STATES.....	55
FIGURE 3.8. RELATIVE BRIGHTNESS OF Nd <sup>3+</sup> -RENPs.....	56
FIGURE 4.1. STRUCTURAL CHARACTERIZATION OF Nd <sup>3+</sup> -BASED MULTILAYERED RENPs.....	58
FIGURE 4.2. UC EMISSION OF Nd <sup>3+</sup> -BASED MULTILAYERED RENPs.....	59
FIGURE 4.3. UC EMISSION-EXCITATION SCHEME FOR Nd <sup>3+</sup> -BASED MULTILAYERED RENPs.....	61
FIGURE 4.4. DS EMISSION OF Nd <sup>3+</sup> -BASED MULTILAYERED RENPs.....	62
FIGURE 4.5. DS EMISSION-EXCITATION SCHEME FOR Nd <sup>3+</sup> -BASED MULTILAYERED RENPs.....	63
FIGURE 4.6. PHOTOLUMINESCENCE OF Nd <sup>3+</sup> -BASED MULTILAYERED RENPs IN WATER.....	64

FIGURE 4.7. RENPs-CE <sub>6</sub> COMPLEX.....	65
FIGURE 4.8. THROUGH-TISSUE VISUALIZATION OF Nd <sup>3+</sup> -BASED MULTILAYERED RENPs.....	66
FIGURE 5.1. STRUCTURAL CHARACTERIZATION OF Nd <sup>3+</sup> -BASED RENPs FOR NANOTHERMOMETRY.....	70
FIGURE 5.2. UC AND DS SPECTRA OF Nd <sup>3+</sup> -BASED RENPs FOR NANOTHERMOMETRY.....	71
FIGURE 5.3. NIR NANOTHERMOMETRY WITH Nd <sup>3+</sup> -BASED RENPs.....	71
FIGURE 5.4. TEMPERATURE SENSING PROPERTIES OF Nd <sup>3+</sup> -BASED RENPs.....	72
FIGURE 5.5. NIR NANOTHERMOMETRY WITH Nd <sup>3+</sup> -BASED RENPs IN HEXANE.....	73
FIGURE 5.6. DS EMISSION-EXCITATION OF Nd <sup>3+</sup> -BASED RENPs AND TEMPERATURE DEPENDENCE.....	74
FIGURE 5.7. RELATIVE SENSITIVITY IN DIFFERENT ENVIRONMENTS.....	75
FIGURE 6.1. STRUCTURAL CHARACTERIZATION OF DECOUPLED THERANOSTICS RENPs.....	79
FIGURE 6.2. UC AND DS EMISSION SPECTRA OF DECOUPLED THERANOSTICS RENPs IN HEXANE.....	80
FIGURE 6.3. EXCITATION-EMISSION OF DECOUPLED THERANOSTICS RENPs.....	81
FIGURE 6.4. UC AND DS EMISSION SPECTRA OF DECOUPLED THERANOSTICS RENPs IN WATER.....	81
FIGURE 6.5. NIR NANOTHERMOMETRY WITH DECOUPLED THERANOSTICS RENPs.....	83
FIGURE 6.6. MEASURING TRANSIENT TEMPERATURES WITH DECOUPLED THERANOSTICS RENPs.....	84
FIGURE 6.7. EVALUATING CYTOTOXICITY OF DECOUPLED THERANOSTIC RENPs.....	85
FIGURE 6.8. DECOUPLED THERANOSTIC RENPs INSIDE CANCER CELLS.....	85
FIGURE 6.9. DECOUPLED THERANOSTIC RENPs-CE <sub>6</sub> COMPLEX.....	86
FIGURE 6.10. ON-DEMAND PDT WITH DECOUPLED THERANOSTICS RENPs-CE <sub>6</sub> .....	87
FIGURE 6.11. CELL VIABILITY POST PDT TREATMENT WITH DECOUPLED THERANOSTICS RENPs-CE <sub>6</sub> .....	88
FIGURE 6.12. ON-DEMAND PDT WITH DECOUPLED THERANOSTICS RENPs-CE <sub>6</sub> IN CANCER SPHEROIDS.....	89
FIGURE 7.1. STRUCTURAL CHARACTERIZATION OF LiYF <sub>4</sub> :Tm <sup>3+</sup> , Yb <sup>3+</sup> RENPs SYNTHESIZED IN THE PRESENCE OF OM.....	91
FIGURE 7.2. UC OF LiYF <sub>4</sub> :Tm <sup>3+</sup> , Yb <sup>3+</sup> RENPs SYNTHESIZED IN THE PRESENCE OF OM.....	93
FIGURE 7.3. UNCONTROLLED SHELLING OF LiYbF <sub>4</sub> :Tm <sup>3+</sup> RENPs.....	95
FIGURE 7.4. CHARACTERIZATION OF LiYbF <sub>4</sub> :Tm <sup>3+</sup> AND LiYF <sub>4</sub> :Tm <sup>3+</sup> , Yb <sup>3+</sup> RENPs AFTER OA TREATMENT.....	97
FIGURE 7.5. CHARACTERIZATION OF LiYbF <sub>4</sub> :Tm <sup>3+</sup> AND LiYF <sub>4</sub> :Tm <sup>3+</sup> , Yb <sup>3+</sup> RENPs AFTER OA (OR OM) TREATMENT.....	98

FIGURE 7.6. LiYBF <sub>4</sub> :Tm <sup>3+</sup> RENPs STABILIZED AT VARIOUS CONDITIONS.....	99
FIGURE 7.7. CHARACTERIZATION OF LiYBF <sub>4</sub> AND LiYF <sub>4</sub> RENPs AFTER OA TREATMENT.....	99
FIGURE 7.8. CHARACTERIZATION OF LiLAF <sub>4</sub> , LiGDF <sub>4</sub> AND LiLuF <sub>4</sub> RENPs AFTER OA TREATMENTS.....	100
FIGURE 7.9. LiYBF <sub>4</sub> :Tm <sup>3+</sup> /LiYBF <sub>4</sub> VS LiYBF <sub>4</sub> :Tm <sup>3+</sup> /LiYF <sub>4</sub> RENPs .....	101
FIGURE 7.10. STRUCTURAL AND SPECTRAL CHARACTERIZATION OF LiYBF <sub>4</sub> :Tm <sup>3+</sup> /LiYF <sub>4</sub> RENPs.....	102
FIGURE 7.11. LiYBF <sub>4</sub> :Tm <sup>3+</sup> /LiYF <sub>4</sub> VS LiYF <sub>4</sub> :Tm <sup>3+</sup> , Yb <sup>3+</sup> RENPs.....	104
FIGURE 8.2. STRUCTURAL CHARACTERIZATION OF LiYBF <sub>4</sub> :Er <sup>3+</sup> /LiYF <sub>4</sub> RENPs.....	107
FIGURE 8.1. STRUCTURAL CHARACTERIZATION OF LiYBF <sub>4</sub> :Tm <sup>3+</sup> /LiYF <sub>4</sub> RENPs.....	107
FIGURE 8.3. STRUCTURAL CHARACTERIZATION OF LiYBF <sub>4</sub> :Ho <sup>3+</sup> /LiYF <sub>4</sub> RENPs.....	108
FIGURE 8.4. SPECTRAL CHARACTERIZATION OF LiYBF <sub>4</sub> :Tm <sup>3+</sup> /LiYF <sub>4</sub> RENPs.....	109
FIGURE 8.5. UC EMISSION INTENSITY OF LiYBF <sub>4</sub> :Tm <sup>3+</sup> /LiYF <sub>4</sub> RENPs ADJACENT EMISSION BANDS.....	110
FIGURE 8.6. CROSS-RELAXATION IN LiYBF <sub>4</sub> :Tm <sup>3+</sup> /LiYF <sub>4</sub> RENPs.....	110
FIGURE 8.7. POWER PLOT ANALYSIS OF LiYBF <sub>4</sub> :Tm <sup>3+</sup> /LiYF <sub>4</sub> RENPs.....	111
FIGURE 8.8. EXCITED STATE LIFETIMES OF LiYBF <sub>4</sub> :Tm <sup>3+</sup> /LiYF <sub>4</sub> RENPs.....	112
FIGURE 8.9. PLQY OF UC EMISSION OF LiYBF <sub>4</sub> :Tm <sup>3+</sup> /LiYF <sub>4</sub> RENPs.....	113
FIGURE 8.11. POWER PLOT ANALYSIS OF LiYBF <sub>4</sub> :Er <sup>3+</sup> /LiYF <sub>4</sub> RENPs.....	114
FIGURE 8.10. SPECTRAL CHARACTERIZATION OF LiYBF <sub>4</sub> :Er <sup>3+</sup> /LiYF <sub>4</sub> RENPs.....	114
FIGURE 8.12. POSSIBLE ER <sup>3+</sup> 4F <sub>9/2</sub> ENERGY LEVEL EXCITATION IN LiYBF <sub>4</sub> :Er <sup>3+</sup> /LiYF <sub>4</sub> RENPs.....	115
FIGURE 8.13. EXCITED STATE LIFETIMES OF LiYBF <sub>4</sub> :Er <sup>3+</sup> /LiYF <sub>4</sub> RENPs.....	116
FIGURE 8.14. PLQY OF UC EMISSION OF LiYBF <sub>4</sub> :Er <sup>3+</sup> /LiYF <sub>4</sub> RENPs.....	116
FIGURE 8.15. SPECTRAL CHARACTERIZATION OF LiYBF <sub>4</sub> :Ho <sup>3+</sup> /LiYF <sub>4</sub> RENPs.....	117
FIGURE 8.16. POWER PLOT ANALYSIS OF LiYBF <sub>4</sub> :Ho <sup>3+</sup> /LiYF <sub>4</sub> RENPs.....	118
FIGURE 8.17. POSSIBLE Ho <sup>3+</sup> 5S <sub>2</sub> /5F <sub>4</sub> ENERGY LEVELS EXCITATION IN LiYBF <sub>4</sub> :Ho <sup>3+</sup> /LiYF <sub>4</sub> RENPs.....	118
FIGURE 8.19. PLQY OF UC EMISSION OF LiYBF <sub>4</sub> :Ho <sup>3+</sup> /LiYF <sub>4</sub> RENPs.....	119
FIGURE 8.18. EXCITED STATE LIFETIMES OF LiYBF <sub>4</sub> :Ho <sup>3+</sup> /LiYF <sub>4</sub> RENPs.....	119
FIGURE 8.21. PERCEIVED COLOR OF LiYBF <sub>4</sub> :RE <sup>3+</sup> /LiYF <sub>4</sub> RENPs.....	121
FIGURE 8.20. NUMBER OF RE <sup>3+</sup> CONSIDERATION IN LiYBF <sub>4</sub> :RE <sup>3+</sup> /LiYF <sub>4</sub> RENPs.....	121
FIGURE 8.22. DS EMISSION OF LiYBF <sub>4</sub> :RE <sup>3+</sup> /LiYF <sub>4</sub> RENPs.....	122

FIGURE 9.1. STRUCTURAL CHARACTERIZATION OF $\text{LiLuF}_4:\text{Nd}^{3+}/\text{LiLuF}_4$ ( $\text{LiYF}_4$ ) RENPs. ....	126
FIGURE 9.2. STRUCTURAL CHARACTERIZATION OF $\text{LiLuF}_4:\text{Nd}^{3+} + \text{LiGdF}_4$ RENPs.....	126
FIGURE 9.3. SPECTRAL CHARACTERIZATION OF $\text{LiLuF}_4:\text{Nd}^{3+}/\text{LiLuF}_4$ ( $\text{LiYF}_4$ ) RENPs. ....	127
FIGURE 9.4. NIR NANOTHERMOMETRY WITH $\text{LiLuF}_4:\text{Nd}^{3+}/\text{LiLuF}_4$ RENPs.....	128
FIGURE 9.5. TEMPERATURE SENSING PROPERTIES OF $\text{LiLuF}_4:\text{Nd}^{3+}/\text{LiLuF}_4$ RENPs.....	129
FIGURE 9.6. SPECTRUM OF $\text{LiLuF}_4:\text{Nd}^{3+}/\text{LiLuF}_4$ RENPs AROUND 1060 NM AND ENERGY LEVELS.....	130
FIGURE 9.7. RELATIVE SENSITIVITY OF $\text{LiLuF}_4:\text{Nd}^{3+}/\text{LiLuF}_4$ ( $\text{LiYF}_4$ ) RENPs AS NANOTHERMOMETERS. ....	130
FIGURE 9.8. TEMPERATURE UNCERTAINTY OF $\text{LiLuF}_4:\text{Nd}^{3+}/\text{LiLuF}_4$ RENPs AS NANOTHERMOMETERS. ....	131
FIGURE 9.9. SUBCUTANEOUS IMAGING WITH $\text{LiLuF}_4:\text{Nd}^{3+}/\text{LiLuF}_4$ RENPs <i>EX VIVO</i> .....	132
FIGURE 9.10. SUBCUTANEOUS TRANSIENT TEMPERATURE MEASUREMENT WITH $\text{LiLuF}_4:\text{Nd}^{3+}/\text{LiLuF}_4$ RENPs. ....	133
FIGURE 9.11. TEMPERATURE SENSING PROPERTIES OF $\text{LiLuF}_4:\text{Nd}^{3+}/\text{LiLuF}_4$ RENPs <i>EX VIVO</i> .....	134
FIGURE 9.12. DS EMISSION OF $\text{LiLuF}_4:\text{Nd}^{3+}/\text{LiLuF}_4$ RENPs <i>EX VIVO</i> . ....	135
FIGURE 10.1. STRUCTURAL CHARACTERIZATION OF $\text{LiErF}_4:\text{Ce}^{3+}/\text{LiYF}_4$ RENPs.....	138
FIGURE 10.2. SPECTRAL CHARACTERIZATION OF $\text{LiErF}_4/\text{LiYF}_4$ RENPs.....	139
FIGURE 10.3. SPECTRAL CHARACTERIZATION OF $\text{LiErF}_4:\text{Ce}^{3+}/\text{LiYF}_4$ RENPs.....	140
FIGURE 10.4. NIR NANOTHERMOMETRY WITH $\text{LiErF}_4:\text{Ce}^{3+}/\text{LiYF}_4$ RENPs.....	141
FIGURE 10.5. TEMPERATURE SENSING PROPERTIES OF $\text{LiErF}_4:\text{Ce}^{3+}/\text{LiYF}_4$ RENPs VIA DS EMISSION. ....	142
FIGURE 10.6. TEMPERATURE SENSING PROPERTIES OF $\text{LiErF}_4:\text{Ce}^{3+}/\text{LiYF}_4$ RENPs VIA UC EMISSION. ....	143
FIGURE 10.7. TEMPERATURE SENSING PROPERTIES OF $\text{LiErF}_4:\text{Ce}^{3+}/\text{LiYF}_4$ RENPs IN HEXANE AND HEAVY WATER. ....	144
FIGURE 10.8. TEMPERATURE DEPENDENCE OF $\text{LiErF}_4:\text{Ce}^{3+}/\text{LiYF}_4$ RENPs' DS EMISSION. ....	145
FIGURE 10.9. TEMPERATURE SENSING WITH $\text{LiErF}_4/\text{LiYF}_4$ RENPs UNDER DIFFERENT EXCITATION POWER.....	147
FIGURE 10.10. TEMPERATURE SENSING WITH $\text{LiErF}_4/\text{LiYF}_4$ RENPs AGAINST WATER ABSORPTION.....	148
FIGURE 10.11. $\Delta_{DS}$ AND $\Delta_{DS\text{ NARROW}}$ OF $\text{LiErF}_4/\text{LiYF}_4$ RENPs AGAINST WATER ABSORPTION.....	149
FIGURE 11.1. 2 <sup>ND</sup> GENERATION DECOUPLED THERANOSTICS RENPs – EXAMPLE I. ....	150
FIGURE 11.2. 2 <sup>ND</sup> GENERATION DECOUPLED THERANOSTICS RENPs – EXAMPLE II. ....	152
FIGURE 12.1. THESIS IN A NUT-SHELL. ....	158

## LIST OF TABLES

---

TABLE 1. CHEMICALS EMPLOYED IN THE PREPARATION OF THE PRECURSORS AND SYNTHESIS OF RENPs..... 38



## LISTE OF ABBREVIATIONS

---

NPs	nanoparticles
UV	ultraviolet
vis	visible
NIR	near-infrared
BW	biological imaging windows
OCT	optical coherence tomography
PTT	photothermal therapy
PDT	photodynamic therapy
RE <sup>3+</sup>	rare earth ions
RENPs	rare earth nanoparticles
DS	downshifting (abbreviated only together with emission, as DS emission)
UC	upconversion (abbreviated only together with emission, as UC emission)
ESA	excited state absorption
GSA	ground state absorption
ET	energy transfer
ETU	energy transfer upconversion
BET	back energy transfer
PS	photosensitizer
ROS	reactive oxygen species
FRET	Förster resonance energy transfer
TPP	tetraphenylporphyrin
Ce <sub>6</sub>	chlorin e <sub>6</sub>
RB	rose bengal
MB	methylene blue
ZnPC	zinc phthalocyanine
LIR	luminescence intensity ratio
PLQY	photoluminescence quantum yield
Na-TFA	sodium trifluoroacetate
Li-TFA	lithium trifluoroacetate
RE <sub>2</sub> O <sub>3</sub>	rare earth oxides

RE-TFA	rare earth trifluoroacetate
OA	oleic acid
OM	oleylamine
ODE	1-octadecene
RT	room temperature
DOPC	1,2-dipalmitoleoyl- <i>sn</i> -glycero-3-phosphocholine
PEG-DOPE	1,2-dioleoyl- <i>sn</i> -glycero-3-phosphoethanolamine-N-[methoxy(polyethylene glycol)-2000]
XRD	X-ray powder diffraction
TEM	transmission electron microscopy
HAADF-STEM	high-angle annular dark-field scanning transmission electron microscopy
EDX	energy-dispersive X-ray analysis
ICP-OES	inductively coupled plasma optical emission spectroscopy
FTIR	Fourier transform infrared spectroscopy
LP	long-pass
SOSG	singlet oxygen sensor green
DMEM	modified Eagles cell culture medium
LDH	lactate dehydrogenase
SD	standard deviation
c	core
s	shells
EVET	electronic-to-vibrational energy transfer
FN	first nuclei
CIE	Commission Internationale de l'éclairage
FWHM	full width at half maximum
TC	thermocouple
ICG	indocyanine green

# 1 INTRODUCTION

---

## 1.1 Nanomedicine

Back in 1966 a science-fiction movie “Fantastic Voyage” depicted a crew on board of a submarine, miniaturized to the cellular level, and sent on a mission inside a scientist’s body to treat his brain injury. As incredible as this may sound even in the present time, the birth of nanotechnology and its “light-speed” development does promise to turn this futuristic vision into reality. Nanometer scale (1-100 nm) objects – nanoparticles (NPs), nanorods, or nanosheets – have unique physico-chemical properties that can be exploited in medicine for diagnosis, therapy, sensing, or actuation of physiological responses.<sup>[1]</sup> In fact, there are already a number of nanomedicines available on the market, or undergoing clinical testing, which offer better drug delivery,<sup>[2]</sup> high-precision therapy,<sup>[3]</sup> and enhanced imaging.<sup>[4]</sup>

The focal point of materials science research has become the so called *theranostic* NPs – multifunctional nanoplatforms equipped with *therapeutic* as well as *diagnostic* means for personalized medicine.<sup>[5–7]</sup> Diagnostics-wise, these NPs can serve as imaging contrast agents (optical, magnetic, X-ray, and photoacoustic) and enriched with the therapeutic capacity, they can act as drug carriers, mediators of chemical processes, or heat delivery sources.<sup>[8]</sup> In particular, optical theranostic NPs offer laser-point-accuracy in non-invasive disease (i.e. cancer) detection and eradication.<sup>[9]</sup> It is envisioned that photoluminescent theranostic NPs will be able to illuminate the malignancy and treat it under remote control with reduced damage to healthy tissues (Figure 1.1). However, many obstacles are yet to be overcome before these NPs can be sent on their own fantastic voyages for the betterment of human health.

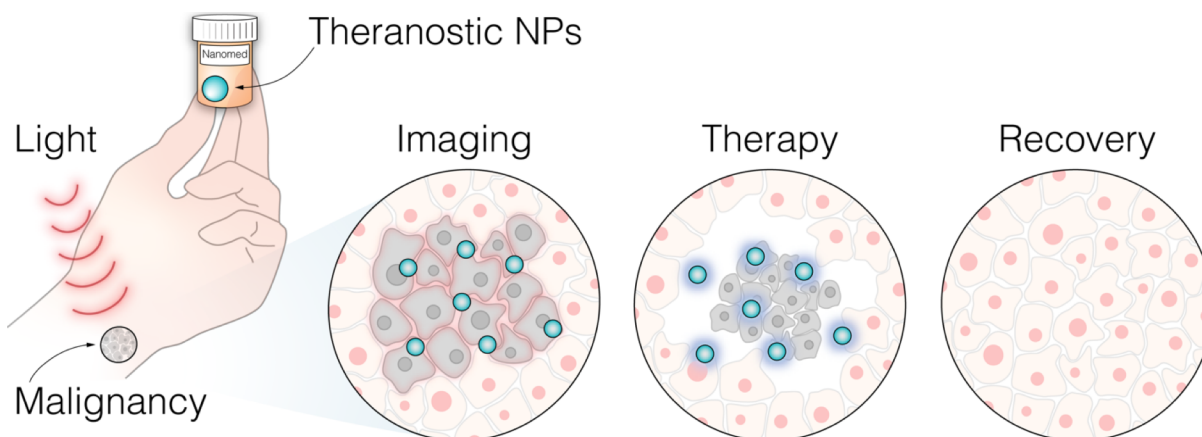


**Figure 1.1. Light based theranostics and nanomedicine.**

**Schematic depiction of photoluminescent theranostic NPs that accumulate at the site of malignancy and under light excitation visualize and treat the cause at a cellular level, presenting minimal healthy tissue damage and rapid patient recovery.**

## 1.2 Near-infrared excitation and emission

By definition photoluminescent NPs act as light converters, absorbing excitation energy and re-emitting it at frequencies that are specific to each NP, allowing to discriminate structures of interest against the surrounding background. However, many NPs operate at optical wavelengths corresponding to the ultraviolet-visible (UV-vis) spectral range where biological tissues greatly absorb and scatter the light.<sup>[10]</sup> In such case, excitation light can neither penetrate deep inside the tissue nor can the emergent emission escape to be detected. Even if it could be detected, the photon path is perturbed by scattering to the extent that it is impossible to pinpoint the exact location of a target. Endogenous biological molecules (porphyrins, flavins, NADH/NADPH, collagen, etc.) also exhibit photoluminescence under UV-vis excitation (a.k.a. tissue autofluorescence), which mixes with the emission of NPs located at similar wavelengths, further compromising the imaging.<sup>[11]</sup> Combined, tissue optical properties dictate the imaging depth, resolution and contrast that can be attained, thus photoluminescent agents need to be custom tailored to maximize useful information gathered.

A solution to many of these issues is to move into the near-infrared (NIR) spectral region. Absorption of major tissue components, such as hemoglobin, melanin, fat and water, all have minima within the so called biological imaging windows (BW) in the NIR.<sup>[12-14]</sup> These BW correspond to 750-950 nm (BW-I), 1000-1350 nm (BW-II), and 1500-1800 nm (BW-III) spectral ranges, where light is less attenuated and penetrates tissues deeper (Figure 1.2). Crucially, there is little to no autofluorescence in BW-II and BW-III. Also light scattering in tissues inversely depends on its wavelength ( $\mu_s \sim \lambda^{-\alpha}$ , where  $\alpha$  is 0.2-4), meaning that as light attenuation by scattering is reduced at longer wavelengths – high-contrast photoluminescence images can be acquired.<sup>[15]</sup>

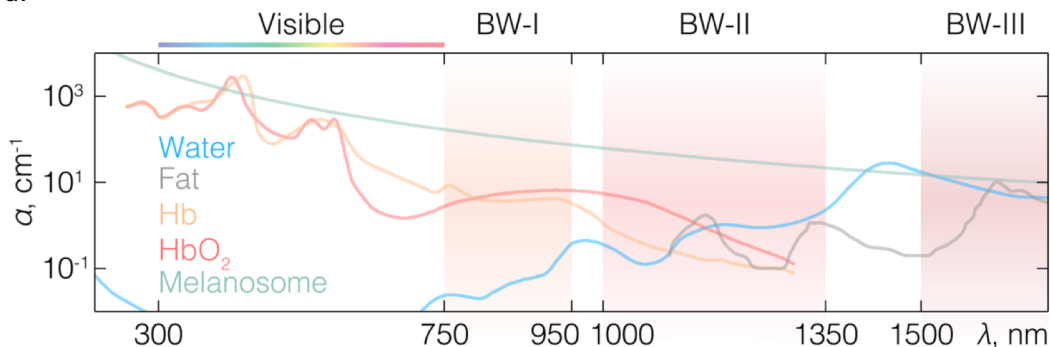


**Figure 1.2. Tissue extinction and biological imaging windows.**

Extinction spectra of tissue components primarily responsible for light attenuation and reduced imaging depth. Highlighted spectral ranges correspond to BW-I, -II, and -III, where light can pierce deeper within tissues, and emission can be detected with greater contrast.

Effective shift towards NIR imaging wavelengths requires development of NIR radiation absorbing and emitting contrast agents. As such, NIR-emitting organic molecules,<sup>[16]</sup> quantum dots,<sup>[17]</sup> noble metal NPs,<sup>[18]</sup> chalcogenide NPs,<sup>[19,20]</sup> and carbon nanotubes,<sup>[21]</sup> are all actively researched as NIR contrast agents. It is important to note early, however, that current state-of-the-art NIR deep-tissue imaging implies that high-contrast images are acquired from depths down to few millimeters.<sup>[22]</sup> Although NIR radiation can penetrate few centimeters of tissue, imaging at those depths with micrometer-scale resolution is impossible, and can reasonably be used only for contrast agent's rough localization. Perhaps tissue clearing methods could negate part of these limitations and advance high-resolution imaging to greater depths,<sup>[23]</sup> while endoscopic techniques can be used to reach internal organs, otherwise inaccessible to light.<sup>[24]</sup>

The potential of NIR imaging has been exemplified on numerous occasions. The group of Hongjie Dai, for instance, combined NIR emitting carbon nanotubes with dynamic image acquisition for high spatial and temporal resolution deep-tissue imaging. These techniques enabled subcutaneous measurements of blood flow velocity in femoral arteries for ischemia detection,<sup>[22]</sup> as well as blood perfusion in cerebral vessels that are helpful to advance research on impaired neurovascular and neurometabolic regulation.<sup>[21]</sup> More recently, Carr et al., introduced a NIR imaging concept that exploits water absorption between BW-II and BW-III.<sup>[25]</sup> The authors showed that NIR photoluminescence of quantum dots can be spatially "filtered" by water attenuation as it propagates through the tissue, eliminating highly scattered photons and detecting only those that retained their propagation direction from the origin of photoluminescence. Non-photoluminescent agents such as NIR radiation scattering gold nanorods can also be used for NIR imaging as in the case of optical coherence tomography (OCT).<sup>[26]</sup> Furthermore, Marin et al. showed that CuS nanoparticles with near-unity absorption coefficient can be used as dark-contrast OCT agents within all three BWs.<sup>[19]</sup>

However, in the framework of theranostic nanomaterials, the above-mentioned NPs have their application limited to imaging alone, and therapeutic action, if any, is technically challenging to obtain. Plasmonic NPs or quantum dots can be used for photothermal therapy (PTT) and multi-photon photodynamic therapy (PDT), respectively,<sup>[27,28]</sup> but in such cases their deep-tissue imaging capabilities might be compromised. For instance, multi-photon PDT needs quantum dots with visible light emission in order to drive singlet oxygen generation; furthermore, expensive and cumbersome pulsed laser set-ups are required for multi-photon excitation. Thus, to develop theranostic agents that could be used for deep-tissue imaging just as well as for therapy, alternative photoluminescent nanomaterials are ought to be explored.

### 1.3 Rare earth doped nanoparticles

The strongest case to-date of what could constitute an all-optical multifunctional theranostic nanoplatform are the rare earth doped nanoparticles (RENPs), which under NIR excitation exhibit photoluminescence in the UV-vis and NIR spectral ranges simultaneously. These exceptional optical properties of RENPs are owed to the rare earth ion ( $\text{RE}^{3+}$ ) dopants and their fascinating spectral characteristics.

#### 1.3.1 Basics of $\text{RE}^{3+}$ spectroscopy

Lanthanide series – the outcasts of the period table – together with yttrium and scandium, comprise the rare earth elements whose photophysical properties have been beguiling researchers since their discovery, and which lead to many a technological progress throughout the 20<sup>th</sup> and the 21<sup>st</sup> century.

In their trivalent form,  $\text{RE}^{3+}$  lose 5d, 6s, and some 4f electrons, retaining  $5s^25p^64f^n$  outer electronic configuration, where n runs from 1( $\text{Ce}^{3+}$ ) to 13 ( $\text{Yb}^{3+}$ ) for optically active  $\text{RE}^{3+}$  and indicates the number of electrons in the unfilled 4f shell. This shell is shielded by the 5s and 5p electrons, as a result, 4f electrons of  $\text{RE}^{3+}$  are only weakly affected by the ligand ions in crystals, and exhibit spectral features analogous to their free ion form. Consequently, the  $(2S+1)L_J$  energy states of  $\text{RE}^{3+}$  in crystals can be described by the S, L, and J quantum numbers just as for the free ion, where S is spin momentum, L – orbit angular momentum, and J – total angular momentum. When  $\text{RE}^{3+}$  are introduced into crystals as dopants, the crystal field imposes only slight shift to the position of their energy levels or causes additional splitting of the  $(2S+1)L_J$  multiplet into Stark components. The degree of splitting, lifting of the  $M_J$  degeneracy, is  $(2J+1)$  for integer J, and  $(J+1/2)$  for half-integer J. However, these changes occur on the energy scale of  $\sim 10^2 \text{ cm}^{-1}$ , compared to the Columbic electron-electron repulsion ( $\sim 10^4 \text{ cm}^{-1}$ ) and spin-orbit coupling ( $\sim 10^3 \text{ cm}^{-1}$ ) between the 4f electrons (Figure 1.3). As a result, spectral features of  $\text{RE}^{3+}$  always remain similar regardless of the crystal host. Knowing the energy level positions of different  $\text{RE}^{3+}$  allows to interpret their absorption and photoluminescence in different crystals, as each  $\text{RE}^{3+}$  has its unique signature. Experimentally, energy levels have been determined by Dieke and coworkers in  $\text{LaCl}_3$  crystal,<sup>[29]</sup> and were used to construct what is now referred to as Dieke's diagram (Figure 1.4). Dieke's diagram has become essential in the development of  $\text{RE}^{3+}$  doped materials, including RENPs, as it allows to explain as well as predict energy exchange pathways among  $\text{RE}^{3+}$  ions.

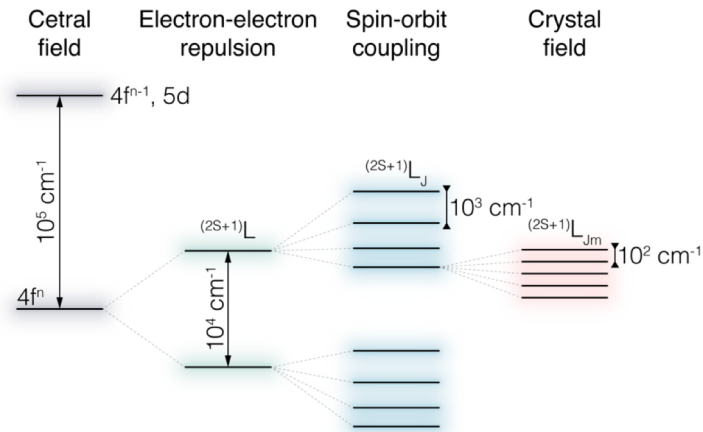


Figure 1.3. RE<sup>3+</sup> energy level splitting.

Representation of physical interactions that cause energy level splitting in the 4f<sup>n</sup> shell of RE<sup>3+</sup>, as a free ion and when embedded into a crystal.

The f→f transitions between <sup>(2S+1)</sup>L<sub>J</sub> energy levels of RE<sup>3+</sup> are in fact parity forbidden, but can become partially allowed at the electric dipole order as a result of mixing with different parity orbitals in non-symmetric crystal fields. Thus, low-symmetry host materials are preferred in order to relax selection rules for electric dipole transitions. In combination with 4f electrons being shielded by the outermost 5s and 5p shells, this means that RE<sup>3+</sup> energy levels are long-lived and give rise to sharp and intense radiative transitions. As further presented, the long-lived excited states are crucial to obtain UV-vis emission from RENPs under NIR excitation.

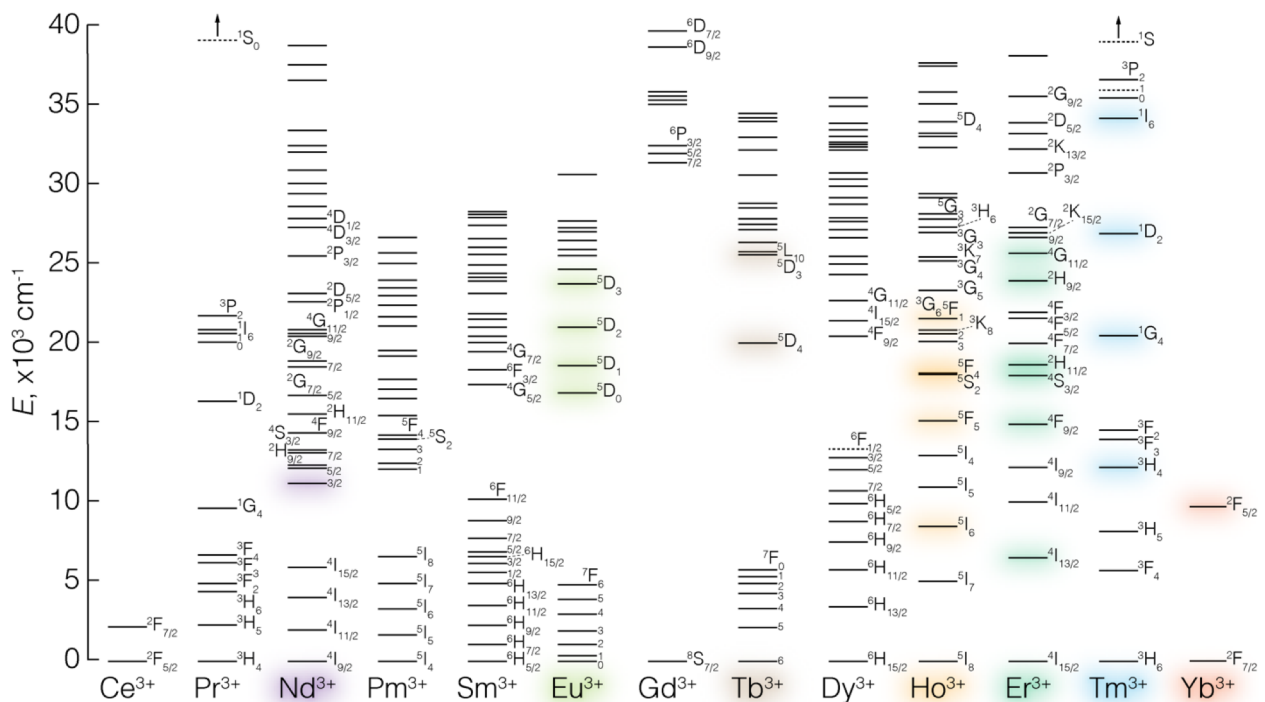


Figure 1.4. Dieke's diagram.

Dieke's diagram of RE<sup>3+</sup> energy levels, labeled by <sup>(2S+1)</sup>L<sub>J</sub> notation. Highlighted are the common RE<sup>3+</sup> embedded in RENPs and their emissive states that give rise to radiative transitions in the UV-NIR range.

### 1.3.2 Photoluminescence of RENPs

From Dieke's diagram (Figure 1.4) it can be seen that many excited states of different  $RE^{3+}$  assume very close positions, which allows for energy exchange between the neighboring ions when in close proximity, as is the case of RENPs (Figure 1.5). Radiative and non-radiative energy exchange can occur between the  $RE^{3+}$ , however non-radiative pathways are most common at the atomic scale. The two ions can either have their energy levels in near-perfectly matching positions or shifted to a small degree relative to one another. When energy levels are at a close or the same position, resonant energy transfer occurs, and is most effective between the excited states of the same  $RE^{3+}$  (Figure 1.5 – energy migration). Energy transfer between  $RE^{3+}$  with offset excited state positions can also happen, but requires release or consumption of host lattice phonons (heat) to compensate for the energy mismatch. Consequently, the greater the energy gap between the two states, the more phonon assistance is required and the less likely is the energy transfer. Yet, in the case of perfect energy match between the two excited states, energy can be easily transferred from one state to the other and back, making it difficult to control the direction of the energy flow. Multi-phonon energy transfer processes are also extremely sensitive to temperature and have outreaching implications for diagnostic properties of theranostic RENPs (see Section 1.5).

In  $RE^{3+}$  doped materials, such as RENPs, ions that are either energy donors or acceptors, are respectively called sensitizers and activators. Upon  $RE^{3+}$  excitation by light, multiple energy exchange mechanisms can occur between sensitizer and activator ions, that eventually lead to energy dissipation by non-radiative and radiative processes.

The probability of non-radiative vs radiative decay for  $RE^{3+}$  is strongly dependent on the energy gap between a particular excited state and the one just below it. As a rule of thumb, for low

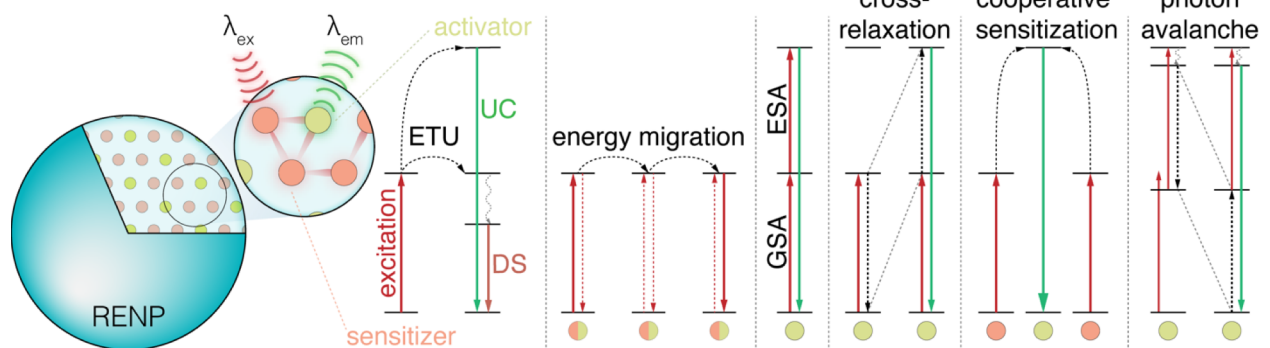


Figure 1.5. RENPs and their excitation-emission.

Schematic representation of RENPs and energy exchange pathways between  $RE^{3+}$  that give rise to photoluminescence of RENPs. ETU – energy transfer upconversion, UC – upconversion, DS – downshifting, GSA – ground state absorption, ESA – excited state absorption. Solid arrows represent radiative processes, dashed – non-radiative energy exchange, wavy – non-radiative decay.

energy gaps energy is dissipated non-radiatively, while energy levels with large energy separation are the emissive states. Empirical studies have confirmed the so-called *energy-gap law* which shows how non-radiative decay rate  $k_{nr}$  depends on the multi-phonon emission:

$$k_{nr} = k_{nr}(0)e^{-\alpha\Delta E} \quad (1.1)$$

Here,  $k_{nr}(0)$  and  $\alpha$  are constants dependent on the host material, and  $\Delta E$  is energy gap between the two states. It can be seen that the larger is the gap, the lesser the likelihood for a non-radiative decay to happen. Furthermore, the larger the energy gap, the higher number of phonons is needed to bridge it. The phonons that are expected to participate in non-radiative energy dissipation are the highest energy phonons with an appreciable density of states. For a given phonon energy  $\hbar\Omega$  ( $\hbar$  being the reduced Planck's constant and  $\Omega$  the phonon frequency), the number of phonons  $N$  involved in a multi-phonon emission is  $N = \Delta E / \hbar\Omega$ . It can be seen that selection of host materials with low effective phonon energies is of outmost importance to reduce the likelihood of multi-phonon emission and increase the radiative decay rate. Particular hosts for RENPs are discussed in the next section.

Photoluminescence – radiative decay – of RENPs can take place from an excited state that was directly populated by light absorption, or through energy transfer from a sensitizer that acted as energy harvester. There are three photoluminescence processes that are distinct for  $RE^{3+}$  doped materials. The single photon absorption and emission is termed downshifting (DS) and represents a classic scenario of Stokes-shifted photoluminescence ( $\lambda_{ex} > \lambda_{em}$ ). The anti-Stokes-shifted photoluminescence ( $\lambda_{ex} < \lambda_{em}$ ) occurs when multiple excitation photons are consumed to generate single emission photon, known as upconversion (UC) emission. An opposite, downconversion process, can also be observed between  $RE^{3+}$ , in which case a single absorbed photon is emitted as multiple photons of lower energy ( $\lambda_{ex} > \lambda_{em}$ ).

Of remarkable significance to the therapeutic aspect of RENPs is the UC emission. The first upconversion mechanism, based on the excited state absorption (ESA), was proposed by N. Bloembergen in 1959. In a most simple case UC emission can be obtained by consecutive addition of incoming photons first by the ground state absorption (GSA) and then by consecutive ESA steps.<sup>[30]</sup> However, absorption cross-sections for ESA are typically low and addition of photons in this way is often ineffective. In Dieke's diagram there can be found many excited states with near identical energy gaps between different  $RE^{3+}$  ions, thus climbing up the energy level ladder of one ion can be done with the help of another. A multistep energy transfer process that produces UC emission in this way is energy transfer upconversion (ETU; Figure 1.5), or

*addition de photon par transferts d'énergie*, pioneered by F. Auzel in 1966.<sup>[31]</sup> At the same time, V. V. Ovsyankin and P. P. Feofilov, have suggested UC emission through cooperative sensitization, where two excited sensitizer ions would donate their energy to an activator simultaneously, without an intermediate energy transfer step (Figure 1.5 – cooperative sensitization).<sup>[32]</sup> However, ETU is several orders of magnitude more efficient to generate UC emission, than ESA or cooperative sensitization, and is thus mainly exploited in RENPs.<sup>[33]</sup>

A classic example of UC emission in RENPs is given by the  $\text{Yb}^{3+}/\text{Er}^{3+}$  sensitizer/activator pair (Figure 1.6).  $\text{Yb}^{3+}$  has only one excited state ( ${}^2\text{F}_{5/2}$ ) that is above the ground level ( ${}^2\text{F}_{7/2}$ ) by an energy difference corresponding to  $\sim 980$  nm radiation. Similar energetic separation can be found from the  ${}^4\text{I}_{15/2}$  ground level of  $\text{Er}^{3+}$  to its  ${}^4\text{I}_{11/2}$  excited state, and from it to the  ${}^4\text{F}_{7/2}$  excited state. Thus, when  $\text{Yb}^{3+}$  are excited by 980 nm radiation ( ${}^2\text{F}_{7/2} \rightarrow {}^2\text{F}_{5/2}$ ) they can transfer the excitation energy to  $\text{Er}^{3+}$  in a multistep fashion:  ${}^2\text{F}_{5/2} \rightarrow {}^2\text{F}_{7/2}$  ( $\text{Yb}^{3+}$ ):  ${}^4\text{I}_{15/2} \rightarrow {}^4\text{I}_{11/2}$  ( $\text{Er}^{3+}$ ) and  ${}^2\text{F}_{5/2} \rightarrow {}^2\text{F}_{7/2}$  ( $\text{Yb}^{3+}$ ):  ${}^4\text{I}_{11/2} \rightarrow {}^4\text{F}_{7/2}$  ( $\text{Er}^{3+}$ ). In turn, the emissive energy levels of  $\text{Er}^{3+}$  ( ${}^2\text{H}_{11/2}$  and  ${}^4\text{S}_{3/2}$ ), just below the  ${}^4\text{F}_{7/2}$  excited state, are populated via non-radiative decay, eventually giving out the prominent green UC emission of  $\text{Er}^{3+}$ . Of course, this is only a few of many possible exchange pathways between  $\text{Er}^{3+}$  and  $\text{Yb}^{3+}$  that produce UC emission across a broad vis spectral range (Figure 1.6), and which are discussed in more detail in chapters 4 and 8 of this thesis. Concurrently to UC emission, DS emission of  $\text{Er}^{3+}$  at around  $1.55 \mu\text{m}$  ( ${}^4\text{I}_{13/2} \rightarrow {}^4\text{I}_{15/2}$ ) is generated following the non-radiative  ${}^4\text{I}_{11/2} \rightarrow {}^4\text{I}_{13/2}$  decay after the first  $\text{Yb}^{3+} \rightarrow \text{Er}^{3+}$  energy transfer event.

In addition to energy migration and transfer processes, excitation energy can be shared

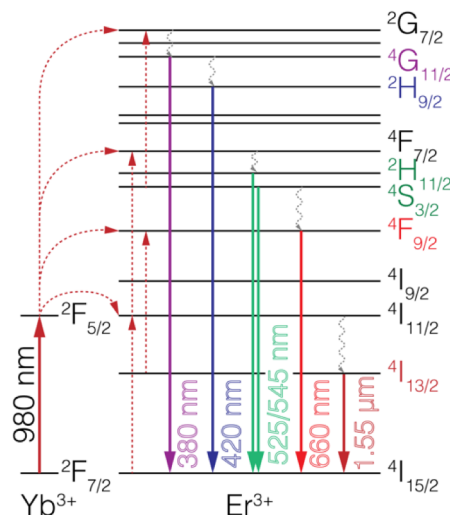


Figure 1.6.  $\text{Yb}^{3+}/\text{Er}^{3+}$  excitation-emission.

Simplified UC (and DS) emission scheme in  $\text{Yb}^{3+}/\text{Er}^{3+}$  sensitizer/activator pair via ETU. Solid arrows represent radiative processes, dashed – non-radiative energy exchange, wavy – non-radiative decay.

between the same type RE<sup>3+</sup> ions among their equidistantly (or nearly so) spaced energy levels via cross-relaxation (Figure 1.5 – cross relaxation). Cross-relaxation is a non-radiative process that can depopulate intermediate excited states of two ions by bringing one to its ground state and the other to a higher excited state. The same process also happens in reverse, thus depending on its “direction” cross-relaxation can redistribute excitation population in RE<sup>3+</sup> by either promoting or quenching higher energy level excitation.<sup>[33]</sup> Although self-quenching by cross-relaxation is most commonly observed in highly doped RENPs, cross-relaxation can be positively harnessed in Yb<sup>3+</sup>/Tm<sup>3+</sup> doped structures to promote UV-blue emission under NIR excitation,<sup>[34]</sup> and is one of the corner-stones for photon avalanche type UC emission.

Finally, UC emission can be generated through photon avalanche process which is typically observed at cryogenic temperatures and in bulk materials (Figure 1.5 – photon avalanche).<sup>[35]</sup> For photon avalanche to occur the GSA cross-section of RE<sup>3+</sup> for a specific excitation wavelength has to be smaller than that of ESA, and RE<sup>3+</sup> doping has to be high enough to promote cross-relaxation assisted population of an intermediate long-lived excited state. If these conditions are satisfied, as soon as the intermediate state of one RE<sup>3+</sup> gets populated the ESA excites that ion to its higher energy level, from which cross-relaxation among two nearby RE<sup>3+</sup> brings them both to the intermediate state. Subsequent iterations of this looping mechanism ensure that all RE<sup>3+</sup> end up in an intermediate excited state. UC emission becomes particularly efficient in photon avalanche, as RE<sup>3+</sup> in their intermediate excited state can now be easily excited to higher energy levels via ESA, from which UC emission takes place. As mentioned above, photon avalanche is mostly observed in bulk materials, however, photon avalanche-like processes have also been reported for RENPs and exploited in super-resolution microscopy, deep-tissue imaging, and NP microlasers.<sup>[36–38]</sup>

To determine the nature of a particular photoluminescence process in RE<sup>3+</sup> doped materials, it is common to investigate the relationship of emission band intensity ( $I$ ) vs excitation power ( $P$ ).<sup>[39]</sup> For linear processes, like downshifting, this relationship remains linear. On the other hand, the intensity of UC emission depends on the photon order  $n$  required to populate respective excited states through  $n$ -step excitation and can be expressed as:

$$I \propto P^n \quad (1.2)$$

By measuring the slope of the  $\log(I)$  vs  $\log(P)$  plots (a.k.a. power plots),  $n$  values can be calculated and photon order determined. However, deviations from the theoretically expected values are often observed since the probability of the upconversion process from a given energy

level versus the non-radiative relaxation to the lower lying level, cross-relaxation and the three-ion energy transfer, among other processes, are known to reduce the measured minimum number of photons required for  $n$ -step upconversion excitation. Furthermore, relationship in equation 1.2 is valid only for low excitation powers, as in high power regime excited states tend to saturate, decreasing the measured  $n$  value. In general power plots in combination with excited state lifetime measurements are powerful tools to understand excitation dynamics in RENPs, and how those depend on specific dopants and their concentration.

### 1.3.3 Morphology and structure of RENPs

Due to the fact that any number of  $RE^{3+}$  combinations can be embedded in RENPs, it makes these host-guest systems extremely flexible in terms of their spectral tuning by dopant type and concentration selection. However, photoluminescence of RENPs is not determined by that alone – host composition, crystalline phase, NP size, and multilayered architecture, all can influence color and intensity of the emission (Figure 1.7).

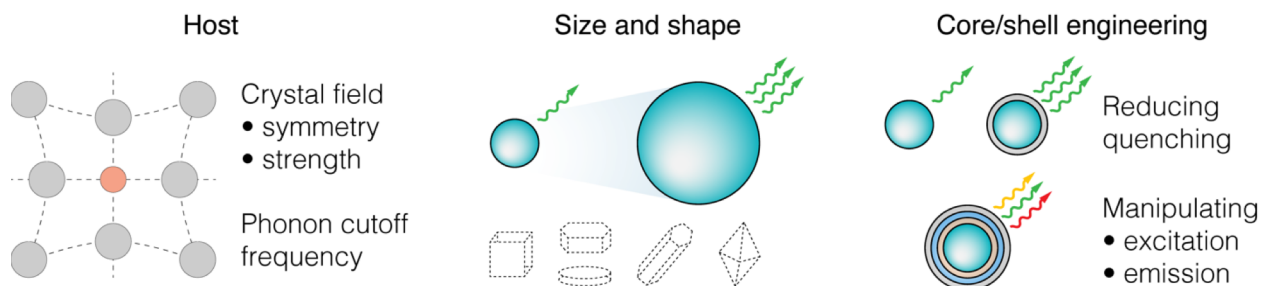


**Figure 1.7. RENPs' photoluminescence vs structure.**

**Photoluminescence color and intensity of RENPs are primarily tuned through host selection, morphology, and core/shell engineering (which also applies to the excitation pathway manipulation).**

*Host.* RENP hosts are typically selected in a manner to obtain most intense photoluminescence, keeping in mind that they also have to be optically transparent to the excitation and emission wavelengths of the optically active dopants, chemically stable, and allow for the synthesis of highly crystalline and monodisperse in size nanocrystals. Host matrices of RENPs determine the distance between  $RE^{3+}$ , their spatial position relative to each other, coordination number, type of neighboring anions, phonon dynamics and local crystal field experienced by the dopants.

As discussed above, the phonon cutoff frequency of the host lattice directly influences the rate of multi-phonon emission between an excited state and the one below. Thus, to promote radiative transitions, RENP hosts with low phonon cutoff frequencies are chosen. Typical hosts are fluorides, oxides, vanadates, oxysulfides, and oxy-fluorides/-chlorides.<sup>[40]</sup> Although the lowest phonon energies ( $< 300 \text{ cm}^{-1}$ ) are present in chloride, bromide, and iodide systems,

these are highly hygroscopic and thus chemically unstable. Oxides are highly chemically stable, but they exhibit  $> 500 \text{ cm}^{-1}$  phonon cutoff frequencies, and are relatively difficult to synthesize with low size dispersity and as core/shell heterostructures. Fluorides, on the other hand, have  $\sim 350 \text{ cm}^{-1}$  phonon energies, are reasonably chemically stable, can be synthesized with high size monodispersity, and as multilayered heterostructures. Thus, for the past 15 years various synthesis methods have been developed and perfected to obtain desired fluoride-type RENPs of virtually any shape, structure or composition. These typically are, but not limited to,  $\text{LaF}_3$ ,<sup>[41]</sup>  $\text{Na(RE)F}_4$ ,<sup>[42]</sup>  $\text{Li(RE)F}_4$ ,<sup>[43]</sup>  $\text{CaF}_2$ ,<sup>[44]</sup>  $\text{SrF}_2$ ,<sup>[44]</sup>  $\text{KYb}_2\text{F}_7$ ,<sup>[45]</sup>  $\text{KSc}_2\text{F}_7$ ,<sup>[46]</sup>  $\text{KGdF}_4$ ,<sup>[47]</sup> here, RE stands for all lanthanide series elements, including yttrium and scandium.

The composition and associated crystalline phase of RNP host determines the crystal field strength and symmetry experienced by the dopants. Low symmetry hosts are preferred in RENPs, as they lift restrictions on  $f \rightarrow f$  transitions by intermixing 4f energy levels with higher electronic configurations. For instance,  $\text{NaYF}_4:\text{Er}^{3+}$ ,  $\text{Yb}^{3+}$  RENPs can be synthesized in both cubic or hexagonal crystalline phases, however the latter structure exhibits about an order of magnitude more intense UC emission due to its lower symmetry.<sup>[48]</sup> Similarly,  $\text{LiYF}_4$  or  $\text{LiLuF}_4$  RENPs have high crystal field strength exerted on the dopants, promoting intense photoluminescence and appreciable splitting of  $^{2S+1}L_J$  multiplets into their Stark components.<sup>[49–51]</sup> Another possibility to increase the crystal field strength is to reduce the cation size (or unit-cell volume) of the host, by introducing i.e.  $\text{Li}^+$  in  $\text{Na}^+$ -type RENPs.<sup>[52]</sup> A noteworthy example of crystal structure engineering are the  $\text{KYb}_2\text{F}_7:\text{Er}^{3+}$  RENPs. Wang et al., have demonstrated that due to the orthorhombic crystal phase of this material,  $\text{Yb}^{3+}$  ions are distributed in arrays of tetrad clusters, the distance between which is larger than the inter-ion separation within each cluster.<sup>[45]</sup> This allows to overcome concentration quenching effect, typically observed for highly doped samples, and confines the excitation energy within each cluster for it to be more efficiently transferred to  $\text{Er}^{3+}$ , subsequently leading to increased intensity of higher-order UC emission.

*Size.* Opposite to materials like quantum dots, where emission color depends on the quantum confinement effect,<sup>[53]</sup> “color” (peak positions) of RENPs’ UC and DS emission is considered size-insensitive, since emission is determined by spectral properties of individual  $\text{RE}^{3+}$  dopants. Photoluminescence intensity, on the other hand, strongly depends on the RNP size. Typically, larger RENPs are brighter as they accommodate more optical centers, leading to  $d^3$  emission intensity scaling, where  $d$  is the size of the RNP.<sup>[54]</sup> However, in the biomedical framework, smaller NPs (typically below 50 nm) are appreciated. As the size of RENPs is decreased the

surface-to-volume ratio increases, which leads to greater photoluminescence quenching by ligands on the RENP surface, solvent vibrational modes, and surface defects. In the case of UC emission certain radiative transitions will be quenched more than others, since energy-gap law dictates the quenching strength between adjacent energy level, leading to a possible change in the perceived emission color.<sup>[55]</sup>

*Multilayered architecture.* Although nanocrystal size, composition and phase affect photoluminescence of RENPs, spectral properties of RENPs are subject to influence by their structural engineering with an unmatched robustness.

RENP synthesis protocols can be tailored to create “onion-like” nanostructures, epitaxially growing different functional layers on pre-formed RENP cores. The so-called core/shell engineering is used to manipulate energy transfer dynamics in RENPs in order to increase emission intensity, vary color, reduce inter-ion and surface quenching, introduce novel excitation or emission pathways. RENP shells (as well as cores in certain cases) are typically classified as active and passive, which respectively signifies if the particular layer is doped with optically active  $RE^{3+}$  and participates in energy exchange or not.

Vetrone et al., explored active-core/active-shell  $NaGdF_4$ : 2 mol%  $Er^{3+}$ , 20 mol%  $Yb^{3+}/NaGdF_4$ : 20 mol%  $Yb^{3+}$  RENPs and showed that  $Yb^{3+}$ -doped shell enhanced UC emission under 980 nm excitation by: i) shielding  $Er^{3+}$  activators from external quenchers, and ii) by harvesting more of incoming NIR photons.<sup>[56]</sup> Active-core/active-shell RENPs also appeared to be brighter than their active-core/passive-shell analogs, and core-only  $NaGdF_4$ : 2 mol%  $Er^{3+}$ , 40 mol%  $Yb^{3+}$  RENPs. Although subsequent research established that active-core/passive-shell approach is more suitable for suppressing surface quenching, this study was imperative to show that excitation energy can be shared among different layers of RENPs. Nowadays, active-shells are crucial to relay excitation energy across different RENPs' layers, dopants of which would otherwise quench each other when in close proximity. Prominent example of active-shelling are  $Nd^{3+}$ -doped RENPs, where  $Nd^{3+}$  act as sensitizers for 800 nm radiation harvesting. If  $Nd^{3+}$  are co-doped with activators like  $Er^{3+}$  in the same layer,  $Nd^{3+}$  quenches  $Er^{3+}$  emission making it necessary to separate the two ions in different layers, and to use an  $Yb^{3+}$  network to transfer excitation energy from one layer to another.<sup>[57]</sup> This particular scenario is discussed in chapter 5.

When it comes to the passive-shelling of RENPs, Wang et al., have illustrated that undoped  $NaGdF_4$  shell protects optically active  $RE^{3+}$  of the  $NaGdF_4$ : 0.3 mol%  $Tm^{3+}$ , 25 mol%  $Yb^{3+}$  core from high energy quenchers, like vibrational OH stretching modes of water.<sup>[58]</sup> Yet, further research by Liu's group presented evidence for energy migration among the  $Gd^{3+}$  ions

themselves.<sup>[59]</sup> In NaGdF<sub>4</sub>:Tm<sup>3+</sup>, Yb<sup>3+</sup> RENPs excitation energy can reach <sup>6</sup>P<sub>7/2</sub> excited state of Gd<sup>3+</sup> via energy transfer from <sup>1</sup>I<sub>6</sub> energy level of Tm<sup>3+</sup>, that requires five photon order ETU to be populated in the Yb<sup>3+</sup>/Tm<sup>3+</sup> pair under 980 nm irradiation. Once at the <sup>6</sup>P<sub>7/2</sub> energy level, excitation can migrate across the vast network of Gd<sup>3+</sup>, and can be used to tune UC emission color by introducing additional NaGdF<sub>4</sub>:A<sup>3+</sup> shell, with Dy<sup>3+</sup>, Sm<sup>3+</sup>, Tb<sup>3+</sup>, and Eu<sup>3+</sup> as activator (A<sup>3+</sup>) dopants. However, energy migration across the Gd<sup>3+</sup> network also means that quenching by solvent molecules cannot be completely prevented by additional NaGdF<sub>4</sub> shelling in every case. Only when Gd<sup>3+</sup> ions in the outermost shell were substituted by completely optically inactive Y<sup>3+</sup>, appreciable emission signal could be observed in NaGdF<sub>4</sub>:Tm<sup>3+</sup>, Yb<sup>3+</sup>/NaGdF<sub>4</sub>:A<sup>3+</sup>/NaYF<sub>4</sub> RENPs. Later work by Johnson et al., have decisively proved the link between surface and concentration quenching in highly doped RENPs, and that it can be broken by the growth of a thick passive-shell.<sup>[60]</sup> This study has also impacted re-evaluation of optimal RE<sup>3+</sup> doping concentrations in RENPs, as it showed that cross-relaxation among certain optically active dopants had less impact on RENPs' photoluminescence quenching compared to energy dissipation by coupling to the vibrational modes of surface ligands and solvent molecules.<sup>[61]</sup> More on this will be discussed in chapter 3 and 8 of this thesis. Overall, passive-shelling has become indispensable in boosting RENPs photoluminescence intensity, and it plays vital role in designing small and bright RENPs slated for biomedical applications.

#### 1.3.4 Surface modification of RENPs

It is important to note that the highest quality RENPs are synthesized in organic solvents and bear capping ligands, typically oleic acid, which do not allow for direct RENP dispersibility in an aqueous environment. In order to use RENPs in biomedical research their surface needs to be modified, rendering them water dispersible. Common strategies are ligand exchange,<sup>[62]</sup> ligand oxidation,<sup>[63]</sup> ligand removal,<sup>[64]</sup> silanization,<sup>[65]</sup> amphiphilic coating,<sup>[66]</sup> layer-by-layer assembly.<sup>[67]</sup> Depending on the surface modification strategy used, further functionalization can be granted to RENPs, like attachment of targeting moieties,<sup>[68]</sup> incorporation of dyes for emission sensitization<sup>[69]</sup> or bio-sensing,<sup>[70]</sup> light sensitive groups for controlled drug release,<sup>[71]</sup> or decoration with other type of NPs for expanded multifunctionality,<sup>[72,73]</sup> etc.

### 1.4 RENPs in biomedicine

Since the conception of RENPs, they have arguably "colonized" the landscape of biomedical research. The modular flexibility of RENPs provides access to construct photoluminescent

nanoplatfroms suited for deep-tissue imaging, drug delivery, release and activation, multi-modal sensing, or modulation of physiological responses (Figure 1.8). Theranostic RENPs are being designed by tapping into different combinations of the aforementioned features; or by creating hybrid nanostructures made out of RENPs and nanomaterial of another class, each bringing their respective strengths in pursuit for all-in-one nanomedicines of the future.

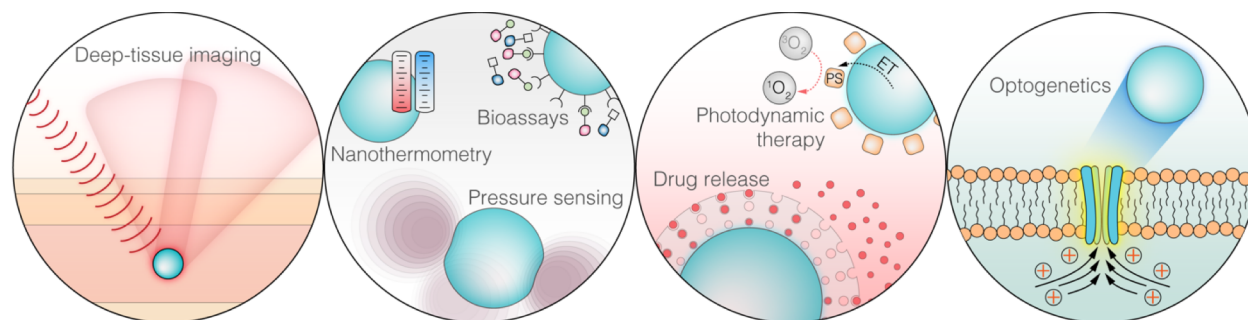


**Figure 1.8. Application of RENPs in biomedicine.**

**In biomedicine RENPs are explored for diagnostics (deep-tissue imaging, multi-parameter sensing), therapy (i.e. drug release and photodynamic therapy), and optical modulation (i.e. optogenetics).**

### 1.4.1 Imaging

As discussed in section 1.2 deep-tissue biological imaging requires contrast agents that operate in the BWs located in the NIR spectral region. Fortunately, RENPs easily satisfy these conditions through rational selection of  $RE^{3+}$  and their combinations. Most popular RENP excitation wavelengths are 800 and 980 nm, respectively absorbed by  $Nd^{3+}$  and  $Yb^{3+}$ , and lie within the BW-I.<sup>[74–76]</sup> Although strictly speaking 980 nm radiation is outside of the BW-I and has certain ramifications for RENP excitation in biological objects, which will be mentioned in subsequent chapters, this wavelength remains the most abundantly used for emission sensitization. Recently excitation wavelengths in BW-II and BW-III, for improved light penetration in tissues, have also been proposed, such as 1064,<sup>[37]</sup> 1150,<sup>[77]</sup> and 1532 nm,<sup>[78]</sup> where  $Tm^{3+}$ ,  $Ho^{3+}$ , and  $Er^{3+}$  act as sensitizers, respectively (Figure 1.9A). Upon NIR excitation, RENPs can exhibit a plethora of emission bands across UV-vis-NIR spectral range through upconversion and/or downshifting processes. Although UC emissions of different  $RE^{3+}$  are situated mostly in the UV-vis range and are reserved for mediation of high photon energy demanding processes (see sections 1.4.3 and 1.4.4) or microscopy imaging, some reports have proposed to use the red emission (660 nm) of  $Er^{3+}$  or the NIR band (790) of  $Tm^{3+}$  for deep-tissue imaging as well. Unfortunately, imaging at those wavelengths is prone to severe image deterioration because of scattering and tissue autofluorescence. DS emissions of RENPs, on the other hand, extend further in the NIR, overcoming the above-mentioned complications.

Downshifting is also at least an order of magnitude more efficient process compared to upconversion, and is thus better suited for applications like imaging, where collection of every single photon counts.<sup>[79,80]</sup> Many of the optically active RE<sup>3+</sup> have radiative transitions in the NIR that can be exploited in high-contrast deep-tissue imaging: Nd<sup>3+</sup> – 880, 1050, 1320 nm, Yb<sup>3+</sup> – 1000 nm, Ho<sup>3+</sup> – 1200 nm, Pr<sup>3+</sup> – 1300 nm, Er<sup>3+</sup> – 1550 nm (Figure 1.9A).<sup>[81,82]</sup> Among these, DS emission bands of Nd<sup>3+</sup> and Er<sup>3+</sup> are mostly used for imaging as they perfectly coincide with BW-II and BW-III, respectively.

NIR imaging with RENPs can be traced back to the work by Yu et al., where NdF<sub>3</sub> RENPs coated with SiO<sub>2</sub> for water dispersity were used as deep-tissue contrast agents.<sup>[83]</sup> Nd<sup>3+</sup> DS emission around 1050 nm (<sup>4</sup>F<sub>3/2</sub> → <sup>4</sup>I<sub>11/2</sub>) in the BW-II was acquired from as deep as the abdominal cavity of a mouse under local injection, as well as used to trace RENPs' accumulation in one of the earlobe vessels after tail vein injection. This emission band of Nd<sup>3+</sup> is frequently employed for deep-tissue imaging as it is the most intense among <sup>4</sup>F<sub>3/2</sub> → <sup>4</sup>I<sub>J</sub> (J = 9/2, 11/2, and 13/2) radiative transitions of Nd<sup>3+</sup>. However, image quality using this DS emission band can be still compromised by scattering and autofluorescence. Villa et al., have demonstrated that 1340 nm (<sup>4</sup>F<sub>3/2</sub> → <sup>4</sup>I<sub>13/2</sub>) emission of SrF<sub>2</sub>:Nd<sup>3+</sup> RENPs is better suited for deep-tissue imaging.<sup>[84]</sup> Compared to broadband emission collection in the 900-1500 nm range,

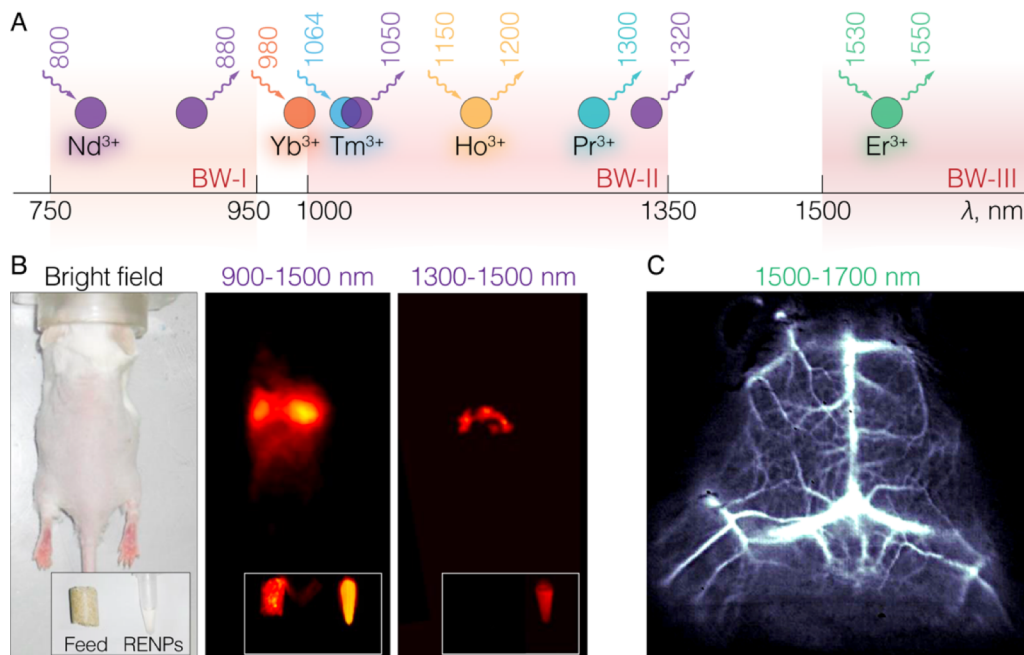


Figure 1.9. Deep-tissue imaging with RENPs.

A – RE<sup>3+</sup> ions and their emission/excitation wavelengths in the BWs. B – Bright field, 900-1500 nm photoluminescence, and 1300-1500 nm photoluminescence images of a mouse with intravenously injected Nd<sup>3+</sup>-doped RENPs. Insets show images of a mouse feed and RENPs dispersion. Reproduced from [84]. C – Cerebral vascular image of a mouse acquired with Er<sup>3+</sup>-doped RENP as photoluminescence contrast agents in the 1500-1700 nm range. Reproduced from [89].

accommodating both 1060 and 1340 nm bands of  $\text{Nd}^{3+}$ , more precise delineation of imaged structures can be made by limiting signal acquisition to 1300-1500 nm range (Figure 1.9B). The difference has been ascribed not only to the reduced scattering, but also to complete elimination of parasitic autofluorescence signal which might extend as far as 1100 nm. Interestingly, autofluorescence was observed from the mouse feed (Figure 1.9B – inset) that carries plant components, like chlorophyll, with photoluminescence ranging from 850 to 1120 nm.<sup>[85]</sup>

For highest contrast autofluorescence-free images, a move even further into the NIR has been done with  $\text{Er}^{3+}$ -doped RENPs. Although some concerns exist over the attenuation of  $\text{Er}^{3+}$  DS emission around 1550 nm ( $^4\text{I}_{13/2} \rightarrow ^4\text{I}_{15/2}$ ) by water absorption, it remains most suited for deep-tissue imaging with micrometer scale spatial resolution. Starting from the seminal paper by Soga et al., on 1550 nm deep-tissue imaging with  $\text{Y}_2\text{O}_3:\text{Er}^{3+}$ ,<sup>[86]</sup> many different formulations of RENPs have been developed to effectively satisfy NIR imaging in the BW-III.<sup>[87]</sup> Naczynski et al., have prepared aggregates of  $\text{NaYF}_4:\text{Er}^{3+}$ ,  $\text{Yb}^{3+}/\text{NaYF}_4$  RENPs and human serum albumin (HSA) for NIR imaging in BW-III via  $\text{Er}^{3+}$  DS emission.<sup>[88]</sup> On their own, RENPs were able to resolve anatomical structures of mice, tumors and blood vessels; while RENPs-HSA nanocomposites systematically accumulated at the tumor site. A prominent example of RNP rational design for deep-tissue imaging was showcased by Zhong et al.<sup>[89]</sup> Core/shell engineering and co-doping strategies were employed to boost the DS emission intensity of  $\text{NaYbF}_4:\text{Er}^{3+}$ ,  $\text{Ce}^{3+}/\text{NaYF}_4$  RENPs at 1550 nm. As discussed in section 1.3.3, a thick (7 nm)  $\text{NaYF}_4$  passive shell enhanced emission intensity by reducing surface quenching, whereas  $\text{Ce}^{3+}$  ions inhibited population of the higher excited states of  $\text{Er}^{3+}$  via ETU, leading to greater population of  $^4\text{I}_{13/2}$  emissive energy level. These RENPs were successfully employed in dynamic imaging of mouse cerebral vasculature and blood perfusion, all carried out through scalp skin and skull of a total thickness  $\sim 1.3$  mm, with high spatiotemporal resolution (Figure 1.9 – C). In their subsequent work, Zhong et al. introduced  $\text{Zn}^{2+}$  doping in  $\alpha$ -phase  $\text{NaYbF}_4:\text{Er}^{3+}$ ,  $\text{Ce}^{3+}$ ,  $\text{Zn}^{2+}/\text{NaYF}_4$  RENPs, which led to local symmetry distortion around  $\text{Er}^{3+}$  ions further increasing intensity of DS emission around 1550 nm.<sup>[90]</sup> Owing to high brightness of these RENPs, real-time deep-tissue imaging could be carried out using low-power 970 nm LED source.

A particularly interesting future direction for RENPs is time-gated NIR imaging, where RENPs emission decay under pulsed excitation, rather than the steady-state emission, is measured.<sup>[91]</sup> Due to the long-lived excited states, decay times of RNP photoluminescence are in the  $\mu\text{s}$ -ms range, significantly longer than any photoluminescence of a molecular origin (generally on the order of ns). Accordingly, time-gated imaging permits to eliminate autofluorescence entirely, by

delaying image acquisition to the point when parasitic fluorescence has subsided, but RENPs still emit. Time-gated NIR imaging with RENPs is expected to facilitate NIR deep-tissue multiplexing for disease visualization and rapid recognition. It is important to recognize that RENPs can also be used for magnetic resonance and X-ray computer tomography imaging, when  $Gd^{3+}$  or  $Lu^{3+}$  are incorporated in their matrix, respectively.<sup>[92]</sup> Additional functionalization can grant RENPs an even broader range of multimodal imaging capabilities.<sup>[93]</sup> Overall, RENPs enable deep-tissue imaging in the BW-II and BW-III at unprecedented spatial and temporal resolution, while their surface chemistry can be tailored to improve blood circulation, accumulation at tumor sites, and to enable rapid clearance from the body.

### 1.4.2 Sensing

UC and DS emission bands of RENPs can be used for optical sensing, either exploiting their own innate sensitivity to the environment or in coordination with other optical agents. In the latter case, nanocomposites are made where one optical component influences the emission of another. Energy exchange between RENPs and conjugated optical species is then engineered to change upon the presence of an analyte. Since RENPs are excited via single NIR wavelength and emit across a wide optical spectral range, this allows for high throughput multiplexed sensing strategies,<sup>[70]</sup> without cross-talk between different sensor components or false sensing due to autofluorescence. In this manner RENPs are researched and applied in pH sensing,<sup>[94]</sup> identification of heavy metals and small molecules,<sup>[95,96]</sup> nucleic acid and protein recognition,<sup>[97]</sup> voltage measurement of neuronal membrane potential,<sup>[98]</sup> and bioassays.<sup>[99]</sup>

Inherently RENPs could be used as stand-alone biosensors too, if their emission intensity and/or color are influenced by external cues, which affect radiative and non-radiative decay rates of  $RE^{3+}$  excited states. This can be done by modulating the absorption/emission of lattice phonons or vibrational modes of the environment. For instance, hydration level in the vicinity of RENPs can be checked by their emission intensity decrease, prompted by water quenching.<sup>[100]</sup> At the same time thermal changes in the vicinity of RENPs influence their excitation-emission dynamics and can be used for temperature measurement at the nanoscale. The concept of nanothermometry and the role RENPs play as temperature sensors is describe at greater length in section 1.5, which stands in direct relation to this thesis.

It is also possible to sense external pressure/force exerted on RENPs. The Dionne group has been exploring changes in the UC emission of RENPs induced by external strain.<sup>[101,102]</sup> Deformation of RENPs crystal structure leads to changes in the proximity between neighboring  $RE^{3+}$  ions, as well as crystal field symmetry experienced by the dopants. The latter directly

impacts inter-ion separation and energy transfer rates, while the former can help to relax the selection rules on the parity forbidden  $f \rightarrow f$  transitions in centrosymmetric crystals, like  $\alpha$ -phase  $\text{NaYF}_4$ . In biomedicine, pressure sensing with RENPs is thus proposed for force transduction studies in fluid-filled organs like digestive system or vertebrate eye.

### 1.4.3 Therapy

As can be seen from the previous two sections, RENPs are versatile diagnostic instruments, but their optical toolkit is equally fit to tackle therapeutic tasks. Here, UC emission of RENPs is of critical importance, as high-energy photons can be generated under NIR excitation *in situ* at tissue depths unreachable under direct UV-vis irradiation. In addition, RENPs add NIR photons by climbing up the ladder of their long-lived energy levels under relatively low excitation power densities  $10^{-3}$ - $10^3$   $\text{W}/\text{cm}^2$ , which makes it safer and more cost effective for implementation in clinics. Note, except for few cases, RENPs alone do not enact therapeutic action, but function as energy mediators. To that end, advancements in RENPs as therapeutic agents take equal part on the front of i) engineering ever more efficient RENPs as energy donors, and ii) coming up with new techniques and drugs that take advantage of UC emission. Controlled drug delivery and PDT are the main therapeutic research avenues with RENPs.

Precision delivery of medication at the site of illness is a long-standing aim in pharmaceuticals, which is necessary to reduce whole-body toxicity under exposure to a drug, and minimize dosages needed for positive treatment outcome. In drug delivery, RENPs combine the functions of a train and passenger control. Their surfaces are engineered to incorporate therapeutic payload, have targeting moieties to reach the site of interest at maximum capacity, and prompt release or activation of the drug only under light stimulus. The latter element is typically obtained by using molecules with photocleavable bonds or capable of cis-trans isomerization induced conformational change. These are high-photon energy demanding reactions, for which  $\text{Tm}^{3+}/\text{Yb}^{3+}$  doped RENPs are best candidates producing UV and blue light in 330-480 nm range through 3, 4 and 5 photon order upconversion processes.

Yang et al., have coated  $\text{Tm}^{3+}$ -doped RENPs with mesoporous silica, loaded with anti-cancer drug doxorubicin, and capped the pores of the silica coating with a photocleavable linker.<sup>[103]</sup> Under NIR excitation, generated UV light would cleave the linker and release doxorubicin. Similarly, Liu et al., have used mesoporous silica RENPs loaded with doxorubicin, and capped the pores with photolabile azobenzene groups. Subjected to UV emission from RENPs, azobenzene groups would switch from cis to trans conformation and release doxorubicin in a

controlled manner.<sup>[104]</sup> Although these systems appear to be extremely promising for on-demand drug release, some concerns have been raised that UV light generated by RENPs is insufficient in intensity to drive such reactions, and cargo release is more likely due to the heat generated by water absorbed 980 nm radiation.<sup>[105]</sup> Photoactive release of macromolecules has also been demonstrated with the hydrogel structures, where polymers were crosslinked with photoresponsive *o*-nitrobenzyl groups.<sup>[106]</sup> Jalani et al. devised silica coated LiYF<sub>4</sub>:Tm<sup>3+</sup>, Yb<sup>3+</sup> RENPs modified with a photodegradable chitosan hydrogel.<sup>[107]</sup> LiYF<sub>4</sub>:Tm<sup>3+</sup>, Yb<sup>3+</sup> RENPs are highly efficient in generating UV UC emission under NIR radiation, and thus were able to release model bovine serum albumin molecules loaded into the hydrogel under low power irradiation and with utmost control. Recently, Chu et al. used Tm<sup>3+</sup>-doped RENPs for NIR radiation controlled immunotherapy.<sup>[108]</sup> NaGdF<sub>4</sub>:Tm<sup>3+</sup>, Yb<sup>3+</sup>/NaGdF<sub>4</sub> core/shell RENPs were coated with silica and further modified with cationic polymers to load CpG oligonucleotides hybridized to complimentary ssDNA (single-stranded DNA) containing photocleavable bonds. Under NIR irradiation, UV light produced by RENPs would break down the complementary ssDNA part and release CpG for controlled anti-tumor immune response.

PDT – photodynamic therapy – is a light-based remedy that uses photoactive molecules, photosensitizers (PS), to produce reactive oxygen species (ROS) and singlet oxygen by type I and type II reaction, respectively. These oxygen species are extremely toxic to cells, and are used for tumor therapy. The drawback of classical PDT, however, is that it uses PS excitable in the UV-vis spectral range, which means that PDT is limited to treating surface lesions, and cannot be used to eradicate deep-seated tumors. Leveraging on the photon upconversion, RENPs-PS systems are developed for deep-tissue PDT. Emission of RENPs is tailored to match absorbance of classic PS, so that radiative or non-radiative (Förster resonance) energy transfer could take place from NIR excited RENPs and activate the PS molecules (Figure 1.10). RENP-PS systems are made by covalently attaching PS to the RENP surface,<sup>[109]</sup> loading into the mesoporous silica coating,<sup>[110]</sup> or intercalating amphiphilic/hydrophobic PS into the amphiphilic coating of RENPs through hydrophobic interactions.<sup>[111,112]</sup> In addition to PDT at greater tissue depths, RENPs-PS nanocomposites limit ROS and singlet oxygen generation to the area where they are located, reducing undesired photo-damage to healthy tissues. PDT effect can also be obtained with ROS generating TiO<sub>2</sub> or ZnO NPs.<sup>[113,114]</sup> Hou et al., have combined synergistic ROS production from TiO<sub>2</sub> and PS – hypocrellin A, which were excited by Tm<sup>3+</sup>-doped RENPs under 808 nm radiation.<sup>[115]</sup> UV and blue emission of RENPs was absorbed by TiO<sub>2</sub> and hypocrellin A, respectively, which in tandem would produce more of ROS and attain greater anti-tumor effect than if used individually.

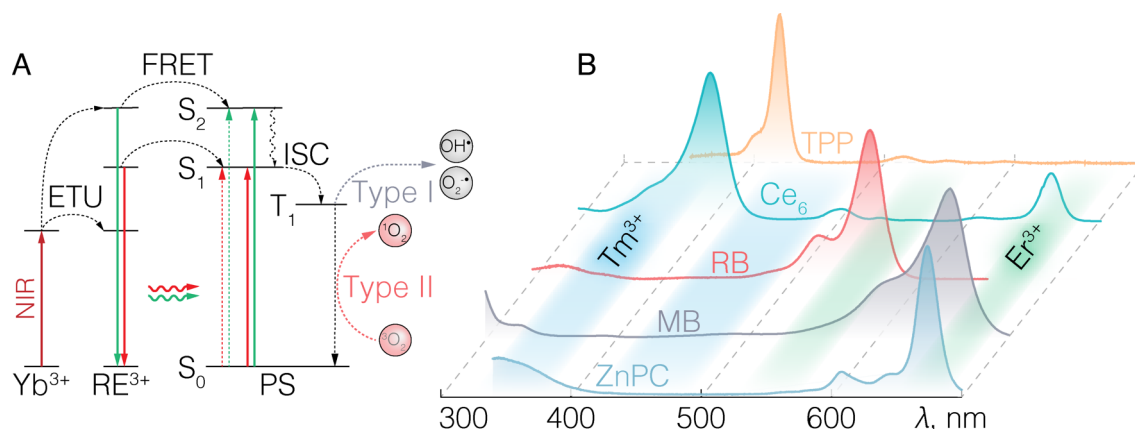


Figure 1.10. RENPs as energy donors in PDT.

**A** – Indirect excitation of PS by RENPs. NIR excited RENPs transfer excitation energy either radiatively or via non-radiative Förster’s resonance energy transfer (FRET) to PS, which undergo inter-system crossing (ISC) from singlet to triplet excited state. From here, PS drive type I and type II reactions that generate reactive oxygen species and singlet oxygen, respectively. Solid arrows represent radiative processes, dashed – non-radiative energy exchange, wavy-dashed – non-radiative decay. **B** – Absorption spectra of classic PS for PDT and their overlap with emission bands of  $Tm^{3+}$ ,  $Er^{3+}$ -doped RENPs. TPP – tetraphenylporphyrin,  $Ce_6$  – chlorin  $e_6$ , RB – rose bengal, MB – methylene blue, ZnPC – zinc phthalocyanine.

Although to a very little extent, RENPs themselves can also enact therapy. One study has demonstrated direct singlet oxygen generation by  $NaYbF_4$ .<sup>[116]</sup> While Mironova et al. has proposed PDT with  $Tm^{3+}$ -doped RENPs by UV excitation of endogenous tissue porphyrins acting as PS.<sup>[117]</sup> Highly  $Nd^{3+}$ -doped RENPs have also been considered for PTT, taking advantage of cross-relaxation between  $Nd^{3+}$  ions and release of excitation energy in a non-radiative manner – heat.<sup>[118]</sup> However, it is more effective to couple dedicated PTT agents to RENPs for controlled heat-based therapy (see section 1.5).

Research on RENPs for therapy is still actively ongoing, especially, different formulation are being tested to obtain multi-functional theranostic RENPs that combine imaging/sensing properties (sections 1.4.1 and 1.4.2) with the therapeutic ones.

#### 1.4.4 Modulation

One of the more recent application areas of RENPs have become optogenetics.<sup>[119]</sup> Optogenetics works on the basis of neural response manipulation by optically sensitive cation channels, opsins, in nerve cells. This technique has become a game changer in the study of neuronal activity, particularly in live subjects. However, as most biological molecules, opsins are sensitive to light of the vis spectrum making deep-brain or through-skull modulation of neural responses challenging. Yet, it can be addressed using RENPs as mediators between deep-penetrating NIR excitation and vis light absorbing opsins. RNP-based optogenetics allows to conduct *in vivo* experiments in freely moving mice, without the need for invasive approaches.<sup>[120]</sup>

A study worth noting on the use of RENPs as optical modulators was carried out by Ma et al.<sup>[121]</sup> Here, researchers used green-light emitting  $\text{NaYF}_4:\text{Er}^{3+}, \text{Yb}^{3+}/\text{NaYF}_4$  RENPs anchored to the retinal photoreceptors of mice, in order to give them NIR vision. These nano-enhanced mice were able to see beyond the 700 nm limit, typical for mammals, and recognize NIR patterns. Similar future studies are expected to pave the way not only to vision enhancement in mammals, but also to improved research on vision-related behavior, and repair of visual function.

## 1.5 Nanothermometry

Temperature is one of the principal parameters by which physical systems can be described and through which they are influenced. In biology, temperature controls the physiological and chemical processes that take place from molecular all the way to the whole-body level. It is key to the functioning and survival of living organisms, having effect over the environmental adaptation via thermoregulation, protein conformation and enzymatic signaling, stiffness of cellular membrane and cross-membrane molecular transportation, gene expression, etc.<sup>[122]</sup> Temperature also manifests itself as an immune response to pathogens and cancer,<sup>[123]</sup> and is essential in execution of heat-based therapies.<sup>[124]</sup> However, to attain truly fundamental understanding regarding temperature's overarching impact in biology and medicine, there is a need for precise and noninvasive thermal sensing at the nanoscale.

### 1.5.1 Photoluminescence nanothermometry

Small organic molecules, fluorescent proteins, and NPs can be affected by temperature, leading to changes in attributes that describe their emission. It is thus possible to correlate the influence of temperature to the photoluminescence of these fluorophores and employ them in light-based temperature sensing at the sub-cellular level – nanothermometry. A myriad of the so-called nanothermometers have been proposed over the years, the working principle of which is grounded in the change of emission intensity, lifetime, polarization, or band width/position (Figure 1.11).

*Intensity.* Since non-radiative deactivation of excited states in photoluminescent materials is temperature-dependent, change in emission intensity is a common parameter through which nanothermometers operate. Temperature also governs population of energy levels following Boltzmann statistics, as well as phonon-assisted non-resonant energy transfer, cross-relaxation, or Auger recombination. Correlating change in emission intensity against temperature has been

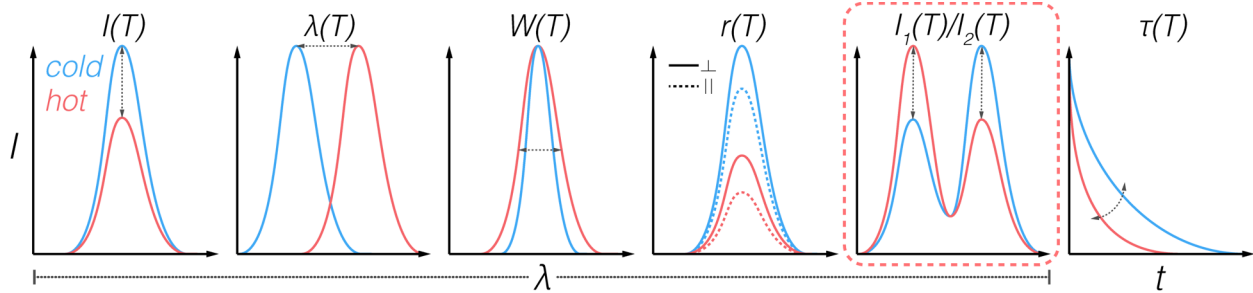


**Figure 1.11. Photoluminescence nanothermometry.**

**Schematic representation of the influence of temperature on the spectral features of photoluminescence nanothermometers: intensity  $I$ , band position  $\lambda$  or width  $W$ , polarization anisotropy  $r$ , and lifetime  $\tau$ . The most abundant nanothermometers, including those presented in this thesis, rely on the change of intensity ratio between two emission regions.**

carried out in quantum dots,<sup>[125]</sup> organic dyes,<sup>[126]</sup> fluorescent proteins,<sup>[127]</sup> polymers,<sup>[128]</sup> or gels.<sup>[129]</sup> However most of these fluorophores typically have a single emission band, meaning that net emission intensity is also prone to vary with the local probe concentration, fluctuations in the irradiation power, detection signal-to-noise ratio, and non-thermal quenching factors (sensitivity to pH, energy or charge transfer). These features make absolute intensity based nanothermometers highly unreliable as their calibration can be easily compromised. Instead of taking the change of emission intensity as a whole, luminescence intensity ratio (LIR) based nanothermometry has been developed.

*Intensity ratio.* The intensity ratio, or band-shape, technique exploits the change in the intensity ratio between two different emission bands (or different regions of the same band) of the fluorophore. The LIR based approach, although not only limited to RENPs, has become a staple in these materials and spurred the development of a whole range of sophisticated and sensitive RE<sup>3+</sup>-based nanothermometers. LIR relies on the thermal repopulation of emitting levels of the same photoluminescent center (single-center nanothermometers) or two photoluminescent centers with unique emission profiles (double-center nanothermometers).<sup>[130]</sup>

In the single-center case, LIR is defined with radiative transitions stemming from  $|2\rangle$  and  $|1\rangle$  excited states to the ground state  $|0\rangle$ , where  $|2\rangle$  and  $|1\rangle$  are thermally coupled. Given intensity  $I_1 = I(|1\rangle \rightarrow |0\rangle)$  and  $I_2 = I(|2\rangle \rightarrow |0\rangle)$ , LIR thermometric parameter  $\Delta$ , can be expressed as:

$$\Delta = \frac{I_2}{I_1} = \frac{A_{02} h \nu_{02} N_2(T)}{A_{01} h \nu_{01} N_1(T)} \quad (1.3)$$

Here,  $A_{01}$  and  $A_{02}$  are the total spontaneous emission rates for  $|1\rangle \rightarrow |0\rangle$  and  $|2\rangle \rightarrow |0\rangle$  radiative transitions, respectively, and  $\nu_{01}$ ,  $\nu_{02}$  are frequencies of these transitions.  $N_1$  and  $N_2$  are temperature ( $T$ ) dependent populations of the  $|2\rangle$  and  $|1\rangle$  excited states, and  $h$  is Planck's

constant. Given that states  $|2\rangle$  and  $|1\rangle$  are thermally coupled, with the energetic separation of the order of thermal energy  $k_B T$ , at a thermal equilibrium  $N_1$  and  $N_2$  follow Boltzmann distribution:

$$\frac{N_2}{N_1} = \frac{g_2}{g_1} \exp\left(\frac{\delta E}{k_B T}\right) \quad (1.4)$$

Here,  $g_2$  and  $g_1$  are the degeneracies of the two energy levels,  $\delta E$  is energy gap between the barycenters of  $|1\rangle \rightarrow |0\rangle$  and  $|2\rangle \rightarrow |0\rangle$  emission bands, and  $k_B$  is Boltzmann constant. Hence,  $\Delta$  is:

$$\Delta = \frac{g_2 A_{02} h \nu_{02}}{g_1 A_{01} h \nu_{01}} \exp\left(\frac{\delta E}{k_B T}\right) = B \exp\left(\frac{\delta E}{k_B T}\right) \quad (1.5)$$

The pre-exponential factor  $B = (g_2 A_{02} h \nu_{02} / g_1 A_{01} h \nu_{01})$  and energy gap  $\delta E$ , are typically determined experimentally, fitting  $\Delta(T)$  after an external thermal calibration. As a rule of thumb thermally coupled energy levels are considered when separated by no more than  $2000 \text{ cm}^{-1}$ . Separation lower than  $200 \text{ cm}^{-1}$  can make it hard to resolve individual photoluminescence bands at room temperature (RT), and results in lower sensitivity nanothermometers. In  $\text{RE}^{3+}$ , either adjacent  $J$  manifolds can be thermally coupled, or Stark split  $M_J$  sub-levels of a particular state.

Double-center nanothermometers operate on the basis of two emission bands (representing the excited states of the same emitter or two different emitters), intensities of which change dissimilarly with temperature. Influence of temperature on the emission intensities comes from the temperature-dependent non-radiative multi-phonon relaxation discussed in section 1.3.2, as well as non-resonant phonon-assisted energy transfer described by the Miyakawa-Dexter model.<sup>[131]</sup> Temperature dependence of multi-phonon relaxation and phonon-assisted energy transfer rate  $k_{nr}$  take a general form of:

$$k_{nr} = k_{nr}(0)(n + 1)^N \quad (1.6)$$

Here,  $k_{nr}(0)$  is multi-phonon relaxation rate at  $T = 0 \text{ K}$ ,  $n$  is the number of phonons excited at a given temperature of the system, and  $N = \Delta E / \hbar \Omega$  is the process order (number of phonons involved in non-radiative energy decay/transfer). The occupation number of the phonon mode  $n$ , can be replaced by its Bose-Einstein average, yielding  $N$ -phonon process at a frequency  $\Omega$  as:

$$k_{nr} = k_{nr}(0) \left[ \frac{\exp(\hbar \Omega / k_B T)}{\exp(\hbar \Omega / k_B T) - 1} \right]^N = k_{nr}(0) [1 - e^{-(\hbar \Omega / k_B T)}]^{-N} \quad (1.7)$$

The dominant term in equation 1.7 is the process order  $N$ , hence most sensitive photoluminescence nanothermometers tend to exploit higher-order phonon-assisted energy transfer, i.e. between excited states of  $RE^{3+}$  ions separated by more than  $2000\text{ cm}^{-1}$ .

*Lifetime.* As an alternative to intensity and LIR based nanothermometers, lifetime of a fluorophore can be used for temperature sensing.<sup>[132]</sup> Lifetime nanothermometry has the advantage over other techniques as being independent of the absorption properties of the solvent/tissue in which nanothermometers operate. Lifetime of a given excited state  $\tau$  is:

$$\frac{1}{\tau} = k_r + k_{nr} \quad (1.8)$$

Here,  $k_r$  and  $k_{nr}$  are radiative and non-radiative decay rates, respectively. Temperature dependent multi-phonon relaxation and phonon-assisted non-resonant energy transfer, among other non-radiative processes, contribute to the change of the  $k_{nr}$  and in turn affect the total lifetime of an excited state. Lifetime as a function of temperature is then used as thermometric parameter, which, similarly to  $\Delta$ , can be expressed as an Arrhenius-type equation

$$\frac{1}{\tau} = \frac{1}{\tau_0} + C \exp\left(\frac{-E_A}{k_B T}\right) \quad (1.9)$$

where  $1/\tau_0$  is temperature independent decay rate,  $C$  is pre-exponential constant, and  $E_A$  – activation energy.

*Polarization.* Temperature also affects the polarization state of fluorophore's emission under Brownian dynamics. When illuminated by a linearly polarized light, output photoluminescence is partially polarized, due to random orientation of the fluorophores. Polarization anisotropy,  $r$ , of a probe suspended in fluid changes from its maximum value of 0.4 due to the rotational dynamics that are impacted by the temperature:

$$r = (I_{\parallel} - I_{\perp}) / (I_{\parallel} + 2I_{\perp}) = 0.4 [1 + (\eta V / k_B T \tau)]^{-1} \quad (1.10)$$

Here,  $I_{\parallel}$  and  $I_{\perp}$  are intensities of photoluminescence polarized parallel or perpendicular to the excitation polarization,  $V$  is hydrodynamic volume of a fluorophore,  $\eta$  is fluid viscosity, and  $\tau$  photoluminescence lifetime. Polarization anisotropy based temperature sensing is common to organic molecules, and also been carried out with gold nanorods.<sup>[133]</sup>

*Band width and position.* Temperature-driven changes in the vibrational molecular dynamics and lattice phonon-ion interactions, can also lead to perturbations in the emission bandwidth and position. In crystals, temperature dependent phonon-ion interactions lead to homogeneous line broadening, width  $W(T)$  of which is expressed from the initial  $W_0=W(0\text{ K})$  as:

$$W = W_0 \sqrt{\coth\left(\frac{\hbar\Omega}{2k_B T}\right)} \quad (1.11)$$

Band shift  $\delta\nu$  against temperature is given by a Debye-type function:

$$\delta\nu = \delta\nu_0 + \alpha \left(\frac{T}{T_D}\right)^4 \int_0^{T_D/T} \frac{x^3}{e^x - 1} \quad (1.12)$$

Here,  $\delta\nu_0$  is band shift from band's position at  $T = 0\text{K}$  to initial  $T$  of the measurements,  $\alpha$  is phonon-ion interaction coupling coefficient,  $T_D$  is the effective Debye temperature, and  $x = \hbar\Omega/k_B T$ . Both  $W$  and  $\delta\nu$  can be used as thermometric parameters,<sup>[134]</sup> however high spectral resolution measurements and host materials giving significant Stark splitting of  $J$  manifolds are both necessary to observe these changes in RENPs, especially when working in the narrow physiological temperature range.

### 1.5.2 Characterization of nanothermometers

Irrespective of the thermometric parameter that defines the operation of an optical temperature sensor, photoluminescence nanothermometers are nominally characterized by their relative thermal sensitivity  $S_r$ , thermal uncertainty  $\delta T$ , and measurement repeatability  $R$ .

Thermal sensitivity  $S_a$  defines the rate of change of thermometric parameter  $\Delta$  with temperature:

$$S_a = \frac{\partial\Delta}{\partial T} \quad (1.13)$$

However, this measure is rarely used as it does not allow for direct comparison between nanothermometers working by the different physical principle, having different composition, or measured with different experimental setups. In light of that,  $S_r$ , the relative thermal sensitivity, is a preferred figure of merit:<sup>[135]</sup>

$$S_r = \frac{1}{\Delta} \left| \frac{\partial \Delta}{\partial T} \right| \quad (1.14)$$

$S_r$  is typically expressed in  $\% \cdot K^{-1}$  or  $\% \cdot ^\circ C^{-1}$  and allows for direct comparison of different nanothermometers, regardless of their working principle, composition, or experimental setup.

The temperature uncertainty (or temperature resolution),  $\delta T$ , is the smallest temperature that can be resolved with a given nanothermometer.  $\delta T$  can be determined experimentally by evaluating the fluctuation in time of the measured temperature given by a thermometric parameter  $\Delta$ . From the cumulative of these measurements, standard deviation from the actual set temperature represents the uncertainty  $\delta T$ . Alternatively,  $\delta T$  can be estimated as:<sup>[136]</sup>

$$\delta T = \frac{1}{S_r} \frac{\delta \Delta}{\Delta} \quad (1.15)$$

Here,  $\delta \Delta / \Delta$  is the relative uncertainty of the thermometric parameter  $\Delta$ , which depends on the measurement setup and is estimated from  $\Delta$  error. For intensity based nanothermometers, this value depends on the signal-to-noise ratio of the emission spectrum, and can be improved by using longer signal acquisition times and/or averaging of consecutive measurements.

The repeatability characteristic,  $R$ , describes how well a nanothermometer provides accurate temperature measured repeatedly under the same circumstances, and is given as:

$$R = 1 - \frac{\max |\Delta_c - \Delta_i|}{\Delta_c} \quad (1.16)$$

$\Delta_c$  is thermometric parameter extracted from a calibration curve at a given temperature and  $\Delta_i$  represents thermometric parameter at that temperature of repeated measurements  $i$ .

In the case of thermal imaging and measurements of transient temperatures, spatial  $\delta x$  and temporal  $\delta t$  resolution of nanothermometers is respectively given as minimum distance or time interval between measurements of larger than  $\delta T$  temperature change.<sup>[137]</sup>

$$\delta t = \delta T / \left| \frac{\partial T}{\partial t} \right|_{\max} \quad (1.17)$$

### 1.5.3 RENPs as nanothermometers

When it comes to RENPs operating as nanothermometers, many have been developed over the years, operational principles of which are grounded in temperature dependent photophysics described in section 1.5.1. Below, are some notable examples in the development of RENP nanothermometers, with focus towards RENPs that could be used or have been used in a biomedical framework. For a more comprehensive overview the reader is encourage to refer to articles by Brites et al.,<sup>[130]</sup> Quintanilla et al.,<sup>[137]</sup> Jaque and Vetrone,<sup>[138]</sup> Dramićanin et al.,<sup>[132]</sup> and Wang et al.<sup>[139]</sup>

As mentioned before most RENPs are constructed as single-center or double-center LIR-based nanothermometers. In the case of single-center nanothermometry, RENPs take advantage of the thermally coupled  $RE^{3+}$  energy levels to define LIR thermometric parameters.<sup>[140]</sup> Vetrone et al. were the first to show that  $NaYF_4:Er^{3+}$ ,  $Yb^{3+}$  RENPs can be used as upconverting nanothermometers under NIR excitation.<sup>[141]</sup> Green light emitting  ${}^2H_{11/2}$  and  ${}^4S_{3/2}$  energy levels of  $Er^{3+}$  are thermally repopulated following the Boltzmann distribution. Hence LIR between  ${}^2H_{11/2} \rightarrow {}^4I_{15/2}$  and  ${}^4S_{3/2} \rightarrow {}^4I_{15/2}$  radiative transitions can be used to define a thermometric parameter  $\Delta$ . Furthermore, nanometer scale of these  $Er^{3+}$ -doped RENPs were demonstrated to enable sub-cellular temperature sensing. Following this seminal study, RENPs of various compositions are continuously explored as single-center LIR-based nanothermometers, where in addition to  $Er^{3+}$ , also emissions stemming from the thermally coupled excited states of  $Tm^{3+}$ ,  $Pr^{3+}$ , and  $Nd^{3+}$  are used for all-optical nanothermometry. As single-center LIR nanothermometers,  $Nd^{3+}$ -doped RENPs utilize the thermally coupled Stark sub-levels ( $R_1$  and  $R_2$ ) of the  ${}^4F_{3/2}$  manifold.<sup>[142]</sup> Since  $Nd^{3+}$  radiative transitions  ${}^4F_{3/2} \rightarrow {}^4I_J$  ( $J = 9/2, 11/2, 13/2$ ) in the NIR region all stem from the same excited state, alongside deep-tissue imaging, sub-cutaneous temperature sensing in the BW-I and BW-II can be carried out with these RENPs.<sup>[143–145]</sup> However, due to the small energy gap ( $< 100 \text{ cm}^{-1}$ ) between Stark sub-levels of  ${}^4F_{3/2}$  manifold, LIR between  $R_1, R_2 \rightarrow Z_{i,j}$ , emission bands (here,  $Z_{i,j}$  corresponds to Stark sub-levels of  ${}^4I_{9/2}$  energy level;  $i$  and  $j$  can be equal) is of low relative thermal sensitivity, on the order of  $0.1\text{-}0.2 \text{ \%}\cdot\text{C}^{-1}$ . In RENPs with high crystal field strength the fine structure of  ${}^4F_{3/2} \rightarrow {}^4I_J$  radiative transitions of  $Nd^{3+}$  can be spectrally resolved, and temperature dependent change of peak position and width can be intermixed in LIR calculations, thus improving  $S_r$  attainable with  $Nd^{3+}$ -doped RENPs (see chapter 9).<sup>[146]</sup> Even more substantial improvement in  $S_r$  of single-center nanothermometers has been demonstrated with the thermally enhanced excited state absorption. Souza et al., have used  $Y_2O_3:Eu^{3+}$  RENPs to show that  ${}^5D_0 \rightarrow {}^7F_4$  DS emission intensity can represent the thermal population of  ${}^7F_1$  and

${}^7F_2$  excited states with respect to the non-degenerate  ${}^7F_0$  ground state.<sup>[147]</sup> Hence, LIR thermometric parameter could be constructed from the  ${}^5D_0 \rightarrow {}^7F_4$  DS emission intensity obtained at different excitation wavelengths. In this case, between excitation at 580 nm ( ${}^7F_0 \rightarrow {}^5D_0$ ) and 593 nm ( ${}^7F_1 \rightarrow {}^5D_0$ ), or 580 nm ( ${}^7F_0 \rightarrow {}^5D_0$ ) and 611 nm ( ${}^7F_2 \rightarrow {}^5D_0$ ) for temperature sensing in the physiological temperature range.  $S_r$  for the latter thermometric parameter was  $> 1 \text{ \%}\cdot\text{C}^{-1}$  in the 12-52 °C range. Marciniak et al. has expanded the excited state absorption nanothermometry to the  $\text{Nd}^{3+}$ -doped RENPs.<sup>[148]</sup> Exploiting the photon-avalanche-like energy looping mechanism at 1064 nm excitation, thermally driven population of the  ${}^4I_{11/2}$  excited state from  ${}^4I_{9/2}$  ground state could be measured by the LIR defined between  ${}^4F_{3/2} \rightarrow {}^4I_{9/2}$  emission under direct 808 ( ${}^4I_{9/2} \rightarrow {}^4F_{5/2}$ ) and indirect 1064 nm ( ${}^4I_{11/2} \rightarrow {}^4F_{3/2}$ ) excitation. At temperature of 37 °C,  $S_r$  values between 2 and 5  $\text{\%}\cdot\text{C}^{-1}$  were obtained, which were dependent on the crystal host of RENPs, that defines the energy separation between  ${}^4I_{9/2}$  and  ${}^4I_{11/2}$  energy levels and specific phonon cut-off frequencies.

In addition to single-center nanothermometers, RNP double-center nanothermometers of high thermal sensitivity and covering a wide spectral range have been designed. One of the classical double-center nanothermometers are  $\text{Yb}^{3+}$ - and  $\text{Nd}^{3+}$ -doped RENPs, where LIR is defined between  $\text{Yb}^{3+}$  and  $\text{Nd}^{3+}$  DS emissions in the NIR. Marciniak et al. have studied  $\text{LiLaP}_4\text{O}_{12}:\text{Nd}^{3+}, \text{Yb}^{3+}$  RENPs, with LIR between the  ${}^4F_{3/2} \rightarrow {}^4I_{9/2}$  emission of  $\text{Nd}^{3+}$  (~880 nm) and  ${}^2F_{5/2} \rightarrow {}^2F_{7/2}$  emission of  $\text{Yb}^{3+}$  (~980 nm).<sup>[149]</sup> Temperature sensing with these RENPs is governed by the temperature dependent non-resonant phonon-assisted energy transfer, from  $\text{Nd}^{3+}$  ( ${}^4F_{3/2}$ ) to the  $\text{Yb}^{3+}$  ( ${}^2F_{5/2}$ ) ions, described by the Miyakawa-Dexter model. The  $S_r$  of  $\text{Yb}^{3+}, \text{Nd}^{3+}$ -doped RENPs was found to depend on the molar concentration of the  $\text{Yb}^{3+}$  ions (5-50 mol%). The varying amounts of  $\text{Yb}^{3+}$  would shift the balance between the  $\text{Nd}^{3+} \rightarrow \text{Yb}^{3+}$  energy transfer and  $\text{Yb}^{3+} \rightarrow \text{Nd}^{3+}$  back energy transfer (BET), the latter being more prominent at low  $\text{Yb}^{3+}$  concentrations and high temperatures. Highest  $S_r$  of  $0.3\text{\%}\cdot\text{C}^{-1}$  was found for the 50 mol%  $\text{Yb}^{3+}$  doped RENPs and was ascribed to the increased energy diffusion among the  $\text{Yb}^{3+}$  ions rather than  $\text{Yb}^{3+} \rightarrow \text{Nd}^{3+}$  BET. Ximendes et al. have also investigated  $\text{Yb}^{3+}, \text{Nd}^{3+}$  pair based nanothermometry in  $\text{LaF}_3$  RENPs of different core/shell architectures.<sup>[150]</sup> Here, LIR was defined between the  ${}^4F_{3/2} \rightarrow {}^4I_{11/2}$  emission of  $\text{Nd}^{3+}$  (~1060 nm) and  ${}^2F_{5/2} \rightarrow {}^2F_{7/2}$  emission of  $\text{Yb}^{3+}$  (~1000 nm). Equal doping amounts of both  $\text{Yb}^{3+}$  and  $\text{Nd}^{3+}$  were either co-localized in the core-only RENPs or separated within the different layers of core/shell RENPs:  $\text{Yb}^{3+}$  in the core and  $\text{Nd}^{3+}$  in the shell ( $\text{Yb}^{3+}/\text{Nd}^{3+}$ ) and vice versa ( $\text{Nd}^{3+}/\text{Yb}^{3+}$ ). Core-only RENPs had  $S_r \sim 0.10 \text{ \%}\cdot\text{C}^{-1}$ , while the core/shell structures had  $S_r$  values of approximately  $0.36 \text{ \%}\cdot\text{C}^{-1}$  and  $0.41 \text{ \%}\cdot\text{C}^{-1}$  for  $\text{Yb}^{3+}/\text{Nd}^{3+}$  and  $\text{Nd}^{3+}/\text{Yb}^{3+}$ , respectively. As with increased  $\text{Yb}^{3+}$  doping in the study by Marciniak et al., these

differences have been tentatively ascribed to the balance between the phonon-assisted  $\text{Nd}^{3+} \rightarrow \text{Yb}^{3+}$  energy transfer and  $\text{Yb}^{3+} \rightarrow \text{Nd}^{3+}$  BET; the latter being more suppressed as the two optically active  $\text{RE}^{3+}$  ions are spatially separated within the core/shell heterostructures. Cortelletti et al. have recently demonstrated that  $\text{Er}^{3+}$  co-doping alongside  $\text{Nd}^{3+}$  and  $\text{Yb}^{3+}$ , can act as an energy sink eliminating the deleterious  $\text{Yb}^{3+} \rightarrow \text{Nd}^{3+}$  BET.<sup>[151]</sup> In this case,  $S_r$  of LIR between  $\text{Nd}^{3+}$  and  $\text{Yb}^{3+}$  DS emission was increased from 0.18 to 1.62  $\% \cdot ^\circ\text{C}^{-1}$  (at 50  $^\circ\text{C}$ ) for  $\text{Er}^{3+}$  concentration from 0 to 8 mol%, respectively. Worth noting that until recently the NIR emitting double-center nanothermometers took advantage of BW-I and BW-II only, yet, as is presented in chapters 5 and 10,  $\text{Er}^{3+}$ -doped RENPs have enabled to shift the concept of sub-cutaneous temperature sensing to BW-III.<sup>[152]</sup>

Although of lesser relevance to biomedical applications, some examples of double-center RNP nanothermometers that are worth mentioning include the use of temperature dependent ligand-assisted energy transfer. Martínez et al., have used upconverting RENPs of different size to construct highly sensitive hybrid nanothermometers.<sup>[153]</sup> Large RENPs showed temperature dependent UC emission intensity quenching, while UC emission of small RENPs was enhanced at elevated temperatures. Although thermal intensity quenching is a commonly observed phenomenon, it has been proposed that surface phonons, originating from the coordination between optically active  $\text{RE}^{3+}$  and oxygen atoms of capping ligands, can enhance emission intensity in small RENPs at higher temperatures.<sup>[154]</sup> Thus, simultaneously measuring the UC emission from the mixture of these RENPs permitted to define LIR thermometric parameter  $\Delta$  with  $S_r$  of 5.88  $\% \cdot ^\circ\text{C}^{-1}$ . Mi et al., have also exploited the thermal emission enhancement by the surface phonons to create a series of RENPs of different shape and architecture, showing that segmented rod-like  $\text{NaYF}_4:\text{Yb}^{3+}$ ,  $\text{Nd}^{3+}/\text{NaYF}_4/\text{NaYF}_4:\text{Yb}^{3+}$ ,  $\text{Er}^{3+}$  RENPs can be used as nanothermometers with  $S_r$  as high as 9.6  $\% \cdot ^\circ\text{C}^{-1}$  at 30  $^\circ\text{C}$ .<sup>[155]</sup>

#### 1.5.4 Practical use of nanothermometry

The potential of optical nanothermometry has been recognized in many fields of fundamental and applied research. Various nanothermometers have been used to study nanofluids, microelectronics, thermal properties of materials, including biological tissues, or to obtain controlled adjustment of absolute temperatures in the course of thermal therapies.

In biomedical sciences, the group of Daniel Jaque has pioneered the concept of thermo-optical biopsy, which allows to discriminate between different tissue types by measuring transient temperature changes in tissues after a mild heating (Figure 1.12). Ximendes et al., used

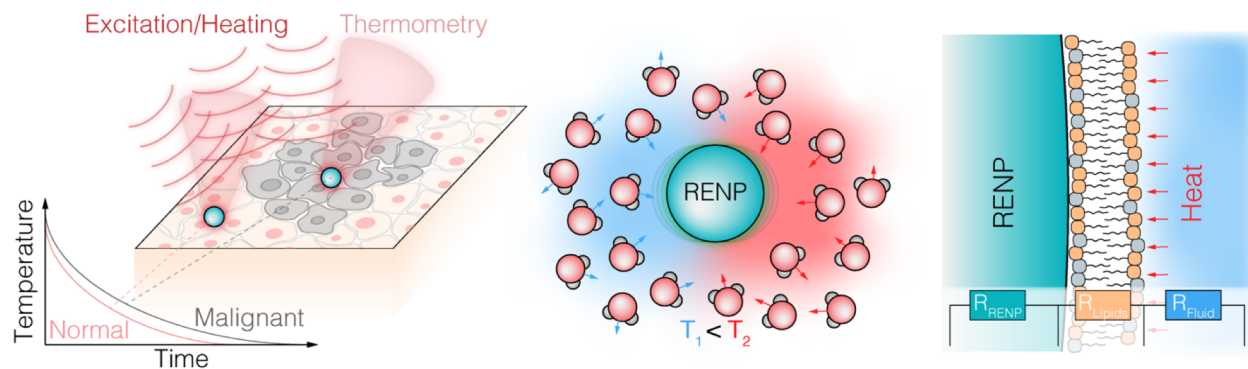


**Figure 1.12. Application of RENPs as nanothermometers.**

**Photoluminescence nanothermometry enables control over heat based treatments or discrimination between normal and malignant tissues in biomedicine; it allows to study properties of nanofluids, such as their instantaneous Brownian velocity; or to measure phenomenological parameters of materials that are inaccessible to conventional techniques, like thermal conductivity of lipid bilayers.**

$\text{Nd}^{3+}/\text{Yb}^{3+}$  RENPs, described in the previous section, to extract phenomenological tissue parameters like absorption coefficient and thermal diffusivity of tissue.<sup>[150]</sup> This concept was later expanded from point-like information collection *in vivo* to whole body imaging with supersensitive ( $S_r = 5 \text{ \%} \cdot \text{°C}^{-1}$ )  $\text{LaF}_3:\text{Er}^{3+}$ ,  $\text{Yb}^{3+}/\text{LaF}_3:\text{Tm}^{3+}$ ,  $\text{Yb}^{3+}$  nanothermometers.<sup>[156]</sup> These seminal studies showcased how information beyond “hot” or “cold” can be extracted with the help of nanothermometry, and further used to identify damaged tissues. Specifically, quantum dots as optical thermometers have been later used to recognize ischemic,<sup>[157]</sup> or cancerous tissues.<sup>[158]</sup> In the latter case, thermo-optical biopsy provided information about tumor development in mice models 6 days before it would be evident from visual inspection. del Rosal et al. have also demonstrated that NIR emitting  $\text{Ag}_2\text{S}$  NPs could be used for through scalp and skull nanothermometry.<sup>[159]</sup> These nanothermometers allowed to pick up minute temperature changes in the brain during a barbiturate-induced coma, which could be subsequently correlated to changes in brain activity.

Another avenue of biomedical research that is expected to benefit significantly from nanothermometry is PTT of cancer. PTT uses light to create local heating at a diseased area, with the help of NPs that have high light-to-heat conversion efficiency, in order to selectively eradicate the malignancy. As PTT agents noble metal NPs, chalcogenide NPs, carbon-based NPs, or even  $\text{Nd}^{3+}$ -doped RENPs have been explored. A successful outcome of PTT is considered not only elimination of the underlying disease but also doing so with minimal damage to healthy tissues. In order to achieve this, the heating intensity has to be accurately controlled through real-time and local temperature feedback. Unfortunately, the non-invasive temperature sensing with thermal cameras at the skin surface depends on the relative orientation angle between the camera and the surface, which can lead to unreliable

measurements. Furthermore, this technique is limited to superficial measurements, whereas intratumoral temperature can differ significantly from that measured at the surface. The use of nanothermometers alongside PTT agents could overcome these issues, as real-time temperature information could be gathered during the therapeutic process *in situ*.

Rocha et al. have demonstrated that combining the  $\text{LaF}_3:\text{Nd}^{3+}$  RENPs (thermometers) with gold nanorods (heaters) has the possibility of exciting both structures at 1 mm depth of phantom tissue and monitoring local temperature through thermometric response of the  $\text{Nd}^{3+} \ ^4\text{F}_{3/2} \rightarrow \ ^4\text{I}_{9/2}$  emission.<sup>[160]</sup> The study was subsequently extended to show that difference between superficially measured temperature and that measured locally – at 2 mm depth of chicken breast tissue – can be up to 62 °C, at the highest laser excitation power density studied.<sup>[161]</sup> Zhu et al., have constructed a hybrid heater-thermometer out of  $\text{NaLuF}_4:\text{Er}^{3+}$ ,  $\text{Yb}^{3+}/\text{NaLuF}_4$  RENPs coated with a carbon shell.<sup>[162]</sup> Using green UC emission of  $\text{Er}^{3+}$  to measure temperature, it was concluded that local heating from the carbon shell at the nanoscale is significantly higher than measuring temperature of the whole aqueous dispersion with a conventional thermocouple. Hence, to avoid collateral damage to healthy cells and contain thermal treatment to the region of malignancy, laser irradiation power during the PTT has to be significantly reduced. Quintanilla et al., used polystyrene beads as a colloidal support for gold nanostars – heaters, and  $\text{CaF}_2:\text{Nd}^{3+}$ ,  $\text{Y}^{3+}$  RENPs – nanothermometers.<sup>[163]</sup> The performance of this heater-thermometer nanoplatform was analyzed in depth in 3D tumor cell models (spheroids) *in vitro*, showing that  $\text{Nd}^{3+}$  emission around 1050 nm ( $\ ^4\text{F}_{3/2} \rightarrow \ ^4\text{I}_{11/2}$ ) can be used for tracking and simultaneous temperature measurements in BW-II, while gold nanostars provided the photothermal effect. Under 808 nm induced heating, *in situ* acquired temperatures from within cellular spheroids were systematically higher than those measured superficially by the thermal camera, particularly at higher concentration of nanobeads and laser excitation power densities, illustrating the importance of local temperature measurements during the PTT.

Beyond biomedicine, nanothermometers have been used to observe phenomena at the nanoscale otherwise concealed from the sight of conventional methods. In nanofluidics, Brites et al. employed  $\text{NaYF}_4:\text{Er}^{3+}$ ,  $\text{Yb}^{3+}$  RENPs as nanothermometers to measure their instantaneous Brownian velocity when dispersed in different media (Figure 1.12).<sup>[164]</sup> By marking the temperature sensing onset at different positions along RNP dispersion, externally heated in a unidirectional fashion, the instantaneous Brownian velocity could be calculated for different RENPs. It was concluded that the instantaneous Brownian velocity depends on the volume fraction of the RENPs, yet at very low concentrations it is independent of the RENPs size or

shape, as well as the suspension media. These experiments have showcased how nanothermometry can help to understand nanofluids in terms of their thermal conductivity, convective heat, and mass transport. Nanothermometry has also been exploited to evaluate thermal conductivity of materials such as SiO<sub>2</sub> and TiO<sub>2</sub> nanofilms,<sup>[165]</sup> AlGaIn:Er<sup>3+</sup> film,<sup>[166]</sup> and KLuWO<sub>4</sub>:Tm<sup>3+</sup>, Ho<sup>3+</sup> RENPs.<sup>[167]</sup> Recently, Bastos et al. have experimentally determined the thermal conductivity of a lipid bilayer around LiYF<sub>4</sub>:Er<sup>3+</sup>, Yb<sup>3+</sup> RENPs (Figure 1.12).<sup>[168]</sup> Prior to this study thermal conductivities of lipid bilayers were predicted only from numerical simulations. In addition, it was noticed that the lipid bilayer can serve as a thermal barrier that limited heat transfer between RENPs and water. Exploring thermal conductivity of model lipid bilayers has direct implications towards understanding spatial temperature variations and heat transfer across actual cellular membranes. On the other end of practical applicability of nanothermometers, Hartman et al. used NaYF<sub>4</sub>:Er<sup>3+</sup>, Yb<sup>3+</sup> RENPs for *in operando* temperature monitoring during high temperature gas catalysis.<sup>[169]</sup> The *in situ* temperatures, measured with the help of nanothermometers, were found to deviate from the preset values of 300 and 350 °C by as much as 20 and 40 °C, respectively, due to heat dissipation during gas change.

Overall, nanothermometry is continuously being adopted in various fields of fundamental and practical research, as more and more evidence is gathered about the necessity for temperature measurements at the scales relevant to nanoscopic processes and under local conditions at which these processes prevail. Furthermore, to the delight of the biomedical community optical nanothermometry adds an additional layer of information that can make a difference in timely and accurate disease diagnosis, and in providing efficient treatment with minimized side effects.

### 1.5.5 Challenges of nanothermometry

Despite the widespread appeal of nanothermometry with RENPs, there are caveats that ought to be discussed. Besides the obvious demand for nanothermometers that are the brightest, most sensitive, and inert to other cues but temperature, few pitfalls have been voiced and addressed only recently.

Irrespective of the type of RENP nanothermometers, single- or double-center, the LIR-based approach requires external calibration by an independent temperature measurement with a thermocouple, infrared thermal camera, or a pyrometer. However, the LIR vs temperature calibration only holds for the environment and conditions at which the calibration was performed. Any change to these factors requires re-calibration of LIR nanothermometers, which is a tedious and at times impossible task, particularly in biomedical research where

nanothermometers are present in tissues, cells, or other milieu. This intrinsic limitation of secondary nanothermometers (requiring external calibration) can be by-passed with primary nanothermometers, LIR of which is extracted from the thermodynamic laws or phenomenological parameters describing radiative transitions in RENPs. Nanothermometers governed by the Boltzmann statistics (equation 1.5) could be operated without the need for external calibration if parameters  $B$  and  $\delta E$  are known. Balabhadra et al., demonstrated that green UC emission of  $\text{SrF}_2:\text{Er}^{3+}$ ,  $\text{Yb}^{3+}$  RENPs intrinsically defines a primary-nanothermometer.<sup>[170]</sup> The energy gap  $\delta E$  between the thermally coupled  $^2\text{H}_{11/2}$  and  $^4\text{S}_{3/2}$  excited states was calculated as distance between the barycenters of radiative transitions stemming from these levels, while parameter  $B$  was empirically extracted from the  $\Delta$  vs laser excitation power plot. In the absence of laser induced heating (at the limit of no excitation) the temperature  $T_0$  and thermometric parameter  $\Delta_0 = B \cdot \exp(-\delta E/k_B \cdot T_0)$  can be used to readily extract the absolute measured temperature ( $T$ ) by the nanothermometer:

$$\frac{1}{T} = \frac{1}{T_0} - \frac{k_B}{\delta E} \ln\left(\frac{\Delta}{\Delta_0}\right) \quad (1.17)$$

Through equation 1.17 the accurate temperature readout of these RENPs was confirmed in their powder form or when dispersed in aqueous medium. It is worth noting that these primary nanothermometers do not only avoid necessity for the recalibration but could serve to calibrate secondary nanothermometers under conditions where thermocouple or infrared camera measurements are impossible. In general, primary nanothermometers can be defined for any RENPs where thermometric parameter  $\Delta$  is given by the emission from the thermally coupled excited states. While studying the heater-thermometer beads described in the previous section, Quintanilla et al. employed a pre-calibration step to define parameter  $B$  for the thermally coupled Stark sub-levels ( $R_1$  and  $R_2$ ) of  $\text{Nd}^{3+}$ .<sup>[163]</sup> This allowed for *in situ* temperature sensing within 3D tumor spheroids without the need for external calibration of RENPs, which is a challenging task in itself. Furthermore, it was demonstrated that parameter  $B$  can be extracted from the few first points of transient temperatures curves that were used to observe absolute temperature change within spheroid models during the PTT. Also, parameter  $B$  can be calculated following the Judd-Ofelt formalism, yet this approach has been scarcely employed.<sup>[130]</sup> Still more primary nanothermometers are to be developed, especially those working in the NIR at the BW-III, which would be quite pertinent given the recent concerns regarding the accuracy of temperature measurements *in vivo*.

Since the optical profile of various tissues is not constant across a wide spectral range, NIR emission bands of RENPs, and other photoluminescent nanothermometers, are non-evenly affected by tissue scattering and absorption. This inhomogeneity of tissue optical properties has been just recently acknowledged to lead to significant inaccuracies in measuring temperature, as *ex vivo/vitro* calibration of the nanothermometers would not hold once applied in *in vivo* models.<sup>[171,172]</sup> Moreover, tissue optical properties are subject to change with temperature, making it ever so non-trivial to compensate for the distortion in emission bands by pre-defined tissue absorption profile. Nonetheless, several options have been proposed to solve this problem. As decay rates of excited states are (for most cases) insensitive to tissue optical properties, lifetime-based nanothermometry could be of great value in deep-tissue temperature sensing, yet both lifetime nanothermometers and affordable easy-to-implement lifetime imaging set-ups, working entirely in the NIR, are lagging behind in development. Another more pragmatic approach is to create a database of optical properties of different tissues and at different temperatures, which could be used to correct emission of nanothermometers after propagating through tissues. Also, nanothermometers whose emission bands would be evenly attenuated by tissue absorption might keep their calibration irrespective of that. As such, single-band nanothermometers working in the very narrow spectral range could be preferable, like Nd<sup>3+</sup>-doped RENPs with LIR thermometric parameter  $\Delta$  defined for spectrally adjacent transitions from the R<sub>1</sub> and R<sub>2</sub> Stark sub-levels. It is also possible that a middle ground between the above mentioned approaches will prove best to attain reliable deep-tissue temperature sensing with optical nanothermometers.

In addition to measurement artifacts associated with optical properties of tissues, RENP nanothermometers themselves can suffer from false temperature readout. L. Labrador-Páez et al. have demonstrated that RENPs accurate response to temperature can be affected by i) excitation power density, ii) emission attenuation by self-absorption, and iii) medium absorption *in vitro*.<sup>[173]</sup> In the case of nanothermometry by UC emission of RENPs, variations in excitation power can cause uneven changes in the emission intensity of different bands used to construct LIR thermometric parameter, especially if these emissions originate from excited states of different photon order of population. Despite low absorption cross-sections of RE<sup>3+</sup>, emission profile distortion by self-absorption was demonstrated in the Nd<sup>3+</sup>-doped RENPs for the emission corresponding to the  $^4F_{3/2} \rightarrow ^4I_{9/2}$  radiative transition. The self-absorption by these RENPs would result in observed apparent temperature increase measured at different positions of RENPs dispersion, although actual temperature was kept constant. While absorption properties of the medium, in which RENPs are dispersed, present additional level of apparent

heating if not accounted for adequately. Furthermore, Pickel et al. reported the apparent self-heating of  $\text{NaYF}_4:\text{Er}^{3+}$ ,  $\text{Yb}^{3+}$  RENPs when applied as nanothermometers at a single-particle level.<sup>[174]</sup> The artificial rise of measured temperature with increasing the excitation power was attributed to the increased radiative and non-radiative decay rates from higher lying  $\text{Er}^{3+}$  energy levels.

Overall, various artifacts that can curb application of optical nanothermometry point to how detrimental it is to thoroughly characterize any potential nanothermometer in different environments and at different measurement conditions, prior to their practical implementation.

## 1.6 Motivation, aims and outline

Following this brief introduction on RENPs' optical properties and uses thereof, their vast potential in scientific research, particularly biomedical, is undeniable, and excitingly so remains to be completely tapped into. The RENPs are highly modular structures, composition and architecture of which need to be rationally designed to attain a nanoplatform best suited for a specific task. In order to do so, multidisciplinary efforts of physics, chemistry and biology have to be put together. In this thesis, theranostic RENPs are design and investigated step-by-step, building on the current RENP research practices, pushing certain limitations, and reevaluating state-of-the-art theranostic approaches. With a singular aim preserved, to create a theranostic nanoplatform that is versatile, effective, and discretely controlled by light – bearing resemblance to the miniature submarine with a medical crew, like in the “Fantastic Voyage”.

Specifically, the potential of Nd<sup>3+</sup>-doped RENPs is explored. Starting with simple Nd<sup>3+</sup>-doped core/shell RENPs, suitable for imaging and temperature sensing, their DS emission efficiency is investigated by measuring absolute photoluminescence quantum yield (*PLQY*) as a function of Nd<sup>3+</sup> doping, core/shell architecture, and dispersion media (chapter 3). Insights gained from this study are beneficial towards optimizing and understanding the limitation of such RENPs. Furthermore, it provides quantitative information about RENPs' spectral characteristics that are often lacking to make judgement statements about how one system is better than the other. The design of these RENPs is further expanded in order to accommodate both DS and UC emission in a single theranostic probe, that could respectively be used for imaging and therapy (chapter 4). RENP excitation pathways via 806 or 980 nm irradiation are studied across the wide spectral range of emissions covered by photoluminescence bands of Ho<sup>3+</sup>, Er<sup>3+</sup>, Yb<sup>3+</sup>, and Nd<sup>3+</sup>. Results indicated that ~800 nm excitation is not only better suited for biomedical use as it is less absorbed by water, thus reducing undesired tissue heating, but also has the capacity to expand the range of observable emission of RENPs and promotes excitation of higher laying energy states more effectively. Finally, the architecture of these RENPs is adjusted by adding an Yb<sup>3+</sup>-doped energy relay layer between Nd<sup>3+</sup> sensitizers and Er<sup>3+</sup>, Ho<sup>3+</sup> activators, which is intended to reduce emission quenching. These multilayered RENPs are then explored as first of their kind nanothermometers operating in the BW-II and BW-III (chapter 5). Importantly, the thermal response of these nanothermometers is recognized to be governed by a temperature dependent energy transfer between Er<sup>3+</sup> excited states and water molecules.

Despite having a theranostic nanoplatform that is equipped for imaging, nanothermometry, and therapy, perhaps there is a better way to execute these functions in real life than “all-at-once”,

as commonly is suggested. A multilayered  $\text{LiYF}_4$  RENPs were thus studied as decoupled theranostics RENPs, meaning that therapy and diagnostics with these RENPs can be exercised independently of each other, by simple control of excitation wavelength (chapter 6). It is decisively shown that under 806 nm excitation these RENPs have no therapeutic effect and solely act as NIR imaging probes and nanothermometers, whereas therapeutic action can be triggered only by excitation with 980 nm radiation. The decoupling of these tasks provides the ability to safely track RENPs inside the body and observe their accumulation at the target area, without involuntarily damaging healthy tissues and/or exhausting therapeutic capacity of RENPs prematurely (i.e. off target drug release).

Following the concept of decoupled theranostics RENPs, their further optimization and improvement became imperative. In depth studies have been performed in order to create decoupled theranostic RENPs of relatively small size, improved temperature sensing capacity, and of optimized UC emission for therapeutic action. First, the synthesis methods of Li-based RENPs have been reinvented in a way that would allow to make RENPs 3-4 times smaller than previously employed  $\text{LiYF}_4$  nanostructures, while maintaining their optical performance (chapter 7). A library of  $\text{LiYbF}_4:\text{RE}^{3+}/\text{LiYF}_4$  RENPs (where  $\text{RE}^{3+}$  is  $\text{Tm}^{3+}$ ,  $\text{Er}^{3+}$ , or  $\text{Ho}^{3+}$ ) is then created and scrutinized over their UC emission, excited state lifetimes and *PLQY*, as a function of  $\text{RE}^{3+}$  doping concentration (chapter 8). This study underlines the selection for the brightest upconverting RENPs that can be used in drug release or PDT. Second, more detailed analysis was performed on the  $\text{Nd}^{3+}$  single-band temperature sensing in  $\text{Li}^+$ -based RENPs (chapter 9); underscoring that thermal sensitivity can be improved across all  $\text{Nd}^{3+}$  emission bands by careful selection of intensity integration ranges used to construct the luminescence intensity ratio thermometric parameter  $\Delta$ . Furthermore, pushing NIR nanothermometry in the BW-III, single-band temperature sensing with  $\text{Er}^{3+}$  DS emission around 1550 nm is demonstrated (chapter 10). While additional doping with  $\text{Ce}^{3+}$  is shown to suppress UC emission, thus permitting integration of BW-III single-band  $\text{Er}^{3+}$  nanothermometry in the decoupled theranostic RENPs.

Finally, based on the results of these individual optimization steps, novel architectures of decoupled theranostic RENPs are proposed (chapter 11). In contrast to the first generation decoupled theranostic RENPs, these structures are significantly smaller, brighter, and are overall better suited for NIR imaging and therapy, constituting further strides towards truly multifunctional theranostics.

## 2 MATERIALS AND METHODS

---

### 2.1 RENP synthesis

#### 2.1.1 Materials

Table 1. Chemicals employed in the preparation of the precursors and synthesis of RENPs.

Name	Abbreviation/Formula	Purity	Manufacturer
Neodymium oxide	Nd <sub>2</sub> O <sub>3</sub>	99.999%	Alfa Aesar
Erbium oxide	Er <sub>2</sub> O <sub>3</sub>	99.99%	Alfa Aesar
Holmium oxide	Ho <sub>2</sub> O <sub>3</sub>	99.997%	Alfa Aesar
Thulium oxide	Tm <sub>2</sub> O <sub>3</sub>	99.997%	Alfa Aesar
Ytterbium oxide	Yb <sub>2</sub> O <sub>3</sub>	99.998%	Alfa Aesar
Gadolinium oxide	Gd <sub>2</sub> O <sub>3</sub>	99.99+%	Alfa Aesar
Yttrium oxide	Y <sub>2</sub> O <sub>3</sub>	99.999%	Alfa Aesar
Lutetium oxide	Lu <sub>2</sub> O <sub>3</sub>	99.9%	Alfa Aesar
Cerium carbonate	Ce <sub>2</sub> (CO <sub>3</sub> ) <sub>3</sub> ·XH <sub>2</sub> O	99.9%	Alfa Aesar
Sodium trifluoroacetate	Na-TFA	98%	Alfa Aesar
Lithium trifluoroacetate	Li-TFA	97%	Alfa Aesar
Trifluoroacetic acid	TFA	99%	Sigma-Aldrich
Milli-Q water	H <sub>2</sub> O	Distilled and filtered	MilliporeSigma
Oleic acid	OA	90%	Alfa Aesar
Oleylamine	OM	70%	Sigma-Aldrich
1-Octadecene	ODE	90%	Alfa Aesar

All materials were used as obtained, without further purification.

#### 2.1.2 Preparation of precursors

RE<sup>3+</sup>-trifluoroacetate (RE-TFA) precursors were prepared out of RE<sub>2</sub>O<sub>3</sub> (or RE<sub>2</sub>(CO<sub>3</sub>)<sub>3</sub>) as starting materials. Typical precursor preparation procedure entails mixing stoichiometric quantities of desired RE<sub>2</sub>O<sub>3</sub> (total amount of oxides always corresponding to half of the required amount of RE-TFA) with 5 mL trifluoroacetic acid and 5 mL of water in 50 (or 100) mL three-neck round bottom flask. The mixture is refluxed under vigorous stirring at 80 °C until the solution becomes clear, at which point the temperature is decreased to 60 °C for residual TFA and water to evaporate. Dried RE-TFA precursors are either used immediately or sealed and stored at RT for later use. Optionally, for portioning of precursors during synthesis, oleate mixtures are prepared beforehand by dissolving RE-TFA together with Li- or Na-TFA in OA and ODE under vacuum at 125 °C.

### 2.1.3 Thermal decomposition

Among multiple RENP synthesis approaches, thermal decomposition of metal-trifluoroacetate precursors has been applied to make all of the RENPs in this thesis.<sup>[175]</sup> This method yields RENP of high crystallinity and narrow size distribution, at the same time core/shell architectures can be easily created. Two distinct approaches of thermal decomposition synthesis have been used to make RENPs: i) heat-up and/or ii) hot-injection. Below the general thermal decomposition synthesis workflow is outlined; details on preparation of specific RENPs are given in the beginning of each chapter 3 through 10.

In a typical heat-up thermal decomposition synthesis, metal-trifluoroacetate precursors are first dissolved in a mixture of OA (also OM) and ODE under vacuum at 110 °C in a 100 mL round bottom flask. (Magnetic stirring is employed throughout the whole duration of the procedure, same applies for the hot-injection approach). After precursor dissolution, and degassing of the mixture, the flask is backfilled with argon and temperature is increased to 330 °C (unless specified otherwise). Maintaining the argon flow, the reaction is allowed to proceed for 1h before it is cooled down to RT. Obtained RENPs are then collected and washed as described below.

The hot-injection approach entails preparation of separate solutions A and B, which are then mixed together to form RENPs. Typically, solution A is a mixture of even parts of OA and ODE in a 100 mL three neck round bottom flask which is degassed under vacuum at 145 °C for at least 30 min. After degassing, solution A is backfilled with argon and argon flow is maintained for the rest of the synthesis. Separately, solution B contains metal-trifluoroacetate precursors dissolved in a mixture of OA and ODE under vacuum at 125 °C in a 50 mL round bottom flask. The temperature of solution A is then increased to 290-315 °C (depending on the desired RENPs), at which point solution B is injected into solution A using a pump-syringe system (Harvard Apparatus Pump 11 Elite) at a preset injection rate. After complete injection, the reaction is allowed to proceed for at least 1h, at which point it is stopped by cooling down to RT; optionally, the reaction is continued by introducing more injection steps in order to obtain core/shell RENPs with desired functional layers.

RENPs obtained either through heat-up or hot-injection approach are precipitated with ethanol and collected via centrifugation (min. speed 5400 RCF). Then, RENPs are washed at least twice with a mixture of hexane/ethanol, hexane/acetone, or toluene/acetone (1/4 v/v) via centrifugation. Finally, RENPs are redispersed in organic solvent like hexane or chloroform for further structural and optical characterization, or surface treatment.

## 2.2 Surface modification

As-synthesized RENPs feature oleic acid coating that restricts their dispersibility only to organic solvents. In order to render RENPs water dispersible and study their photophysical properties in an aqueous milieu, or apply in biological studies, their surface was modified either via ligand removal/exchange (chapters 3, 9, 10) or phospholipid coating (chapters 4-6).

### 2.2.1 Ligand removal/exchange

In a typical ligand removal procedure,<sup>[64]</sup> ligand-free RENPs are prepared by mixing 50 mg of oleate-capped RENPs dispersed in 25 mL of hexane and 25 mL of distilled water (pH 3-4) under vigorous stirring for 3 h. The two-phase (aqueous/organic) mixture is then poured into the separatory funnel, and the aqueous phase containing the RENPs is isolated. The RENPs are precipitated with acetone (1/3 v/v) via centrifugation at 7500 RPM for 30 min. Obtained pellet is re-dispersed in 25 ml of distilled water (pH 3-4) and is left under stirring for additional 2 h. RENPs are then precipitated with acetone (1/3 v/v) via centrifugation at 7500 RPM for 30 min, and washed twice with a mixture of water/acetone (1/3 v/v). The ligand-free RENPs are re-dispersed in distilled water and stored at 4 °C or RT, for further use.

Citrate coated RENPs are prepared in an analogous way, except the pure distilled water is substituted for 0.2 M trisodium citrate (99%; Alfa Aesar, USA) solution. During the first step of mixing, the pH of trisodium citrate solution is also adjusted to around 3-4, while after phase separation RENPs are re-dispersed in 0.2 M trisodium citrate solution of pH 7-8. After ligand exchange and washing steps, citrate-coated RENPs are re-dispersed in distilled water and stored at 4 °C or RT, for further use.

### 2.2.2 Phospholipid coating

RENPs were also transferred into an aqueous environment following a modified, previously reported, phospholipid coating method.<sup>[176]</sup> Typically, 50 mg of oleate-capped RENPs were re-dispersed in 8 mL of chloroform together with 5.6 mg (2  $\mu$ mol) of 1,2-dioleoyl-*sn*-glycero-3-phosphoethanolamine-N-[methoxy(polyethylene glycol)-2000] (PEG-DOPE) phospholipids (Avanti Polar Lipids, Inc.). In chapter 6, a mixture of 8.96 mg (3.2  $\mu$ mol) of PEG-DOPE and 4.67 mg (6.4  $\mu$ mol) of 1,2-dipalmitoleoyl-*sn*-glycero-3-phosphocholine (DOPC; Avanti Polar Lipids, Inc., USA) phospholipids was used. The whole content is lightly swirled by hand, shortly after following chloroform evaporation at 45 °C under inert Ar atmosphere and magnetic stirring, resulting in a dry phospholipid-RENP film. Subsequently, distilled water (5 mL) is added in order

to hydrate the dry phospholipid-RENP film under sonication at 60 °C temperature for 1 h. The mixture is then passed through 0.45 and 0.2 µm filters sequentially in order to remove large phospholipid and RENP-phospholipid structures. Filtered dispersion of phospholipid-coated RENPs is stored at 4 °C or RT, for further use.

### **2.2.3 Complex formation with Ce<sub>6</sub>**

In chapters 4 and 6, RENPs-Ce<sub>6</sub> complex was formed as a model PDT system. Incorporation of amphiphilic Ce<sub>6</sub> photosensitizer (Frontier Scientific Inc.) with phospholipid-coating RENPs was done exploiting the hydrophobic interaction between the non-polar moieties of the photosensitizer and the amphiphilic coating of RENPs.<sup>[177]</sup> A small amount of Ce<sub>6</sub> stock solution (prepared in phosphate buffer of pH 7) was added to the aqueous dispersion of RENPs, resulting in a final molar concentration of Ce<sub>6</sub> of around 10 µM.

## **2.3 Structural characterization**

The crystallinity and phase of all RENPs were determined via X-ray powder diffraction (XRD) analysis on a Bruker D8 Advance Diffractometer using Cu Kα radiation and step size of 0.05 degree. The morphology and size distribution of RENPs was investigated by transmission electron microscopy (TEM; Philips Tecnai 12) working at the accelerating voltage of 80 kV. The particle size was determined from TEM images using ImageJ software. In chapter 6, distribution of RE<sup>3+</sup> in each layer of core/shell RENPs was further investigated by high-angle annular dark-field scanning transmission electron microscopy and energy-dispersive X-ray analysis EDX with Jeol JEM-2100F TEM (JEOL), carried out by Dr. Jean-Philippe Masse at the Polytechnique Montréal, Canada. In chapters 3, 8, and 10, RE<sup>3+</sup> molar doping concentration was determined via inductively coupled plasma optical emission spectroscopy (ICP-OES) with Agilent Technologies 5100 ICP-OES spectrometer with the help of Dr. Galyna Shul at the NanoQAM, Université du Québec à Montréal, Canada. Prior to ICP-OES measurements, RENPs were dissolved in 5 v% HNO<sub>3</sub> solution. In chapters 4 and 5, transmission Fourier transform infrared (FTIR) spectra of oleate-capped RENPs and RENPs encapsulated in phospholipid micelles were recorded with a ThermoFisher Scientific Nicolet 6700 FTIR spectrometer using a mixture of dried samples with KBr as a dispersant.

## 2.4 Optical characterization

### 2.4.1 Steady state spectroscopy and imaging

UC and DS emission spectra of the RENPs have been measured with an optical setup of the Vetrone Group at INRS, Canada. The setup consists of Avaspec-ULS2048L spectrometer (Avantes) for light collection in the 290-830 nm spectral range, and a Shamrock 500i monochromator (Andor) equipped with an iDus InGaAs 1.7 NIR detector (Andor) for spectral recording in the 800-1700 nm range. Available laser sources include laser diodes of 793 (max power 1 W, CNI Lasers), 806 (max power 0.2 W, Lumics), and 960 nm (max power 10 W, BWT Beijing; also referred to as 980 nm excitation) radiation wavelength, and 440 nm LED lamp (Thorlabs). Typically, spectra were acquired at 90° angle between the excitation and emission beams, except for DS emission collection in chapter 5 where 180° configuration was used. In order to remove any stray light from the excitation source a short-pass and long-pass (LP) filters were used in the case of UC and DS emission, respectively. Spectra of different colloidal dispersions of RENPs were collected by placing samples in the temperature controlled cuvette holder (qpod 2e by Quantum Northwest), which also allowed to control the temperature of the sample in the 20-50 °C range in the case of nanothermometry studies.

In model studies of deep-tissue imaging by the RENPs, NIR images were acquired with an InGaAs NIR imaging camera (XEVA-1781, Xenics). Selection of certain NIR emission bands was carried out using different LP filters.

### 2.4.2 Photoluminescence quantum yield

In chapter 3, DS emission spectra and *PLQY* of RENPs was measured with the help of Prof. Carlos D. S. Brites at the University of Aveiro, Portugal. Measurements were carried out on quantum yield measurement system Quantaury-QY (C13534, Hamamatsu), equipped with a 150 W Xenon lamp coupled to a monochromator for wavelength discrimination, an integrating sphere as a sample chamber and two multi-channel analyzers for signal detection in the visible and in the NIR spectral ranges. As an excitation source, 804 nm external laser diode (FC-808 5W, CNI Lasers) was used. The laser power could be adjusted between 0 and 5 W controlling the laser diode current. *PLQY* of all Nd<sup>3+</sup>-doped RENPs was measured in the 0.25-1.33 W power range. Considering the illumination area in the sample holder being 0.0025 cm<sup>2</sup>, according to the manufacturer, this corresponds to 102-532 W/cm<sup>2</sup>. Three measurements were made for each sample and power density value. *PLQY* was found as a fraction of emitted and

absorbed photons by the sample. The method has systemic relative error of  $\pm 10\%$ . All measurements were done in quartz cuvettes of 1 cm optical path length, filled with 2 mL of RENPs at 15 mg/mL concentration. The equipment measured the absolute *PLQY* using the reference spectral power density and the sample spectral power density under the same experimental conditions. As a reference sample empty cuvette, cuvette filled with hexane or water, and cuvette containing undoped RENPs dispersed in hexane or water was used. The equipment's software computes the *PLQY* using user-defined wavelength integration ranges for excitation and emission.

In chapter 7, UC emission *PLQY* of RENPs was measured with the help of Callum M. S. Jones at the Heriot-Watt University, Edinburgh, UK. A calibrated spectrometer FLS920 (Edinburgh Instruments Ltd.), equipped with a double emission monochromator, was used to determine the absolute *PLQY*. Each sample was transferred to an optical cuvette of  $\sim 0.6$  cm optical path length, placed inside an integrating sphere (Jobin-Yvon), and excited using a 10 W 960 nm continuous-wave laser diode (BWT Beijing). The emission was measured using an extended red-sensitive single-photon counting photomultiplier detector (Hamamatsu, PMT, 200-1010 nm). The emission monochromator bandwidth was kept constant for each emission and related absorption measurement. However, it varied depending on excitation power to avoid saturation of the detector. Excitation power density was varied by placing different optical density (OD) filters in the excitation path. A 610 nm long-pass filter was used over the 600-850 nm range to avoid second order emission artifacts when measuring  $\text{Tm}^{3+}$ -doped RENPs. Marginal filter-induced photon loss was later corrected for. The emitted photon number was calculated from the emission spectra of each RENE sample. The absorbed photons were found by subtracting the incident beam intensity on the RENPs sample from the incident beam intensity on a reference sample of pure hexane, with identical volume. By dividing the total number of emitted photons (over the range 310-850 nm) by the total number of absorbed photons at 960 nm, the *PLQY* was determined for each sample over a variety of powers. All spectra were corrected by the system response. All *PLQY* values have  $\pm 10\%$  relative error.

### **2.4.3 Photoluminescence decay**

In chapter 3, photoluminescence decay measurements were performed by Dr. Inocencio R. Martín and Dr. Antonio Benayas at the University of La Laguna, Tenerife, Spain. The photoluminescence decay curves were measured by exciting the colloidal dispersions of RENPs with a 10 ns pulsed optical parametric oscillator (OPO) laser (EKSPLA/NT342/3/UVE) at 575 or

800 nm. Generated photoluminescence was focused on the entrance slit of a monochromator (Triax 180; grating - 600 lines/mm and 1  $\mu\text{m}$  blaze) coupled to a NIR extended photomultiplier tube (Hamamatsu R406), and the electronic signal was registered with a digital oscilloscope (Lecroy WS424).

In chapter 7 and 8, photoluminescence decay measurements were performed with the help of Dr. Artūras Katelnikovas at the University of Vilnius, Lithuania. Lifetime traces were acquired on an FLS980 (Edinburgh Instruments Ltd.) spectrometer equipped with a double emission monochromator, single-photon counting photomultiplier (Hamamatsu R928), and a 1 W 980 nm pulsed laser diode MDL-III-980 (CNI) with 70  $\mu\text{s}$  pulse width and 100 Hz repetition rate.

Average decay (and rise) time values were obtained as integrated area under the measured decay (rise) profiles.<sup>[178]</sup>

## **2.5 Biomedical framework**

In chapter 6, all experiments pertinent to this section have been carried out by Dr. Vitalijus Karabanovas and Ms. Greta Jarockytė at the National Cancer Institute, Vilnius, Lithuania.

### **2.5.1 Singlet oxygen evaluation**

To evaluate singlet oxygen generation by RENPs-Ce<sub>6</sub> complex, singlet oxygen sensor green (SOSG; Thermo Fisher Scientific) was used. SOSG was dissolved in methanol (5 mM) and diluted in water to a final 0.05 mM concentration. RENPs-Ce<sub>6</sub> complex, RENPs or Ce<sub>6</sub> alone were mixed with SOSG and irradiated by 980 or 806 nm CW lasers (Roithner LaserTechnik) at 0.48 W/cm<sup>2</sup> for 15, 30, 60, and 120 min, respectively. Magnetic stirring and constant temperature control were carried out during the irradiation experiments. Emission intensity of SOSG at 525 nm was then measured with FLS920 spectrometer (Edinburgh Instruments Ltd.) after each step of irradiation.

### **2.5.2 Cell culturing**

For cell experiments two human breast cancer cell lines were used, namely MDA-MB-231 (American Type Cell Culture Collection) and MCF-7 (European Collection of Cell Cultures). Cells were cultured in Dulbecco's modified Eagles cell culture medium (DMEM), supplemented with 10% (v/v) fetal bovine serum, 100 U/mL penicillin and 100 mg/mL streptomycin (all obtained from Gibco). Cells were maintained at 37 °C in a humidified atmosphere containing 5% of CO<sub>2</sub>. The cells were routinely subcultured 2–3 times a week in 25 cm<sup>2</sup> culture dishes.

### 2.5.3 In vitro studies

*Accumulation of RENPs and RENPs-Ce<sub>6</sub> in cell monolayers and 3D cell cultures.* For intracellular imaging studies, cells were seeded into an eight-chambered cover glass plate (Thermo Fisher) with a density of  $3 \times 10^4$  cells per chamber. RENP uptake dynamics and intracellular localization were studied after treating the cells with 0.08 mg/mL of RENPs or RENPs-Ce<sub>6</sub> and incubating for the next 1, 3, 6, or 24 h. Prior to imaging studies, cells were fixed with 4% paraformaldehyde solution (Sigma-Aldrich). Nuclei of the cells were stained with 0.01 mg/mL Hoechst 33258 (Sigma-Aldrich) and filamentous actin was stained with 0.165 mM Phalloidin-Alexa488 (Thermo Fisher).

3D cell cultures were formed using the hanging drop technique. MDA-MB-231 cells were seeded in a 96-well hanging drop plate (Biomatrix). After seven days, cellular spheroids were fully formed, then fresh cell growth medium containing RENPs or RENPs-Ce<sub>6</sub> were added to each well. The final concentration of RENPs in each well was 0.08 mg/mL. After 24 h of incubation, 3D spheroids were transferred from the hanging drop plate to a 35 mm cell culture dish with a glass bottom (Greiner bio-one) and then imaged with a confocal microscope.

The accumulation of RENPs and RENPs-Ce<sub>6</sub> in cell monolayers (2D) and 3D cell cultures was observed using a confocal Nikon Eclipse Te2000-S C1 Plus Laser scanning microscope (Nikon) equipped with a diode laser for 405 nm excitation (Melles Griot), an argon laser for 488 nm excitation (Melles Griot) and near-infrared laser for 980 nm excitation. Imaging was performed using 60X/1.4 NA oil immersion (for 2D) and 20X/0.50 NA dry (for 3D) objectives (Nikon). The three-channel red-green-blue detector (band-pass filters 450/34, 545/90, and 688/134 for blue, green, and red channels, respectively) was used. Hoechst 33258 and Ce<sub>6</sub> were excited at 404 nm, Phalloidin-Alexa488 was excited at 488 nm and RENPs were excited at 980 nm. Images were processed with the Nikon EZ-C1 Bronze 3.80 and ImageJ 1.46 software.

*Cell irradiation with 806 and 980 nm lasers.* To determine the PDT effect of the RENPs-Ce<sub>6</sub> complex in 2D cell cultures, MDA-MB-231 and MCF-7 cells were seeded into an eight-chambered cover glass plate and incubated with 0.08 mg/mL of RENPs or RENPs-Ce<sub>6</sub> complex, or 10  $\mu$ M Ce<sub>6</sub> for 24 h. 3D spheroid cell cultures were grown and treated with the RENPs or RENPs-Ce<sub>6</sub> complex as described in the previous sub-section. After incubation, cells were irradiated with 806 or 980 nm laser (power density 0.5 W/cm<sup>2</sup>) up to 900 J/cm<sup>2</sup> dose. After irradiation, 2D and 3D cells were kept in the incubator for 24 h, after that cell viability assays were applied.

*Cytotoxicity of RENPs and RENPs-Ce<sub>6</sub>*. MDA-MB-231 and MCF-7 cells were seeded on a 96-well plate (BD Falcon) at a density of  $1.5 \times 10^4$  cells/well. After 24 h, old medium was replaced with fresh medium containing 0.008 or 0.08 mg/mL RENPs or RENPs-Ce<sub>6</sub>, while medium alone without RENPs was used as a control. Cells were incubated for 24 h in the dark. RENPs may induce cell cytotoxicity and subsequently release of the lactate dehydrogenase (LDH). The LDH released into the medium was transferred to a new plate and mixed with Reaction Mixture (Thermo Scientific). After 30 min incubation at room temperature, reactions were stopped by adding Stop Solution (Thermo Scientific). Absorbance at 490 and 680 nm was measured using a plate-reading spectrophotometer (BioTek) to determine LDH activity. After obtaining absorbance values, they were recalculated as percentage values of viability. Data were expressed as mean  $\pm$  standard deviation (SD). Statistical significance of differences between studied groups was assessed using a two-tailed independent Student's t-test at the 95% confidence level. Significance was represented as p-value  $< 0.05$ .

To determine cytotoxicity of the RENPs and RENPs-Ce<sub>6</sub> complex after irradiation with 806 and 980 nm, a LIVE/DEAD viability/cytotoxicity kit (Thermo Fisher) was used, which indicates the viability of cells in a population based on plasma membrane integrity and esterase activity. Two fluorescent dyes were used in this kit: green-fluorescent calcein-AM to indicate intracellular esterase activity and red-fluorescent ethidium homodimer-1 to indicate loss of plasma membrane integrity to mark live and dead cells, respectively. After triplicate of irradiation experiments, stained cells were automatically counted to determine the viability of the cells.

### 3 Nd<sup>3+</sup>-RENPs. DOWNSHIFTING

---

As mentioned in the introduction, Nd<sup>3+</sup>-doped RENPs are alluring NIR probes for deep-tissue imaging and temperature sensing. Excitation of Nd<sup>3+</sup> is carried out around 800 nm in BW-I and emerging Nd<sup>3+</sup> emission bands reside in the BW-I and BW-II. Notably, 800 nm radiation is well suited for biomedical use as it is negligibly absorbed by water and thus does not introduce significant heating that could otherwise cause thermal damage to the irradiated area. Although Nd<sup>3+</sup>-doped RENPs represent an excellent base for constructing multifunctional theranostic RENPs, there is lack of quantitative information about the actual performance of Nd<sup>3+</sup>-doped RENPs in terms of absolute *PLQY* and brightness. Existing literature reports so far have also been contradictory in regard to the optimal Nd<sup>3+</sup> doping in RENPs. Most,<sup>[179–181]</sup> but not all,<sup>[182]</sup> argue that 1 to 5 mol% Nd<sup>3+</sup> doping range is optimal to attain high *PLQY*; however, the brightest (having the highest product of *PLQY* and absorbance) Nd<sup>3+</sup>-doped RENPs can also be those with 10 to 15 mol% doping.<sup>[160]</sup> In vein to settle this disparity, DS emission spectra, photoluminescence decay, *PLQY*, and brightness of NaGdF<sub>4</sub>:Nd<sup>3+</sup>/NaGdF<sub>4</sub> RENPs (Nd<sup>3+</sup>-RENPs) have been studied and are presented below. These photophysical features of Nd<sup>3+</sup>-RENPs were investigated as a function of Nd<sup>3+</sup> doping, core/shell engineering, and different dispersion media of RENPs. The NaGdF<sub>4</sub> host was prioritized for its wide use in developing photoluminescent RENPs. NaGdF<sub>4</sub> has low phonon cutoff frequency, which reduces the likelihood of non-radiative decay of RE<sup>3+</sup> excited states, and Gd<sup>3+</sup> can be considered optically inert with respect to many RE<sup>3+</sup>

*The study presented in this chapter was carried out through a collaboration between Canadian, Portuguese and Spanish institutions. PLQY of Nd<sup>3+</sup>-RENPs dispersed in water was measured by Prof. Carlos D. S. Brites (University of Aveiro). Photoluminescence lifetime data were acquired by Dr. Inocencio R. Martín at the University of La Laguna, with the help of Dr. Antonio Benayas (Autonomous University of Madrid).*

*Herein results were published as: “Inert Shell Effect on the Quantum Yield of Neodymium-Doped Near-Infrared Nanoparticles: The Necessary Shield in an Aqueous Dispersion” A. Skripka,\* A Benayas,\* C. D. S. Brites, I. R. Martín, L. D. Carlos and F. Vetrone, Nano Lett., 20 (10), 7648-7654, 2020. \*equally contributing authors*

### 3.1 RENP preparation and structural characterization

NaGdF<sub>4</sub>: x mol% Nd<sup>3+</sup>/NaGdF<sub>4</sub> RENPs (x = 0, 5, 12.5 and 25) were prepared via hot-injection thermal decomposition approach. To synthesize different core Nd<sup>3+</sup>-RENPs, 2.5 mmol each of Na-TFA and Nd/Gd-TFA (of varying Nd<sup>3+</sup> molar proportion) were dissolved and degassed in 7.5 mL each of OA and ODE (solution B). For each Nd<sup>3+</sup> doping, solution B was injected into the solution A, containing 12.5 mL each of OA and ODE at 315 °C. For 0, 5, 12.5 and 25 mol% Nd<sup>3+</sup>-doped cores the injection rate was 1.4, 1.45, 1.5 and 1.5 mL/min, respectively. After 1 h of vigorous stirring, the mixture was cooled down to room temperature. The synthesized core-only Nd<sup>3+</sup>-RENPs were stored unwashed at RT for the subsequent shelling step.

Core/shell RENPs were prepared by epitaxial shell growth on the preformed cores via the hot-injection approach. Approximately 0.3 mmol of core RENPs were mixed with equal parts of OA and ODE up to a total volume of 25 mL (Solution A). Solution B contained 1.25 mmol each of Na-TFA and Gd-TFA, and 7.5 mL each of OA and ODE. Prior to injection of the solution B, the temperature of the solution A was raised to 310 °C. Solution B was then injected into Solution A at a 0.5 mL/min injection rate. After 1 h of reaction, the mixture was cooled to RT under Ar and magnetic stirring. Prior to washing, aliquots of obtained core/shell RENPs were sampled and checked for the RENPs size with TEM. Due to evaporation of impurities in the starting materials (such as OA and ODE) and reaction byproducts, as well as minor losses accrued from intermediate steps of liquid handling, some errors were introduced in the determination of exact core amounts that were shelled, leading to lesser-than-expected shell thickness for 0, 12.5 and 25 mol% Nd<sup>3+</sup>-doped RENPs. These RENPs underwent additional shelling step, starting with ~0.15 mmol of pre-formed core/shell RENPs and introducing 0.65 mmol each of Na-TFA and Gd-TFA precursors to obtain all RENPs of similar size and shell thickness. Final core-only and core/shell RENPs were washed and re-dispersed in hexane for further characterization and surface treatment. All Nd<sup>3+</sup>-RENPs were transferred to water via ligand removal procedure.

Core-only Nd<sup>3+</sup>-RENPs were small and monodisperse in size, 11-12 nm, while the addition of NaGdF<sub>4</sub> shell increased the size of RENPs to around 25-26 nm, at which point hexagonal shape of Nd<sup>3+</sup>-RENPs could be better appreciated (Figure 3.1). All RENPs crystallized in pure hexagonal phase, confirmed by powder XRD analysis (see Appendix I). Nd<sup>3+</sup> concentration in RENPs was determined by ICP-OES, and was 0.4, 5.1, 12.9, 25.6 mol% for 0, 5, 12.5 and 25 mol% target values, respectively. Note, the undoped core-only and core/shell NaGdF<sub>4</sub>/NaGdF<sub>4</sub> RENPs were produced to serve as a reference for absolute PLQY, see below.

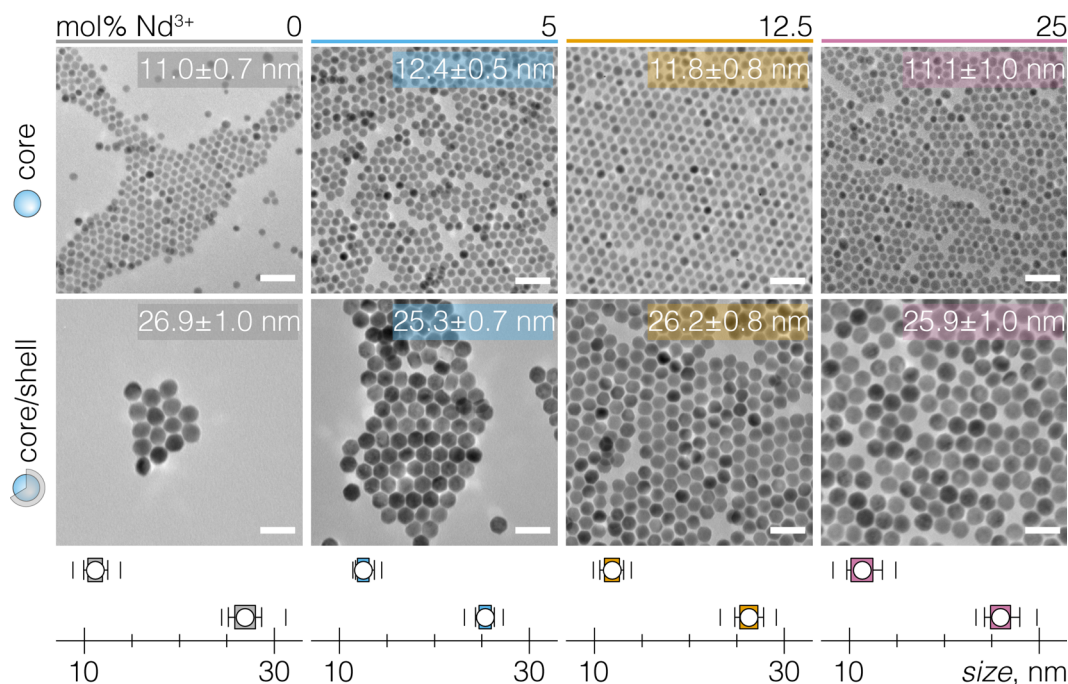


**Figure 3.1. Structural characterization of Nd<sup>3+</sup>-RENPs.**

TEM images and respective size distributions of core-only (top box) and core/shell (bottom box) NaGdF<sub>4</sub>: x mol% Nd<sup>3+</sup>/NaGdF<sub>4</sub> RENPs (x = 0, 5, 12.5, 25). Scale bar 50 nm. Box plots indicate: mean value (dot), SD (box outline), 5<sup>th</sup> and 95<sup>th</sup> percentiles (whiskers), and maximum/minimum values (dashes).

### 3.2 Steady-state and time-resolved photoluminescence

Excited with 804 nm radiation all Nd<sup>3+</sup>-RENPs exhibited NIR emission bands around 880, 1060 and 1340 nm, which respectively correspond to  $^4F_{3/2} \rightarrow ^4I_{9/2}$ ,  $^4I_{11/2}$ , and  $^4I_{13/2}$  radiative transitions of Nd<sup>3+</sup> (Figure 3.2A). The photoluminescence intensity of Nd<sup>3+</sup>-RENPs decreased for both core-only and core/shell architectures as Nd<sup>3+</sup> doping was increased from 5 to 25 mol%.

Nd<sup>3+</sup> ions are prone to concentration quenching by  $^4I_{9/2} \rightarrow ^4I_{15/2}$ :  $^4F_{3/2} \rightarrow ^4I_{15/2}$  cross-relaxation process, which deactivates  $^4F_{3/2}$  emissive state non-radiatively (Figure 3.2B).<sup>[183]</sup> Different doping amounts had not influenced relative contribution of individual emission bands to the net spectrum of Nd<sup>3+</sup>, the most intense transition was observed around 1060 nm ( $^4F_{3/2} \rightarrow ^4I_{11/2}$ ), while 1340 nm ( $^4F_{3/2} \rightarrow ^4I_{13/2}$ ) was the weakest. In contrast to other reports on Nd<sup>3+</sup>-doped RENPs, intensity of the photoluminescence band around 880 nm ( $^4F_{3/2} \rightarrow ^4I_{9/2}$ ) was seen on par with that of 1060 nm ( $^4F_{3/2} \rightarrow ^4I_{11/2}$ ) DS emission. This difference might stems from the fact that Nd<sup>3+</sup> spectra in various NaGdF<sub>4</sub> RENPs are commonly acquired with set-ups not calibrated for the spectral responsivity in the NIR region, leading to general notion that  $^4F_{3/2} \rightarrow ^4I_{9/2}$  radiative transition in this and other hosts is significantly less intense than that of  $^4F_{3/2} \rightarrow ^4I_{11/2}$ .<sup>[184]</sup>

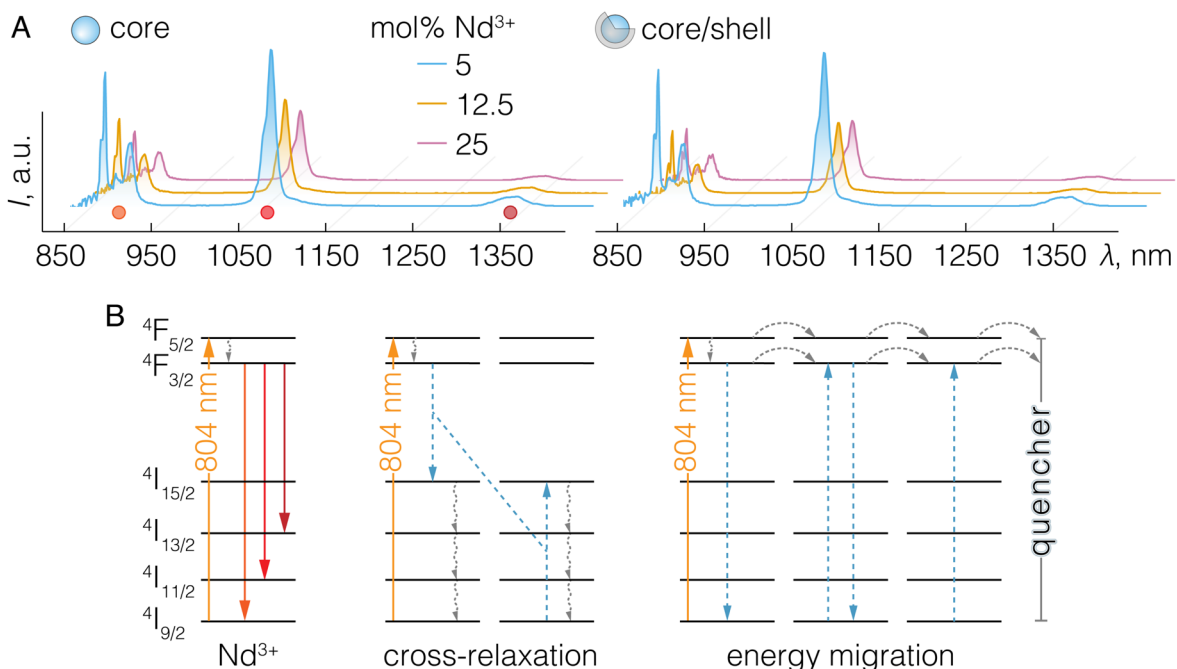


**Figure 3.2. Photoluminescence of Nd<sup>3+</sup>-RENPs.**

**A** – DS emission spectra of core-only and core/shell NaGdF<sub>4</sub>: x mol% Nd<sup>3+</sup>/NaGdF<sub>4</sub> RENPs (x = 5, 12.5, 25). **B** – Simplified energy level diagram of Nd<sup>3+</sup>. Radiative transitions in Nd<sup>3+</sup> are shown as solid lines; corresponding <sup>4</sup>F<sub>3/2</sub> → <sup>4</sup>I<sub>J</sub> (J = 9/2, 11/2, 13/2) transitions are color coded in A with dots below each emission band. Cross-relaxation and energy migration processes that lead to emission quenching are also shown. Dashed lines represent non-radiative energy exchange, wavy – non-radiative decay.

Photoluminescence decay measurements of the emissive <sup>4</sup>F<sub>3/2</sub> excited state, via 880 nm emission band, revealed decay time shortening with increasing Nd<sup>3+</sup> concentration, irrespective of RENP architecture or dispersion media (Figure 3.3). This observation supported the cross-relaxation facilitated non-radiative deactivation of the metastable <sup>4</sup>F<sub>3/2</sub> energy level. Furthermore, average lifetime values increased significantly once inert NaGdF<sub>4</sub> shell was grown over the Nd<sup>3+</sup>-doped RENP cores, indicative of suppressed surface related quenching. Inert shells are expected to protect optically active RE<sup>3+</sup> from quenching by surface defects and ligand/solvent vibrational modes. To prevent the latter phenomenon, thick shells (5-10 nm) are used to separate RE<sup>3+</sup> from outside quenchers, precluding non-radiative energy exchange between the two moieties,<sup>[60,61]</sup> here, core/shell Nd<sup>3+</sup>-RENPs featured ~7 nm thick NaGdF<sub>4</sub> “protective layer”. Notably, the increase of the excited state lifetime, provided by an inert shell, weakened for highly Nd<sup>3+</sup> doped samples: average lifetime improved 3.0 and 1.9 times with the shelling of 5 and 25 mol% Nd<sup>3+</sup>-doped core RENPs dispersed in hexane, respectively. Previous studies on Er<sup>3+</sup>- and Yb<sup>3+</sup>-doped RENPs proved a link between the energy migration via network of optically active RE<sup>3+</sup> and surface quenching, which can be severed by shelling the RENPs.<sup>[60,185]</sup> Photoluminescence lifetime shortening in the core/shell Nd<sup>3+</sup>-RENPs at increasing

$\text{Nd}^{3+}$  concentration, suggests that despite reduced coupling between concentration and surface related quenching, the cross-relaxation among  $\text{Nd}^{3+}$  ions remains relevant to the loss of emission intensity. Surprisingly, only minor decrease in average lifetime values was observed upon transferring  $\text{Nd}^{3+}$ -doped RENPs from hexane to water. In general, water is a notorious quencher of RENPs' photoluminescence. The intense and highly energetic OH stretching ( $\sim 3400\text{ cm}^{-1}$ ) acts as an "energy sink" for  $\text{RE}^{3+}$  excited states deactivating them non-radiatively. Yet, seemingly unaltered photoluminescence lifetime of  $\text{Nd}^{3+}$ -RENPs gives an impression that water has little effect over the  ${}^4\text{F}_{3/2}$  emissive state of  $\text{Nd}^{3+}$ .

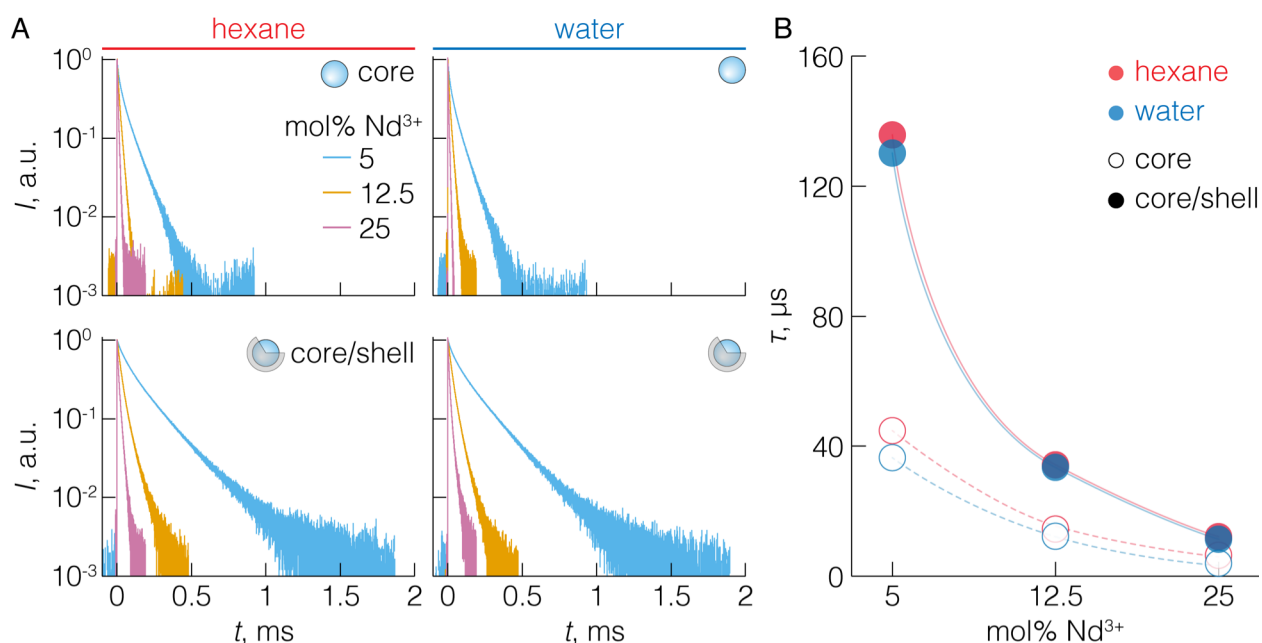


**Figure 3.3. Excited state lifetimes of  $\text{Nd}^{3+}$ -RENPs.**

**A** – Photoluminescence decay traces of core-only and core/shell  $\text{NaGdF}_4$ : x mol%  $\text{Nd}^{3+}/\text{NaGdF}_4$  RENPs (x = 5, 12.5, 25) dispersed in water or hexane.  $\lambda_{\text{ex}} = 800\text{ nm}$ ,  $\lambda_{\text{em}} = 880\text{ nm}$ . **B** – Corresponding average lifetime values for the  ${}^4\text{F}_{3/2}$  emissive state of  $\text{Nd}^{3+}$ . Lines are guides to the eye.

### 3.3 PLQY analysis

The *PLQY* of  $\text{Nd}^{3+}$ -RENPs was investigated under 804 nm laser excitation employing different references for *PLQY* calculation. *PLQY* of a given material is defined as a ratio between the number of absorbed and emitted photons, and describes the efficiency with which the material photoluminesces. Absorbed photons are determined as a difference in the number of excitation photons after propagating through a sample and a reference – i.e. dispersion media alone or non-photoluminescent analogs of NPs under study.

DS emission of  $\text{Nd}^{3+}$ -doped RENPs is a single-photon processes, photoluminescence intensity of which depends linearly on the excitation power density, hence the *PLQY* of  $\text{Nd}^{3+}$ -RENPs is

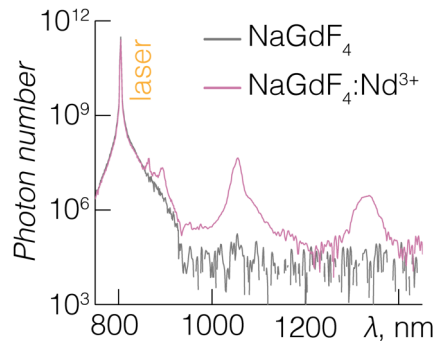


**Figure 3.4. Spectrum of blank NaGdF<sub>4</sub> RENPs.**

Reference spectra of blank NaGdF<sub>4</sub> RENPs dispersed in hexane, against photoluminescence spectra of NaGdF<sub>4</sub>: 25 mol% Nd<sup>3+</sup> RENPs. Spectra measured at the maximum excitation power density of 532 W/cm<sup>2</sup>. Despite detection of trace amounts of Nd<sup>3+</sup> in blank RENPs by ICP, no Nd<sup>3+</sup> emission was observed.

expected to be excitation power density independent. To prove so, and also that PLQY is not altered by artifacts such as laser induced heating, *PLQY* was measured in the 102-532 W/cm<sup>2</sup> power density range. As a reference, empty quartz cuvette, cuvette filled with hexane or water, and cuvette with blank (undoped) RENPs dispersed in hexane or water were used. Blank RENPs were non-photoluminescent analogs of Nd<sup>3+</sup>-RENPs, intended to account for excitation beam attenuation due to light scattering by RENPs themselves (Figure 3.4).<sup>[186]</sup>

The net *PLQY* of all Nd<sup>3+</sup>-RENPs, measured with different references, was independent of the excitation power density (see Appendix II). Some variability in the measured *PLQY* values occurred due to low absorption of the excitation beam and poorer colloidal stability of 5 mol% Nd<sup>3+</sup>-doped core-only and core/shell RENPs in hexane, yet, it can be regarded as random distribution of experimental points rather than a distinctive trend. The net *PLQY* (averaged across all excitation power densities) of core-only and core/shell Nd<sup>3+</sup>-RENPs showed similar tendencies with respect to Nd<sup>3+</sup> doping, core/shell engineering, and dispersion media irrespective of reference employed (Figure 3.5). Notably, estimation of *PLQY* was particularly

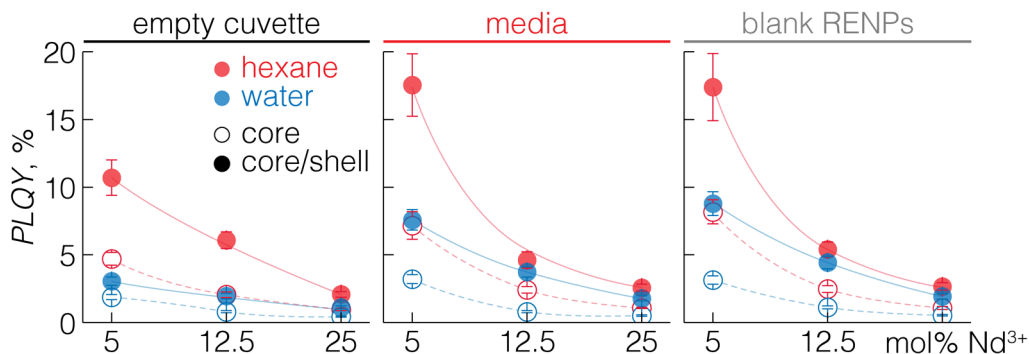


**Figure 3.5. *PLQY* of Nd<sup>3+</sup>-RENPs**

Average *PLQY* values of core-only and core/shell NaGdF<sub>4</sub>: x mol% Nd<sup>3+</sup>/NaGdF<sub>4</sub> RENPs (x = 5, 12.5, 25) dispersed in hexane or water. Data were measured using blank cuvette, cuvette filled with dispersion media, or blank RENPs in dispersion media as a reference. Lines are guides to the eye.

sensitive to reference employed. When absorption of photoluminescent sample is low, in the case of little  $\text{RE}^{3+}$  doping or concentration of RENPs in the dispersion, it becomes paramount to account for laser beam attenuation due to absorption by the dispersion medium and light scattering by the NPs. Hence, pure dispersion media and blank RENPs as a reference allowed to measure *PLQY* values more accurately, which could have been otherwise underestimated (particularly in the case of 5 mol%  $\text{Nd}^{3+}$ -doped RENPs). As a representative case, *PLQY* values measured with blank RENPs as a reference are used for further discussion. Increase in the  $\text{Nd}^{3+}$  concentration from 5 to 25 mol% led to decrease by ~84 and 82% in *PLQY* for core-only and core/shell  $\text{Nd}^{3+}$ -RENPs, respectively, dispersed in either water or hexane. When core-only RENPs were transfer from hexane to water their *PLQY* decreased by ~55%, with minor dependence on the  $\text{Nd}^{3+}$  concentration. However, similar *PLQY* decrease (~50%) in core/shell  $\text{Nd}^{3+}$ -RENPs was observed only for the 5 mol%  $\text{Nd}^{3+}$  doping, as *PLQY* of 12.5 and 25 mol%  $\text{Nd}^{3+}$ -doped RENPs decreased by ~17 and ~26%, respectively. Studies in different media clearly revealed the notorious photoluminescence intensity quenching by water molecules, yet it was less relevant for highly  $\text{Nd}^{3+}$ -doped samples, which featured strong concentration quenching. On average, *PLQY* of  $\text{Nd}^{3+}$ -RENPs was increased moving from core-only to core/shell architecture 2.5 and 3.4 times for hexane and water dispersions, respectively, attesting to the importance of an inert shell towards improving photoluminescence intensity of RENPs. Overall, highest *PLQY* was found for core/shell 5 mol%  $\text{Nd}^{3+}$ -RENPs dispersed in hexane,  $17.4 \pm 2.5\%$ , while their *PLQY* when dispersed in water was  $8.8 \pm 0.9\%$ . Core-only 25 mol%  $\text{Nd}^{3+}$ -RENPs exhibited lowest *PLQY*,  $1.1 \pm 0.1\%$  in hexane and  $0.5 \pm 0.1\%$  in water. Two key aspects can be drawn from these observations: i) *PLQY* of  $\text{Nd}^{3+}$ -doped RENPs decreases with both doping amount and transfer to water, yet ii) emission intensity can be partially restored by an inert shell coating. In terms of *PLQY* of individual DS emission bands of  $\text{Nd}^{3+}$  (Figure 3.6), nearly even contribution of 880 ( $^4\text{F}_{3/2} \rightarrow ^4\text{I}_{9/2}$ ) and 1060 nm ( $^4\text{F}_{3/2} \rightarrow ^4\text{I}_{11/2}$ ) emissions to the net *PLQY* was observed for  $\text{Nd}^{3+}$ -RENPs, irrespective of their architecture or dispersion media. However, relative contribution of NIR emission around 1340 nm ( $^4\text{F}_{3/2} \rightarrow ^4\text{I}_{13/2}$ ) to the net *PLQY* decreased from about 8-9 to 2-3% when  $\text{Nd}^{3+}$ -doped RENPs where transferred from hexane to water. This can be attributed to the partial overlap between the absorption band of water around 1430 nm and 1340 nm emission band of  $\text{Nd}^{3+}$ . Although true contribution of  $^4\text{F}_{3/2} \rightarrow ^4\text{I}_{13/2}$  radiative transition to the net *PLQY* of  $\text{Nd}^{3+}$  can be masked in water, it remains the least intense among  $\text{Nd}^{3+}$  NIR emission bands.

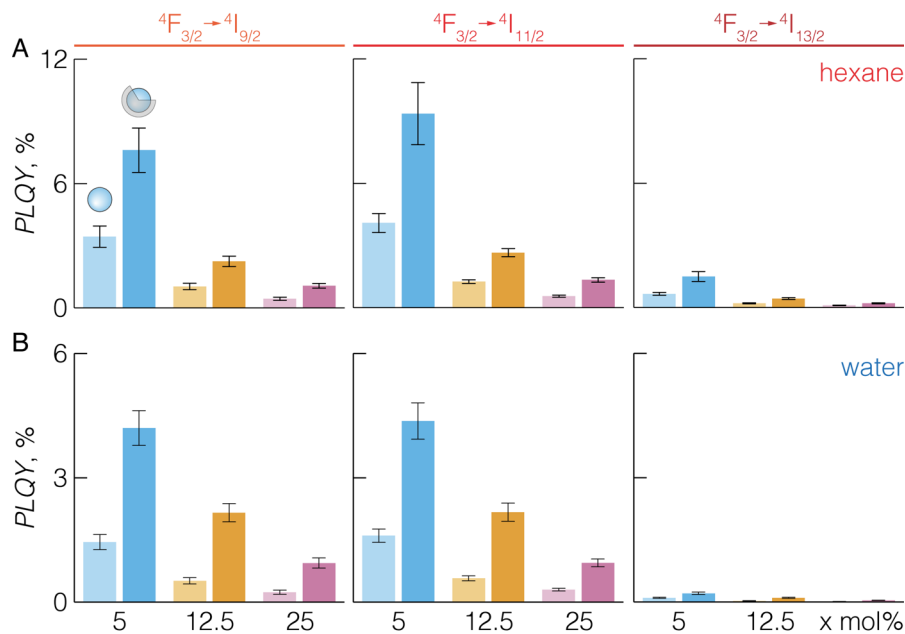


Figure 3.6. *PLQY* of  $\text{Nd}^{3+}$ -RENPs individual emission bands.

A, B – Average *PLQY* values of individual DS emission bands of core-only and core/shell  $\text{NaGdF}_4$ : x mol%  $\text{Nd}^{3+}/\text{NaGdF}_4$  RENPs (x = 5, 12.5, 25) dispersed in hexane (A) or water (B). Data were measured using blank RENPs in a respective dispersion media as a reference.

### 3.4 Further discussion and brightness

A closer look at the photoluminescence lifetime and *PLQY* data of  $\text{Nd}^{3+}$ -RENPs revealed few peculiarities specific to  $\text{Nd}^{3+}$  ions. Both average lifetimes and net *PLQY* decreased with increasing  $\text{Nd}^{3+}$  concentration, pointing towards concentration quenching via cross-relaxation among  $\text{Nd}^{3+}$  ions to be responsible for the loss of emission intensity. However, when moving from hexane to water as a dispersion media, only *PLQY* but not average lifetime of  $\text{Nd}^{3+}$ -RENPs was affected. As a working hypothesis, the following was proposed to reconcile the two observations. Photoluminescence decay measurements account only for the quenching of the  $^4\text{F}_{3/2}$  emitting state of  $\text{Nd}^{3+}$ , whereas decreased *PLQY* can be associated with vibrational quenching of the absorbing  $^4\text{F}_{5/2}$  excited state directly. The fact that this discrepancy is mostly noticeable for core/shell RENPs indicates that addition of a thick inert shell minimizes the non-resonant vibrational quenching, leaving only the near-resonant processes in play (Figure 3.7A). Quenching by OH stretching mode around  $3400\text{ cm}^{-1}$  is in close resonance with the  $^4\text{F}_{5/2}$ - $^4\text{I}_{15/2}$  energy gap, but would require additional release or absorption of multiple lattice phonons to bridge the  $^4\text{F}_{3/2}$ - $^4\text{I}_{15/2}$  or  $^4\text{F}_{3/2}$ - $^4\text{I}_{13/2}$  energy gaps, respectively. Also, the  $^4\text{F}_{5/2} \rightarrow ^4\text{F}_{3/2}$  excitation decay is particularly rapid in  $\text{Nd}^{3+}$  and the extent to which this process can be bypassed by  $^4\text{F}_{5/2}$  excited state quenching via solvent vibrations is uncertain. To test the hypothesis, the lifetime of

${}^4F_{5/2}$  excited state for 5 mol%  $\text{Nd}^{3+}$ -doped RENPs was measured in their core-only or core/shell formulation, when dispersed in hexane or water (Figure 3.7B). However, similar excited state lifetime trends to  ${}^4F_{3/2}$  energy level were observed for the  ${}^4F_{5/2}$  one, thus disproving the proposed hypothesis. Another aspect worth considering is the water absorption, which increases between 1050 nm and 1400 nm (from ca. 0.06 to  $1 \text{ cm}^{-1}$ ). The experimental configuration for the *PLQY* measurements makes the photon, once emitted from  $\text{Nd}^{3+}$ , to reflect of the integrating sphere walls multiple times and have many passes through the cuvette filled with water. This increases the likelihood of photons being lost to water absorption and extrinsically lowering the measured *PLQY*, rather than stemming from an intrinsic excited state quenching by solvent vibrational modes. At this point, this remains an open question that merits more focused future analysis on the possible external and internal factors that could affect the *PLQY* of  $\text{Nd}^{3+}$ -RENPs.

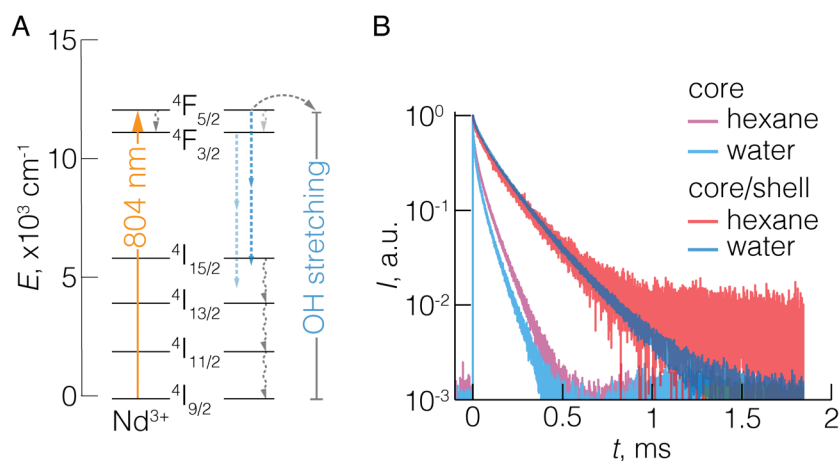


**Figure 3.7. Quenching of  $\text{Nd}^{3+}$  excited states.**

**A** – Simplified energy level scheme of  $\text{Nd}^{3+}$  showing  ${}^4I_{9/2} \rightarrow {}^4F_{5/2}$  excitation with 804 nm light, followed by population of the emissive  ${}^4F_{3/2}$  excited state via non-radiative  ${}^4F_{5/2} \rightarrow {}^4F_{3/2}$  decay. In the extended view OH vibrations ( $\sim 3400 \text{ cm}^{-1}$ ) of water are represented as multiphonon quenching modes for  ${}^4F_{3/2}$  and  ${}^4F_{5/2}$  excited states. Notably, near-resonant bridging of the  ${}^4F_{5/2}$ - ${}^4I_{15/2}$  energy gap is possible via multimodal vibrational quenching, but would require additional lattice phonon assistance to quench  ${}^4F_{3/2}$  excited state directly. **B** - Normalized photoluminescence decay profiles of core-only and core/shell  $\text{NaGdF}_4$ : 5 mol%  $\text{Nd}^{3+}/\text{NaGdF}_4$  RENPs dispersed in hexane or water under 575 nm laser excitation. Photoluminescence decay was measured from emission band around 800 nm ( ${}^4F_{5/2} \rightarrow {}^4I_{9/2}$ ).

Finally, to illustrate the brightness of  $\text{Nd}^{3+}$ -RENPs it was compared in relative terms by the product of *PLQY* and the number of absorbing  $\text{Nd}^{3+}$  per RENPs. The number of  $\text{Nd}^{3+}$  ions was estimated considering the features of  $\text{NaGdF}_4$  unit cell and spherical volume ( $V_{\text{RENPs}}$ ) of core-only  $\text{Nd}^{3+}$ -RENPs, as an approximation. Hexagonal  $\text{NaGdF}_4$  unit cell contains  $Z = 1.5$  number of  $\text{RE}^{3+}$  per cell (unit formula being  $\text{Na}_{1.5}\text{Gd}_{1.5}\text{F}_6$ ), and its parameters are  $a = 6.02 \text{ \AA}$  and  $c = 3.60 \text{ \AA}$ . The unit cell volume  $V_{\text{cell}}$  is thus  $\sim 0.113 \text{ nm}^3$ . The number of  $\text{Nd}^{3+}$  dopants per RENPs' core was then calculated as  $V_{\text{RENPs}}/V_{\text{cell}} \cdot Z \cdot [\text{Nd}^{3+}]$ , where  $[\text{Nd}^{3+}]$  represents the molar concentration of

$\text{Nd}^{3+}$  in RENPs. According to these considerations and normalizing the number of  $\text{Nd}^{3+}$  ions equal to 1 in 5 mol%  $\text{Nd}^{3+}$ -doped RENPs, the 12.5 and 25 mol%  $\text{Nd}^{3+}$ -doped RENPs contained 2.2 and 3.9 times more of  $\text{Nd}^{3+}$ , respectively. The brightest  $\text{Nd}^{3+}$ -RENPs were those featuring an inert shell, and hexane dispersions were brighter than water (Figure 3.8). Although absolute *PLQY* decreased significantly as a function of  $\text{Nd}^{3+}$  doping amount, the relative brightness of these RENPs was less affected, particularly in the case of core/shell  $\text{Nd}^{3+}$ -doped RENPs in water. Reduced *PLQY* of  $\text{Nd}^{3+}$ -doped RENPs can be thus partially compensated by increased absorbance of RENPs due to the presence of higher number of  $\text{Nd}^{3+}$ . However, RENPs with low  $\text{Nd}^{3+}$  doping were overall brighter, settling, at least in the case of  $\text{Nd}^{3+}$ -doped  $\text{NaGdF}_4$ , the dispute among conflicting reports on the optimal  $\text{Nd}^{3+}$  doping. It also has to be noted that, RENPs with lower  $\text{Nd}^{3+}$  doping should be preferred when considering imaging and nanothermometry applications, as higher  $\text{Nd}^{3+}$  content can lead to undesired heating or unreliable temperature measurements due to the self-absorption induced artifacts.<sup>[118,173]</sup>

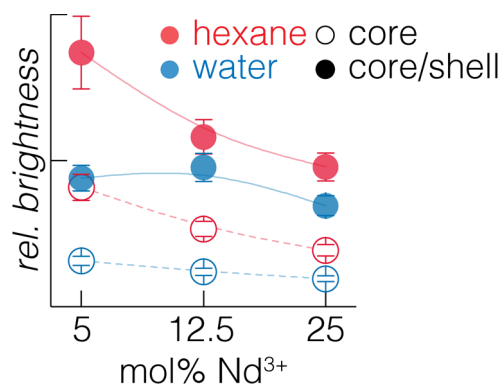


**Figure 3.8. Relative brightness of  $\text{Nd}^{3+}$ -RENPs.**

**Relative brightness of core-only and core/shell  $\text{NaGdF}_4$ : x mol%  $\text{Nd}^{3+}/\text{NaGdF}_4$  RENPs (x = 5, 12.5, 25) dispersed in hexane or water. Lines are guides to the eye.**

In summary, a library of small and monodisperse  $\text{Nd}^{3+}$ -doped  $\text{NaGdF}_4$  RENPs was prepared and their photophysical characteristics were examined as a function of  $\text{Nd}^{3+}$  doping, core/shell engineering, and dispersion media. Matching general consensus, the inert shell substantially improved the photoluminescence intensity of  $\text{Nd}^{3+}$ -RENPs, yet concentration quenching proved to be a significant factor to the loss of photoluminescence intensity in highly doped RENPs. Core/shell 5 mol%  $\text{Nd}^{3+}$ -doped RENPs were overall brightest, and thus similar  $\text{Nd}^{3+}$  doping values and core/shell engineering should be preferred when designing  $\text{Nd}^{3+}$ -RENPs slated for biomedical imaging and nanothermometry.

## 4 Nd<sup>3+</sup>-RENPs. UPCONVERSION AND DOWNSHIFTING

---

Albeit Nd<sup>3+</sup>-doped RENPs are appealing NIR imaging agents, their light-based theranostic capabilities are impeded by the lack of high-energy photon emission. To add the missing functionality, other RE<sup>3+</sup> are usually co-doped alongside Nd<sup>3+</sup>, providing photon upconversion. Exploration of Nd<sup>3+</sup>-based upconverting RENPs was initiated by the groups of Xiaogang Liu and Chun-Hua Yan.<sup>[75,76]</sup> The spur for it came from the attempt to minimize unwanted heating of the aqueous environment with 980 nm radiation, absorbed by Yb<sup>3+</sup> in the classic upconverting RENPs and water. In contrast, Nd<sup>3+</sup> are excited by radiation of around 800 nm where water absorption is minimal and possible overheating of an irradiated area can be avoided. Furthermore, absorption cross-section of Nd<sup>3+</sup> at ~800 nm (~10<sup>-19</sup> cm<sup>2</sup>) is larger than that of Yb<sup>3+</sup> at ~980 nm (~10<sup>-20</sup> cm<sup>2</sup>),<sup>[187,188]</sup> suggesting that Nd<sup>3+</sup> is also better suited for NIR excitation harvesting. Various co-doping strategies and core/shell architectures have been proposed over the years, perfecting the Nd<sup>3+</sup>-based upconverting RENPs.<sup>[189]</sup> A general design using Nd<sup>3+</sup> as sensitizers, Yb<sup>3+</sup> as energy mediators, and Er<sup>3+</sup>, Ho<sup>3+</sup>, or Tm<sup>3+</sup> as activators has been settled on, with a focus on separating Nd<sup>3+</sup> from activator ions to reduce inter-ion quenching. Nonetheless, spectral analysis on different excitation pathways of Nd<sup>3+</sup>/Yb<sup>3+</sup> co-doped RENPs, has been underrepresented when compared to the well-studied Yb<sup>3+</sup>-doped systems. Also, initially little attention has been paid to how these novel RENPs could be used for therapy and diagnostics employing their UC and DS emissions, respectively. To better understand the photophysics of Nd<sup>3+</sup>-based upconverting (and downshifting) RENPs, different excitation routes and their influence on the optical features across a broad emission range have to be investigated. For that purpose, core/shell/shell NaGdF<sub>4</sub>:Er<sup>3+</sup>, Ho<sup>3+</sup>, Yb<sup>3+</sup>/NaGdF<sub>4</sub>:Nd<sup>3+</sup>, Yb<sup>3+</sup>/NaGdF<sub>4</sub> RENPs have been prepared and their UC and DS emission was analyzed under 806 and 980 nm irradiation.

*Herein results were published as: "Covering the Optical Spectrum Through Collective Rare-Earth Doping of NaGdF<sub>4</sub> Nanoparticles: 806 and 980 nm Excitation Routes" A. Skripka,\* R. Marin,\* A. Benayas, P. Canton, E. Hemmer and F. Vetrone, Phys. Chem. Chem. Phys., 19 (19), 11825-11834, 2017. \*equally contributing authors*

### 4.1 RNP preparation and structural characterization

Core/shell1/shell2 RENPs (Figure 4.1A) were prepared via hot-injection thermal decomposition, in a sequence of three injection steps. NaGdF<sub>4</sub>: 2 mol% Er<sup>3+</sup>, 5 mol% Ho<sup>3+</sup>, 20 mol% Yb<sup>3+</sup> core RENPs were synthesized out of 2.5 mmol each of Na-TFA and Gd/Er/Ho/Yb-TFA precursors

(mixed in a stoichiometric amount according to the desired molar doping). Precursors were degassed and dissolved in 7.5 mL each of OA and ODE (solution B), and injected into the solution A, containing 12.5 mL each of OA and ODE at 315 °C. Injection rate was 1.5 mL/min. After 1 h of reaction time, 2.5 mmol each of Na-TFA and Gd/Nd/Yb-TFA, dissolved in 7.5 mL each of OA and ODE (solution C), were injected into the reaction mixture to form NaGdF<sub>4</sub>: 5 mol% Nd<sup>3+</sup>, 20 mol% Yb<sup>3+</sup> shell (shell1). Injection rate was 1.5 mL/min and reaction was allowed to proceed for an additional 1 h. Finally, optically inert NaGdF<sub>4</sub> shell (shell2) was grown over the core/shell1 RENPs injecting 2.5 mmol each of Na-TFA and Gd-TFA, dissolved in 7.5 mL each of OA and ODE (solution D), at 1.5 mL/min and leaving to reacting for 1 h. After a total of 3 h of reaction time the mixture was cooldown, RENPs were washed, and dispersed in hexane for further morphological and spectral characterization. Aliquots of core-only and core/shell1 RENPs were sampled prior to the subsequent shelling steps.

The core of the RENPs, doped with Er<sup>3+</sup>, Ho<sup>3+</sup> and Yb<sup>3+</sup>, comprised the primary upconversion and NIR emitting layer. The dopant concentrations were chosen according to previous studies, showing highest upconversion emission intensities for similar type of RENPs.<sup>[74,190]</sup> Shell1, containing Nd<sup>3+</sup> and Yb<sup>3+</sup>, was grown to harvest 806 nm irradiation by the Nd<sup>3+</sup> which would then transfer the excitation energy to Yb<sup>3+</sup>. The Yb<sup>3+</sup> network in the core and shell1 regions would relay the excitation to the activator ions (Er<sup>3+</sup> and Ho<sup>3+</sup>) for UC and DS emission to take place. The inert NaGdF<sub>4</sub> shell2 was grown as an additional protective layer between the optically active RE<sup>3+</sup> and the surrounding environment, as seen in the previous chapter, reducing the probability of non-radiative quenching by solvent molecules and crystal defects.

Core-only, core/shell1 (c/shell1) and core/shell1/shell2 (c/s/shell2) RENPs were characterized by XRD, revealing the formation of the pure hexagonal phase polymorph of all layers (see

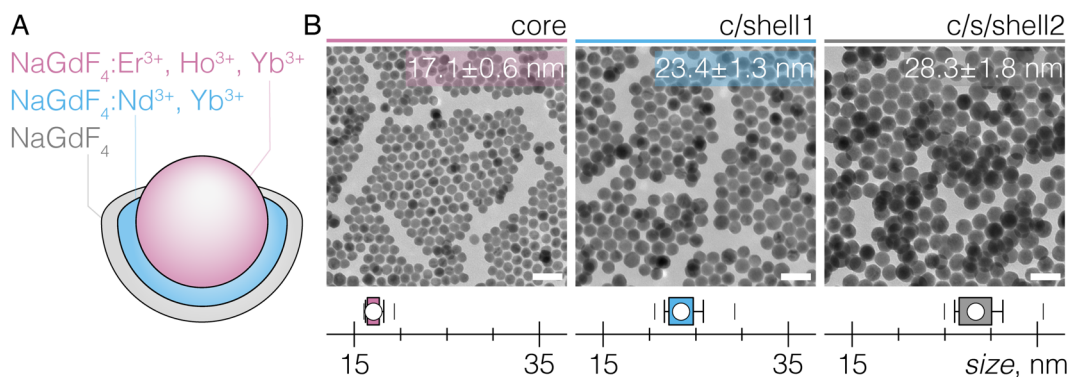


**Figure 4.1. Structural characterization of Nd<sup>3+</sup>-based multilayered RENPs.**

**A** – Schematic representation of NaGdF<sub>4</sub>:Er<sup>3+</sup>, Ho<sup>3+</sup>, Yb<sup>3+</sup>/NaGdF<sub>4</sub>:Nd<sup>3+</sup>, Yb<sup>3+</sup>/NaGdF<sub>4</sub> RENPs. **B** – TEM images and size distributions of core-only, core/shell1 (c/shell1) and core/shell1/shell2 (c/s/shell2) RENPs. Scale bar 50 nm. Box plots indicate: mean value (dot), SD (box outline), 5<sup>th</sup> and 95<sup>th</sup> percentiles (whiskers), and maximum/minimum values (dashes).

Appendix I). The uniform growth of the core and each subsequent shell of the RENPs was confirmed from the TEM micrographs (Figure 4.1B). Core-only RENPs were around 17 nm in size, which subsequently increased to ~23 and ~28 nm with respective additions of shell1 and shell2. Shell thicknesses were ~3.1 and ~2.5 nm for shell1 and shell2, respectively. Although in the previous chapter thicker inert shells were used to improve photoluminescence of RENPs, this study (also the one in chapter 5) preceded the previous one. Subsequently, more literature reports emerged on the influence of inert shell thickness over the optical properties of RENPs, but at the time only one had covered such analysis for both UC and DS emission.<sup>[79]</sup>

## 4.2 UC emission

The UC emission properties of RENPs dispersed in hexane were investigated under 806 and 980 nm excitation (actual excitation wavelength was 960 nm, yet for simplicity 980 nm definition is retained). The 806 nm radiation is absorbed by  $\text{Nd}^{3+}$ , whereas 980 nm excites  $\text{Yb}^{3+}$  directly. Under either of excitation wavelengths, the intensity of the UC emission continuously increased at each step of the RENPs growth (Figure 4.2A). Core-only RENPs showed only dim UC emission under 980 and 806 nm excitation, the latter being absorbed by the  $\text{Er}^{3+}$  directly. The

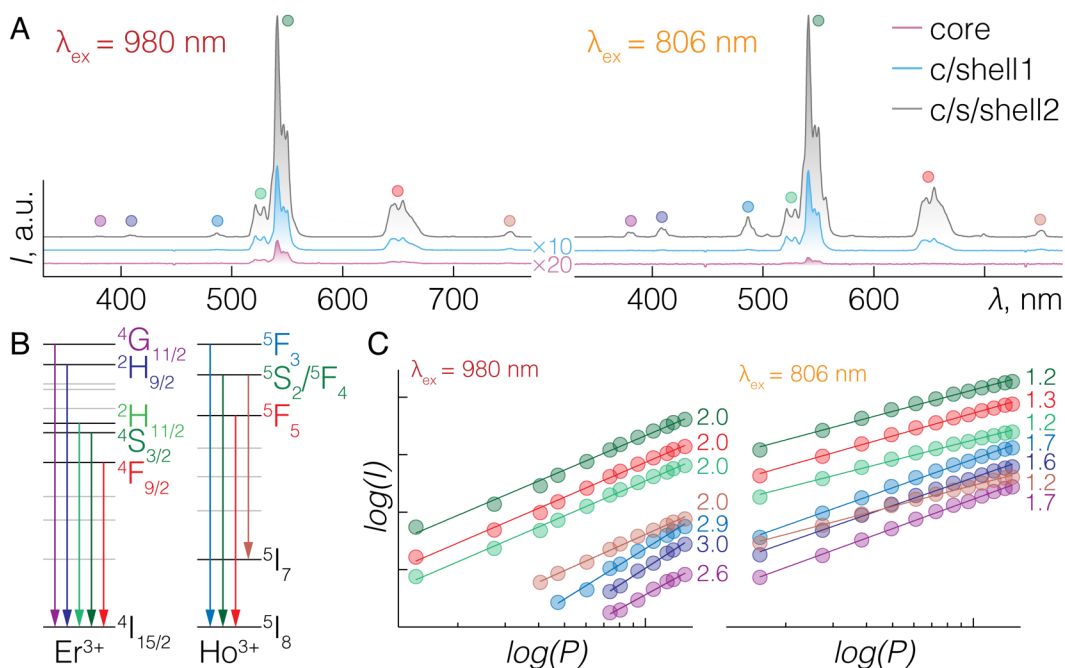


Figure 4.2. UC emission of  $\text{Nd}^{3+}$ -based multilayered RENPs.

A – UC emission spectra of core-only, c/shell1 and c/s/shell2 RENPs under 980 (left) and 806 nm (right) excitation. Core-only and c/shell1 spectra are multiplied 20 and 10 times, respectively, for clarity. Excitation power density  $\sim 140 \text{ W/cm}^2$ . B – Simplified energy level schemes of  $\text{Er}^{3+}$  and  $\text{Ho}^{3+}$ . Radiative transitions are color coded with dots in A above each emission band. C – Intensity ( $I$ ) vs excitation power ( $P$ ) log-log plots of UC emission bands of c/s/shell2 RENPs under 980 (left) and 806 nm (right) excitation. Values next to the data indicate the slope of a linear fit, a.k.a. UC photon order ( $n$ ).

addition of optically active shell1 endowed RENPs with more efficient excitation – more Yb<sup>3+</sup> to absorb 980 nm irradiation and introduction of Nd<sup>3+</sup> as primary 806 nm radiation sensitizers. After the growth of an inert shell2, the final c/s/shell2 RENPs had significantly enhanced UC emission as expected.

Under both excitation wavelengths emission bands spanning broad spectral range (350-750 nm) could be observed. Er<sup>3+</sup> emission bands were located around 380, 420, 525, 545, and 660 nm, attributed to radiative transitions to the <sup>4</sup>I<sub>15/2</sub> ground state from the <sup>4</sup>G<sub>11/2</sub>, <sup>2</sup>H<sub>9/2</sub>, <sup>2</sup>H<sub>11/2</sub>, <sup>4</sup>S<sub>3/2</sub> and <sup>4</sup>F<sub>9/2</sub> excited states, respectively (Figure 4.2B). Ho<sup>3+</sup> emission bands were at 485, 540, 650, and 750 nm, corresponding to the <sup>5</sup>F<sub>3</sub> → <sup>5</sup>I<sub>8</sub>, <sup>5</sup>S<sub>2</sub>/<sup>5</sup>F<sub>4</sub> → <sup>5</sup>I<sub>8</sub>, <sup>5</sup>F<sub>5</sub> → <sup>5</sup>I<sub>8</sub> and <sup>5</sup>S<sub>2</sub>/<sup>5</sup>F<sub>4</sub> → <sup>5</sup>I<sub>7</sub> radiative transitions, respectively (Figure 4.2B). Note, <sup>4</sup>S<sub>3/2</sub>, <sup>4</sup>F<sub>9/2</sub> → <sup>4</sup>I<sub>15/2</sub> (of Er<sup>3+</sup>) and <sup>5</sup>S<sub>2</sub>/<sup>5</sup>F<sub>4</sub>, <sup>5</sup>F<sub>5</sub> → <sup>5</sup>I<sub>8</sub> transitions (of Ho<sup>3+</sup>) overlap at the green and red spectral regions. Interestingly, higher order UC emission bands (UV/blue) were more intense under 806 than 980 nm excitation.

To better understand upconversion excitation pathways under the two irradiation wavelengths, UC emission intensity (*I*) vs excitation power (*P*) study was carried out (Figure 4.2C). As mentioned in the introduction, the illustrative minimum number of photons required to populate each radiative energy level can be determined by the slope value *n* of the linear fit in the log(*I*) vs log(*P*) plot.<sup>[39]</sup> In the case of 980 nm excitation, the *n* values were very close to the expected photon order for observed UC emissions. Two-photon excitation processes converted NIR photons to visible emission bands observed above 500 nm, and three-photon processes were involved in the excitation of emission bands below 500 nm. However, under 806 nm excitation all *n* values were significantly lower; in fact, *n*(806 nm) were almost half of *n*(980 nm). It, thus, appeared that under 980 nm excitation the intensity varies with power as a function of *P*<sup>*n*</sup>, whereas under 806 nm excitation it takes the *P*<sup>*n*/2</sup> form. In general, an estimation of the minimum number of photons required to populate higher lying excited states of RE<sup>3+</sup> can deviate from the theoretical predictions. Excitation dynamics in RENPs often are more complex than as described by simple multilevel excitation systems. The probability of radiative transition from a given excited state versus the non-radiative relaxation to the lower lying level, cross-relaxation, three-ion energy transfer, and other processes are known to reduce the experimentally measured *n* values.<sup>[39]</sup> In addition, when reaching upconversion saturation *n* values tend to sharply decrease and approach unity.

Under 806 nm excitation, Er<sup>3+</sup> can be excited directly via GSA and ESA processes, as evidenced from the presence of UC emission from the core-only RENPs before the Nd<sup>3+</sup>-doped layer is added (Figure 4.2A). The *P*<sup>*n*/2</sup> intensity dependence has been previously demonstrated

for the  $^4G_{11/2}$  and  $^2H_{9/2}$  excited states of  $Er^{3+}$  under direct 800 nm excitation, similar to the herein observations.<sup>[191]</sup> Together, it can be inferred that under 806 nm excitation the GSA and ESA processes complement ETU between  $Yb^{3+}$ - $Er^{3+}/Ho^{3+}$  pairs. This leads to more efficient excitation of higher laying energy levels and quicker upconversion saturation of the excited states, reducing the experimentally measured minimum photon order. GSA and ESA can also take place upon 980 nm excitation,<sup>[192]</sup> but owing to the lower energy of these photons the probability of populating higher laying energy levels becomes less likely.

The UC emission by RENPs under 806 nm excitation can be summarized as follows (Figure 4.3). When RENPs are excited by 806 nm laser,  $Nd^{3+}$  in the shell1 act as primary radiation harvesters, following energy transfer to  $Yb^{3+}$  and energy migration among the  $Yb^{3+}$  in the shell1 and in the core. UC emission sensitization from  $Er^{3+}$  and  $Ho^{3+}$  in the core of the RENPs then takes place via  $Yb^{3+}$  facilitated ETU, together with GSA and ESA by the activator ions themselves. The cumulative effect of these mechanisms results in more efficient RENPs excitation, and it can be readily appreciated from the greater intensity of the three-photon UC emission (Figure 4.2A). Note, additional energy transfer processes between  $Er^{3+}$ - $Ho^{3+}$ ,  $Er^{3+}$ - $Nd^{3+}$ , and  $Ho^{3+}$ - $Nd^{3+}$  were not considered, however it is understood that  $Nd^{3+}$  can quench  $Er^{3+}$  and  $Ho^{3+}$  excitation, as previously reported,<sup>[57]</sup> and as presented below.

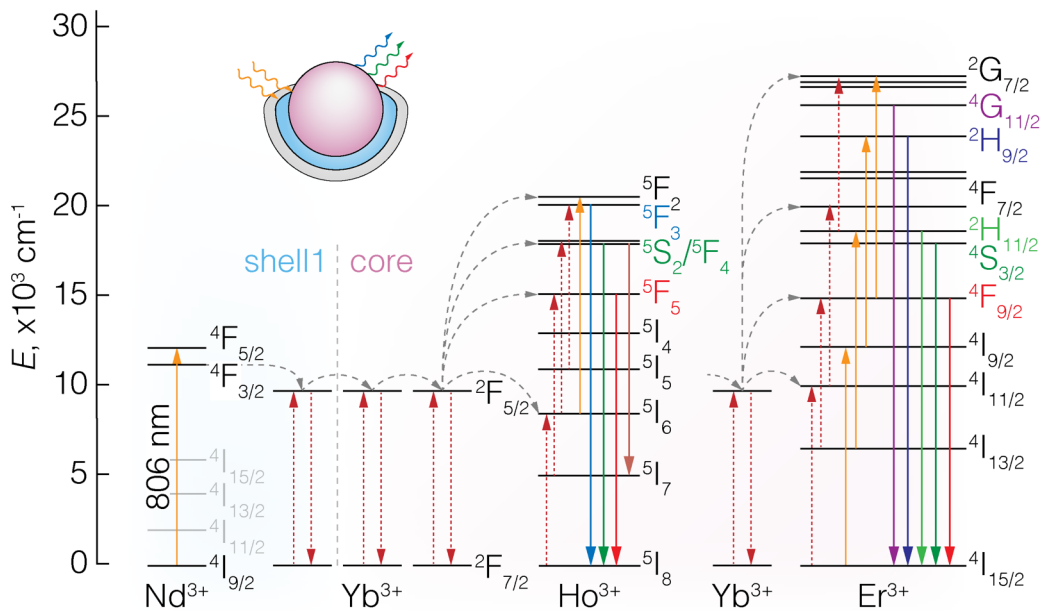


**Figure 4.3. UC emission-excitation scheme for  $Nd^{3+}$ -based multilayered RENPs.**

**Simplified RENP upconversion excitation scheme under 806 nm laser irradiation.  $Nd^{3+}$  is excited by GSA of the laser radiation, following energy transfer to  $Yb^{3+}$  and energy migration among the  $Yb^{3+}$  in the shell1 and the core of the RENPs.  $Ho^{3+}$  and  $Er^{3+}$  are then excited via ETU from  $Yb^{3+}$ . Additionally, GSA and ESA of 806 nm radiation can occur in  $Er^{3+}$ , and to some extent in  $Ho^{3+}$ , which help to populate higher laying excited states of these ions. Solid arrows represent radiative processes (emission, GSA and ESA), dashed – non-radiative energy exchange (energy migration and ETU). The non-radiative decay processes are not shown.**

### 4.3 DS emission

DS emission bands of  $\text{Ho}^{3+}$  and  $\text{Er}^{3+}$  at around 1180 ( $^5I_6 \rightarrow ^5I_8$ ) and 1550 nm ( $^4I_{13/2} \rightarrow ^4I_{15/2}$ ), respectively, were observed at each step of RENPs formation under 980 nm excitation (Figure 4.4). Following the growth of the RENPs' different layers, it could be seen that addition of shell1 increased the  $\text{Ho}^{3+}$  DS emission intensity, however that of  $\text{Er}^{3+}$  decreased. Despite the fact that more 980 nm photons are harvested in the presence of higher  $\text{Yb}^{3+}$  amount (present in the core + shell1), the  $\text{Nd}^{3+}$  associated quenching of  $\text{Er}^{3+}$  photoluminescence prevails via  $\text{Er}^{3+}(^4I_{13/2}) \rightarrow \text{Nd}^{3+}(^4I_{15/2})$  energy transfer, together with other possible energy exchange pathways populating the  $^4I_{13/2}$  and  $^4I_{15/2}$  excited states of  $\text{Nd}^{3+}$ .<sup>[57,193]</sup>  $\text{Er}^{3+}$  emission intensity could be restored after growing the inert shell2, which also largely boosted the  $\text{Ho}^{3+}$  DS emission intensity. Upon 806 nm excitation, the DS emission intensities from both  $\text{Er}^{3+}$  and  $\text{Ho}^{3+}$  continuously increased with the growth of shell1 and shell2 (Fig. 4B). In contrast to the case of 980 nm excitation, the quenching of  $\text{Er}^{3+}$  NIR emission could not be directly observed under 806 nm excitation after shell1 growth. Only weak DS emission of  $\text{Er}^{3+}$  is seen in the core-only RENPs, which is significantly increased, as in the case of the UC studies, after the introduction of  $\text{Nd}^{3+}$ , absorbing 806 nm radiation more efficiently. Notably, together with  $\text{Er}^{3+}$  and  $\text{Ho}^{3+}$  DS emission peaks, those of  $\text{Nd}^{3+}$  and  $\text{Yb}^{3+}$  could also be observed. Namely,  $\text{Nd}^{3+}$  emission at 880 ( $^4F_{3/2} \rightarrow ^4I_{9/2}$ ), 1060 ( $^4F_{3/2} \rightarrow ^4I_{11/2}$ ), 1340 nm ( $^4F_{3/2} \rightarrow ^4I_{13/2}$ ), and  $\text{Yb}^{3+}$  at 980 nm ( $^2F_{5/2} \rightarrow ^2F_{7/2}$ ).

The DS emissions of c/s/shell2 RENPs at 1180, 1340 (806 nm excitation only) and 1550 nm from  $\text{Ho}^{3+}$ ,  $\text{Nd}^{3+}$  and  $\text{Er}^{3+}$ , respectively, were further investigated by varying the 806 and 980 nm laser excitation power density (Figure 4.4 – insets). For both excitation wavelengths,  $n$  values

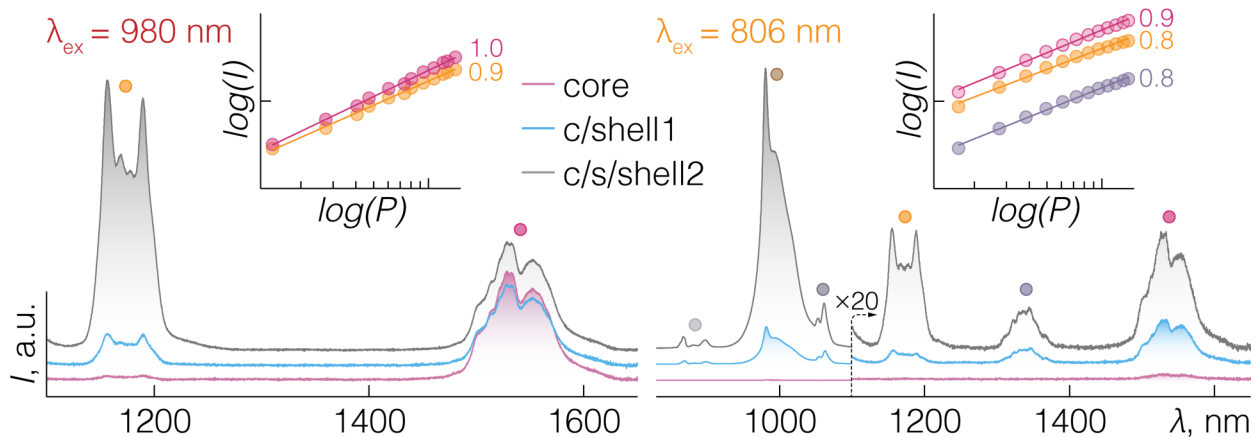
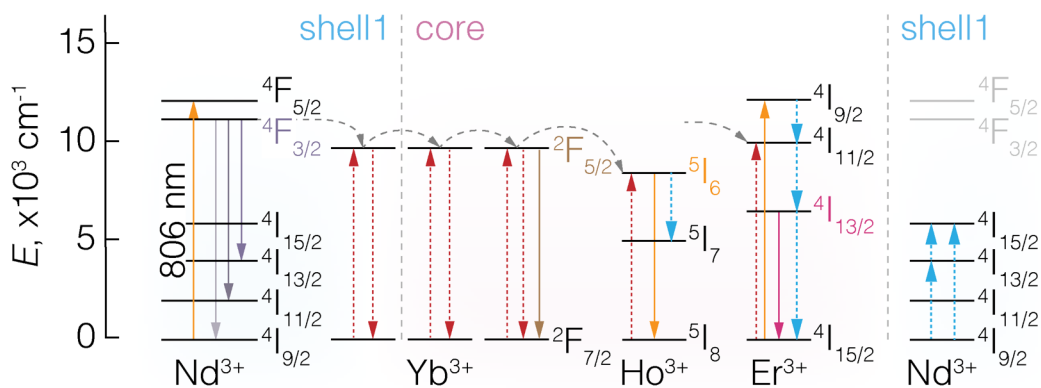


Figure 4.4. DS emission of  $\text{Nd}^{3+}$ -based multilayered RENPs.

DS emission spectra of core-only, c/shell1 and c/s/shell2 RENPs under 980 (left) and 806 nm (right) excitation. Spectra above 1100 nm is magnified 20 times for clarity in the case of 806 nm excitation. Dots above each band are color coded with radiative transitions presented in Figure 4.5. Excitation power density  $\sim 140 \text{ W/cm}^2$ . Insets –  $I$  vs  $P$  log-log plots of emission bands above 1100 nm of c/s/shell2 RENPs under 980 (left) and 806 nm (right) excitation. Values next to the data indicate photon order ( $n$ ).

were close to unity, as expected for the single-photon absorption/emission processes. Slightly smaller  $n$  values were obtained under 806 nm excitation, which, can be explained by the competitive nature of the upconversion and downshifting, due to the presence of numerous ESA and ETU pathways in the current RENPs (Figure 4.3). Excitation of RENPs to generate DS emission follows the same energy absorption and exchange sequence as in the case of UC, however it does not require the multiphoton “climb” of the RE<sup>3+</sup> energy level ladder (Figure 4.5). Possible Er<sup>3+</sup>-Nd<sup>3+</sup> and Ho<sup>3+</sup>-Nd<sup>3+</sup> interactions lead to overall photoluminescence intensity quenching of RENPs and suggest that further separation between Nd<sup>3+</sup> and activator ions is necessary to avoid deleterious inter-ion cross-talk.<sup>[57]</sup> Overall, 806 nm irradiation represents not only a heating-free RENP excitation route, but also provides an enriched palette of available DS emission bands which cover BW-I, -II and -III for NIR imaging applications.



**Figure 4.5. DS emission-excitation scheme for Nd<sup>3+</sup>-based multilayered RENPs.**

**Simplified RENP downshifting excitation scheme under 806 nm laser irradiation. Nd<sup>3+</sup> is excited by GSA of the laser radiation, following energy transfer to Yb<sup>3+</sup> and energy migration among the Yb<sup>3+</sup> in the shell1 and the core of the RENPs. Er<sup>3+</sup> can also be excited directly by the GSA. Possible energy transfer processes between the Er<sup>3+</sup>/Ho<sup>3+</sup> and Nd<sup>3+</sup> that lead to DS emission quenching are shown as blue dashed arrows. Solid arrows represent radiative processes, dashed – non-radiative energy exchange. The non-radiative decay processes are not shown.**

#### 4.4 Proof-of-concept studies

From the previous two sections a picture emerges on how Nd<sup>3+</sup>-based multilayered RENPs could be used in theranostics. Under NIR excitation high-photon energy UC emissions are generated with the potential to be harnessed for therapeutic purposes, and the plethora of DS emission bands could provide deep-tissue imaging capabilities for target of interested detection. However, prior to any biomedical use RENPs are ought to be re-suspended in aqueous environment and their photoluminescence characterized. Water dispersibility to as-synthesized OA-capped RENPs was imparted by surface modification with unsaturated phospholipids grafted with polyethylene glycol (PEG-DOPE).<sup>[176]</sup> Exploiting the hydrophobic interaction

between the non-polar chains of OA and PEG-DOPE phospholipids, the RENPs were enclosed in phospholipid micelles, which provided colloidal stable RENPs' dispersion in water. Presence of PEG-DOPE on the surface of RENPs was confirmed via TEM and FTIR (see Appendix III).

After the successful transfer of the RENPs to water, UC and DS emission spectra of the aqueous RENPs were recorded under 806 nm excitation (Figure 4.6). All of the previously observed UC and DS emission bands were preserved; however, the overall photoluminescence intensity was quenched as compared to the hexane dispersion. UC emission and  $\text{Ho}^{3+}$  DS emission around 1180 nm suffered from quenching by water most notably. Following the discussion of chapter 3, non-radiative energy transfer between  $\text{RE}^{3+}$  and water vibrational modes depopulates excited states of  $\text{RE}^{3+}$  and leads to emission intensity quenching. In the case of  $\text{Ho}^{3+}$  and  $\text{Er}^{3+}$ , radiative transitions in the NIR are in near-perfect resonance with vibrational energies of OH groups.<sup>[194,195]</sup> The asymmetric stretching of water molecules at  $\sim 3400\text{ cm}^{-1}$  matches well the energy level gaps of  $\text{Er}^{3+}$  ( $^4\text{I}_{11/2}$ - $^4\text{I}_{13/2}$ ) and  $\text{Ho}^{3+}$  ( $^5\text{I}_6$ - $^5\text{I}_7$ ). Quenching by water leads to the population of the downshifting  $^4\text{I}_{13/2}$  energy level of  $\text{Er}^{3+}$  and depopulation of  $^5\text{I}_6$  energy level of  $\text{Ho}^{3+}$ . Both processes preclude the excitation of higher laying energy levels for upconversion to take place as efficiently as it did in hexane dispersions of RENPs. In spite of the possible increase in the population of the  $\text{Er}^{3+}$   $^4\text{I}_{13/2}$  energy level, the overall intensity is still quenched due to non-radiative decay between  $^4\text{I}_{13/2}$  and  $^4\text{I}_{15/2}$  energy levels by the effect of multiple vibrational modes of water at  $\sim 3400$ ,  $\sim 2200$  and  $\sim 1650\text{ cm}^{-1}$ . Furthermore, higher order water absorption overtones  $\sim 6800$  ( $\sim 1430\text{ nm}$ ) and  $\sim 8300\text{ cm}^{-1}$  ( $\sim 1180\text{ nm}$ ) directly reabsorb DS emissions of  $\text{Er}^{3+}$  and  $\text{Ho}^{3+}$ , respectively.<sup>[194]</sup>

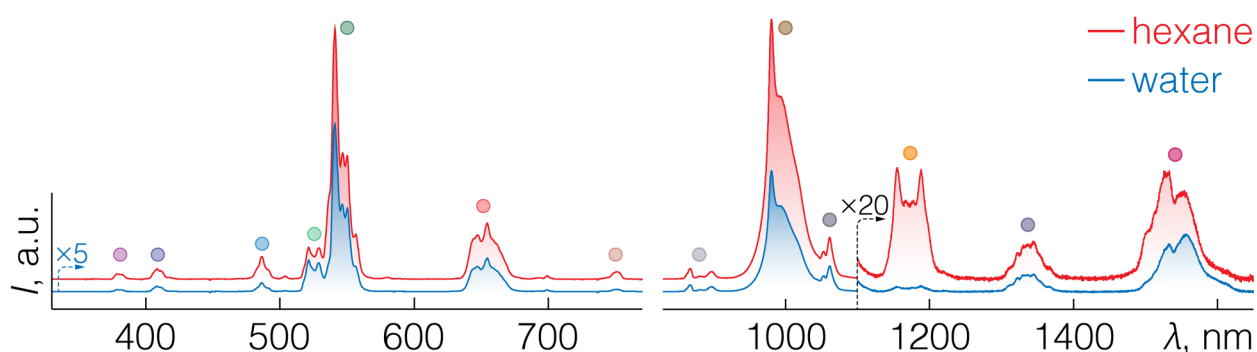


Figure 4.6. Photoluminescence of  $\text{Nd}^{3+}$ -based multilayered RENPs in water.

UC (left) and DS (right) emission of RENPs dispersed in hexane (red) and water (blue) under 806 nm excitation. Upconversion spectrum in water is multiplied 5 times for clarity, and downshifting spectra in both water and hexane are multiplied 20 times above 1100 nm. Excitation power density  $\sim 140\text{ W/cm}^2$ .

To highlight the theranostic potential of the RENPs, they were further tested in terms of: i) triggering secondary light-driven processes by means of UC emission, and ii) through-tissue imaging via DS emission, all under single heating-free 806 nm laser excitation.

Ce<sub>6</sub> – commonly utilized PS in the photodynamic therapy of cancer (PDT; presented in the section 1.4.3) – was used to form a complex with the aqueous RENPs in a similar manner to what has been previously done with semiconductor quantum dots.<sup>[196]</sup> NPs coated with unsaturated phospholipids, like RENPs studied here, allow for Ce<sub>6</sub> amphiphilic molecules to intercalate in the non-polar part of the lipid layer. This interaction usually presents itself as a bathochromic shift in the PS's fluorescence maximum position. Also, Ce<sub>6</sub> localizes exceptionally close to the NPs' surface, allowing for an efficient FRET between the two moieties, and indirect stimulation of PDT. Here, the spectral overlap between the Soret (405 nm) and Q(I) (654 nm) absorption bands of Ce<sub>6</sub> with UV/blue and the red UC emission of the RENPs, respectively, provides the basis for energy exchange from RENPs to Ce<sub>6</sub> (Figure 4.7). Upon the addition of Ce<sub>6</sub> (10 μM) to the aqueous dispersion of RENPs (~1 wt%), UC emission intensity decrease was observed for 380 (<sup>4</sup>G<sub>11/2</sub> → <sup>4</sup>I<sub>15/2</sub>), 410 (<sup>2</sup>H<sub>9/2</sub> → <sup>4</sup>I<sub>15/2</sub>), and 660 nm (Er<sup>3+</sup> <sup>4</sup>F<sub>9/2</sub> → <sup>4</sup>I<sub>15/2</sub> and Ho<sup>3+</sup> <sup>5</sup>F<sub>5</sub> → <sup>5</sup>I<sub>8</sub>) bands, following the simultaneous appearance of the photoluminescence signal around 675 nm, all under 806 nm excitation. The UC emission intensity decrease and the appearance of a new emission, characteristic of Ce<sub>6</sub> in non-polar environment,<sup>[197,198]</sup> indicate of successful complex formation and possibility for indirect excitation of the PS. When excited directly at the 440 nm, Ce<sub>6</sub> in the presence of RENPs has a distinct fluorescence band peaking around 672 nm (Figure 4.7 – Ce<sub>6</sub> in RENPs), as compared to fluorescence of Ce<sub>6</sub> in phosphate buffer positioned at 660 nm (Figure 4.7 – Ce<sub>6</sub> in PBS). These observations firmly support the

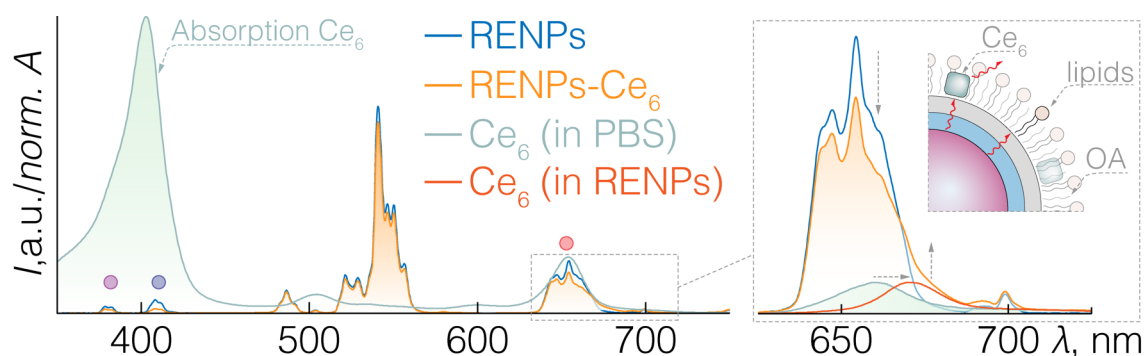


Figure 4.7. RENPs-Ce<sub>6</sub> complex.

UC emission of RENPs dispersed in water under 806 nm excitation: alone (blue) and in the presence of Ce<sub>6</sub> (orange). Normalized absorption spectra of Ce<sub>6</sub> is also shown. The 625-675 nm range is blown-up for clarity, showing the decrease of UC emission and appearance of a shoulder around 675 nm. Normalized emission spectra of Ce<sub>6</sub> under direct 440 nm excitation is shown when present in phosphate buffer solution (PBS; green) and in RENPs (deep orange). Inset – schematic representation of Ce<sub>6</sub> residing in the phospholipid coating of the RENPs, and its indirect excitation by the RENPs.

localization of Ce<sub>6</sub> in the phospholipid coating of the RENPs. Although additional studies are still necessary to determine the exact nature of energy transfer from RENPs to Ce<sub>6</sub>, given the good spectral overlap between the two moieties and presence of Ce<sub>6</sub> close to the activator ions in the core, both radiative and non-radiative (FRET) energy exchange pathways are possible. The ease of the RENPs-Ce<sub>6</sub> complex formation and the possibility for indirect excitation under NIR radiation make such a platform particularly attractive for PDT applications (see chapter 6).

In order to evaluate the applicability of the RENPs for deep-tissue imaging, DS emission under 806 nm excitation was collected with a NIR camera after passing through various thicknesses of chicken breast tissue, a model of optically dense and highly scattering media. Furthermore, a set of LP filters was used to investigate the imaging in different NIR spectral ranges (Figure 4.8). When a 830 nm LP filter was used, collecting almost all of the available NIR emission from the RENPs, up to 40% of the initial emission intensity was retained even passing through 1 cm of tissue. However, due to severe scattering of the shorter-wavelength NIR radiation, the localization of the excitation trace was impossible. Cutting part of the emission coming from Nd<sup>3+</sup> and Yb<sup>3+</sup>, with a 980 nm LP filter, the signal could be slightly better resolved and still observed through 1 cm of tissue. Further reducing the collected NIR radiation to longer emission wavelengths, with 1150 nm LP or 1450 nm LP filters, improved greatly the localization of the excitation trace, due to the substantially reduced scattering of NIR emission above 1100 nm. This was particularly true for the Er<sup>3+</sup> DS emission at 1550 nm in the BW-III. Although the absolute intensities of the Ho<sup>3+</sup>, Nd<sup>3+</sup> and Er<sup>3+</sup> NIR emission bands above 1100 nm are

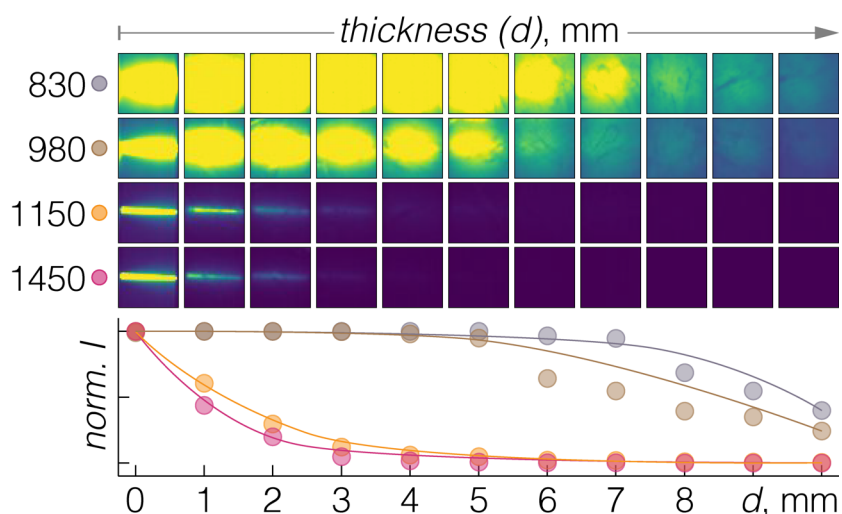


Figure 4.8. Through-tissue visualization of Nd<sup>3+</sup>-based multilayered RENPs.

NIR imaging of the RENC water dispersion through chicken breast tissue of increasing thickness. RENPs were excited with 806 nm laser (~0.2 W) and DS emission was collected utilizing various LP optical filters (cut-off wavelength of each is indicated on the left to the images). Emission intensity (normalized to the initial value at 0 mm) is plotted against increasing tissue thickness. Experimental data points are color coded with the LP filters used to collect the NIR signal.

significantly lower than those of  $\text{Yb}^{3+}$  and  $\text{Nd}^{3+}$  below 1100 nm, NIR signal was still detected through few mm of tissue thickness, attesting to the deep-tissue imaging capabilities of these RENPs. Ultimately, further enhancement of the absolute emission intensity in the NIR above 1100 nm of RENPs could help to achieve even greater signal transmission through biological tissues and high-contrast visualization of deep-seated maladies.

## 4.5 Discussion

The  $\text{Nd}^{3+}$ -based upconverting and downshifting RENPs studied here are befitting representatives of a multifunctional theranostic nanoplatform. Under the heating-free excitation emergent UC and DS emissions cover a wide optical spectral range from 350 to 1650 nm, individual bands of which could be used for therapeutic and diagnostic purposes. However, as already mentioned, further adjustments to this system are necessary to improve overall photoluminescence by suppressing surface and inter-ion quenching. Furthermore, an even more detailed comparison between the two excitation pathways, 800 and 980 nm, is needed to differentiate the efficiency of RENPs excitation in absolute terms.

In the past few years, several studies have dealt with further characterization of  $\text{Nd}^{3+}$ -based upconverting RENPs. D. Przybylska and T. Grzyb have studied  $\text{SrF}_2:\text{Yb}^{3+}$ ,  $\text{Er}^{3+}/\text{SrF}_2:\text{Yb}^{3+}$ ,  $\text{Nd}^{3+}$  RENPs excited with 808 and 975 nm radiation.<sup>[199]</sup> Similarly to results above, minimum photon order of upconversion excitation was found to be much lower when RENPs were excited with 808 nm, compared to those under 975 nm excitation. It was suggested that lower values are the result of extended energy transfer across the  $\text{Yb}^{3+}$  network, cross-relaxation, and excited state saturation. Whereas, J. Hesse et al. investigating  $\text{Nd}^{3+}$ -based  $\text{NaYF}_4$  upconverting RENPs reported no significant difference for the upconversion photon order under 795 or 976 nm excitations.<sup>[200]</sup> As authors explain, their spectral measurements have been performed using excitation power densities below  $200 \text{ mW}/\text{cm}^2$ , thus GSA and ESA processes contributing to more rapid saturation of the excited states under 795 nm excitation would be minimal. These reports come to show that UC emission saturation in RENPs might be reached quickly with increasing power density of  $\sim 800 \text{ nm}$  irradiation, capping their maximum photoluminescence intensity output before 980 nm excitation of equivalent power would. Further evidence for it has been presented by Liao et al.<sup>[201]</sup> UC emission of  $\text{NaYF}_4:\text{Yb}^{3+}$ ,  $\text{Er}^{3+}/\text{NaYF}_4:\text{Yb}^{3+}/\text{NaYF}_4:\text{Yb}^{3+}$ ,  $\text{Nd}^{3+}/\text{NaYF}_4$  RENPs was scrutinized under 808 and 976 nm excitation at a single NP level, in the  $10^2$ - $10^7 \text{ W}/\text{cm}^2$  excitation power density range. It was observed that at moderate excitation power densities UC emission intensity obtained under 808 nm excitation was higher than that

under 976 nm. However, it also reached saturation faster and was eventually surpassed by UC emission intensity under 976 nm excitation. Intriguingly, even further increase in the excitation power density resulted in a saturated UC emission under 976 nm, while in the case of 808 nm excitation it prompted appearance of self-sensitized upconversion from  $\text{Nd}^{3+}$ , additionally contributing to even greater UC emission intensity. The power plot and photoluminescence decay analysis suggested the fast saturation of the  $\text{Nd}^{3+} \rightarrow \text{Yb}^{3+} \rightarrow \text{Er}^{3+}$  energy transfer cascade responsible for rapid UC emission saturation under 808 nm irradiation, before the self-sensitized  $\text{Nd}^{3+}$  upconversion takes place. Finally, Wiesholler et al. evaluated the absolute performance of  $\text{Nd}^{3+}$ -based upconverting RENPs under 805 and 978 nm excitations.<sup>[202]</sup> The authors have measured the absorption cross-section,  $\sigma$ , of  $\text{Nd}^{3+}$  and  $\text{Yb}^{3+}$  in the  $\text{NaYF}_4$  host. It was found that for the excitation wavelengths employed, common in many other studies on  $\text{Nd}^{3+}$ -based RENP,  $\sigma_{\text{Nd}}(805 \text{ nm})$  and  $\sigma_{\text{Yb}}(978 \text{ nm})$  are  $\sim 4.93 \cdot 10^{-20} \text{ cm}^2$  and  $\sim 1.44 \cdot 10^{-20} \text{ cm}^2$ , respectively. This is far from the initially expected whole order of magnitude difference in terms of absorbance between the two ions, which to be reached requires selection of excitation wavelengths that match absorption maxima of the  $^4\text{I}_{15/2} \rightarrow ^4\text{F}_{5/2}$  and  $^2\text{F}_{7/2} \rightarrow ^2\text{F}_{5/2}$  transitions of  $\text{Nd}^{3+}$  and  $\text{Yb}^{3+}$ , respectively. At ideally matching wavelengths,  $\sigma_{\text{Nd}}(794 \text{ nm})$  and  $\sigma_{\text{Yb}}(976 \text{ nm})$  are  $\sim 1.25 \cdot 10^{-19} \text{ cm}^2$  and  $\sim 1.77 \cdot 10^{-20} \text{ cm}^2$ , respectively. It has to be noted that, absorption maxima position and absorption cross-section are highly host dependent; yet, in most common  $\text{NaGdF}_4$ ,  $\text{NaYF}_4$ ,  $\text{LiYF}_4$  RENPs  $\text{Nd}^{3+}$  absorption peak is at  $\sim 793\text{-}794 \text{ nm}$ . Further, the authors confirm that RENP excitation can be carried out at greater depth by the 805 nm irradiation, as it is less absorbed by water. However, absolute *PLQY* and brightness of  $\text{NaYF}_4:\text{Er}^{3+}$ ,  $\text{Yb}^{3+}/\text{NaYF}_4:\text{Nd}^{3+}$ ,  $\text{Yb}^{3+}/\text{NaYF}_4$  RENPs was found to be about an order of magnitude lower when excited with 805 nm radiation as compared to equivalent in power 976 nm excitation. This comes to show that on the ensemble level of RENPs, in contrast to single particle studies, a possible tradeoff exists between choosing heating-free deeper penetrating  $\sim 800 \text{ nm}$  excitation and sacrificing UC emission brightness that could be attained under  $\sim 980 \text{ nm}$  irradiation.

## 5 Nd<sup>3+</sup>-RENPs. NANOTHERMOMETRY IN BW-III

---

In the previous chapter, Nd<sup>3+</sup>-based RENPs, capable of PDT and NIR imaging, were presented as a potential multifunctional theranostic nanoplatform. However, diagnostics-wise these RENPs could serve not only as imaging agents, but also as nanothermometers. The temperature sensing with RENPs is explored towards the more accurate detection of malignancies as well as controlled execution of thermal therapies. Whereas *in vitro* nanothermometry with RENPs can be carried out via their UC emission, *in vivo* temperature sensing demands downshifting RENPs, more specifically, those operating in the NIR at the BWs. High resolution deep-tissue imaging and nanothermometry with RENPs would benefit from the concurrent use of all the three BWs: excitation in the BW-I, and emission collection in BW-II and BW-III. The Nd<sup>3+</sup>-based RENPs of chapter 4 satisfy these conditions, yet, at the time of their investigation, various nanothermometers studied mostly exploited the 800-1100 nm range.<sup>[149,150,203–208]</sup> Only a few were reported to work in the BW-II (>1100 nm),<sup>[145,150,209]</sup> whereas BW-III was yet to be opened for NIR nanothermometry. In order to verify that nanothermometry in BW-III was feasible, Nd<sup>3+</sup>-based RENPs of chapter 4 were improved in structural design, by adding an intermediate energy relay layer to suppress inter-ion quenching, and their DS emissions in the 1100-1700 nm spectral range were studied as a function of temperature. Temperature sensing properties of these RENPs were surveyed in water and in hexane. In different media RENPs showed contrasting thermal responses, underlying the importance to investigate NIR nanothermometers in biologically relevant media, as per their envisioned future use in living organisms.

*Herein results were published as: “Double Rare-Earth Nanothermometer in Aqueous Media: Opening the Third Optical Transparency Window to Temperature Sensing” A. Skripka, A. Benayas, R. Marin, P. Canton, E. Hemmer and F. Vetrone, Nanoscale, 9 (9), 3079-3085, 2017.*

### 5.1 RNP preparation and characterization

Multilayered (core/shell1/shell2/shell3) RENPs (Figure 5.1A) were prepared via hot-injection thermal decomposition, in a sequence of four injection steps. NaGdF<sub>4</sub>: 2 mol% Er<sup>3+</sup>, 5 mol% Ho<sup>3+</sup>, 20 mol% Yb<sup>3+</sup> core RENPs were synthesized out of 2.5 mmol each of Na-TFA and Gd/Er/Ho/Yb-TFA precursors. Precursors were degassed and dissolved in 7.5 mL each of OA and ODE (solution B), and injected into the solution A, containing 12.5 mL each of OA and ODE at 315 °C. Injection rate was 1.5 mL/min. After 1 h of reaction time, 2.5 mmol each of Na-TFA

and Gd/Yb-TFA, dissolved in 4 mL each of OA and ODE (solution C), were injected (1.5 mL/min) into the reaction mixture to form NaGdF<sub>4</sub>: 10 mol% Yb<sup>3+</sup> shell (shell1). After 1 h of reaction, 2.5 mmol each of Na-TFA and Gd/Nd/Yb-TFA, dissolved in 4 mL each of OA and ODE (solution D), were injected (1.5 mL/min) into the reaction mixture to form NaGdF<sub>4</sub>: 5 mol% Nd<sup>3+</sup>, 20 mol% Yb<sup>3+</sup> shell (shell2). Finally, optically inert NaGdF<sub>4</sub> shell (shell3) was grown over the core/shell1/shell2 RENPs injecting 2.5 mmol each of Na-TFA and Gd-TFA, dissolved in 4 mL each of OA and ODE (solution E), at 1.5 mL/min and reacting for 1 h. After a total of 4 h of reaction time the mixture was cooled down, RENPs were washed, and dispersed in hexane for further characterization. Aliquots of core-only, core/shell1, and core/shell1/shell2 RENPs were sampled prior to the subsequent shelling steps.

Herein synthesized Nd<sup>3+</sup>-based RENPs, were quite similar to their predecessors in chapter 4 in terms of structural architecture and ion doping, but featured an additional Yb<sup>3+</sup>-doped layer (shell1) between the activator ions (Er<sup>3+</sup>, Ho<sup>3+</sup>) in the core and sensitizer ions (Nd<sup>3+</sup>) in the shell2. The shell1 was intended to spatially separate Er<sup>3+</sup>/Ho<sup>3+</sup> from Nd<sup>3+</sup> – preventing the inter-ion quenching, while maintaining the energy relay between these ions via an extended Yb<sup>3+</sup> network.<sup>[57]</sup> As before, optically inert outer shell (shell3) was employed to reduce surface quenching and boost overall photoluminescence of RENPs.

The layer-by-layer uniform growth of pure hexagonal phase RENPs was confirmed by the XRD (see Appendix I) and TEM (Figure 5.1B). Core-only RENPs were around 16 nm in size, which subsequently increased to ~19, ~25, and ~30 nm after the addition of shell1, shell2, and shell3, respectively. Final multilayered RENPs were dispersed in water after surface coating with PEG-DOPE phospholipids. TEM and FTIR analysis confirmed successful encapsulation of RENPs in phospholipid micelles (see Appendix III).

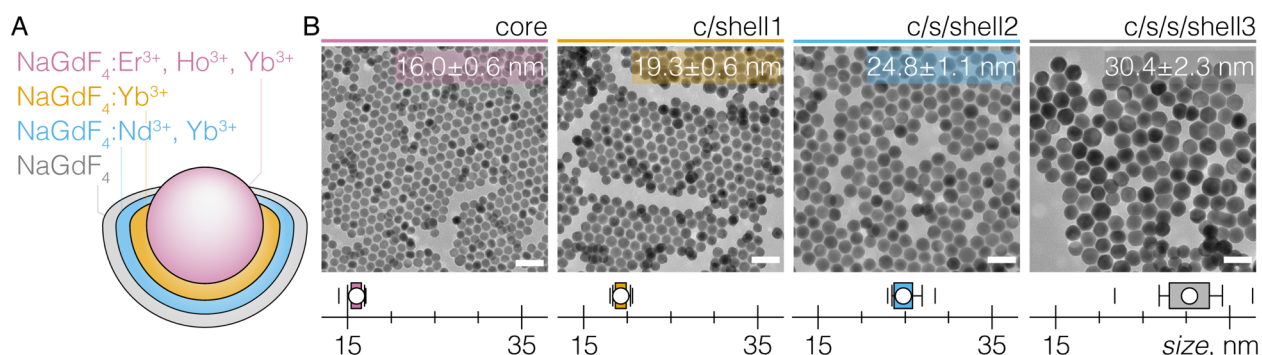


**Figure 5.1. Structural characterization of Nd<sup>3+</sup>-based RENPs for nanothermometry.**

**A** – Schematic representation of NaGdF<sub>4</sub>:Er<sup>3+</sup>, Ho<sup>3+</sup>, Yb<sup>3+</sup>/NaGdF<sub>4</sub>:Yb<sup>3+</sup>/NaGdF<sub>4</sub>:Nd<sup>3+</sup>, Yb<sup>3+</sup>/NaGdF<sub>4</sub> RENPs. **B** – TEM images and size distributions of core-only, c/shell1, c/s/shell2, and c/s/s/shell3 RENPs. Scale bar 50 nm. Box plots indicate: mean value (dot), SD (box outline), 5<sup>th</sup> and 95<sup>th</sup> percentiles (whiskers), and maximum/minimum values (dashes).

Under 806 nm laser excitation of RENPs, UC and DS emission bands within the wide 350 – 1650 nm spectral range were observed (Figure 5.2). Upconversion signal of RENPs was made up of  $\text{Ho}^{3+}$  and  $\text{Er}^{3+}$  radiative transitions, while their DS emissions were also complimented by  $\text{Nd}^{3+}$  radiative transitions, consistent with the spectral features of RENPs in chapter 4. The emission intensity change with temperature was then investigated for  $\text{Ho}^{3+}$ ,  $\text{Nd}^{3+}$ , and  $\text{Er}^{3+}$  DS emission bands around 1180 ( $^5\text{I}_6 \rightarrow ^5\text{I}_8$ ), 1340 ( $^4\text{F}_{3/2} \rightarrow ^4\text{I}_{13/2}$ ), and 1550 nm ( $^4\text{I}_{13/2} \rightarrow ^4\text{I}_{15/2}$ ), respectively.

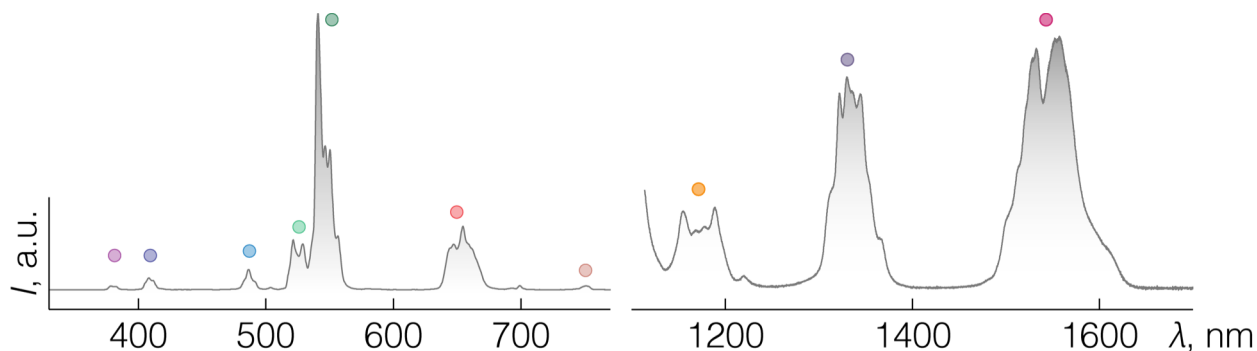


Figure 5.2. UC and DS spectra of  $\text{Nd}^{3+}$ -based RENPs for nanothermometry.

UC (left) and DS (right) emission of RENPs dispersed in water under 806 nm excitation. Excitation power density  $\sim 140 \text{ W/cm}^2$ . Dots indicate radiative transitions of  $\text{Ho}^{3+}$ ,  $\text{Er}^{3+}$ , and  $\text{Nd}^{3+}$ , as described in chapter 4.

## 5.2 NIR Nanothermometry

Temperature of the colloidal water dispersion of RENPs was varied within the physiological range of 20-50 °C and their DS emissions were excited by the heating-free 806 nm radiation. Nanothermometry defining characteristics of RENPs were estimated as described in the section 1.5.2. Elevating the temperature, intensity of  $\text{Ho}^{3+}$  and  $\text{Er}^{3+}$  DS emission bands increased, whereas that of  $\text{Nd}^{3+}$  decreased (Figure 5.3A). The opposing thermal behavior of these bands allowed to define two LIR thermometric parameters,  $\Delta(\text{Ho}^{3+}/\text{Nd}^{3+})$  and  $\Delta(\text{Er}^{3+}/\text{Nd}^{3+})$ . Both

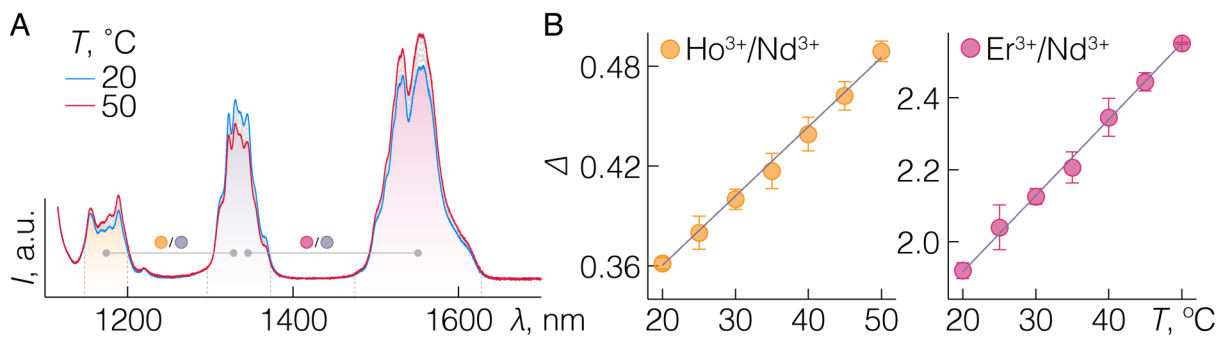
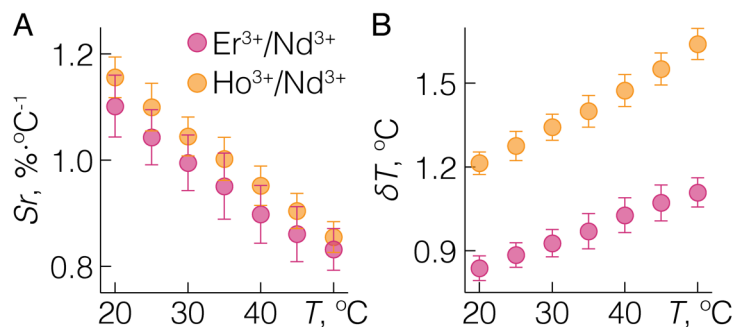


Figure 5.3. NIR nanothermometry with  $\text{Nd}^{3+}$ -based RENPs.

A – DS emission spectra of RENPs under 806 nm excitation ( $\sim 140 \text{ W/cm}^2$ ) at different temperatures in the 20-50 °C range. Shaded areas show the integration ranges for the  $\text{Ho}^{3+}$  (yellow),  $\text{Nd}^{3+}$  (purple), and  $\text{Er}^{3+}$  (red) emission bands used to construct LIR thermometric parameters  $\Delta$ . B – Change of  $\Delta(\text{Ho}^{3+}/\text{Nd}^{3+})$  and  $\Delta(\text{Er}^{3+}/\text{Nd}^{3+})$  against the temperature and their respective linear fits.

parameters  $\Delta$  showed linear thermal dependence in the set temperature range (Figure 5.3B). This indicated that RENPs under study could serve as double optical nanothermometers in the BW-II and BW-III. The performance of the RENPs as NIR nanothermometers was then assessed in terms of relative thermal sensitivity,  $S_r$ , and temperature uncertainty,  $\delta T$  (Figure 5.4). Maximal thermal sensitivities in the 20-50 °C range for  $\Delta(\text{Ho}^{3+}/\text{Nd}^{3+})$  and  $\Delta(\text{Er}^{3+}/\text{Nd}^{3+})$  were  $1.17\% \cdot ^\circ\text{C}^{-1}$  and  $1.10\% \cdot ^\circ\text{C}^{-1}$ , respectively. Reproducibility,  $R$ , of these thermometric parameters were  $\sim 99\%$  (see Appendix IV). At the time this study was published, this represented the very first RNP NIR double nanothermometer that was fully operable in an aqueous environment within BW-II/II ( $\text{Ho}^{3+}/\text{Nd}^{3+}$ ) and BW-II/III ( $\text{Er}^{3+}/\text{Nd}^{3+}$ ). Subsequently, more of NIR nanothermometers taking advantage of BW-III were developed,<sup>[156,210–212]</sup> some of which are among the most sensitive RNP nanothermometers to-date.<sup>[156]</sup>

The temperature uncertainty  $\delta T$  for RENPs was estimated in accordance with the minimal resolvable temperature by the material and the experimental instrumentation in use.  $\delta T$  is given by the product of  $1/S_r$  and the  $\delta\Delta/\Delta$  (eq. 1.15), where the former is attributed to the intrinsic properties of the material, while the latter represents the uncertainty given by the experimental setup. Here, the  $\delta\Delta/\Delta$  was around 1.4 and 0.9% for  $\Delta(\text{Ho}^{3+}/\text{Nd}^{3+})$  and  $\Delta(\text{Er}^{3+}/\text{Nd}^{3+})$ , respectively. Thus, the minimal  $\delta T$  was estimated  $\sim 1.2$  and  $\sim 0.8$  °C for  $\Delta(\text{Ho}^{3+}/\text{Nd}^{3+})$  and  $\Delta(\text{Er}^{3+}/\text{Nd}^{3+})$ , respectively (Fig. 2C). Since  $\delta T$  is mainly determined by the signal-to-noise ratio during the spectral acquisition, this value is expected to vary between different experimental setups and particularly when light propagates through optically absorbing and scattering media like biological tissues. Further improvement of  $\delta T$  could be done by increasing the signal-to-noise of the measurement setup, by boosting the photoluminescence intensity of RENPs, or by improving the  $S_r$  of the defined thermometric parameters. To be able to tackle the latter factor, it is imperative to apprehend the physical mechanisms that govern the thermal behavior of these RENPs.



**Figure 5.4. Temperature sensing properties of  $\text{Nd}^{3+}$ -based RENPs. Change of A –  $S_r$  and B –  $\delta T$  of  $\Delta(\text{Ho}^{3+}/\text{Nd}^{3+})$  and  $\Delta(\text{Er}^{3+}/\text{Nd}^{3+})$  in 20-50 °C temperature range.**

### 5.3 Understanding thermal behavior of RENPs

Present RENPs operate as double-center nanothermometers: their thermometric parameters  $\Delta$  are defined via DS emission bands of different  $RE^{3+}$ . Thermal population of their emissive states can thus be expected to follow the phonon-assisted temperature-dependent energy transfer described by the Miyakawa-Dexter model (Eq. 1.6 and 1.7).<sup>[213]</sup> Considering the  $Nd^{3+} \rightarrow Yb^{3+} \rightarrow Er^{3+}/Ho^{3+}$  energy transfer cascade in the RENPs, and relative arrangement between the energy levels of these  $RE^{3+}$ , it could be safely assumed that temperature driven DS emission intensity decrease of  $Nd^{3+}$  and increase of  $Ho^{3+}$  is driven by the  $Nd^{3+}(^4F_{3/2}) \rightarrow Yb^{3+}(^2F_{5/2})$  and  $Yb^{3+}(^2F_{5/2}) \rightarrow Ho^{3+}(^5I_6)$  phonon-assisted energy transfers, respectively.<sup>[149,214]</sup> However, increase in DS emission intensity of  $Er^{3+}$  at elevated temperatures could not be easily understood following the same reasoning.

In an attempt to resolve this, thermal behavior of RENPs was studied in a hexane dispersion, in the 20-50 °C temperature range. Since RENPs were present in a solvent with lower energy vibrational modes, intense DS emissions of  $Ho^{3+}$ ,  $Nd^{3+}$ , and  $Er^{3+}$  could be seen, particularly boosted intensity was that of  $Ho^{3+}$  emission (Figure 5.5A). Upon temperature increase, intensity of  $Ho^{3+}$  and  $Nd^{3+}$  DS emissions, respectively increased and decreased, as in the case of RENPs dispersed in water. However, contrary to the behavior of  $Er^{3+}$  DS emission of RENPs in water, it decreased at the elevated temperatures of the hexane dispersion. Overall, changing the temperature from 20 to 50 °C, relative emission intensities of  $Ho^{3+}$ ,  $Nd^{3+}$  and  $Er^{3+}$  DS emission bands in hexane were altered by +41, -11 and -22%, respectively (Figure 5.5B). The similar thermal behavior of  $Ho^{3+}$  and  $Nd^{3+}$  DS emission intensities for RENPs dispersed in different media, reaffirm that  $Nd^{3+}(^4F_{3/2}) \rightarrow Yb^{3+}(^2F_{5/2})$  and  $Yb^{3+}(^2F_{5/2}) \rightarrow Ho^{3+}(^5I_6)$  phonon-assisted energy transfers are governing the thermal behavior of these RENPs (Figure 5.6). In a similar manner,  $Er^{3+}$  emission intensity in hexane likely decreases by the phonon-assisted depopulation of the

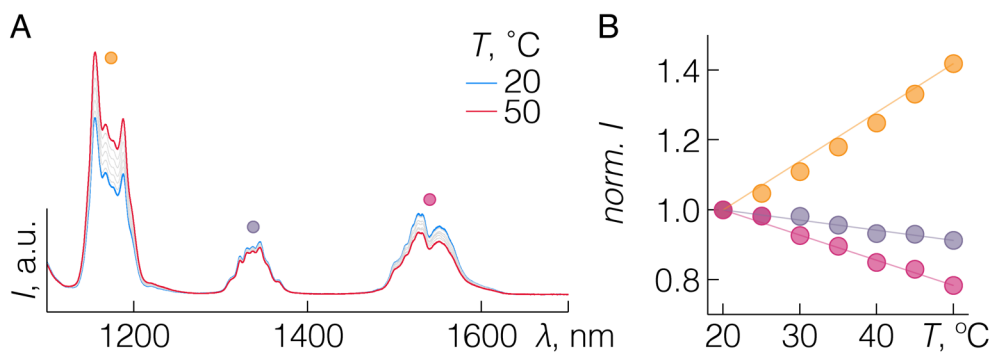


Figure 5.5. NIR nanothermometry with  $Nd^{3+}$ -based RENPs in hexane.

A – DS emission spectra of RENPs under 806 nm excitation ( $\sim 140 \text{ W/cm}^2$ ) at different temperatures in the 20-50 °C range, when dispersed in hexane. B – Change in the integrated emission intensities of  $Ho^{3+}$  (yellow),  $Nd^{3+}$  (purple), and  $Er^{3+}$  (red) DS emission intensities with temperature, normalized to 20 °C point.

$\text{Er}^{3+} \ ^4\text{I}_{13/2}$  energy level via  $\text{Er}^{3+}(\ ^4\text{I}_{13/2}) \rightarrow \text{Ho}^{3+}(\ ^5\text{I}_7)$  energy transfer.<sup>[215]</sup> However, there are additional depopulation channels that are exclusive to RENPs dispersed in an aqueous milieu, which are related to the presence of water vibrational modes.

The  $\ ^4\text{I}_{11/2}-\ ^4\text{I}_{13/2}$  and  $\ ^5\text{I}_6-\ ^5\text{I}_7$  energy gaps of  $\text{Er}^{3+}$  and  $\text{Ho}^{3+}$ , respectively, are in near-resonance with the OH vibrational stretching modes of water molecules at around  $3400\text{--}3500\text{ cm}^{-1}$ . The non-radiative energy transfer from the energy levels of  $\text{Ho}^{3+}$  and  $\text{Er}^{3+}$  towards the vibrational modes of the surrounding medium, directly influences the population of  $\text{Er}^{3+} \ ^4\text{I}_{13/2}$  and depopulation of  $\text{Ho}^{3+} \ ^5\text{I}_6$  energy levels. In fact, as the temperature of water increases, the hydrogen bonding between the  $\text{H}_2\text{O}$  molecules weakens, resulting in the OH groups vibrating at higher frequencies.<sup>[216,217]</sup> In the case of  $\text{Er}^{3+}$ , increase in the vibrational energy of OH groups with temperature leads to better matched resonance with the  $\ ^4\text{I}_{11/2}-\ ^4\text{I}_{13/2}$  energy gap, which results in a more enhanced population of  $\ ^4\text{I}_{13/2}$  emissive state. Additionally, as the temperature of water increases the first overtone ( $\sim 6800\text{ cm}^{-1}$ ) of the OH stretching modes shifts to higher energies,<sup>[218]</sup> resulting in the lesser direct quenching of the  $\ ^4\text{I}_{13/2}$  state that gives rise to 1550 nm DS emission of  $\text{Er}^{3+}$ . Between the competing phonon-assisted inter-ion energy transfer ( $W_{\text{Er}}$ ) and OH assisted electronic-to-vibrational energy transfer (EVET) processes (Figure 5.6), the overall intensity of the  $\text{Er}^{3+}$  DS emission of RENPs dispersed in water increases with the increasing temperature. Together, nanothermometry via  $\Delta(\text{Ho}^{3+}/\text{Nd}^{3+})$  is primarily related to the temperature-dependent phonon-assisted  $\text{Yb}^{3+}(\ ^2\text{F}_{5/2}) \rightarrow \text{Ho}^{3+}(\ ^5\text{I}_6)$  and  $\text{Nd}^{3+}(\ ^4\text{F}_{3/2}) \rightarrow \text{Yb}^{3+}(\ ^2\text{F}_{5/2})$  energy transfer mechanisms, while in the case of  $\Delta(\text{Er}^{3+}/\text{Nd}^{3+})$  the latter pathway is accompanied by the temperature-dependent  $\text{Er}^{3+}(\ ^4\text{I}_{11/2}) \rightarrow \text{OH}(\nu_1)$  EVET.

Based on these findings, a point of concern arises from the fact that the thermometric properties of these RENPs are environment-sensitive. To establish the working limits of the RENPs, the

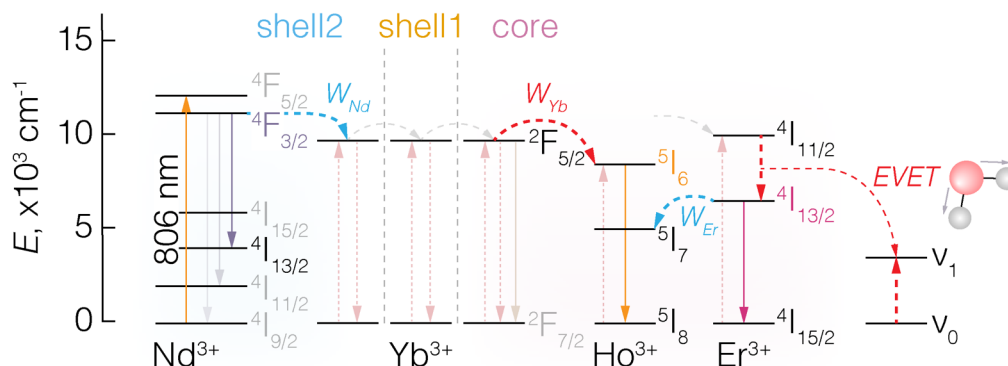


**Figure 5.6.** DS emission-excitation of  $\text{Nd}^{3+}$ -based RENPs and temperature dependence.

**Simplified RENP downshifting excitation scheme under 806 nm laser irradiation and temperature dependent pathways responsible for  $\text{Nd}^{3+}$ ,  $\text{Ho}^{3+}$  and  $\text{Er}^{3+}$  DS emission intensity changes.  $W_{\text{Nd}}$  and  $W_{\text{Yb}}$  phonon-assisted energy transfers that respectively lead to  $\text{Nd}^{3+}$  DS emission intensity decrease and increase of that of  $\text{Ho}^{3+}$ . On the other hand, in water, DS emission intensity of  $\text{Er}^{3+}$  increases due to EVET to OH vibrational modes.**

temperature related DS emission intensity changes were tested against an increasing amount of heavy water ( $D_2O$ ) in the distilled water dispersion of the RENPs, as well as in the cell culture medium. Since, the DO stretching (at  $\sim 2500\text{ cm}^{-1}$ ) is considerably mismatched with the  $^4I_{11/2}$ - $^4I_{13/2}$  energy gap of  $Er^{3+}$ , alterations in the  $S_r$  of RENPs as nanothermometers could be expected. As it stands, a decrease in the  $S_r$  of the  $\Delta(Er^{3+}/Nd^{3+})$  was observed when the  $H_2O:D_2O$  wt% ratio reached 1:3, while no change from the control (100% distilled water) was observed for the RENPs dispersed in cell culture medium (DMEM). Importantly, when  $D_2O$  constituted the majority (75 wt%) of the RENPs colloidal dispersion, the DS emission intensity of  $Er^{3+}$  did not increase with temperature anymore. This further supports the role of OH-assisted EVET mechanism behind the temperature-dependent alteration of the DS emission intensity of RENPs in water. In general, it can be considered that the nanothermometric performance of the present RENPs remains reliable in surroundings with a hydration level of 60 wt% and higher, which is within the average 70 wt% of water considered to be present in cells.<sup>[219]</sup>

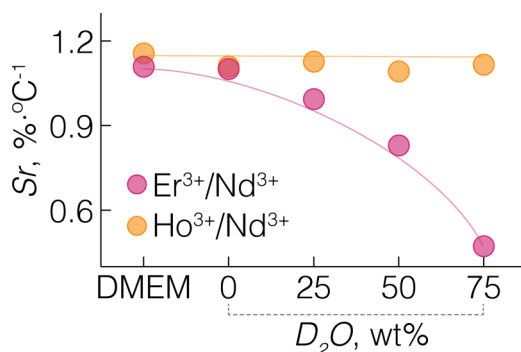


**Figure 5.7. Relative sensitivity in different environments.**

$S_r$  of  $\Delta(Ho^{3+}/Nd^{3+})$  and  $\Delta(Er^{3+}/Nd^{3+})$  at 20 °C for RENPs dispersed in cell culture media DMEM or distilled water with varied wt% amount of  $D_2O$ .

## 5.4 Discussion

Herein presented  $Nd^{3+}$ -based RENPs constituted the very first nanothermometers operating in the BW-II and BW-III. However, beyond this proof-of-concept nanothermometry in the BW-III is yet to see major impact in biomedical applications, several roadblocks still obstruct the path towards their routine use *in vivo*. As discussed in section 1.5.5 heterogeneous tissue absorption properties in the NIR preclude from the reliable subcutaneous temperature measurement, as uneven attenuation of emission bands in the BW-II and BW-III deteriorates the calibration of NIR nanothermometers. Correcting for the tissue attenuation has great potential to solve this issue, however a more straightforward approach could also be to develop RENP nanothermometers that operate in the very narrow spectral range within BW-II and BW-III (see chapters 6, 9, and

10). In such a case, different emission ranges used to define the LIR thermometric parameters  $\Delta$  would be attenuated more evenly, maintaining calibration of the nanothermometer in relative terms – allowing to accurately measure temperature differences, rather than absolute temperatures.

Furthermore, the present study highlights the importance of measuring temperature sensing properties of RENPs in the environment in which they are designed to operate. The observed opposing temperature behavior of  $\text{Er}^{3+}$  DS emission of the RENPs when dispersed in hexane and in water, comes to show that if RENPs are studied in organic environments or in powder form the same temperature driven changes of their photoluminescence cannot be guaranteed when transferred to water. In fact, for the herein studied RENPs dispersed in hexane, inverse temperature sensitivity of  $\text{Ho}^{3+}$  and  $\text{Er}^{3+}$  DS emission bands could also be used to define thermometric parameter  $\Delta(\text{Ho}^{3+}/\text{Er}^{3+})$  with the relative sensitivity  $S_r$  as high as  $2.7 \text{ \%}\cdot\text{C}^{-1}$ , yet intensity of both DS emission bands in water increase with temperature and  $\Delta(\text{Ho}^{3+}/\text{Er}^{3+})$  does not change significantly anymore. Actually, the long and winding road of developing the present  $\text{Nd}^{3+}$ -based RENPs as nanothermometers in the BW-III started with simple  $\text{Er}^{3+}$ ,  $\text{Ho}^{3+}$  and  $\text{Yb}^{3+}$ -doped RENPs, which readily showed temperature sensing in hexane under 980 nm excitation, but would not function as nanothermometers once transferred in water. Following multiple iterations of different RENP architectures, the multilayered  $\text{Nd}^{3+}$ -based RENPs were conceived as potent multifunctional nanoplatform which under heating-free 800 nm excitation could be used for therapy (PDT) and diagnostics (imaging and temperature sensing).

## 6 DECOUPLED THERANOSTICS WITH RENPs

---

Throughout the course of previous chapters, RENPs have been introduced and studied as multifunctional theranostic agents, accommodating: NIR imaging, nanothermometry, and mediation of secondary photochemical processes (via UC emission). However, these functions are typically invoked simultaneously, there is no clear temporal distinction between therapy and diagnostics as both are forced to happen at once. But just like surgeons first ascertain where the diseased area is localized before making the cut, future theranostic RENPs should have the flexibility to switch between their disease detection and eradication modes on-demand. It is thus imperative to create theranostic RENPs that would allow for safe visualization of the area of interest, or the circulation of RENPs in the blood stream towards it, without preemptive and potentially harmful initiation of drug release or generation of ROS. At the same time, the therapeutic arsenal on board of the RENPs could be lunched into effect completely on-demand, once deemed proper. Furthermore, such decoupled theranostics RENPs would allow to safely conduct post-treatment follow-up without the fear of additional damage to healthy tissues. Decoupled theranostics RENPs represent a necessary evolutionary step to the current state-of-the-art all-in-one theranostic nanoplatforms – matching their efficacy in terms of diagnostics and therapy, while being much safer and versatile to implement in biomedical research and medical practice. Fortunately, owing to the modular design of RENPs they do have the potential for realizing such a vision, through rational core/shell engineering and RE<sup>3+</sup> doping.

As seen in chapter 4, individual RE<sup>3+</sup> could be excited with light of different wavelengths and have wavelength specific emission profile. This, so called, orthogonal excitation has been previously implemented to obtain excitation wavelength-dependent UC emission in RENPs, that could be used for on-off switching of chromophores in various applications.<sup>[220,221]</sup> Yet, at the time no RENPs have been considered where different excitation wavelengths would prompt either UC or DS emissions, respectively used for on-demand therapy and diagnostics. In an attempt to create such decoupled theranostic RENPs, with wavelength-dependent UC and DS emissions, and promote a more thoughtful approach towards theranostics – LiYF<sub>4</sub>:Tm<sup>3+</sup>, Yb<sup>3+</sup>/LiYF<sub>4</sub>/LiYF<sub>4</sub>:Nd<sup>3+</sup> RENPs were conceived. Li<sup>+</sup>-based host was selected for its prominence in generating high energy UC emission of Tm<sup>3+</sup>, useful in therapeutic applications of RENPs.

*This study was carried out through a joint collaboration between Canadian and Lithuanian institutions. Dr. Vitalijus Karabanovas and Ms. Greta Jarockytė, from the National Cancer*

*Institute in Vilnius, Lithuania, have evaluated singlet oxygen generation, RENP accumulation and cytotoxicity in cells, and demonstrated the decoupled theranostics in vitro.*

*Herein results were published as: "Decoupling Theranostics with Rare Earth Doped Nanoparticles" A. Skripka, V. Karabanovas, G. Jarockyte, R. Marin, V. Tam, M. Cerruti, R. Rotomskis and F. Vetrone, Adv. Funct. Mater, 29 (12), 1807105, 2019.*

## 6.1 RENP preparation and structural characterization

The multilayered  $\text{LiYF}_4:\text{Tm}^{3+}$ ,  $\text{Yb}^{3+}/\text{LiYF}_4/\text{LiYF}_4:\text{Nd}^{3+}$  RENPs (Figure 6.1A) were prepared via modified heat-up and hot-injection thermal decomposition approaches.  $\text{LiYF}_4$ : 0.5 mol%  $\text{Tm}^{3+}$ , 25 mol%  $\text{Yb}^{3+}$  core RENPs (UC-core) were made out of 2.5 mmol each of Li-TFA and Y/Tm/Yb-TFA precursors, degassed and dissolved in 17.5 mL OA, 2.5 mL OM and 20 mL ODE at 110 °C under vacuum and magnetic stirring (solution A). The flask was then backfilled with argon and the temperature was increased to 330 °C. After 1 h of reaction time, 2.5 mmol each of Li-TFA and Y-TFA, dissolved in 4 mL each of OA and ODE (solution B), were injected into the solution A to form  $\text{LiYF}_4$  shell (idle-shell). Injection rate was 1 mL/min and reaction was allowed to proceed for an additional 1 h. Finally,  $\text{LiYF}_4$ : 1 mol%  $\text{Nd}^{3+}$  shell (DS-shell) was grown over the UC-core/idle-shell RENPs injecting 2.5 mmol each of Li-TFA and Y/Nd-TFA, dissolved in 4 mL each of OA and ODE (solution C), at 1 mL/min rate and leaving the mixture to react for 1 h. After a total of 3 h of reaction time the mixture was cooled down to RT, RENPs were washed, and dispersed in hexane for further morphological and spectral characterization. Aliquots of UC-core and UC-core/idle-shell RENPs were sampled prior to the subsequent shelling steps.

The UC-core/idle-shell/DS-shell architecture of RENPs was devised to ensure contrasting photoluminescence of RENPs under different NIR irradiation, namely 806 and 980 nm.  $\text{Yb}^{3+}/\text{Tm}^{3+}$  in the UC-core of the RENPs represented a classical sensitizer/activator pair, which under 980 nm excitation would upconvert NIR radiation to that in the UV-vis spectral range. The  $\text{Nd}^{3+}$ -doped DS shell, on the other hand, could be excited independently via 806 nm with its DS emission bands residing in the NIR, as seen in previous chapters. The optically inert idle-shell was put between the optically active layers to ensure decoupling of energy exchange between  $\text{Tm}^{3+}/\text{Yb}^{3+}$  and  $\text{Nd}^{3+}$ , thus preventing cross-talk among them, which could lead to quenching of  $\text{Tm}^{3+}$  UC emission or its undesired excitation by the 806 nm irradiation.<sup>[57]</sup> Minimal thickness of the idle-shell (in the range of 1.6–2.1 nm) was considered following studies on interface energy transfer between  $\text{RE}^{3+}$ .<sup>[222]</sup> The layer-by-layer formation of the decoupled theranostic RENPs was observed with the TEM (Figure 6.1B). Morphologically, RENPs assumed a bi-pyramidal

shape, characteristic of a tetragonal ( $I4_1/a$ ) crystal structure of  $\text{LiYF}_4$ , confirmed via XRD analysis (see Appendix I). Physical dimensions of the RENPs were obtained factoring in minor  $\times$  major axis of an elliptical fit for individual bi-pyramidal RENPs, and were estimated to be  $\sim 44 \times 62$  nm for the UC-core,  $\sim 53$  nm  $\times$  78 nm for the UC-core/idle-shell, and  $\sim 64 \times 93$  nm for the UC-core/idle-shell/DS-shell. The presence of  $\text{Yb}^{3+}$  solely in the UC-core, and  $\text{Nd}^{3+}$  in the DS-shell was confirmed with EDX elemental mapping (Figure 6.1C).  $\text{Yb}^{3+}$  were clearly visible only at the UC-core position of the RENPs, while  $\text{Nd}^{3+}$  were observed at the periphery of RENPs in the DS-shell. Only small traces of  $\text{Nd}^{3+}$  were detected by EDX due to the low doping amount of these ions, whereas due to even lower doping of  $\text{Tm}^{3+}$  it could not be observed by elemental mapping.

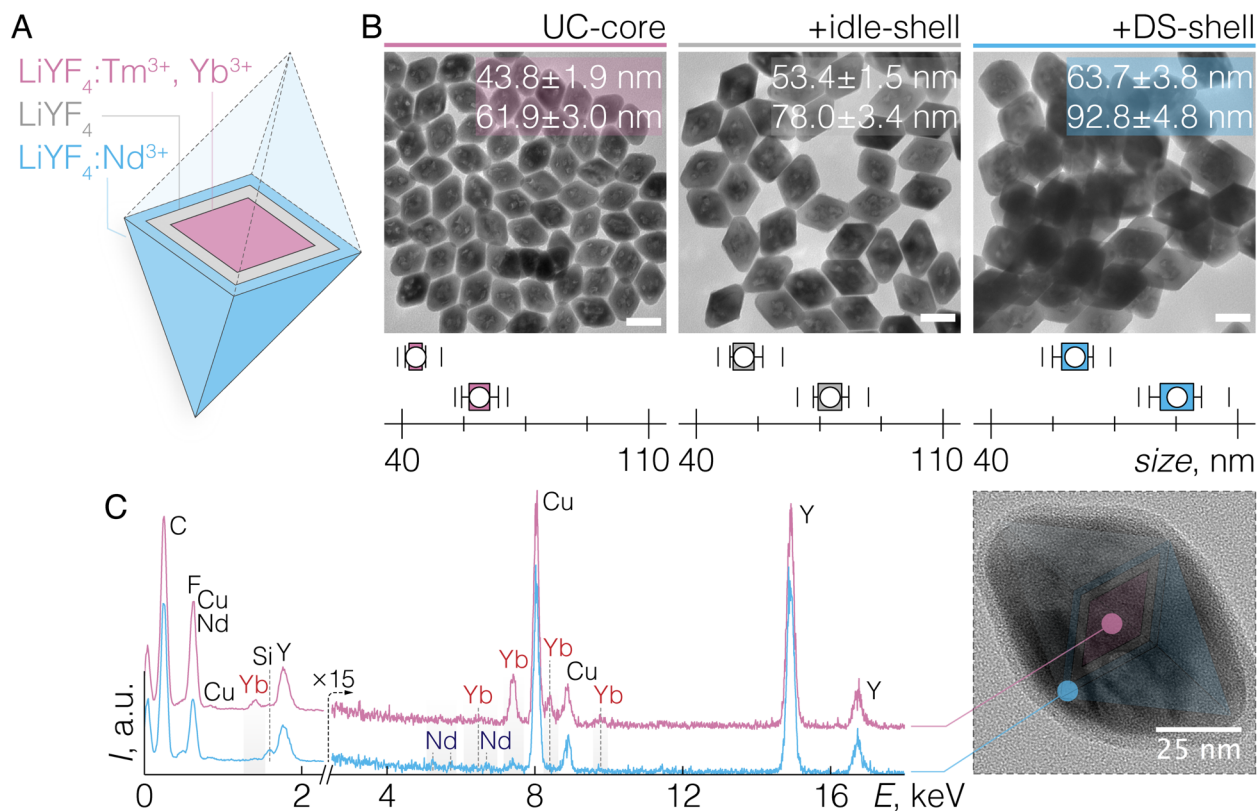


**Figure 6.1. Structural characterization of decoupled theranostics RENPs.**

**A** – Schematic representation of  $\text{LiYF}_4:\text{Tm}^{3+}, \text{Yb}^{3+}/\text{LiYF}_4/\text{LiYF}_4:\text{Nd}^{3+}$  RENPs. **B** – TEM images and size distributions of UC-core, UC-core/idle-shell and UC-core/idle-shell/DS-shell RENPs. Scale bar 50 nm. Box plots indicate: mean value (dot), SD (box outline), 5<sup>th</sup> and 95<sup>th</sup> percentiles (whiskers), and maximum/minimum values (dashes). Upper and lower boxes represent the length of minor and major axes of the RENPs, respectively. **C** – EDX spectra of the two regions of interest taken at the center and outer part of the RENPs (TEM image on the right).  $\text{Yb}^{3+}$  are seen to be confined to the UC-core of RENPs, while small traces of  $\text{Nd}^{3+}$  were present in the DS-shell.

## 6.2 Optical characterization of RENPs

The segregated RE<sup>3+</sup> distribution in different layers of as-synthesized RENPs was also evaluated spectroscopically, following the layer-by-layer growth of the decoupled theranostics RENPs (Figure 6.2). The photoluminescence emission of RENPs was measured within the 300–1400 nm spectral range under 806 or 980 nm excitation. Irradiated by 980 nm laser, the LiYF<sub>4</sub>:Tm<sup>3+</sup>, Yb<sup>3+</sup> UC-core showed typical UC emission profile of Tm<sup>3+</sup> covering most of the 300–800 nm spectral range (Figure 6.2A). In the Tm<sup>3+</sup>/Yb<sup>3+</sup> pair, Yb<sup>3+</sup> harvest the 980 nm radiation and transfer it to the nearby Tm<sup>3+</sup> via multiple ETU steps, which gives rise to many UC emission bands of Tm<sup>3+</sup> from high-lying energy levels. UC emission bands were seen at around 340 (<sup>1</sup>I<sub>6</sub> → <sup>3</sup>F<sub>4</sub>), 360, (<sup>1</sup>D<sub>2</sub> → <sup>3</sup>H<sub>6</sub>), 450 (<sup>1</sup>D<sub>2</sub> → <sup>3</sup>F<sub>4</sub>), 480 (<sup>1</sup>G<sub>4</sub> → <sup>3</sup>H<sub>6</sub>), 510 (<sup>1</sup>D<sub>2</sub> → <sup>3</sup>H<sub>5</sub>), 650 (<sup>1</sup>G<sub>4</sub> → <sup>3</sup>F<sub>4</sub>), and 790 nm (<sup>3</sup>H<sub>4</sub> → <sup>3</sup>H<sub>6</sub>).<sup>[223]</sup> The addition of an inert idle-shell increased (by about 75%) the overall intensity of the emission by suppressing surface defects and solvent vibrational quenching.<sup>[60,61]</sup> Further growth of Nd<sup>3+</sup>-doped DS-shell marginally influenced the UC emission intensity of fully formed decoupled theranostics RENPs. Most crucially, under 806 nm irradiation of equivalent power density none of the Tm<sup>3+</sup> UC emission bands could be seen. On the NIR side of the optical spectrum, no Nd<sup>3+</sup> DS emission was observed from the UC-core or UC-core/idle-shell RENPs irradiated by 806 or 980 nm (Figure 6.2B). Only when the Nd<sup>3+</sup>-containing DS-shell was formed, 806 nm excited RENPs exhibited DS emission of Nd<sup>3+</sup> with bands around 880, 1060 and 1340 nm, which respectively correspond to <sup>4</sup>F<sub>3/2</sub> → <sup>4</sup>I<sub>9/2</sub>, <sup>4</sup>I<sub>11/2</sub>, and <sup>4</sup>I<sub>13/2</sub> radiative transitions. Part of the Yb<sup>3+</sup> DS emission around 1020 nm, stemming from <sup>2</sup>F<sub>5/2</sub> → <sup>2</sup>F<sub>7/2</sub> radiative

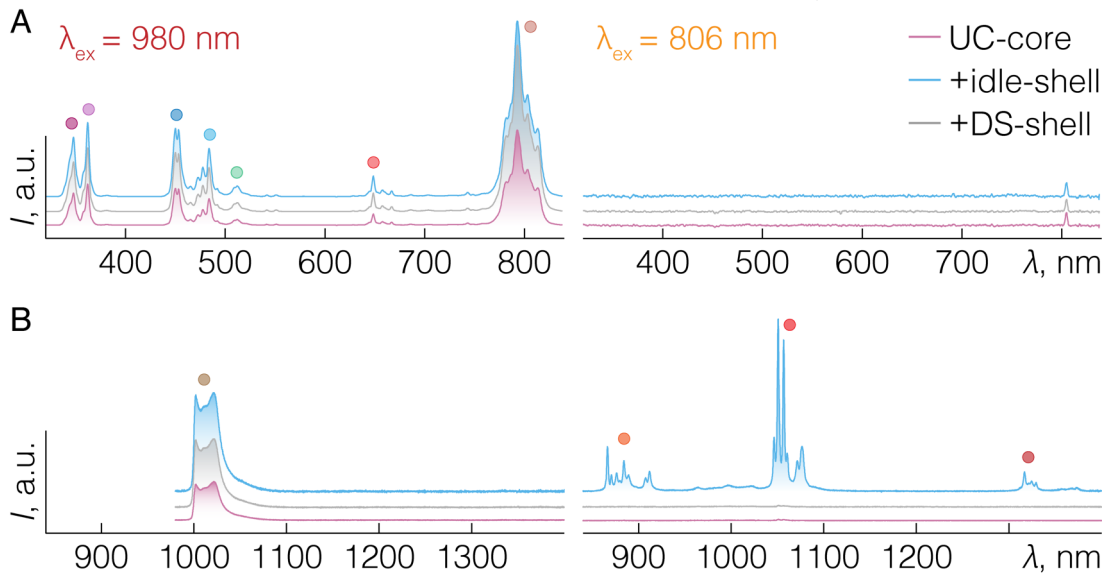
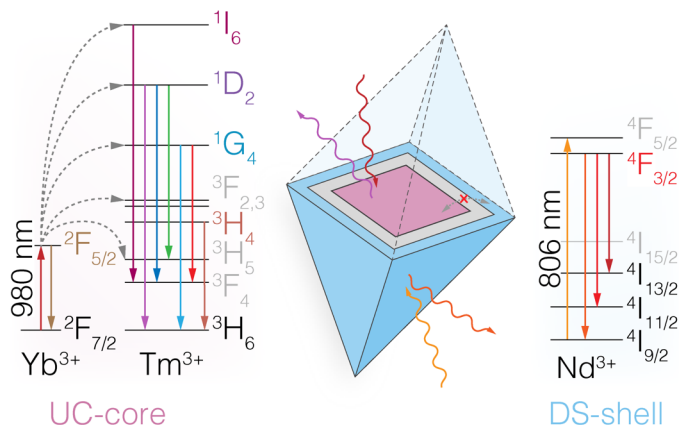


Figure 6.2. UC and DS emission spectra of decoupled theranostics RENPs in hexane.

A – UC and B – DS emission spectra of UC-core, UC-core/idle-shell and UC-core/idle-shell/DS-shell RENPs under 980 (left) and 806 nm (right) excitation. Excitation power density  $\sim 140 \text{ W/cm}^2$ . Dots above each emission band are color-coded with radiative transitions summarized in Figure 6.3.

transition, was observed from RENPs excited by 980 nm. Overall, spectral and structural characterization of RENPs unequivocally proved the separation of the optically active RE<sup>3+</sup> in the respective functional layers, that under orthogonal 806 and 980 nm excitation provided DS and UC emissions, respectively (Figure 6.3).



**Figure 6.3. Excitation-emission of decoupled theranostics RENPs.**

**Orthogonal excitation of the RENPs with on-demand UC and DS emissions, as well as simplified energy level schemes and excitation-emission processes of Tm<sup>3+</sup>/Yb<sup>3+</sup> pair in the UC-core of the RENPs and Nd<sup>3+</sup> in the DS-shell. Solid arrows – radiative transitions, dashed – energy transfer processes.**

The as-synthesized RENPs were dispersible only in non-polar solvents, thus their use in a biomedical setting was restricted. As before, dispersity in water was imparted on the multilayered decoupled theranostics RENPs via encapsulation in phospholipid micelles, using a mixture of PEGylated and non-PEGylated unsaturated phospholipids. The decoupled optical response was preserved for the aqueous dispersion of RENPs: UC emission by Tm<sup>3+</sup>/Yb<sup>3+</sup> was observed solely under 980 nm excitation, while only the Nd<sup>3+</sup> DS emission could be seen under 806 nm (Figure 6.4). The high energy UC emission of RENPs can be exploited for therapy purposes by initiating secondary photochemical processes (i.e. drug release or PDT), while the three major Nd<sup>3+</sup> transitions (<sup>4</sup>F<sub>3/2</sub> → <sup>4</sup>I<sub>9/2</sub>, <sup>4</sup>I<sub>11/2</sub>, and <sup>4</sup>I<sub>13/2</sub>) within the NIR spectral region coincide

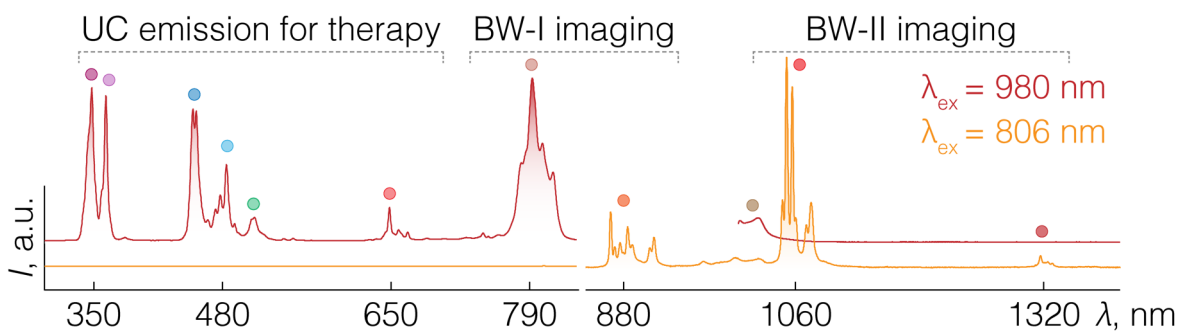


**Figure 6.4. UC and DS emission spectra of decoupled theranostics RENPs in water.**

**UC (right) and DS (left) emission spectra of decoupled theranostic RENPs under 980 (~240 W/cm<sup>2</sup>) and 806 nm (~140 W/cm<sup>2</sup>) excitation. Dots above each emission band are color-coded with radiative transitions summarized in Figure 6.3.**

with the BW-I and BW-II, suitable for subcutaneous imaging. Similarly to the proof-of-concept imaging experiments in the chapter 4, here, Nd<sup>3+</sup> DS emissions were observed penetrating through tissues as thick as 5 mm (see Appendix V). This reassured that the DS-shell under 806 nm excitation endows the decoupled theranostic RENPs with the possibility to serve as stand-alone NIR contrast agents, where each of the Nd<sup>3+</sup> DS emissions can be used individually or all-at-once to visualize the target of interest. Around 790 nm emission of Tm<sup>3+</sup> in the BW-I (<sup>3</sup>H<sub>4</sub> → <sup>3</sup>H<sub>6</sub>) was also converted by the UC-core from the 980 nm excitation, which can be employed for imaging purposes as well.<sup>[224]</sup> Nevertheless, NIR DS emission provides higher contrast subcutaneous imaging, due to the greater efficiency of the DS process and reduced light attenuation exerted by tissues for wavelengths over 1000 nm.

### 6.3 Nd<sup>3+</sup> single-band nanothermometry

As explored in chapter 5, aside from the NIR imaging, DS emissions also carry spectrally encoded information about local temperature cues, which could be extracted at the same time. This enables real-time temperature monitoring with the possibility of avoiding overheating and damage to the surrounding tissues during laser-induced therapy, i.e. due to the water absorption of 980 nm radiation used to promote UC emission in decoupled theranostics RENPs. In the context of Nd<sup>3+</sup> nanothermometry, the <sup>4</sup>F<sub>3/2</sub> → <sup>4</sup>I<sub>9/2</sub> transition has been mostly used for temperature sensing, but NIR radiation in the BW-I can still be obscured by autofluorescence and severe scattering. Although sharp and intense, the <sup>4</sup>F<sub>3/2</sub> → <sup>4</sup>I<sub>11/2</sub> transition (~1060 nm) at the time was regarded to be temperature insensitive and thus not suitable for nanothermometry. Still, several studies had proposed NIR nanothermometry through the Stark sub-levels of the <sup>4</sup>F<sub>3/2</sub> → <sup>4</sup>I<sub>11/2</sub> transition.<sup>[143,144,225]</sup> In fact, RE<sup>3+</sup> transitions have clearly pronounced Stark splitting when doped in the LiYF<sub>4</sub> host, due to the high crystal field strength exerted on the dopants, and can be easily spectrally resolved for nanothermometry via emissions between different Stark sub-levels.<sup>[226]</sup>

In the decoupled theranostics RENPs, the fine structure of the <sup>4</sup>F<sub>3/2</sub> → <sup>4</sup>I<sub>11/2</sub> transition can be clearly discriminated at ambient temperatures (Figure 6.5A, B). Under thermal fluctuation, the absolute intensity of the Nd<sup>3+</sup> <sup>4</sup>F<sub>3/2</sub> → <sup>4</sup>I<sub>11/2</sub> transition remained nearly constant; however, relative changes in the intensity of its Stark components could be observed. Most notably, the R<sub>2</sub> (<sup>4</sup>F<sub>3/2</sub>) → Y<sub>1</sub> (<sup>4</sup>I<sub>11/2</sub>) (~1046 nm) and R<sub>1</sub> (<sup>4</sup>F<sub>3/2</sub>) → Y<sub>2</sub> (<sup>4</sup>I<sub>11/2</sub>) (~1057 nm) transitions showed inverse change towards one another (Figure 6.5A). At elevated temperatures, the intensity of the R<sub>2</sub> → Y<sub>1</sub> band increased while the R<sub>1</sub> → Y<sub>2</sub> band decreased, indicating that the R<sub>2</sub> and R<sub>1</sub> sub-levels

are thermally coupled. The LIR thermometric parameter  $\Delta$  between these two Stark components showed a linear trend with respect to temperature change in the 20–50 °C range (Figure 6.5C). The relative thermal sensitivity  $S_r$  was around 0.22 %·°C<sup>-1</sup> at room temperature (Figure 6.5D), which was on par to other reports on the Nd<sup>3+</sup> <sup>4</sup>F<sub>3/2</sub> → <sup>4</sup>I<sub>11/2</sub> single-band nanothermometry, and highest among the fluoride based hosts. The temperature uncertainty  $\delta T$  was around 1 °C, and temperature read-out repeatability,  $R \sim 99\%$  (see appendix IV).

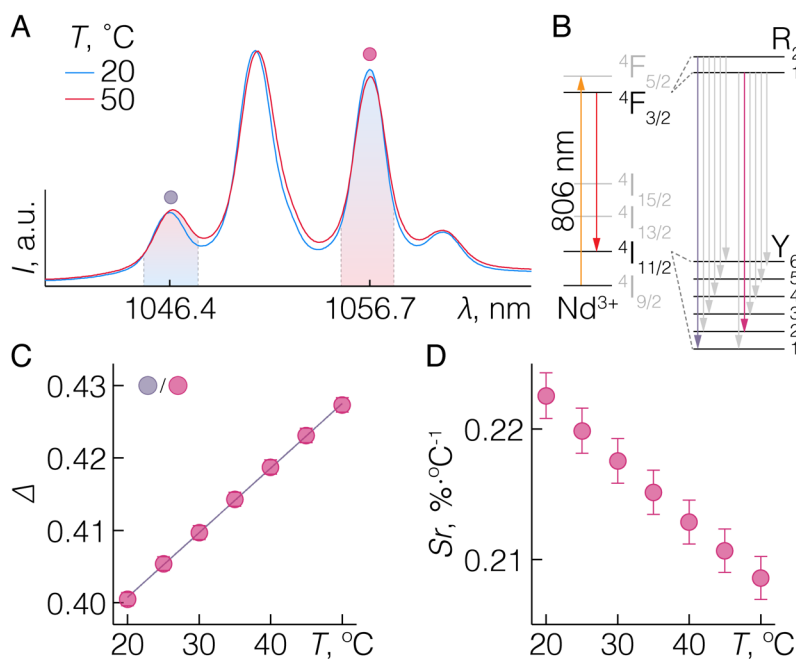


**Figure 6.5. NIR nanothermometry with decoupled theranostics RENPs.**

**A** – DS emission spectra of the <sup>4</sup>F<sub>3/2</sub> → <sup>4</sup>I<sub>11/2</sub> transitions of the decoupled theranostic RENPs under 806 nm excitation (~140 W/cm<sup>2</sup>). Dots above emission bands around 1046 and 1065 nm, correspond to R<sub>2</sub> → Y<sub>1</sub> and R<sub>1</sub> → Y<sub>2</sub> transitions, respectively, used to define LIR thermometric parameter  $\Delta$ . **B** – Simplified energy level scheme of Nd<sup>3+</sup> with blown-up view of the inter Stark transitions between the <sup>4</sup>F<sub>3/2</sub> and <sup>4</sup>I<sub>11/2</sub> energy levels. **C** –  $\Delta$  and **D** –  $S_r$  change with temperature.

Furthermore, a proof-of-concept experiment was conducted by placing a water dispersion of RENPs under continuous 806 nm excitation (140 W/cm<sup>2</sup>), followed by periods of 980 nm excitation (140, 320, and 620 W/cm<sup>2</sup>). Both beams were superimposed within a 400 μm focal point within a 1 cm optical path glass cuvette. The RENPs' optical response was simultaneously recorded in the visible (UC emission) and NIR (DS emission) spectral regions, accessing the local temperature information from the latter (Figure 6.5). Excited only by the 806 nm radiation, RENPs showed neither significant temperature variation (Figure 6.6 –  $\Delta T$ ) nor any UC emission (UV-blue integrated intensity, Figure 6.6 –  $I_{UC}$ ). Once the 980 nm irradiation was turned ON, it prompted the appearance of the UC emission and a steady temperature increase. A change in temperature as high as 35 °C was reached under the largest power density tested (620 W/cm<sup>2</sup>),

meaning that if uncontrolled, 980 nm irradiation can greatly overheat the biological tissues. Also, since non-radiative quenching amplifies at higher temperatures,<sup>[33]</sup> the UC emission intensity from the  $Tm^{3+}$  decreased as the temperature increased, with a drop as large as 30%. Such a large quenching of UC emission intensity would also adversely affect its use for therapeutic purposes. When the 980 nm laser was turned OFF, the UC emission vanished instantaneously and the temperature in the vicinity of the RENPs rapidly returned to the initial value. The total DS emission intensity of the  $Nd^{3+} \ ^4F_{3/2} \rightarrow \ ^4I_{11/2}$  transition (Figure 6.6 –  $I_{DS}$ ) did not change significantly throughout the multiple heating-cooling cycles. It can be seen that the integrated nanothermometric capabilities of decoupled theranostics RENPs, under the 806 nm excitation, provide a means to observe the temperature offset caused by the 980 nm irradiation. This built-in temperature monitoring tool is useful to adjust the intensity of the 980 nm excitation in real time, thus minimizing photothermal damage to healthy tissues and ensuring a continuous supply of UC emission, which in turn helps to maintain consistent therapeutic effect, i.e. properly dosed ROS generation during the PDT.

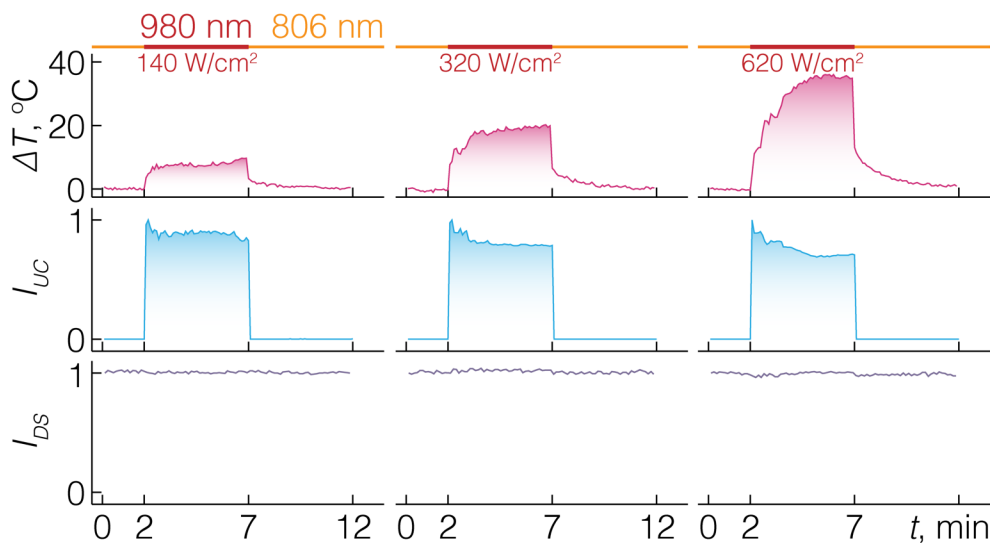


**Figure 6.6. Measuring transient temperatures with decoupled theranostics RENPs.**

Real-time temperature measurement in the vicinity of decoupled theranostics RENPs, continuously excited with 806 nm ( $\sim 140 \text{ W/cm}^2$ ) radiation, and periodically with that of 980 nm at  $\sim 140$ , 320, and  $620 \text{ W/cm}^2$ . Temperature change ( $\Delta T$ ), UV-blue integrated UC emission intensity ( $I_{UC}$ ), and integrated DS emission intensity ( $I_{DS}$ ) were monitored during the experiment. The UC and DS emission intensities are 0–1 normalized.

#### 6.4 RENPs-Ce<sub>6</sub> and *in vitro* characterization

To demonstrate the on-demand functionality of the decoupled theranostic RENPs, the therapeutic modality was brought forth by preparing a RENPs-Ce<sub>6</sub> complex (as described in chapter 4) to generate ROS under 980 nm excitation.

Prior to exploring the therapeutic action of RENPs-Ce<sub>6</sub>, RENPs' accumulation and cytotoxicity in cells, as well as ROS generation in solution were examined. The dark cytotoxicity (in the absence of NIR excitation) of RENPs and RENPs-Ce<sub>6</sub> was studied towards MDA-MB-231 and MCF-7 breast cancer cells (Figure 6.7). The two cell lines with different tumorigenicity were chosen to screen the biocompatibility and PDT effect of the RENPs on a broader range of cancer cells; in fact, MDA-MB-231 cells are more resistant to treatment and exhibit properties of cancer stem-like cells.<sup>[227]</sup> Neither RENPs alone nor RENPs-Ce<sub>6</sub> significantly decreased the MCF-7 cells viability after 24 h of incubation. Despite the 5% drop in a viability observed for MDA-MD-231 cells in all groups, RENPs and RENPs-Ce<sub>6</sub> could be still considered non-toxic.

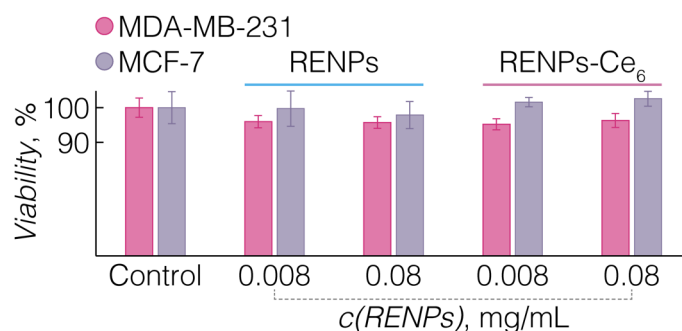


**Figure 6.7. Evaluating cytotoxicity of decoupled theranostic RENPs.**

**Viability of MDA-MB-231 and MCF-7 breast cancer cells incubated at different concentrations of RENPs and RENPs-Ce<sub>6</sub> complex for 24 h.**

Subsequently, accumulation of RENPs and RENPs-Ce<sub>6</sub> complex was studied in 2D cell cultures (Figure 6.8). Both RENPs and RENPs-Ce<sub>6</sub> were found to reside in the MDA-MB-231 and MCF-7 cells, even after the shortest studied incubation time points. No significant differences were observed between the accumulation of RENPs and RENPs-Ce<sub>6</sub> in the cells, however RENPs' photoluminescence signal in cells without Ce<sub>6</sub> appeared brighter. The UC emission of RENPs

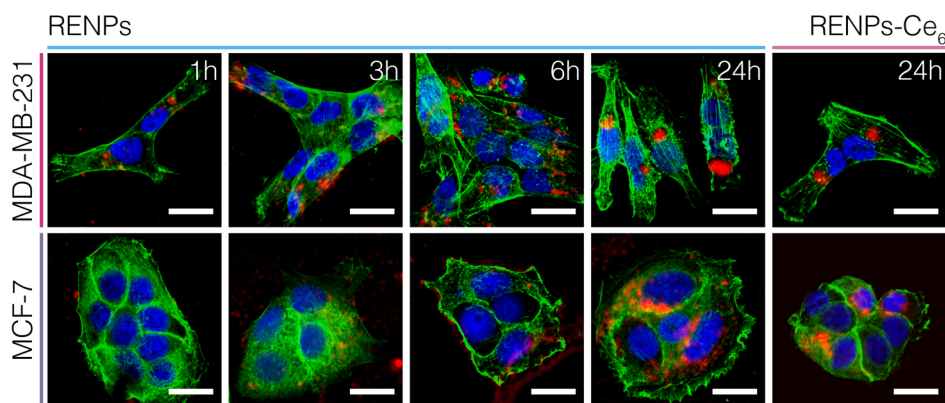


**Figure 6.8. Decoupled theranostic RENPs inside cancer cells.**

**Confocal fluorescence microscopy images of MDA-MB-231 and MCF-7 cells after 1, 3, 6, and 24 h of incubation with RENPs and after 24 h of incubation with RENPs-Ce<sub>6</sub> complex. UC signal is red. Cell nuclei are stained with Hoechst (blue) and filamentous actin with Phalloidin-Alexa 488 (green). Scale bar 20 μm.**

was coming from the intracellular region, suggesting that they were non-specifically internalized into the cells and concentrated within the cytoplasm and in the perinuclear region. No UC emission was collected from the cell nuclei. Both RENPs and RENPs-Ce<sub>6</sub> accumulated better in MDA-MB-231 cells, which can be attributed to the fact that MCF-7 cells tend to form colonies to the edges of which RENPs adhere, restricting their further internalization.

From the spectroscopic point of view, after RENPs-Ce<sub>6</sub> complex formation Tm<sup>3+</sup> UC emission bands around 350 and 650 nm were quenched by the Soret (405 nm) and Q(I) (654 nm) absorption bands of Ce<sub>6</sub>, respectively (Figure 6.9A). Which indicated that energy from RENPs to Ce<sub>6</sub> could be transferred in a radiative-manner, given the large separation between the Tm<sup>3+</sup> in the core and Ce<sub>6</sub> molecules present in the phospholipid coating of the RENPs at the surface. To affirm therapeutic potential of RENPs-Ce<sub>6</sub>, SOSG was used to measure the generation of ROS, namely singlet oxygen (<sup>1</sup>O<sub>2</sub>),<sup>[228]</sup> under 980 and 806 nm excitations. RENPs-Ce<sub>6</sub> complex, RENPs, or Ce<sub>6</sub> alone were irradiated with different laser dosages while keeping the temperature of the dispersions constant during the experiments, to eliminate any temperature-related false ROS readout. The photoluminescence intensity of SOSG was measured after each step of irradiation (Figure 6.9B). No changes in the photoluminescence intensity of SOSG were noticed in the Ce<sub>6</sub> sample irradiated at either of the excitation wavelengths, as well as for the RENPs or RENPs-Ce<sub>6</sub>, subjected to the diagnostic 806 nm radiation. A six-fold increase in the SOSG photoluminescence intensity was observed when pure RENPs were irradiated by 980 nm radiation. Possibly due to indirect excitation of the SOSG molecules by the UC emitted light, which could lead to photochemical changes in the sensor molecule,<sup>[229]</sup> or even ROS production by RENPs themselves.<sup>[116]</sup> More prominently, up to 15-fold increase in SOSG

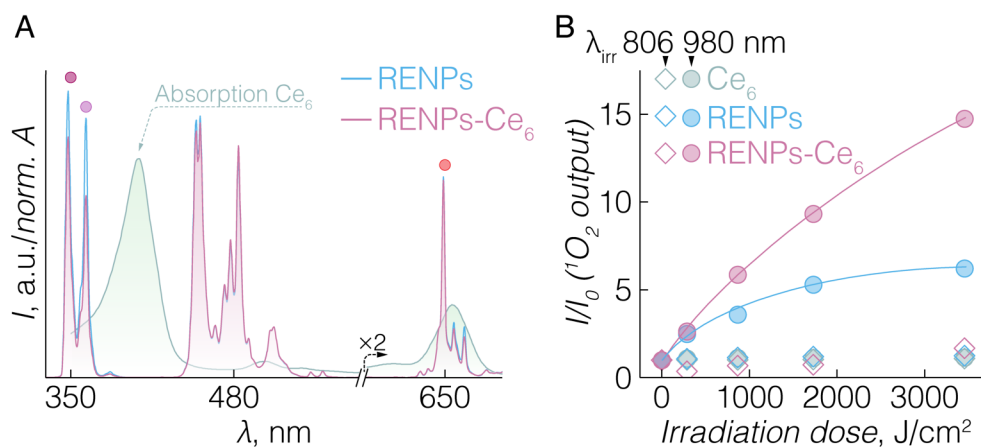


**Figure 6.9. Decoupled theranostic RENPs-Ce<sub>6</sub> complex.**

**A** – UC emission of RENPs under 980 nm excitation: alone (blue) and in the presence of Ce<sub>6</sub> (rose). Normalized absorption spectra of Ce<sub>6</sub> is also shown. The spectral range around <sup>1</sup>G<sub>4</sub> → <sup>3</sup>F<sub>4</sub> transition (~650) of Tm<sup>3+</sup> is blown-up twice for clarity. **B** - <sup>1</sup>O<sub>2</sub> production by Ce<sub>6</sub>, RENPs and RENPs-Ce<sub>6</sub> complex when excited by 806 or 980 nm radiation at various doses. Lines are guides to the eye.

photoluminescence intensity, and thus  $^1\text{O}_2$  output, was observed for the RENPs- $\text{Ce}_6$  complex excited with 980 nm. These results confirm that the UC emission is harnessed by the bound  $\text{Ce}_6$  molecules to trigger the PDT effect only when RENPs are excited with the therapeutic wavelength at 980 nm, and not the diagnostic one at 806 nm.

## 6.5 On-demand therapy

The on-demand PDT with the decoupled theranostics RENPs- $\text{Ce}_6$  complex was surveyed in the 2D cell cultures under 980 and 806 nm excitation (at  $0.5 \text{ W/cm}^2$ , equivalent to  $900 \text{ J/cm}^2$  over the irradiation period) using live/dead cell viability test (Figure 6.10). As a control, untreated cells and those incubated with  $\text{Ce}_6$  or RENPs alone were irradiated under the same conditions. From the visual inspection of cells, no damage was observed for the untreated cells, and cells treated with  $\text{Ce}_6$  or RENPs and irradiated with either of excitation wavelengths. Cells also appeared viable and morphologically unaffected when incubated with RENPs- $\text{Ce}_6$  and exposed to 806 nm radiation. Only when incubated with RENPs- $\text{Ce}_6$  complex and irradiated by 980 nm, significant number of dead cells could be observed. Even the live (green) cells showed deviations from

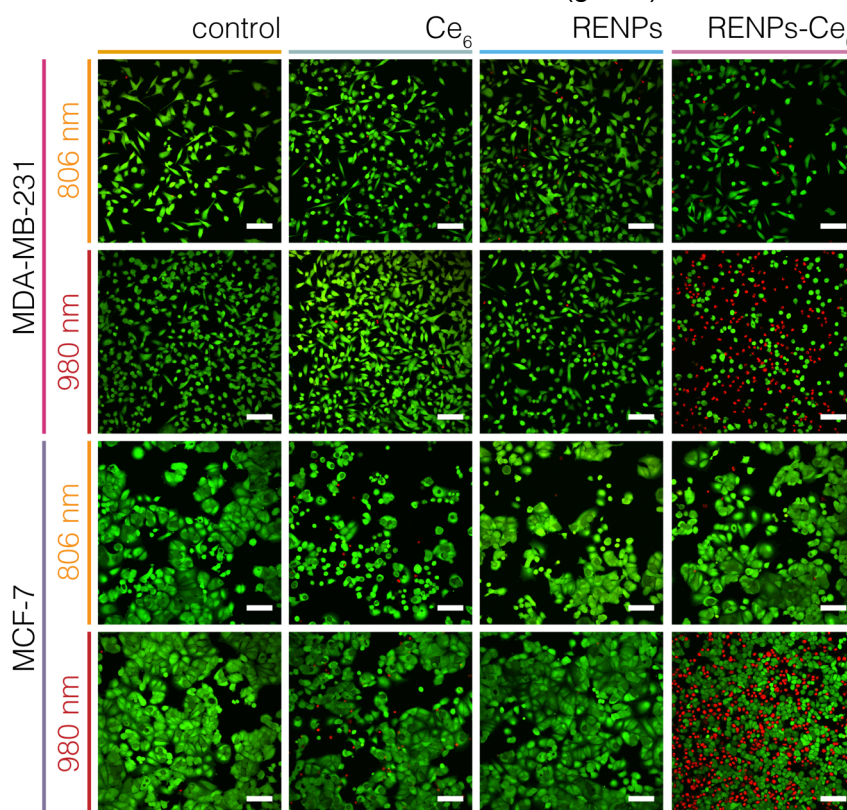


Figure 6.10. On-demand PDT with decoupled theranostics RENPs- $\text{Ce}_6$ .

Confocal fluorescence microscopy images of MDA-MB-231 and MCF-7 cells: untreated (control), incubated with  $\text{Ce}_6$  ( $10^{-5} \text{ M}$ ), RENPs (0.08 mg/mL), and RENPs- $\text{Ce}_6$  complex (0.08 mg/mL). After 24 h of incubation cells were irradiated either by 806 or 980 nm ( $900 \text{ J/cm}^2$ ) and treated with live/dead cell viability markers (green—alive, red—dead). Scale bar 100  $\mu\text{m}$

their normal morphology: MDA-MB-231 cells contracted to a more spherical shaped, instead of normally being elongated, while MCF-7 cells shrunk and their colonies broke apart. These changes indicate that, although marked alive, the normal functioning of these cells was modified and they possibly were entering into an apoptotic cycle. The live/dead cell count allowed to assess the decrease of the viable cell number quantitatively (Figure 6.11). After incubation with RENPs-Ce<sub>6</sub> and irradiation with 980 nm, only 45% and 61% of MDA-MB-231 and MCF-7 cells, respectively, remained alive.

In addition to 2D cell culture, the accumulation and PDT effect of RENPs and RENPs-Ce<sub>6</sub> was assessed in MDA-MB-231 3D cellular spheroids. Both RENPs and RENPs-Ce<sub>6</sub> accumulated in the spheroids, localizing at their periphery as far as the fourth to seventh cell layer, with no visible accumulation in the central part (Figure 6.12A). This is in line to what has been reported for quantum dots.<sup>[230]</sup> Similarly to 2D cultures, the cells exposed to RENPs remained alive after irradiation with both 980 and 806 nm (Figure 6.12B). 3D spheroid that had RENPs-Ce<sub>6</sub> complex and was irradiated with 806 nm, was not damage either. However, dead cells appeared after irradiation of a similar spheroid, containing RENPs-Ce<sub>6</sub>, with 980 nm. Cell death occurred only at the periphery, which is expected considering that the RENPs-Ce<sub>6</sub> complex accumulated only in this region. These results decisively show that on-demand production of <sup>1</sup>O<sub>2</sub> by RENPs-Ce<sub>6</sub> complex, and subsequent damage to cancer cells, is initiated only with the therapeutic 980 nm radiation, while exposure to 806 nm irradiation is therapy-free and could be safely used for diagnostic purposes.

## 6.6 Discussion

Overall, decoupled theranostics RENPs constitute a significant step forward towards the truly multifunctional nanoplatforms. It is important to stress that due to the modular design of RENPs,

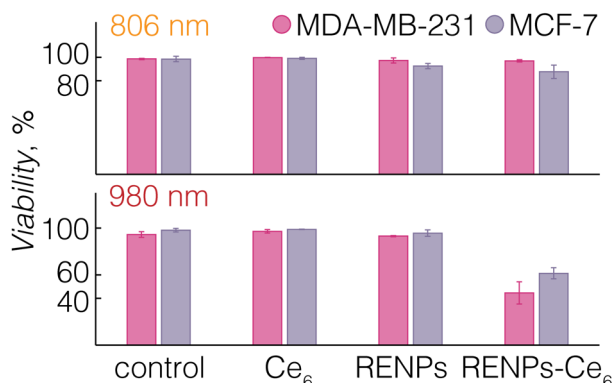


**Figure 6.11. Cell viability post PDT treatment with decoupled theranostics RENPs-Ce<sub>6</sub>.**

Count of live and dead cells represented in Figure 6.10, showing the viability of MDA-MB-231 and MCF-7 cells: untreated, and exposed to Ce<sub>6</sub>, RENPs, or RENPs-Ce<sub>6</sub> and irradiation with 806 nm 980 nm.

they can be easily engineered to obtain contrasting optical responses under orthogonal excitation. Here presented multilayered  $\text{LiYF}_4$  RENPs are fairly simple in their structure and synthesis, yet provide the exactly desired photoluminescence output in the UV/vis or NIR spectral ranges under 980 or 806 nm excitation, respectively. The individual spectral signatures of decoupled theranostics RENPs can then be used for on-demand therapy and diagnostics.

However further improvement of these decoupled theranostic RENPs in terms of their brightness, thermal sensitivity, and expansion of available emission bands is required prior to *in vivo* studies, and routine clinical and biomedical laboratory research of the distant future. Particularly pressing task is, how to combine and maintain all the high fidelity optical features of the decoupled theranostics RENPs in a smaller format? Here, the final size of RENPs was around 100 nm, while many innovative nanomedicines are adjusted towards 20-50 nm range to promote accumulation and retention of NPs in cells.<sup>[231]</sup> In line with this, the following chapter is focused on the minimization of  $\text{Li}^+$ -based RENPs without sacrificing their UC and DS emission intensities. Subsequently, decoupled theranostics RENPs are “deconstructed” and their individual parts (UC emission, nanothermometry) are optimized prior to reassembly in the form of 2<sup>nd</sup> generation decoupled theranostics RENPs.

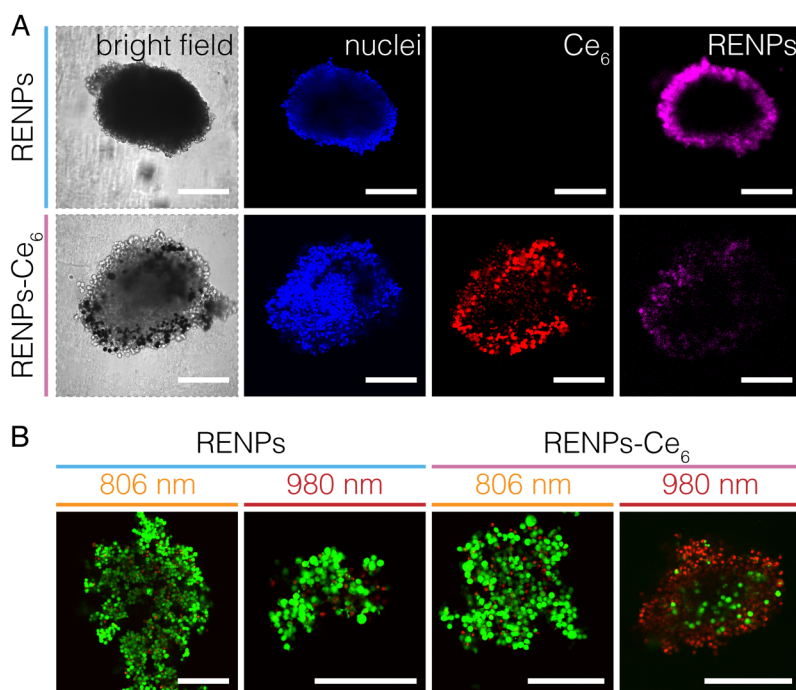


**Figure 6.12.** On-demand PDT with decoupled theranostics RENPs- $\text{Ce}_6$  in cancer spheroids.

**A** – Bright field and confocal fluorescence microscopy images of MDA-MB-231 cellular spheroids, incubated with RENPs (0.08 mg/mL), and RENPs- $\text{Ce}_6$  complex (0.08 mg/mL). **B** – Confocal fluorescence microscopy images of cellular spheroids after 24 h incubation with RENPs or RENPs- $\text{Ce}_6$  and subsequent irradiation with either 806 or 980 nm ( $900 \text{ J/cm}^2$ ). Cells were treated with live/dead cell viability markers to show alive (green) and dead (red) cells. Scale bar 200  $\mu\text{m}$ .

## 7 MINIATURIZATION OF Li<sup>+</sup>-BASED RENPs

---

In RENPs research, the desire to make nanostructures as small as possible, while at the same retaining their brightness, has kept material scientists occupied since the very first reports. The low number of optically active dopants and large surface-to-volume ratio of very small RENPs (5-10 nm) often render them unsuitable for biomedical research as their emission is just too dim. The core/shell strategies are thus employed to make RENPs brighter at the expense of increasing their size, which is typically acceptable if contained within the 20-50 nm range, imposed by the studies on size-dependent internalization of RENPs in cells.<sup>[231,232]</sup> Bright Na<sup>+</sup>-based RENPs, like those introduced in chapters 3-5, can be easily synthesized to fit within this size range. However, when it comes to Li<sup>+</sup>-based RENPs, that provide much greater crystal field-induced Stark splitting of the RE<sup>3+</sup> energy levels and are arguably most efficient hosts to upconvert NIR irradiation to UV emission, there is no clear direction on how to synthesize these RENPs small enough to fit in the outlined 20-50 nm size range. Even though such small Li<sup>+</sup>-based RENPs have been reported, the robustness of therein employed synthesis protocols does not allow for controlled core/shell engineering, or to make RENPs that could reach the lower, 20 nm, limit of the imposed size range (see below).<sup>[233]</sup>

In chapter 6, core-only RENPs have been synthesized with the help of OM as coordinating ligands alongside OA. This effectively reduced the size of LiYF<sub>4</sub> RENPs by 20-30% with respect to the originally reported protocol.<sup>[49]</sup> It seems that introduction of OM in the reaction mixture might prove to be a viable strategy to prepare small Li<sup>+</sup>-based RENPs, however, what are the limitations of this approach and whether it can be successfully applied towards core/shell engineering of decoupled theranostics RENPs remained unknown.

*This study was carried out jointly with Dr. Ting Cheng and Dr. Riccardo Marin. Dr. Cheng has performed most of the syntheses of RENPs and TEM imaging. Dr. Marin has spurred the idea of using OM in the synthesis protocol of LiYF<sub>4</sub> RENPs and performed XRD analysis.*

*Herein results were published as: “Small and Bright Lithium-Based Upconverting Nanoparticles” T. Cheng,\* R. Marin,\* A. Skripka\* and F. Vetrone, J. Am. Chem. Soc., 140 (40), 12890–12899, 2018. \*equally contributing authors.*

## 7.1 Size of RENPs vs OM/OA ratio

To explore the size tuning possibilities by introducing OM in the reaction mixture,  $\text{LiYF}_4$ : 0.5 mol%  $\text{Tm}^{3+}$ , 25 mol%  $\text{Yb}^{3+}$  RENPs were synthesized at various OM/OA ratios following heat-up or hot-injection thermal decomposition methods.

In a heat-up approach, 2.5 mmol each of Li-TFA and Y/Tm/Yb-TFA precursors were degassed and dissolved in a mixture of 20 mL each of (OA+OM) and ODE at 110 °C under vacuum and magnetic stirring. The flask was then backfilled with argon and the temperature was increased to 330 °C. After 1 h of reaction time, the mixture was cooled down to RT, RENPs were washed, and dispersed in hexane for further morphological and spectral characterization.

Different RENPs were made by substituting part of the OA content with OM – 0 to 50 vol%. From the TEM analysis the size of the RENPs was seen to decrease from ~90 to ~5 nm, with the increasing volume fraction of OM in the reaction mixture (Figure 7.1A). Using solely OA as the ligand, the largest RENPs were formed with the size of 92 x 55 nm along their respective major x minor axes. Increasing the OM content from 0 to 35 vol%, the RNP size decreased gradually down to 42 x 34 nm, still retaining the bi-pyramidal morphology characteristic of  $\text{LiYF}_4$ . Instead, once OM content was increased to 40 vol%, almost spherical RENPs as small as 5 nm were obtained. It is evident that greater volumes of OM lead to the preparation of smaller

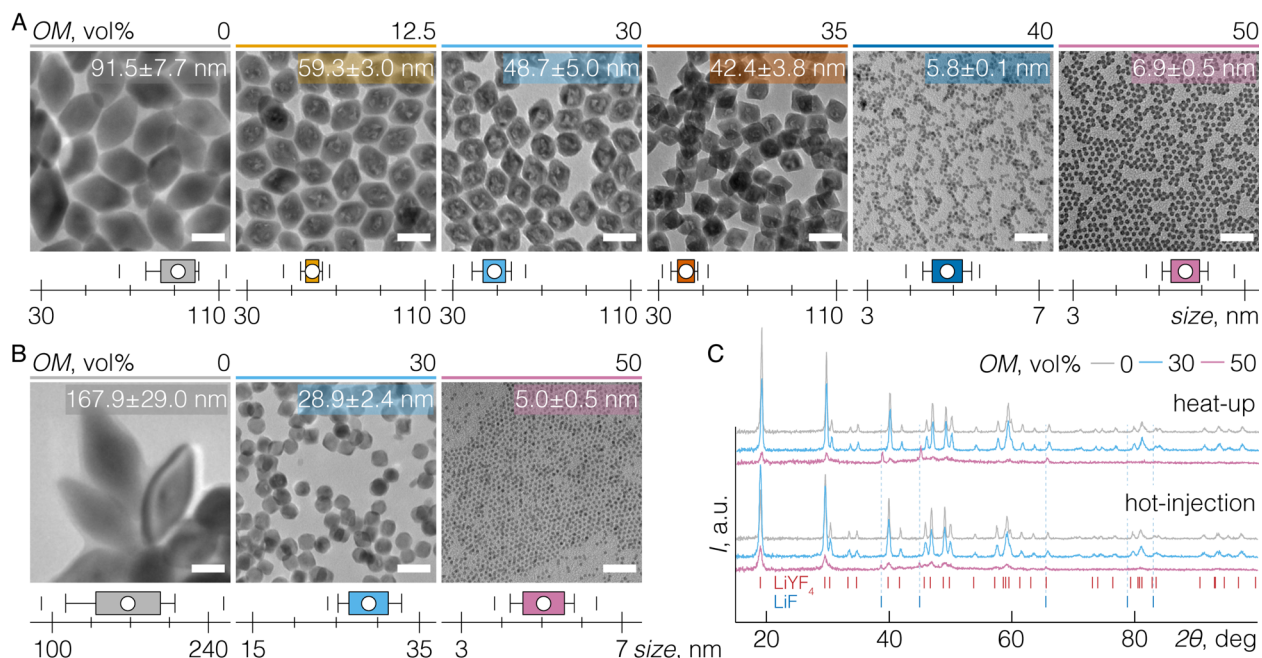


**Figure 7.1. Structural characterization of  $\text{LiYF}_4$ : $\text{Tm}^{3+}$ ,  $\text{Yb}^{3+}$  RENPs synthesized in the presence of OM.**

**A and B** – TEM images of  $\text{LiYF}_4$ : $\text{Tm}^{3+}$ ,  $\text{Yb}^{3+}$  RENPs and their size distributions (along major axis), synthesized via heat-up (A) or hot-injection (B) approaches, at various amounts of OM in the reaction. Scale bar 50 nm. Box plots indicate: mean value (dot), SD (box outline), 5<sup>th</sup> and 95<sup>th</sup> percentiles (whiskers), and maximum/minimum values (dashes). **C** – Representative XRD patterns of RENPs synthesized in the presence of 0, 30 and 50 vol% of OM in the reaction. Reference patterns of  $\text{LiYF}_4$  and  $\text{LiF}$  are also shown.

RENPs. A similar trend in size change was obtained when RENPs were synthesized via the hot-injection approach (Figure 7.1B). In this case, 2.5 mmol each of Li-TFA and Y/Tm/Yb-TFA were dissolved and degassed in 6 mL each of (OA+OM) and ODE (solution B). Solution B was then injected (1.5 mL/min) into solution A, containing 14 mL each of (OA+OM) and ODE at 330 °C. ODE/OA/OM proportions were the same in both solutions (A and B). After 1 h of reaction, the mixture was cooled down and treated identically to that prepared via the heat-up approach.

Changes in the size of the RENPs correlated with the XRD analysis in the case of heat-up and hot-injection synthesis methods (Figure 7.1C). All RENPs had a tetragonal *I*41/a crystal phase (PDF #01-077-0816). In the case of 50 vol% OM syntheses, presence of diffraction peaks attributable to LiF was also observed. The crystallite size estimated from the Rietveld refinement of the XRD patterns followed the trend previously observed with the TEM. For 0, 12.5 and 30 vol% OM syntheses, RENPs sizes were estimated to be 77, 66 and 59 nm, respectively. However, the smaller RENPs (synthesized in the presence of 40 and 50 vol% of OM) displayed rather weak and broad reflections, as expected from RENPs of this size, where the disorder/defects in the crystal lattice are large. This made it impossible to reliably fit the experimental data using the Rietveld approach.

Stemming from these observations, the following interpretation of the OA and OM role in the growth of the RENPs is given. The carboxylic group of OA can be deprotonated, thus yielding metal-oleates upon interaction with the RE<sup>3+</sup> ions. This interaction is both electrostatic and via the lone electron pairs featured by the oxygens of the carboxylic group. In the case of OM, the ligand molecules can interact with RE<sup>3+</sup> only via the lone electron pair on the nitrogen of the primary amine group. The amine group of OM can also be protonated, making the interaction with the metal ions less likely because of the electrostatic repulsion. Clearly that implies that the interaction of OM with RE<sup>3+</sup> is weaker than the one with OA. In that respect, the OM-RE adduct is less stable than OA-RE one, and the decomposition rate of the former is expected to be greater. For the sake of the discussion, OM- and OA-containing adducts are simply referred to as OM-RE and OA-RE, respectively, but it is implied that trifluoroacetate molecules also compose these precursors. It is also understood that OA and OM adducts with RE<sup>3+</sup> are indeed more complex species where the ligand molecules dynamically enter the coordination sphere of the metal ions along with trifluoroacetate anions.

Overall, OM-RE are the nucleation-favoring species that can quickly provide RE-F building blocks, while OA-RE are growth-favoring species and act as a reservoir of precursors that are consumed more slowly. The unstable OM coordination with metal-TFA leads to an increased

nucleation rate and a faster depletion of the monomer reservoir. Indeed, as observed from the thermal decomposition results, continuous growth of the RENPs and thus larger sizes are obtained when OA constitutes the major part of the reaction mixture. Instead, a higher number of nuclei are formed in the case of 40 and 50 vol% of OM, preventing further growth of the RENPs. Additionally, the size disparity between RENPs synthesized with 35 or 40 vol% of OM indicates of an existence of a critical point in balancing the nucleation and growth process of RENPs fostered by OM and OA, respectively. More than 35 vol% OM in the reaction mixture induces the depletion of the metal adducts reservoir, forming small nuclei. In these conditions, the ripening and size increase for the first nuclei formed is hindered due to the restrained availability of the OA and corresponding OA-RE species. Indeed, observed tendencies are analogous to those reported for  $\text{Na}^+$ -based RENPs, where the alpha-to-beta phase transition is restricted by high content of OM in the reaction.<sup>[42]</sup>

Following structural characterization, UC emission spectra of RENPs was measured under NIR irradiation. Upon 980 nm excitation, multiple emission peaks spanning the optical spectrum from UV to NIR could be seen to originate from these RENPs (Figure 7.2).  $\text{Tm}^{3+}$  UC emission bands were located at around 340 ( $^1\text{I}_6 \rightarrow ^3\text{F}_4$ ), 360, ( $^1\text{D}_2 \rightarrow ^3\text{H}_6$ ), 450 ( $^1\text{D}_2 \rightarrow ^3\text{F}_4$ ), 480 ( $^1\text{G}_4 \rightarrow ^3\text{H}_6$ ), 510 ( $^1\text{D}_2 \rightarrow ^3\text{H}_5$ ), 650 ( $^1\text{G}_4 \rightarrow ^3\text{F}_4$ ), and 790 nm ( $^3\text{H}_4 \rightarrow ^3\text{H}_6$ ). Peak positions corresponded with the radiative transitions identified in the previous chapter (figures 6.2 and 6.3). The different sizes of the RENPs synthesized by varying the volume fraction of OM also correlated with the intensity of their upconversion spectrum. Note, all upconversion spectra were adjusted to represent the same number of RENPs per unit volume in the dispersion, which varies for different sized RENPs in the same m/v concentration. The number of RENPs was estimated considering their crystalline phase, physical dimensions and material density properties. The intensity of the UC emission gradually decreased with the reduction of the RENPs' size from around 90 (0 vol%

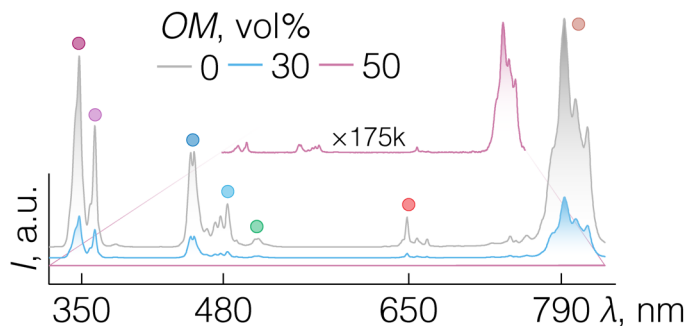


Figure 7.2. UC of  $\text{LiYF}_4:\text{Tm}^{3+}, \text{Yb}^{3+}$  RENPs synthesized in the presence of OM.

UC emission spectra of  $\text{LiYF}_4:\text{Tm}^{3+}, \text{Yb}^{3+}$  RENPs synthesized via heat-up approach in the presence of 0, 30 and 50 vol% of OM. Spectrum of RENPs synthesized with 50 vol% of OM is multiplied 175k times for clarity. Excitation power density  $\sim 346 \text{ W/cm}^2$ . Dots above each emission band are color-coded with radiative transitions summarized in Figure 6.3.

OM) to 50 (30 vol% OM) nm. Meanwhile, sub-10 nm RENPs (50 vol% OM) barely featured any UC emission due to the high surface-to-volume ratio that leads to a prominent surface defect, capping ligand, and solvent quenching. Moreover, presence of LiF (observed from XRD analysis) implied poor crystallinity of sub-10 nm RENPs which can also adversely impact UC emission intensity. Spectrum of these small RENPs featured mostly NIR emission, which dominated over higher-order upconversion processes responsible for NIR excitation upconversion to UV/blue emission.

## 7.2 Uncontrolled shell growth

In order to overcome the dim emission of sub-10 nm RENPs, an optically inert shell was grown over the core RENPs. However, prior to shell formation, the RENP composition was changed from  $\text{LiYF}_4:\text{Tm}^{3+}, \text{Yb}^{3+}$  to  $\text{LiYbF}_4:\text{Tm}^{3+}$ . The pure  $\text{LiYbF}_4$  host, compared to  $\text{Yb}^{3+}$  doping, was selected to enhance the overall 980 nm radiation harvesting, as more sensitizer ions ( $\text{Yb}^{3+}$ ) are available to collect the excitation energy and funnel it to the activator –  $\text{Tm}^{3+}$ .<sup>[54, 234, 235]</sup> Although initial doping optimization have indicated that more than 25 mol% of  $\text{Yb}^{3+}$  doping results in severe upconversion emission quenching,<sup>[49]</sup> recent studies have demonstrated that, once passivated by an inert shell, the  $\text{RE}^{3+}$  cation lattice sites of the RENPs core can be entirely occupied by the sensitizer ions.<sup>[236]</sup> As shown by Johnson et al.,<sup>[60]</sup> inert shell neutralizes the coupling between the UC emission concentration quenching and the deactivation of the  $\text{RE}^{3+}$  excited states by surface defects and vibrational modes of ligand and solvent molecules. This phenomenon is precisely valid for  $\text{Er}^{3+}$ - or  $\text{Yb}^{3+}$ -based RENPs; yet, as seen in chapter 3, concentration quenching in  $\text{Nd}^{3+}$ -doped RENPs remains relevant despite inert shell growth. Overall, the use of the active-core/passive-shell type RENPs allows exploiting pure sensitizer-type hosts like  $\text{LiYbF}_4$  or  $\text{NaYbF}_4$ , simultaneously minimizing the surface quenching and maximizing excitation light absorption, ultimately leading to brighter UC emission. Ideally, growing thicker shells ensures a higher emission intensity, but at the same time increases the overall size of the RENPs. Therefore, it is desirable to be able to precisely optimize the UC emission intensity vs the size of RENPs, tailoring them to the specific applications sought after.

The  $\text{LiYbF}_4: 0.5 \text{ mol\% Tm}^{3+}$  core-only RENPs were prepared via hot-injection approach in the presence of 50 vol% of OM in the reaction, as described above. 0.1 mmol of as-synthesized core material (~1.5 mL) was then subjected to shelling with a layer of  $\text{LiYF}_4$ . Equal parts of OA and ODE were added to the 0.1 mmol of core RENPs up to a total volume of 20 mL (solution A), obtaining almost pure OA/ODE mixture as OM was severely diluted. Solution B consisted of 0.2

mmol each of Li-TFA and Y-TFA precursors in 10 mL each of OA and ODE. Both solutions were stirred and degassed under vacuum at 110 °C for 30 min. Backfilled with argon, the temperature of solution A was raised to 315 °C, and solution B was injected into solution A at a 1.5 mL/min rate. After completing the injection, the mixture was kept at 315 °C for 30 min. Subsequent steps included cooling, washing and characterization, as already described.

Following this standard core/shell synthesis protocol, the size of RENPs more than doubled after the addition of precursors forming  $\text{LiYF}_4$  shell (Figure 7.3A), which was unexpected considering the relatively little amount of injected precursor material. Ideally, the size of the RENPs after the shelling procedure can be estimated with the assumption that the influence of cation intermixing at the core/shell interface is negligible.<sup>[237]</sup> The size of  $\text{LiYbF}_4:\text{Tm}^{3+}/\text{LiYF}_4$  core/shell RENPs should thus stoichiometrically correlate with the material added, considering the geometry and size of RENPs, and molecular weight and density of the materials employed. To better understand what has happened during the core/shell synthesis, various approaches of shell precursor injection were systematically investigated: i) injecting shell precursors dissolved in OA/ODE into cores dispersed in OA/ODE (the above protocol), ii) injecting shell precursors dissolved in OA/ODE into cores dispersed in OA/OM/ODE, and iii) injecting the shell precursors dissolved in OA/OM/ODE into cores dispersed in OA/OM/ODE. Several injections steps were carried out for every condition, at each step 0.1 mmol of shelling precursors were added.

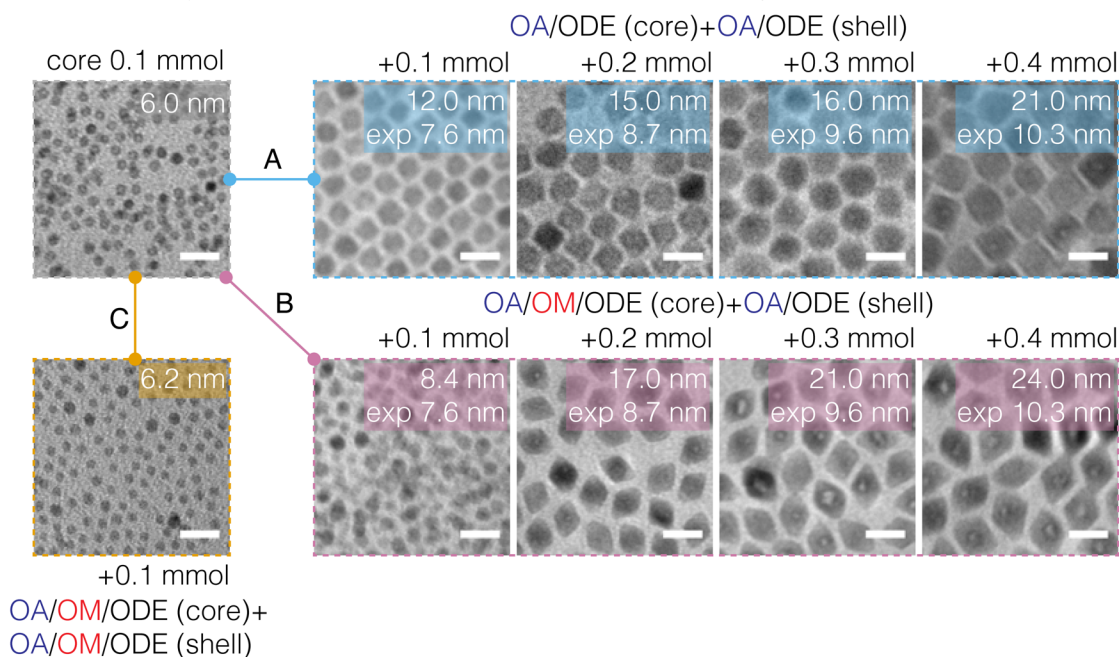


**Figure 7.3. Uncontrolled shelling of  $\text{LiYbF}_4:\text{Tm}^{3+}$  RENPs.**

Representative TEM images  $\text{LiYbF}_4:\text{Tm}^{3+}$  core RENPs before and after the  $\text{LiYF}_4$  shelling, following different protocols and adding increasing amount of shell precursors. A – shell precursors in OA/ODE are injected into cores in OA/ODE. B – shell precursors in OA/ODE are injected into cores in OA/OM/ODE. C – shell precursors in OA/OM/ODE are injected into cores in OA/OM/ODE. Scale bar 20 nm.

All of the shelling approaches have led to an uncontrolled shell growth, indicated by increased shell thickness, uncorrelated to the amount of shell precursors added (Figure 7.3 insets indicate the measured and expected, “exp”, size of the RENPs). Intriguingly, the unexpected size increase correlated with the amount of the OA present in the reaction mixture. The uncontrolled growth of the RENPs was observed immediately after the injection of shell precursors dissolved in OA/ODE into core RENPs also dispersed in an OA/ODE mixture (Figure 7.3A), while the same effect was noticeable only after the second shell injection in the case of OA/OM/ODE dispersed cores (Figure 7.3B). For both OA/OM/ODE dispersed cores and shelling precursors, no change in the size of original RENPs was observed, while secondary population of slightly smaller RENPs has appeared (Figure 7.3C). Similar disproportionate shelling of Li<sup>+</sup>-based RENPs has been observed before,<sup>[233]</sup> and although uncontrolled shelling could still enhance the UC emission intensity it inhibits the photoluminescence vs size optimization of RENPs and the creation of multi-shell nanostructures in a controlled and deliberate manner.

Following these initial observations, few pivotal conclusions could be drawn. First, the presence of OM inhibits the shell growth and fosters the appearance of a secondary RNP population alongside the original cores of substantially unchanged size. Second, shell precursors dissolved in the presence of OA and added to the different dispersions of sub-10 nm core-only RENPs promote their coarsening and coalescence, leading to drastic size changes. It is also important to note that after an initial sudden size increase, subsequent addition of shell precursors results in more stoichiometrically correlated shell growth. Overall, it appears that the 5-6 nm core RENPs, obtained in the presence of high concentration of OM, are not thermodynamically stable and the injection of a ligand with stronger coordinating capability like OA can induce size focusing of the primary cores into slightly larger but thermodynamically stable species. Razgoniaeva et al. have also reported a similar behavior for quantum dots, observing that injecting pure coordinating ligands led to their size focusing.<sup>[238]</sup>

### 7.3 Stabilization protocol

The stabilization of as-synthesized sub-10 nm core RENPs was further explored by introducing fresh OA/ODE into the reaction mixture, without any shell forming precursors. In the following, the as-synthesized sub-10 nm RENPs, formed in OA/OM (v/v 1/1), are referred to as first nuclei. To distinguish from the core synthesis step, where vol% OM is used to illustrate OA/OM composition, here v/v ratio for OA/OM is used instead. In order to stabilize the first nuclei RENPs, a modified hot-injection approach was used. Solution A was prepared by mixing 0.5

mmol of the first nuclei with 12 mL of OA/OM (1/1 v/v) and 12 mL ODE. Solution B contained a 10 mL each of OA and ODE (1/1 v/v), or OM and ODE (1/1 v/v). Both solutions were stirred and degassed under vacuum at 110 °C for 30 min. Backfilled with argon, the temperature of solution A was raised and maintained at 315 °C for 30 min. Solution B was injected into solution A in two steps: for each step, 10 mL of solution B was injected at an injection rate of 1.5 mL/min, at time intervals of 40 min. After the annealing (stabilization), the mixture was cooled down and the majority of stabilized core RENPs was stored under argon atmosphere without washing for further shell growth. A small portion of stabilized core RENPs was washed for structural characterization.

The size focusing process of  $\text{LiYbF}_4:\text{Tm}^{3+}$  first nuclei by sequential injection of pure OA/ODE in the reaction flask can be directly observed with TEM imaging (Figure 7.4). Initially, the first nuclei have an average diameter of  $\sim 5.8$  nm, which is maintained after 30 min at 315 °C in a starting reaction mixture of OA/OM/ODE (v/v/v 1/1/2). Once first batch of precursor-free OA/ODE (v/v 1/1) mixture (10 mL) was injected in the dispersion of first nuclei, their size increased to  $9.4 \times 8.0$  nm and a bi-pyramidal morphology of RENPs emerged, typical of larger  $\text{LiREF}_4$  nanocrystals. Most importantly, a second injection of 10 mL of OA/ODE, which further changed the OA/OM volume ratio from 2/1 to 3/1, did not alter the size of RENPs, indicating that a stable configuration has been reached. On the basis of these findings, stabilization of  $\text{LiYF}_4:\text{Tm}^{3+}$ ,  $\text{Yb}^{3+}$  first nuclei (prepared in analogous way as  $\text{LiYbF}_4:\text{Tm}^{3+}$ ) was attempted by injecting fresh OA/ODE mixture (Figure 7.4). In this case, relatively large RENPs ( $\sim 20$  nm) were obtained after the first injection step, along with a fraction of smaller RENPs colony. Further addition of OA/ODE focused most of the RENPs to above-20 nm size. In both cases,

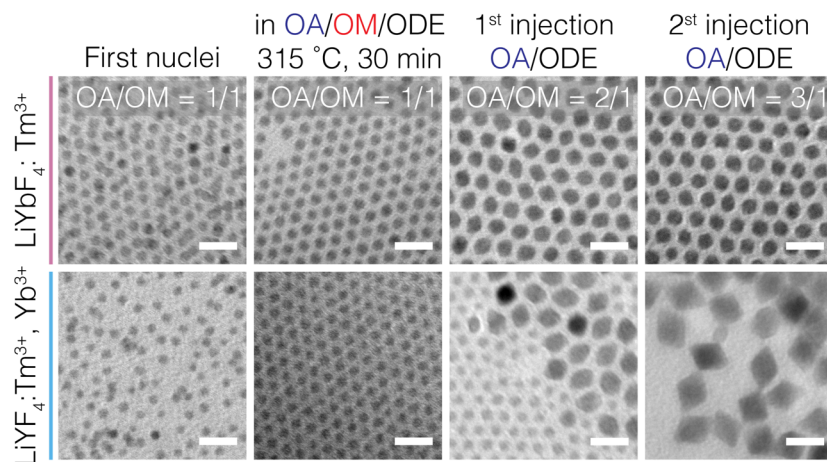


**Figure 7.4. Characterization of  $\text{LiYbF}_4:\text{Tm}^{3+}$  and  $\text{LiYF}_4:\text{Tm}^{3+}$ ,  $\text{Yb}^{3+}$  RENPs after OA treatment.**

TEM images  $\text{LiYbF}_4:\text{Tm}^{3+}$  and  $\text{LiYF}_4:\text{Tm}^{3+}$ ,  $\text{Yb}^{3+}$  RENPs as first nuclei and after 30 min of vigorous stirring at 315 °C in a mixture with 1/1 v/v ratio of OA/OM; as well as after step-wise introduction of fresh OA/ODE in the reaction mixture, changing OA/OM v/v ratio to 2/1 and 3/1. Scale bar 20 nm.

LiYbF<sub>4</sub>:Tm<sup>3+</sup> and LiYF<sub>4</sub>:Tm<sup>3+</sup>, Yb<sup>3+</sup>, the appearance of well-defined reflections in the XRD patterns of the stabilized cores confirmed the improved crystallinity and increased size of RENPs, compared to the first nuclei (Figure 7.5A). Furthermore, injecting fresh OM/ODE (v/v 1/1) into LiYbF<sub>4</sub>:Tm<sup>3+</sup> or LiYF<sub>4</sub>:Tm<sup>3+</sup>, Yb<sup>3+</sup> first nuclei mixtures had no effect on the RENPs shape or size, further attesting towards the necessity for a high affinity coordinating ligand like OA to drive the stabilization process (Figure 7.5B).

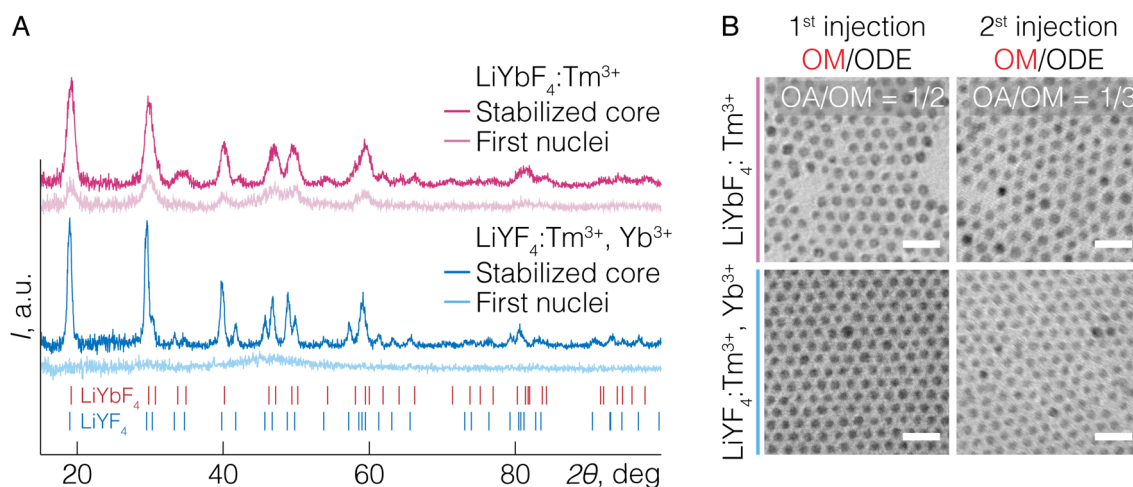


**Figure 7.5. Characterization of LiYbF<sub>4</sub>:Tm<sup>3+</sup> and LiYF<sub>4</sub>:Tm<sup>3+</sup>, Yb<sup>3+</sup> RENPs after OA (or OM) treatment.**

**A** – Representative XRD patterns of LiYbF<sub>4</sub>:Tm<sup>3+</sup> and LiYF<sub>4</sub>:Tm<sup>3+</sup>, Yb<sup>3+</sup> first nuclei and stabilized core RENPs. Reference patterns of LiYF<sub>4</sub> and LiYbF<sub>4</sub> are also shown. Scale bar 20 nm. **B** – TEM images LiYbF<sub>4</sub>:Tm<sup>3+</sup> and LiYF<sub>4</sub>:Tm<sup>3+</sup>, Yb<sup>3+</sup> RENPs after step-wise introduction of fresh OM/ODE in the reaction mixture, changing OA/OM v/v ratio to 1/2 and 1/3.

The robustness of OA-assisted LiYbF<sub>4</sub>:Tm<sup>3+</sup> first nuclei stabilization was further checked by extending the procedure time from 1 to 3 h, as well as dispersing the first nuclei in a fresh OA/ODE mixture (as in the case of heat-up RENPs synthesis) and subjecting the first nuclei to different stabilization temperatures, 270 to 330 °C (Figure 7.6). All but one of the investigated conditions led to the same final size (9.3–9.4 nm) of the stabilized RENPs. First nuclei stabilization at 270 °C resulted in no change in the RNP size as it remained below 5 nm, suggesting that higher temperatures are necessary to overcome the energy barrier for the first nuclei stabilization, i.e., ripening, to take place.

In order to rationalize the discrepancies observed in the first nuclei stabilization for the two compositions of RENPs, undoped LiYF<sub>4</sub> and LiYbF<sub>4</sub> first nuclei were prepared following the same core synthesis protocol and were subjected to stabilization procedure as above (Figure 7.7). Similar to LiYF<sub>4</sub>:Tm<sup>3+</sup>, Yb<sup>3+</sup>, pure LiYF<sub>4</sub> first nuclei continuously grew as OA/OM v/v ratio was increased, while, as in the case of LiYbF<sub>4</sub>:Tm<sup>3+</sup>, pure LiYbF<sub>4</sub> reached a stable core size of 9.3 x 7.8 nm immediately, without further size change. It can be inferred that LiYF<sub>4</sub>-based sub-

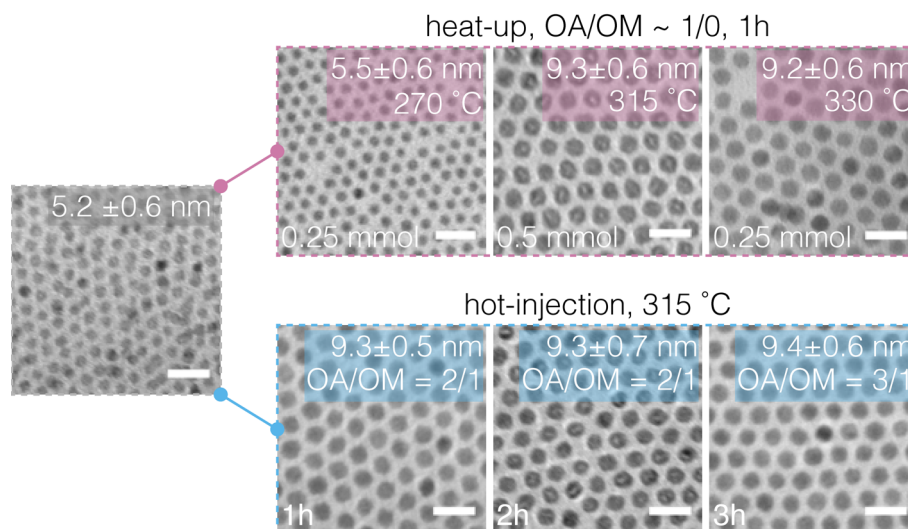


Figure 7.6.  $\text{LiYbF}_4:\text{Tm}^{3+}$  RENPs stabilized at various conditions.

TEM images of  $\text{LiYbF}_4:\text{Tm}^{3+}$  first nuclei before and after being subjected to the stabilization in the presence of fresh OA, following heat-up (top) or hot-injection (bottom) approaches. Different stabilization temperatures were studied in the heat-up scenario, while in the case of hot-injection stabilization time was extended from 1 to 3 h, and OA/OM v/v ratio was changed from 2/1 to 3/1 for the last hour of the procedure. Scale bar 20 nm.

10 nm core is thermodynamically unstable. The larger size of the  $\text{LiYF}_4$  RENPs can be attributed to the larger ionic radius of  $\text{Y}^{3+}$  ( $r = 115.9$  pm) compared with  $\text{Yb}^{3+}$  ( $r = 112.5$  pm).<sup>[43,239–241]</sup> Moreover, following the model proposed by Wang et al., it is possible that the increase in the surface electron charge density, provided here by  $\text{Yb}^{3+}$ , slows down the diffusion of  $\text{F}^-$  to the RENP's surface, hence rendering the stabilized  $\text{LiYbF}_4$  RENPs significantly smaller than those of  $\text{LiYF}_4$  composition. Given these observation, if small and bright UV emitting nanostructures are sought after,  $\text{LiYbF}_4$  is intrinsically better host not only due to increased sensitization of the upconversion processes, but also due to the added benefit of forming small and stable upconverting RENPs.

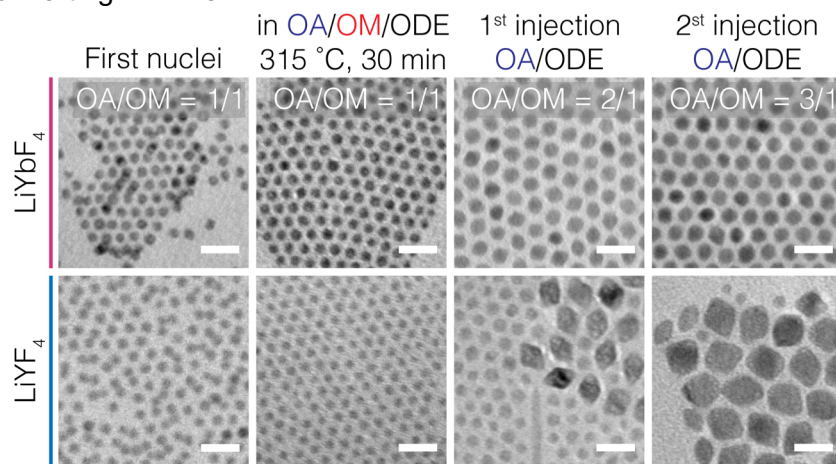
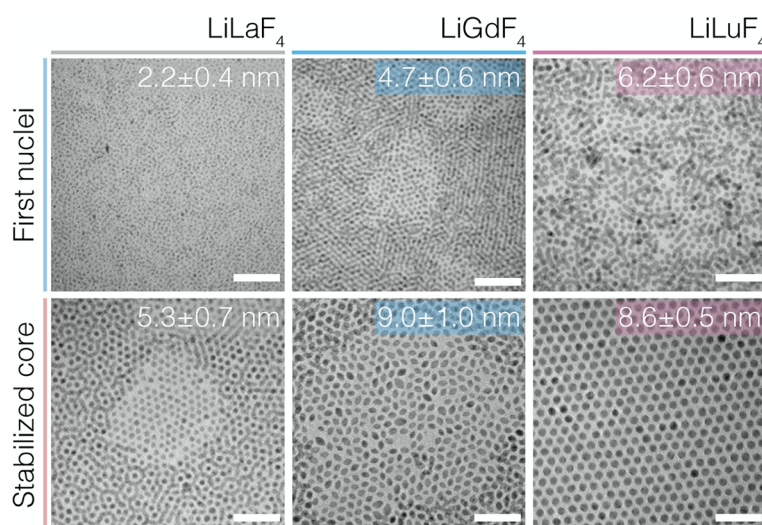


Figure 7.7. Characterization of  $\text{LiYbF}_4$  and  $\text{LiYF}_4$  RENPs after OA treatment.

TEM images  $\text{LiYbF}_4$  and  $\text{LiYF}_4$  RENPs as first nuclei and after 30 min of vigorous stirring at 315 °C in a mixture with 1/1 v/v ratio of OA/OM; as well as after step-wise introduction of fresh OA/ODE in the reaction mixture, changing OA/OM v/v ratio to 2/1 and 3/1. Scale bar 20 nm.

The first nuclei stabilization process in the presence of OA as coordinating species could be more generally extended to the synthesis of various small LiREF<sub>4</sub> host nanostructures, like LiLaF<sub>4</sub>, LiGdF<sub>4</sub> and LiLuF<sub>4</sub> RENPs (Figure 7.8). Notably, the size of the as-synthesized LiREF<sub>4</sub> (RE<sup>3+</sup> being La<sup>3+</sup>, Gd<sup>3+</sup>, Lu<sup>3+</sup>) first nuclei increased with RE<sup>3+</sup> atomic number. After the stabilization, LiLuF<sub>4</sub> displayed similar morphology and size as LiYbF<sub>4</sub>, whereas stabilized LiGdF<sub>4</sub> showed a morphology akin to LiYF<sub>4</sub>. LiLaF<sub>4</sub> RENPs were the smallest and mostly ill-shaped. Subsequently, LiREF<sub>4</sub> structures using all RE<sup>3+</sup> (lanthanide elements, Sc<sup>3+</sup>, and Y<sup>3+</sup>) were subjected to first nuclei synthesis and stabilization, showing distinct sizes and morphologies, which also depended on the stabilization temperature. These experiments and data interpretation are still ongoing, while the first nuclei stabilization approach has been already adapted to create libraries of LiYbF<sub>4</sub>, LiLuF<sub>4</sub> and LiErF<sub>4</sub> RENPs (see subsequent chapters).



**Figure 7.8. Characterization of LiLaF<sub>4</sub>, LiGdF<sub>4</sub> and LiLuF<sub>4</sub> RENPs after OA treatments.**

TEM images of LiLaF<sub>4</sub>, LiGdF<sub>4</sub> and LiLuF<sub>4</sub> RENPs as first nuclei and after heat-up stabilization in the presence of fresh OA at 315 °C for 1 h. Scale bar 50 nm.

## 7.4 Controlled shell growth

After obtaining stabilized LiYbF<sub>4</sub>:Tm<sup>3+</sup> core-only RENPs, possibility for controlled core/shell engineering was studied by growing optically active LiYbF<sub>4</sub> or passive LiYF<sub>4</sub> shells on the core RENPs (Figure 7.9A). Following a hot-injection protocol of shell growth, 0.2 mmol of desired shelling material was injected in a dispersion of stabilized cores (0.1 mmol), which lead to an increase in the size of RENPs from ~9 to ~14 nm. Similar final sizes of core/shell RENPs were obtain regardless of the type of precursors, as well-defined active-core/passive-shell or active-core/active-shell RENPs were formed. Importantly, size of core/shell RENPs matched well the expected 13.5 nm value, attesting to the controlled shell growth.

Steady-state photoluminescence measurements of these RENPs exemplified the function of an inert (optically passive) shell to suppress surface quenching and significantly enhance UC emission intensity (Figure 7.9B). The optical performance of 1 mg/mL dispersions of LiYbF<sub>4</sub>: 0.5 mol% Tm<sup>3+</sup> stabilized core, LiYbF<sub>4</sub>: 0.5 mol% Tm<sup>3+</sup>/LiYbF<sub>4</sub> and LiYbF<sub>4</sub>: 0.5 mol% Tm<sup>3+</sup>/LiYF<sub>4</sub> RENPs was compared under identical 980 nm laser irradiation conditions. When an active-shell was grown over the stabilized cores, UC emission intensity of LiYbF<sub>4</sub>:Tm<sup>3+</sup>/LiYbF<sub>4</sub> RENPs increased several times compared to the parent LiYbF<sub>4</sub>:Tm<sup>3+</sup> cores, primarily owing to the increased RENPs size and the larger number of available sensitizer ions. Nonetheless, since the energy migration to the surface was not mitigated, the overall UC emission intensity was still low and NIR emission at 790 nm remained dominant. A completely contrasting effect was observed when an inert shell was introduced. LiYbF<sub>4</sub>:Tm<sup>3+</sup>/LiYF<sub>4</sub> RENPs showed few orders of magnitude increase in the net UC emission intensity compared to the stabilized LiYbF<sub>4</sub>:Tm<sup>3+</sup> parent cores. Prominently, the LiYbF<sub>4</sub>:Tm<sup>3+</sup>/LiYF<sub>4</sub> RENPs displayed intense UC emission in the UV and blue spectral regions. The inert shell, acting as a barrier to limit energy loss to the surroundings, allows to funnel most of the Yb<sup>3+</sup>-gathered excitation energy to Tm<sup>3+</sup>, promoting higher order upconversion processes that are otherwise clearly observed only in above-50 nm LiYF<sub>4</sub>:Tm<sup>3+</sup>, Yb<sup>3+</sup> RENPs (Figure 7.2).

To optimize the UC emission intensity vs size of small core/shell RENPs, inert LiYF<sub>4</sub> shell of increasing thickness was formed around the LiYbF<sub>4</sub>:Tm<sup>3+</sup> core-only RENPs (Figure 7.10A).

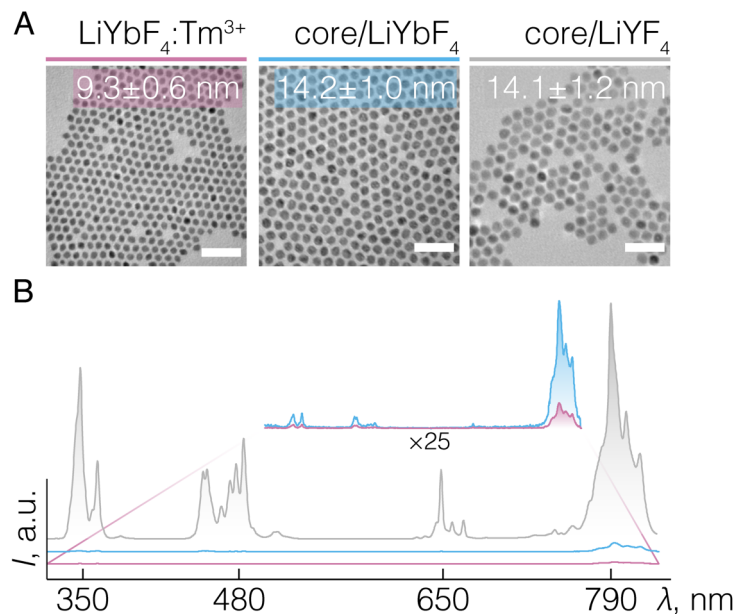


**Figure 7.9. LiYbF<sub>4</sub>:Tm<sup>3+</sup>/LiYbF<sub>4</sub> vs LiYbF<sub>4</sub>:Tm<sup>3+</sup>/LiYF<sub>4</sub> RENPs**

**A** – TEM images and **B** – UC emission spectra of LiYbF<sub>4</sub>:Tm<sup>3+</sup> core-only, core/LiYbF<sub>4</sub> and core/LiYF<sub>4</sub> core/shell RENPs. Scale bar 50 nm. Spectra of LiYbF<sub>4</sub>:Tm<sup>3+</sup> and LiYbF<sub>4</sub>:Tm<sup>3+</sup>/LiYbF<sub>4</sub> RENPs is multiplied 25 times for clarity. Excitation power density ~346 W/cm<sup>2</sup>. Spectra are color-coded with labels in A.

Following the hot-injection synthesis of core/shell RENPs, 0.2, 0.4, and 0.8 mmol of shell precursors were injected into the reaction mixture of stabilized cores (0.1 mmol), which resulted in the growth of 2, 4, and 5 nm-thick shells, respectively. The size of RENPs subsequently increased from 9.3 x 8.2 nm to 13.8 x 13.2, 17.7 x 16.7 and 19.6 x 19.5 nm. Vitally, the final size of core/shell RENPs was consistent, within the 10% margin, with the size estimated based on the amount of precursors injected (Figure 7.10A – the measured and expected, “exp”, size of the RENPs). These calculations were carried out neglecting cation intermixing at the core/shell interface and thus assuming the shell density being the same as pure LiYF<sub>4</sub>. The possibility of estimating *a priori* the shell thickness, based on the amount of precursors injected, attests to the high degree of control that can be exerted over the synthesis of these RENPs and that precise design of multi-shell architectures is possible.

UC emission intensity of different RENPs under 980 nm excitation increased substantially as thicker inert shell was grown (Figure 7.10B). However, net UC emission intensity did not change significantly after increasing the shell thickness from 4 to 5 nm, indicating that the latter thickness can be already regarded as optimal to achieve bright UC emission while keeping the

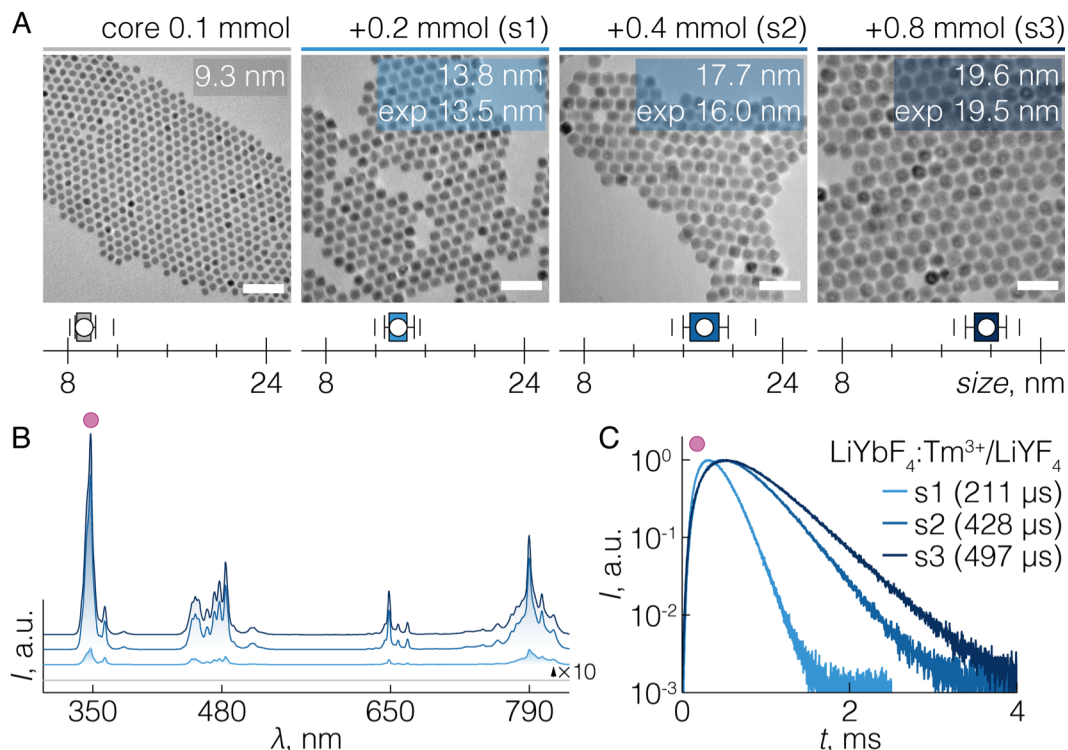


Figure 7.10. Structural and spectral characterization of LiYbF<sub>4</sub>:Tm<sup>3+</sup>/LiYF<sub>4</sub> RENPs.

**A** – TEM images and size distribution (along major axis), and **B** – UC emission spectra of LiYbF<sub>4</sub>:Tm<sup>3+</sup> core-only and LiYbF<sub>4</sub>:Tm<sup>3+</sup>/LiYF<sub>4</sub> core/shell RENPs featuring an inert shell of different thickness. Scale bar 50 nm. Box plots indicate: mean value (dot), SD (box outline), 5<sup>th</sup> and 95<sup>th</sup> percentiles (whiskers), and maximum/minimum values (dashes). **C** – Normalized photoluminescence decay profiles of UC emission at 347 nm (labeled with a dot in B) of LiYbF<sub>4</sub>:Tm<sup>3+</sup>/LiYF<sub>4</sub> core/shell RENPs featuring inert shell of different thickness. Excitation power density ~346 W/cm<sup>2</sup>. Spectra and decay profiles are color-coded with labels in A.

overall size of these RENPs around 20 nm, in line with other observations for different kind RENPs.<sup>[65,66]</sup> Steady-state upconversion photoluminescence measurements were further corroborated by the lifetime analysis of the LiYbF<sub>4</sub>:Tm<sup>3+</sup>/LiYF<sub>4</sub> core/shell RENPs (Figure 7.10C). The average lifetime of the <sup>1</sup>I<sub>6</sub> excited state (monitored via <sup>1</sup>I<sub>6</sub> → <sup>3</sup>F<sub>4</sub> radiative transition at approximately 347 nm, following 980 nm pulsed excitation) was measured to be 211, 428 and 497 μs for core/shell RENPs featuring 2, 4, and 5 nm thick shells, respectively. UV emission intensity of core-only RENPs was too low for photoluminescence lifetime measurements. The significant increase in average lifetime of different core/shell RENPs, unequivocally indicated towards the suppression of non-radiative decay pathways (surface, ligand, and solvent related) responsible for the UC emission quenching.

Intriguingly, UC emission intensity of LiYbF<sub>4</sub>:Tm<sup>3+</sup>/LiYF<sub>4</sub> RENPs (~20 nm in size) was comparable to the classical LiYF<sub>4</sub>:Tm<sup>3+</sup>, Yb<sup>3+</sup> core-only RENPs (~90 nm in size) (Figure 7.11A). In fact, the UV emission intensity of the LiYbF<sub>4</sub>:Tm<sup>3+</sup>/LiYF<sub>4</sub> RENPs appeared to even surpass that of classic LiYF<sub>4</sub>:Tm<sup>3+</sup>, Yb<sup>3+</sup> RENPs, which could be directly inferred about from the UV/NIR emission intensity ratio as a function of excitation power (Figure 7.11A – insets). UV/NIR ratio was calculated from the integrated intensities of the 340 nm (<sup>1</sup>I<sub>6</sub> → <sup>3</sup>F<sub>4</sub>) and 790 nm (<sup>3</sup>H<sub>4</sub> → <sup>3</sup>H<sub>6</sub>) UC emission bands. Due to the different photon-order of these transitions, the UV/NIR ratio typically increases with increasing the power of the laser excitation. At each power value studied, LiYbF<sub>4</sub>:Tm<sup>3+</sup>/LiYF<sub>4</sub> core/shell RENPs outperformed to the large LiYF<sub>4</sub>:Tm<sup>3+</sup>, Yb<sup>3+</sup> RENPs by having a much higher UV/NIR ratios. In the LiYbF<sub>4</sub>:Tm<sup>3+</sup>/LiYF<sub>4</sub> RENPs the UV/NIR ratio asymptotically approached unity, suggesting that UC emission at 340 nm can be comparable in intensity to that at 790 nm. Although, more accurate quantitative studies (see chapter 8) showed that UC emission of LiYbF<sub>4</sub>:Tm<sup>3+</sup>/LiYF<sub>4</sub> RENPs in the NIR spectral range remains few order of magnitude more efficient than that in the UV, these results clearly showed that small UV-emitting upconverting RENPs as bright as large classical structures could be conceived. Also, average lifetimes of <sup>1</sup>I<sub>6</sub> and <sup>3</sup>H<sub>4</sub> excited states for small LiYbF<sub>4</sub>:Tm<sup>3+</sup>/LiYF<sub>4</sub> RENPs were, respectively, 32 and 13% longer as compared to the classic LiYF<sub>4</sub>:Tm<sup>3+</sup>, Yb<sup>3+</sup> nanostructures. This clearly attests to the fact that inert shells can suppresses UC emission quenching more effectively than increasing the overall size of core-only RENPs (Figure 7.11B).

Altogether, the first nuclei synthesis and stabilization proved to be a successful and viable strategy to synthesize small and thermodynamically stable Li<sup>+</sup>-based RENPs, whose photoluminescence intensity can be substantially improved by surface passivation with an inert shell. In fact, the development of this protocol has far reaching implications towards creating

efficient multi-layered decoupled theranostics RENPs with an overall size maintained within the recommended 20-50 nm range for application in living objects. Yet prior to the synthesis of improved and miniaturized decoupled theranostic RENPs, it is important to quantitatively assess the performance of small and bright  $\text{LiYbF}_4:\text{RE}^{3+}$ , so that optimal  $\text{RE}^{3+}$  doping can be chosen to obtain UC emission best suited for the foreseeable use of these RENPs in biomedicine.

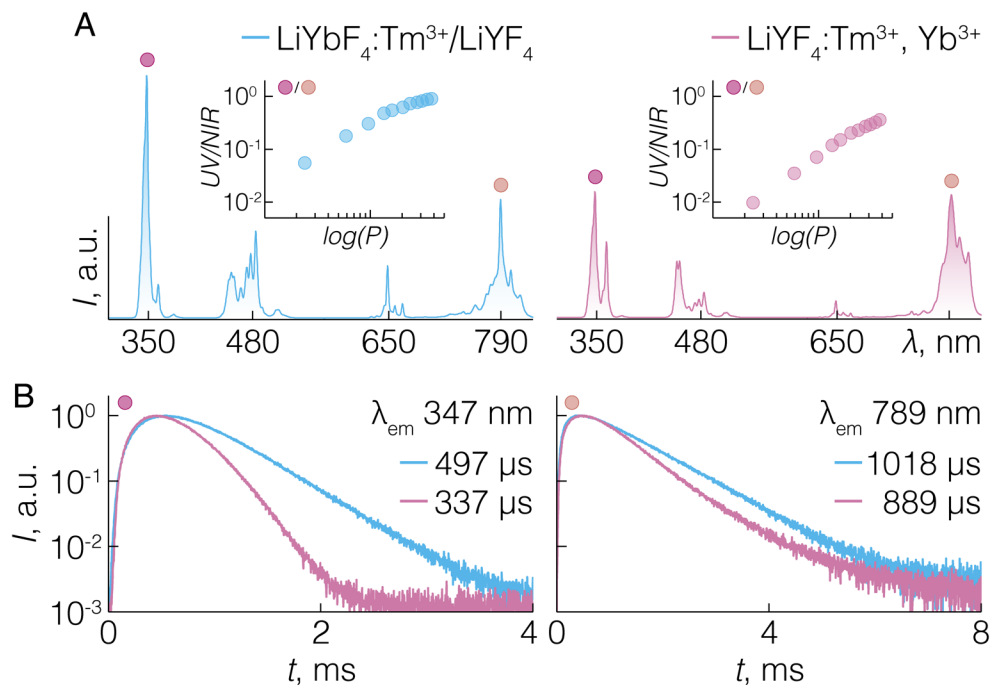


**Figure 7.11.  $\text{LiYbF}_4:\text{Tm}^{3+}/\text{LiYF}_4$  vs  $\text{LiYF}_4:\text{Tm}^{3+}, \text{Yb}^{3+}$  RENPs.**

**A** – UC emission spectra of  $\sim 20$  nm in size  $\text{LiYbF}_4:\text{Tm}^{3+}/\text{LiYF}_4$  core/shell and  $\sim 90$  nm in size  $\text{LiYF}_4:\text{Tm}^{3+}, \text{Yb}^{3+}$  core-only RENPs. Excitation power density  $\sim 346 \text{ W/cm}^2$ . Insets show the UV/NIR ratio (taken as the intensity ratio of UC emission bands at around 340 and 790 nm) vs excitation power. **B** – Normalized photoluminescence decay profiles of UC emission at 347 (left) and 789 nm (right) of  $\text{LiYbF}_4:\text{Tm}^{3+}/\text{LiYF}_4$  core/shell and  $\text{LiYF}_4:\text{Tm}^{3+}, \text{Yb}^{3+}$  core-only RENPs.

## 8 OPTIMIZING LiYbF<sub>4</sub>:RE<sup>3+</sup>/LiYF<sub>4</sub> RENPs

---

RENPs whose hosts are comprised entirely of Yb<sup>3+</sup> (i.e. NaYbF<sub>4</sub>, LiYbF<sub>4</sub>, KYb<sub>2</sub>F<sub>7</sub>) can absorb significantly more of incoming photons and efficiently funnel that excitation to their higher energy states, due to the close proximity between Yb<sup>3+</sup> and activator dopants.<sup>[54]</sup> Thus, Yb<sup>3+</sup>-based RENPs have received much attention in terms of their controlled and reproducible synthesis, including LiYbF<sub>4</sub> RENPs presented in the previous chapter.<sup>[234,242,243]</sup> But little is known about their spectral properties or how those are influenced by different activators and their concentration. Ergo, our continuously expanding understanding on how to synthesize high-quality Li<sup>+</sup>-based RENPs of various sizes and architectures needs to be complemented with a better grasp on their spectral properties and alteration thereof. Timely fulfilment of this task will allow to effectively move forward with the development of LiYbF<sub>4</sub> multifunctional RENPs best-suited for theranostics, optogenetics or other high-photon-energy demanding applications.

To that end, UC emission spectra, excited state lifetimes and upconversion PLQY of LiYbF<sub>4</sub>:RE<sup>3+</sup>/LiYF<sub>4</sub> RENPs were systematically studied (RE<sup>3+</sup> – Tm<sup>3+</sup>, Er<sup>3+</sup> or Ho<sup>3+</sup>). These properties were investigated as a function of doping concentration and laser excitation power density. The acquired information is pertinent to the optimization of the therapeutic part of novel decoupled theranostics RENPs, in terms of their light mediated PDT or drug release capacity.

*This study was carried out jointly with Dr. Ting Cheng, and a research group of Prof. Jose Marques-Hueso at the Heriot-Watt University, UK. PLQY was measured at the Heriot-Watt University with the assistance from Mr. Callum M. S. Jones. Dr. Cheng has performed most of the RNP syntheses and TEM imaging.*

*Herein results were published as: "Spectral Characterization of LiYbF<sub>4</sub> Upconverting Nanoparticles" A. Skripka\*, T. Cheng,\* C. M.S. Jones, R. Marin, J. Marques-Hueso and F. Vetrone, Nanoscale, 12 (33), 17545-17554, 2020 \*equally contributing authors.*

### 8.1 RNP preparation and structural characterization

The LiYbF<sub>4</sub>: x mol% RE<sup>3+</sup>/LiYF<sub>4</sub> core/shell RENPs (RE<sup>3+</sup> – Tm<sup>3+</sup> 0.2, 0.5, 1, 2 mol%; Er<sup>3+</sup> 1, 2, 5, 10 mol%; Ho<sup>3+</sup> 1, 2, 5 mol%) were prepared *via* the first nuclei (FN) synthesis/stabilization method reported in the previous chapter.<sup>[242]</sup> FN were synthesized *via* hot-injection approach, where 2.5 mmol each of Li-TFA and Y/RE-TFA precursors were degassed and dissolved in a mixture of 3 mL each of OA and OM, and 6 mL ODE (solution B), and injected into the solution

A containing 7 mL each of OA and OM, and 14 mL ODE at 330 °C. Injection rate was 1.5 mL/min. After 1 h of vigorous stirring, the mixture was cooled down to RT and the synthesized FN were transferred to Falcon centrifuge tubes (50 mL) for the subsequent stabilization step. Due to evaporation of impurities in the starting materials (such as OA and ODE) and reaction byproducts, as well as minor losses accrued from intermediate steps of liquid handling, the final volume of FN mixtures was around 36-37 mL. Core RENPs were then formed by the stabilization of FN in an excess of OA. FN (1.25 mmol, ~ 18-18.5 mL of stock solution) were mixed with 16 mL each of OA and ODE, and degassed at 110 °C under vacuum and magnetic stirring for 30 min. Then, the reaction flask was backfilled with argon and the temperature was raised to 315 °C. After 1 h of reaction, the mixture was cooled down to RT and a small portion (1 mL) of core RENPs was sampled for structural characterization. Core/shell RENPs were prepared by hot-injection shelling of ~0.5 mmol of stabilized core RENPs, dispersed in equal parts of OA and ODE up to a total volume of 20 mL (Solution A). 4 mmol each of Li-TFA and Y-TFA in 10 mL each of OA and ODE constituted the shelling solution B. Both solutions were degassed under vacuum and magnetic stirring at 110 °C for 30 min. After degassing, the flask was backfilled with argon and the temperature was raised to 290 °C. At this point, solution B was injected into solution A at a 0.75 mL/min injection rate in three steps. After each ~7 mL injection step, the mixture was allowed to react for 40 min. After the last reaction step, the mixture was cooled to room temperature. Resultant core/shell RENPs were washed and re-dispersed in hexane for further structural and optical characterization.

Altogether, three sets of  $\text{LiYbF}_4:\text{RE}^{3+}/\text{LiYF}_4$  RENPs were synthesized, distinct by the activator ion of varying doping concentration. Dopants and doping amounts were confirmed with ICP-OES elemental analysis and matched well the target (values):  $\text{Tm}^{3+}$  – 0.22 (0.2), 0.51 (0.5), 1.03 (1), 2.09 (2) mol%;  $\text{Er}^{3+}$  – 1.06 (1), 1.83 (2), 4.89 (5), 9.96 (10) mol%;  $\text{Ho}^{3+}$  – 1.32 (1), 2.02 (2), 5.34 (5) mol%. 10 mol%  $\text{Ho}^{3+}$ -doped RENPs were also synthesized, however the size of these RENPs was too large compared to the rest of the  $\text{Ho}^{3+}$  series, and thus were excluded from spectral analysis. Just as in chapter 7, all  $\text{LiYbF}_4:\text{RE}^{3+}/\text{LiYF}_4$  RENPs displayed bi-pyramidal morphology (Figure 8.1-8.3) and were of tetragonal ( $I4_1/a$ ) crystal structure, confirmed by XRD (see Appendix I). All  $\text{LiYbF}_4:\text{RE}^{3+}$  cores were 10-12 nm in size measured along their major axis, and featured at least 5-nm thick  $\text{LiYF}_4$  inert shell. The final core/shell size of the three sets was: 25-28, 22-23 and 25-27 nm for  $\text{Tm}^{3+}$ -,  $\text{Er}^{3+}$ - and  $\text{Ho}^{3+}$ -RENPs, respectively. Although some size discrepancy existed between the different RENPs sets, RENPs within the same set were very similar in size so that changes of their photoluminescence could be compared exclusively on the basis of varying doping amount.

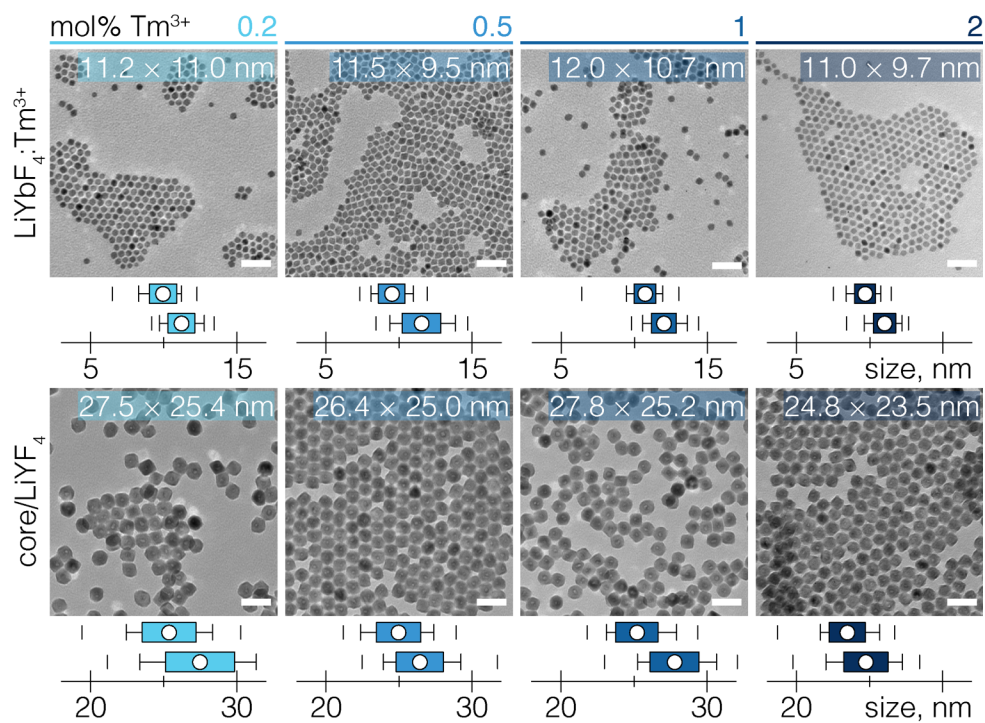


Figure 8.1. Structural characterization of  $\text{LiYbF}_4:\text{Tm}^{3+}/\text{LiYF}_4$  RENPs.

TEM images of  $\text{LiYbF}_4: x \text{ mol}\% \text{ Tm}^{3+}/\text{LiYF}_4$  RENPs and their respective size distributions along major (bottom boxes) and minor axis (top boxes). Scale bar 50 nm. Box plots indicate: mean value (dot), SD (box outline), 5<sup>th</sup> and 95<sup>th</sup> percentiles (whiskers), and maximum/minimum values (dashes).

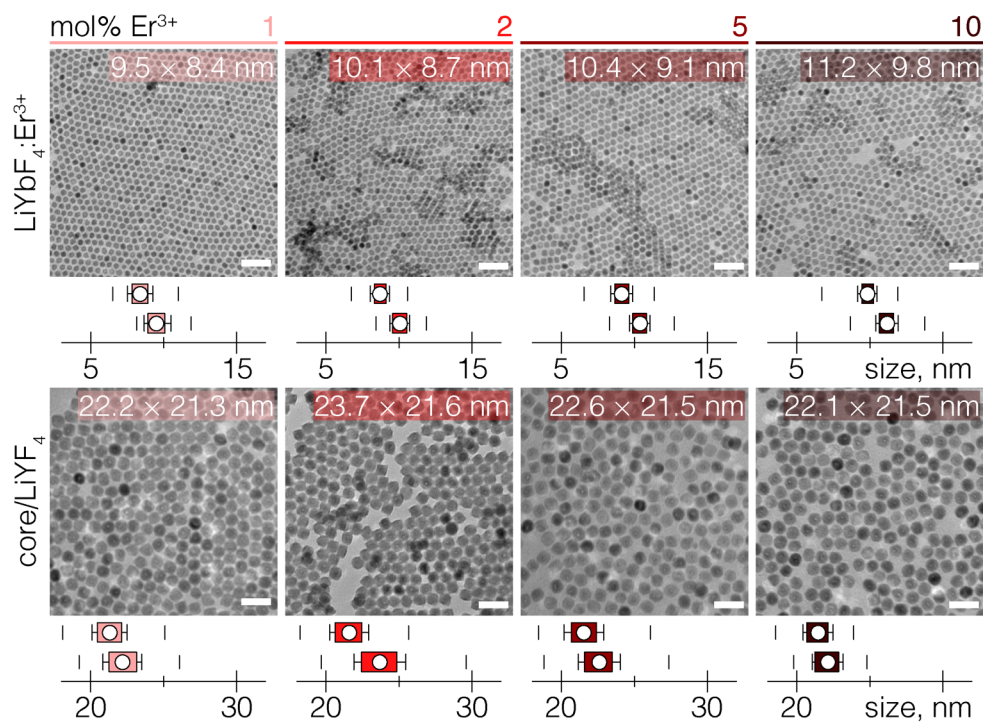


Figure 8.2. Structural characterization of  $\text{LiYbF}_4:\text{Er}^{3+}/\text{LiYF}_4$  RENPs.

TEM images of  $\text{LiYbF}_4: x \text{ mol}\% \text{ Er}^{3+}/\text{LiYF}_4$  RENPs and their respective size distributions along major (bottom boxes) and minor axis (top boxes). Scale bar 50 nm. Box plots indicate: mean value (dot), SD (box outline), 5<sup>th</sup> and 95<sup>th</sup> percentiles (whiskers), and maximum/minimum values (dashes).

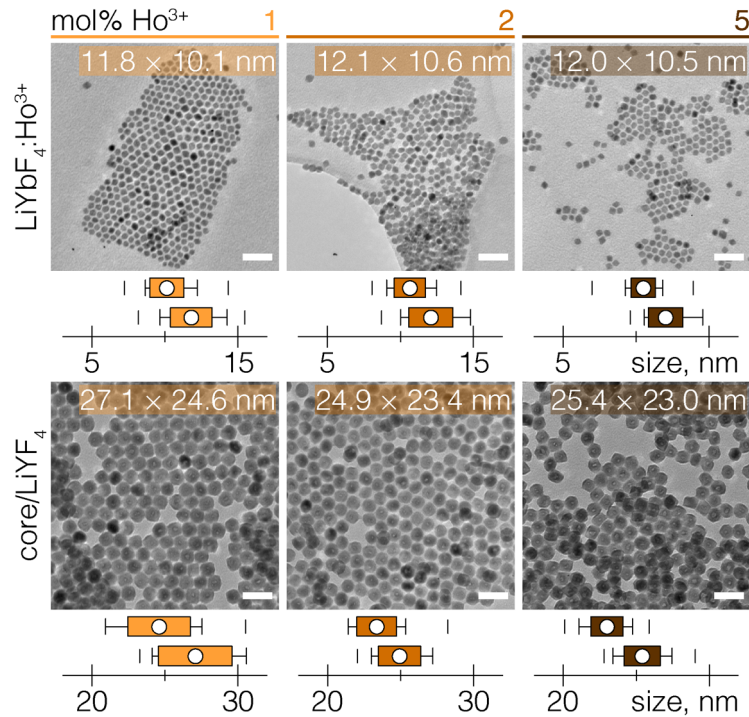


Figure 8.3. Structural characterization of  $\text{LiYbF}_4:\text{Ho}^{3+}/\text{LiYF}_4$  RENPs.

TEM images of  $\text{LiYbF}_4: x \text{ mol}\% \text{ Ho}^{3+}/\text{LiYF}_4$  RENPs and their respective size distributions along major (bottom boxes) and minor axis (top boxes). Scale bar 50 nm. Box plots indicate: mean value (dot), SD (box outline), 5<sup>th</sup> and 95<sup>th</sup> percentiles (whiskers), and maximum/minimum values (dashes).

## 8.2 $\text{LiYbF}_4:\text{Tm}^{3+}/\text{LiYF}_4$

Under 960 nm excitation, the UC emission of  $\text{LiYbF}_4: x \text{ mol}\% \text{ Tm}^{3+}/\text{LiYF}_4$  ( $x = 0.2, 0.5, 1, 2$ ) RENPs' photoluminescence spanned the UV, visible, and NIR spectral regions, with major radiative transitions located at roughly: 340 ( $^1\text{I}_6 \rightarrow ^3\text{F}_4$ ), 360 ( $^1\text{D}_2 \rightarrow ^3\text{H}_6$ ), 450 ( $^1\text{D}_2 \rightarrow ^3\text{F}_4$ ), 480 ( $^1\text{G}_4 \rightarrow ^3\text{H}_6$ ), 660 ( $^1\text{G}_4 \rightarrow ^3\text{F}_4$ ) and 790 nm ( $^3\text{H}_4 \rightarrow ^3\text{H}_6$ ;  $^1\text{G}_4 \rightarrow ^3\text{H}_5$ ) (Figure 8.4A, B). It is worth noting that the NIR upconversion of  $\text{Tm}^{3+}$  actually originates from two- and three-photon upconversion processes that populate either  $^3\text{H}_4$  or  $^1\text{G}_4$  energy levels, respectively. To individually assess emission from the  $^1\text{G}_4$  state, spectral profiles of the  $^3\text{H}_4 \rightarrow ^3\text{H}_6$  and  $^1\text{G}_4 \rightarrow ^3\text{H}_5$  radiative transitions at 790 nm were deconvoluted assuming a linear combination of these emission bands (see appendix VI).<sup>[244]</sup> Furthermore, since multiple  $\text{Tm}^{3+}$  UC emission bands originate from the same excited state, steady-state spectral analysis on the individual contribution of these emissive states to the net UC emission spectrum of  $\text{Tm}^{3+}$  was assessed by grouping different emission bands with their corresponding energy levels ( $^1\text{I}_6$ ,  $^1\text{D}_2$ ,  $^1\text{G}_4$  and  $^3\text{H}_4$ ) (Figure 8.4A, B). Similarly, UC emission of  $\text{Ho}^{3+}$ -RENPs were grouped as well (see below).

The relative contribution of each of these emissive states varied considerably with both  $\text{Tm}^{3+}$  doping concentration and excitation power density ( $P_d$ ) (Figure 8.4C). In the case of 0.2 and 0.5

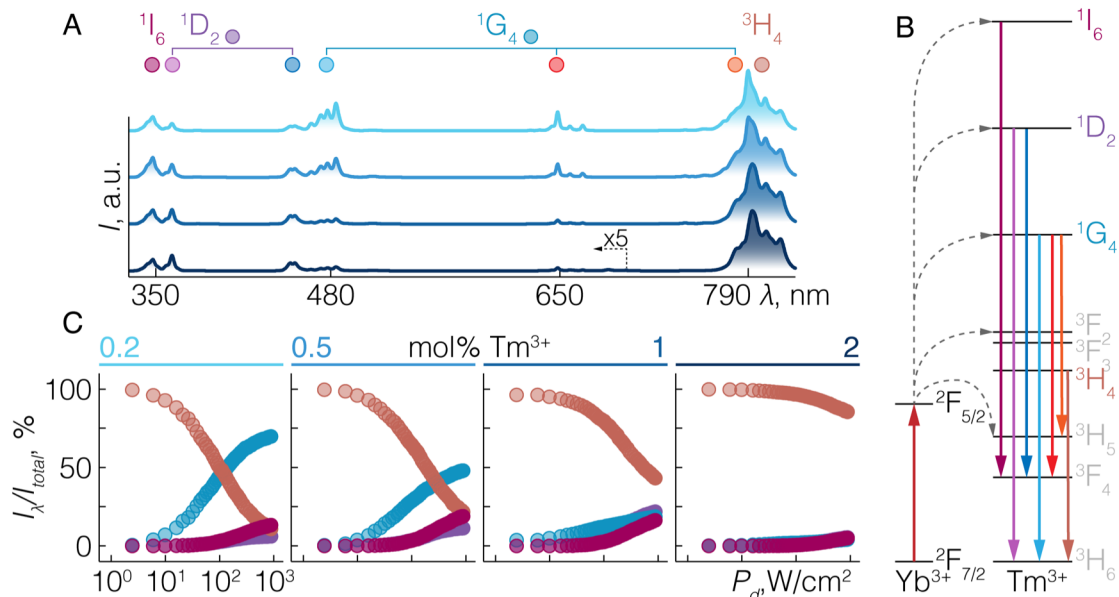
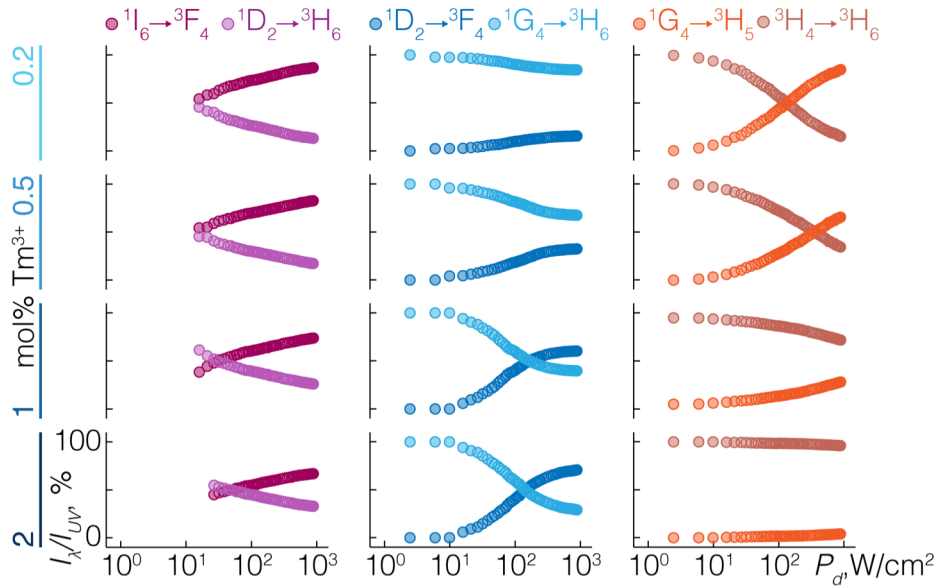


Figure 8.4. Spectral characterization of  $\text{LiYbF}_4:\text{Tm}^{3+}/\text{LiYF}_4$  RENPs.

**A** – UC emission spectra of  $\text{LiYbF}_4: x \text{ mol\% Tm}^{3+}/\text{LiYF}_4$  RENPs under 960 nm excitation.  $P_d \sim 200 \text{ W/cm}^2$ . Emission intensity of 2 mol%  $\text{Tm}^{3+}$ -RENPs below 700 nm is magnified by 5 for clarity. **B** – Simplified  $\text{Yb}^{3+}/\text{Tm}^{3+}$  upconversion excitation-emission scheme. Radiative transitions are color coded with dots in **A** above each emission band. **C** – Relative contribution of  $^1\text{I}_6 \rightarrow ^3\text{F}_4$  (burgundy),  $^1\text{D}_2 \rightarrow ^3\text{H}_6 + ^3\text{F}_4$  (purple),  $^1\text{G}_4 \rightarrow ^3\text{H}_6 + ^3\text{F}_4 + ^3\text{H}_5$  (blue) and  $^3\text{H}_4 \rightarrow ^3\text{H}_6$  (brown) radiative transitions at different  $P_d$  and  $\text{Tm}^{3+}$  mol%  $\text{Tm}^{3+}$ , emissions from  $^1\text{G}_4$  and  $^1\text{I}_6$  states quickly surpassed NIR emission from the  $^3\text{H}_4$  energy level as excitation  $P_d$  was increased. In contrast, at 1 and 2 mol%  $\text{Tm}^{3+}$ , UC emission was mostly in the NIR, stemming from the  $^3\text{H}_4$  energy level. Particularly in the case of 2 mol%  $\text{Tm}^{3+}$  doped RENPs, NIR emission at around 790 nm was absolutely dominant over other UC emission bands. Overall, increasing  $\text{Tm}^{3+}$  concentration led to continuously lessened spectral contribution from the  $^1\text{G}_4$  state, while that of  $^3\text{H}_4$ ,  $^1\text{D}_2$  and  $^1\text{I}_6$  increased with respect to it. Repopulation of these states is indicative of a number of cross-relaxation processes that appear with increasing number of  $\text{Tm}^{3+}$  dopants. The influence of cross-relaxation could be clearly observed from the intensity interplay between UC emissions stemming from neighboring energy levels of  $n$  and  $(n+1)$  photon order population (Figure 8.5). As the  $\text{Tm}^{3+}$  concentration increased, the contribution from the  $^1\text{G}_4$  state to the 790 nm NIR emission band was reduced and the  $^3\text{H}_4 \rightarrow ^3\text{H}_6$  radiative transition became dominant. Concomitantly, depopulation of the  $^1\text{G}_4$  energy level was reflected in the higher excitation occupancy at the  $^1\text{D}_2$  state; the  $^1\text{D}_2 \rightarrow ^3\text{F}_4$  radiative transition became more pronounced with higher  $\text{Tm}^{3+}$  concentration and excitation  $P_d$ . As a consequence, greater  $^1\text{D}_2$  population facilitates  $^2\text{F}_{5/2} (\text{Yb}^{3+}) \rightarrow ^3\text{P}_2 (\text{Tm}^{3+})$  ETU and subsequent population of the  $^1\text{I}_6$  energy level.<sup>[34]</sup> Yet, the intensity between the two UV-emitting states,  $^1\text{D}_2$  and  $^1\text{I}_6$ , was not constant either. In contrast with the study by Wang et al.,<sup>[34]</sup>  $^1\text{D}_2 \rightarrow ^3\text{H}_6$  radiative transition was observed to be increasingly dominant with greater  $\text{Tm}^{3+}$  concentration and



**Figure 8.5. UC emission intensity of  $\text{LiYbF}_4:\text{Tm}^{3+}/\text{LiYF}_4$  RENPs adjacent emission bands.**

Relative intensity contributions of  $n$  and  $n+1$  photon order UC emission bands of  $\text{Tm}^{3+}$ -RENPs in the UV ( $^1\text{I}_6 \rightarrow ^3\text{F}_4$  and  $^1\text{D}_2 \rightarrow ^3\text{H}_6$ ), blue ( $^1\text{D}_2 \rightarrow ^3\text{F}_4$  and  $^1\text{G}_4 \rightarrow ^3\text{H}_6$ ), and NIR ( $^3\text{H}_4 \rightarrow ^3\text{H}_6$  and  $^1\text{G}_4 \rightarrow ^3\text{H}_5$ ) spectral ranges. excitation  $P_d$ . It is thus speculated that these trends are governed by the  $^1\text{I}_6 \rightarrow ^1\text{D}_2$ : $^1\text{G}_4 \rightarrow ^1\text{D}_2$  cross-relaxation, which becomes more relevant as the average distance between neighboring  $\text{Tm}^{3+}$  is reduced (Figure 8.6). Together, the various cross-relaxation processes that lead to the greater population of  $^1\text{D}_2$  and  $^3\text{H}_4$  excited states, mostly at the expense of  $^1\text{G}_4$  energy level, determine the UC emission output of  $\text{LiYbF}_4:\text{Tm}^{3+}/\text{LiYF}_4$  RENPs, which can be finely tuned by varying the  $\text{Tm}^{3+}$  doping concentration.

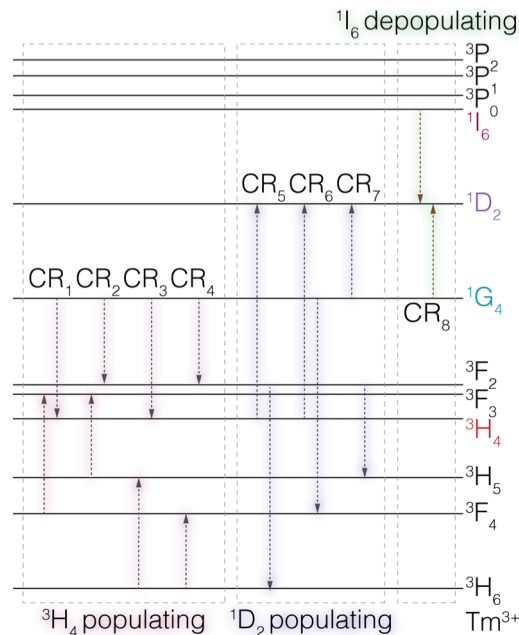


**Figure 8.6. Cross-relaxation in  $\text{LiYbF}_4:\text{Tm}^{3+}/\text{LiYF}_4$  RENPs.**

Representation of cross-relaxation process (CR) that determine UC emission spectra of  $\text{Tm}^{3+}$ -RENPs by repopulating different emissive states of  $\text{Tm}^{3+}$ .

To gain further insight about the UC emission excitation in the  $\text{Tm}^{3+}$ -RENPs, the illustrative value of the minimum photon number (order),  $n$ , required to populate each excited state via a multiphoton process, was calculated following power plot analysis. For all samples and UC emission bands,  $n$  is given as the slope of a linear fit of  $\log(I)/\log(P_d)$  plot in the low  $P_d$  regime (Figure 8.7). An apparent increase of  $n$  with higher spectral energy emissions confirmed the multiphoton nature of upconversion process, although  $n$  values were lower than the theoretically expected ones (5, 4, 3 and 2 for  $^1\text{I}_6$ ,  $^1\text{D}_2$ ,  $^1\text{G}_4$  and  $^3\text{H}_4$  excited states, respectively) (Figure 8.7B). Deviation of experimentally obtained  $n$  is anticipated due to the more complex nature of the upconversion process in reality compared to simplified multilevel excitation description, also similar to previous observations in chapter 4.<sup>[39]</sup> The  $n$  values for the UC emissions stemming from the  $^1\text{D}_2$  and  $^1\text{I}_6$  excited states increased with increasing  $\text{Tm}^{3+}$  concentration from 0.2 to 1 mol%, after which, the  $n$  values decreased. Similar trends were found for  $n(^1\text{G}_4)$  excited state. These results indicate that cross-relaxation combined with  $\text{Yb}^{3+}$  excitation energy being distributed among a larger number of  $\text{Tm}^{3+}$  alleviate saturation of the excited states, which effectively should lead to greater photoluminescence of 0.5 and 1 mol%  $\text{Tm}^{3+}$  doped RENPs. However, as can be seen from the  $n$  values of 2 mol%  $\text{Tm}^{3+}$ -RENPs, cross-relaxation becomes deleterious for higher-order upconversion further increasing the  $\text{Tm}^{3+}$  concentration.

Photoluminescence decay measurements supported the conclusions drawn from the steady-state experiments (Figure 8.8). Shortening of the photoluminescence decay curves and decrease in the corresponding average lifetimes,  $\tau_d$ , of each excited state could be observed

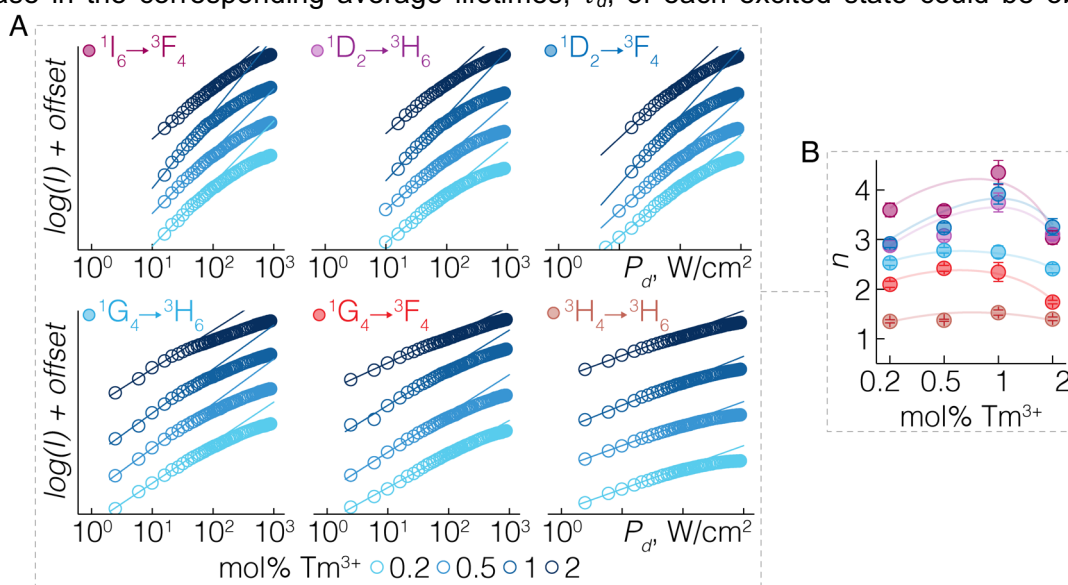
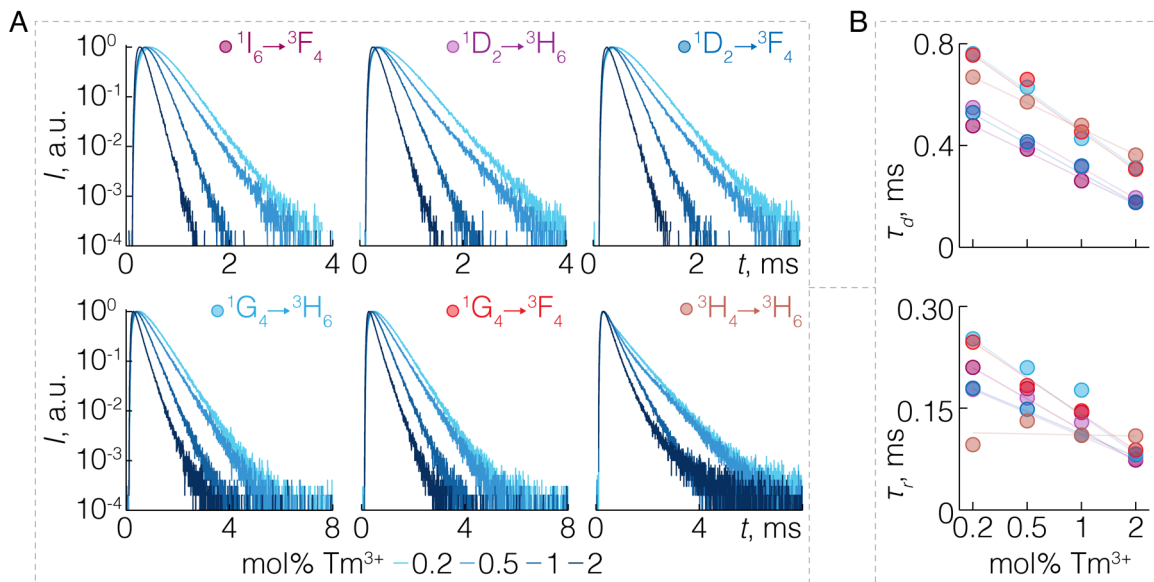


Figure 8.7. Power plot analysis of  $\text{LiYbF}_4:\text{Tm}^{3+}/\text{LiYF}_4$  RENPs.

A – Intensity ( $I$ ) vs excitation power density ( $P_d$ ) log-log plots of UC emission bands of  $\text{LiYbF}_4: x \text{ mol}\% \text{ Tm}^{3+}/\text{LiYF}_4$  RENPs. B – Summary of the slope values,  $n$ , obtained from the linear fits in A at low  $P_d$  regime (2 – 20  $\text{W}/\text{cm}^2$ ; 10 – 40  $\text{W}/\text{cm}^2$  for highest order upconversion emissions).

with the increasing  $\text{Tm}^{3+}$  concentration, attesting to the non-radiative energy decay promoted by cross-relaxation among  $\text{Tm}^{3+}$ . The sharpest change in excited state lifetime could be observed for the  $^1\text{G}_4$  energy level, signifying its importance as an intermediate state for higher-order upconversion excitation, either through ETU or promoted by cross-relaxation population redistribution among the  $\text{Tm}^{3+}$  electronic states. In addition to decay time shortening, average rise times,  $\tau_r$ , required to populate the  $^1\text{I}_6$ ,  $^1\text{D}_2$  and  $^1\text{G}_4$  energy levels also decreased with increasing  $\text{Tm}^{3+}$  doping amount.

Finally, the *PLQY* of  $\text{Tm}^{3+}$ -doped RENPs was measured (Figure 8.9). For all the samples, *PLQY* increased with increasing excitation  $P_d$ , as expected for multiphoton processes. For 0.2 and 0.5 mol%  $\text{Tm}^{3+}$  samples *PLQY* rapidly approached saturation, in contrast to the continuous rise of *PLQY* in the case of 1 and 2 mol%  $\text{Tm}^{3+}$  doping (Figure 8.9A). *PLQY* measurements emphasized the high intensity of the  $\text{Tm}^{3+}$  NIR emission ( $^3\text{H}_4 \rightarrow ^3\text{H}_6$ ), which grew from ~0.10 to 1.38% (at  $P_d \sim 90 \text{ W/cm}^2$ ) increasing  $\text{Tm}^{3+}$  doping from 0.2 to 2 mol%, respectively (Figure 3B). Although 0.2 mol%  $\text{Tm}^{3+}$ -RENPs had greatest spectral contribution from the  $^1\text{G}_4$  excited state, the maximum *PLQY* for  $^1\text{G}_4$  radiative transitions was achieved at 0.5 mol%  $\text{Tm}^{3+}$ , with approximate values of 0.049% for  $^1\text{G}_4 \rightarrow ^3\text{H}_6$  and 0.021% for  $^1\text{G}_4 \rightarrow ^3\text{F}_4$  at  $P_d \sim 90 \text{ W/cm}^2$ . Further increase in  $\text{Tm}^{3+}$  concentration reduced the *PLQY* of these emissions, giving way to radiative transitions from  $^1\text{D}_2$  and  $^1\text{I}_6$  excited states, with a maximum *PLQY* at 1 mol%  $\text{Tm}^{3+}$  – 0.010% ( $^1\text{I}_6 \rightarrow ^3\text{F}_4$ ), 0.006% ( $^1\text{D}_2 \rightarrow ^3\text{H}_6$ ) and 0.021% ( $^1\text{D}_2 \rightarrow ^3\text{F}_4$ ) at  $P_d \sim 90 \text{ W/cm}^2$ . It is obvious that the optimal activator doping in  $\text{LiYbF}_4:\text{Tm}^{3+}/\text{LiYF}_4$  RENPs depends strongly on the



**Figure 8.8. Excited state lifetimes of  $\text{LiYbF}_4:\text{Tm}^{3+}/\text{LiYF}_4$  RENPs.**

**A – Normalized emission decay profiles of different UC emissions of  $\text{LiYbF}_4: x \text{ mol}\% \text{Tm}^{3+}/\text{LiYF}_4$  RENPs. B – Summary of the average decay ( $\tau_d$ ) and rise time ( $\tau_r$ ) values obtained from the decay profiles in A.**

preference for the desired UC emission. For most intense UV and blue photoluminescence, a balance has to be made between increasing the total number of emitters ( $\text{Tm}^{3+}$ ) and activation of cross-relaxation processes in a manner that supports population of higher lying energy levels. Whereas the same cross-relaxation processes began to quench higher order upconversion at the highest  $\text{Tm}^{3+}$  doping studied, the NIR ( ${}^3\text{H}_4 \rightarrow {}^3\text{H}_6$ ) photoluminescence seemed to remain unaffected by it and reached above 1% PLQYs for  $P_d > 20 \text{ W/cm}^2$ . The total PLQY of  $\text{LiYbF}_4:\text{Tm}^{3+}/\text{LiYF}_4$  RENPs across all upconversion emissions at  $P_d \sim 90 \text{ W/cm}^2$  was measured to be 0.13, 0.60, 0.64 and 1.41% for 0.2, 0.5, 1 and 2 mol%  $\text{Tm}^{3+}$ , respectively.

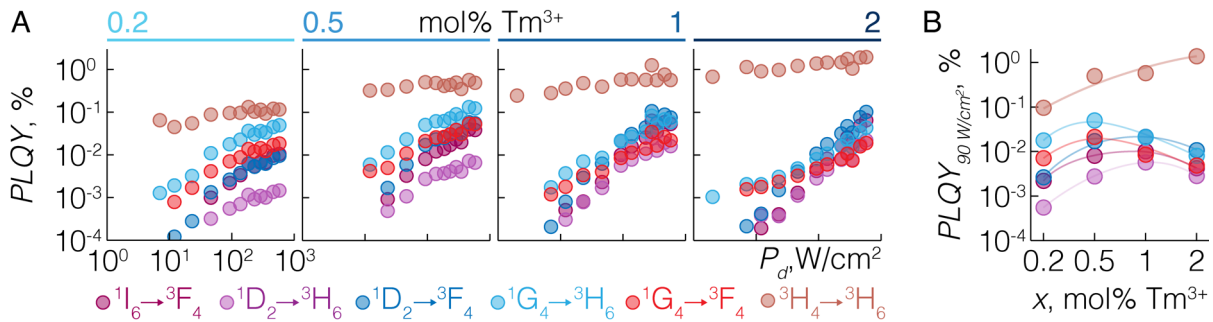


Figure 8.9. PLQY of UC emission of  $\text{LiYbF}_4:\text{Tm}^{3+}/\text{LiYF}_4$  RENPs.

A – PLQY of individual  $\text{Tm}^{3+}$  emission bands of  $\text{LiYbF}_4: x \text{ mol}\% \text{ Tm}^{3+}/\text{LiYF}_4$  RENPs as a function of excitation  $P_d$ . B – PLQY for each of  $\text{Tm}^{3+}$  emission band as a function of  $\text{Tm}^{3+}$  concentration at  $P_d \sim 90 \text{ W/cm}^2$ . Color coding of experimental points in A and B corresponds to legend below, representing radiative transitions of  $\text{Tm}^{3+}$  for which PLQY was measured.

### 8.3 $\text{LiYbF}_4:\text{Er}^{3+}/\text{LiYF}_4$

The  $\text{LiYbF}_4: x \text{ mol}\% \text{ Er}^{3+}/\text{LiYF}_4$  ( $x = 1, 2, 5, 10$ ) RENPs, excited with 960 nm, displayed photoluminescence around 380, 420, 525/545 and 660 nm, attributed to radiative transitions to the  ${}^4\text{I}_{15/2}$  ground state from the  ${}^4\text{G}_{11/2}$ ,  ${}^2\text{H}_{9/2}$ ,  ${}^2\text{H}_{11/2}/{}^4\text{S}_{3/2}$  and  ${}^4\text{F}_{9/2}$  excited states, respectively (Figure 8.10A, B). In terms of relative contribution of different emission bands to the net UC emission of  $\text{Er}^{3+}$ -RENPs, green ( ${}^2\text{H}_{11/2}/{}^4\text{S}_{3/2}$ ) and red ( ${}^4\text{F}_{9/2}$ ) bands showed most variability with  $\text{Er}^{3+}$  doping concentration (Figure 8.10C). As the  $\text{Er}^{3+}$  doping level increased, the relative contribution of the green ( ${}^2\text{H}_{11/2}/{}^4\text{S}_{3/2}$ ) emission to the upconversion spectrum of RENPs also increased. Meanwhile, the red ( ${}^4\text{F}_{9/2}$ ) emission was dominant across all samples with increasing  $P_d$ ; except for the 10 mol%  $\text{Er}^{3+}$ -doped RENPs, which at  $P_d < 2 \text{ W/cm}^2$  featured more of a green ( ${}^2\text{H}_{11/2}/{}^4\text{S}_{3/2}$ ) UC emission. UV ( ${}^4\text{G}_{11/2}$ ) and blue ( ${}^2\text{H}_{9/2}$ ) UC emissions had no clear dependence on the  $\text{Er}^{3+}$  concentration, having minimal relative contributions to the net UC emission spectrum altogether. Notably, the asymptotic saturation of green and red emission bands continuously shifted to higher  $P_d$  with increasing  $\text{Er}^{3+}$  concentration, as a first indication of non-radiative cross-relaxation processes between  $\text{Er}^{3+}$ .

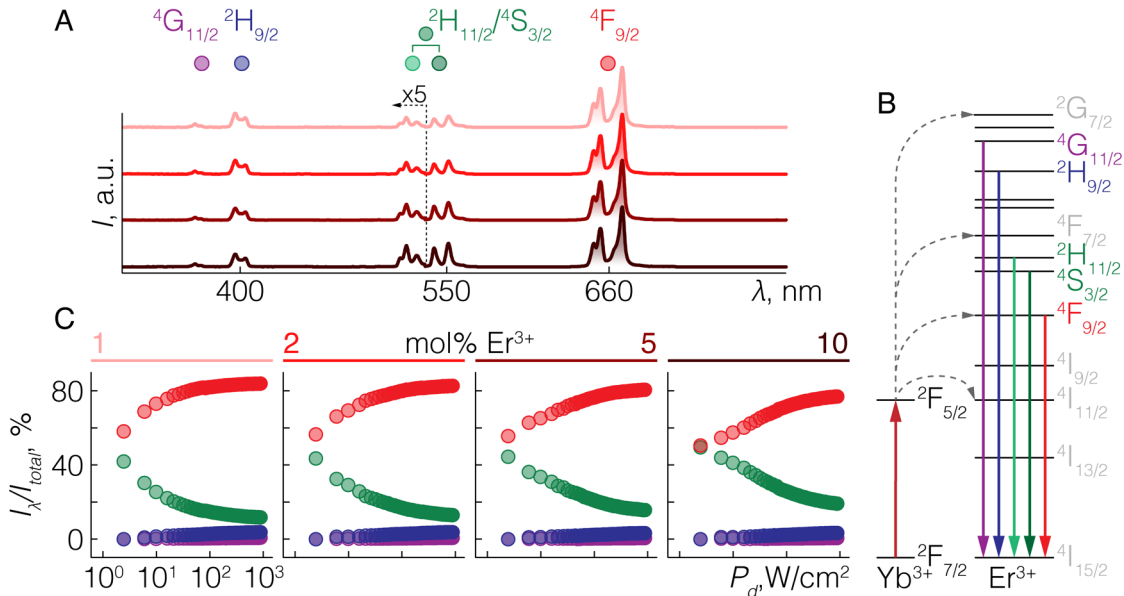


Figure 8.10. Spectral characterization of  $\text{LiYbF}_4:\text{Er}^{3+}/\text{LiYF}_4$  RENPs.

**A** – UC emission spectra of  $\text{LiYbF}_4: x \text{ mol}\% \text{Er}^{3+}/\text{LiYF}_4$  RENPs under 960 nm excitation.  $P_d \sim 200 \text{ W/cm}^2$ . Emission intensity of  $\text{Er}^{3+}$ -RENPs below 540 nm is magnified by 5 for clarity. **B** – Simplified  $\text{Yb}^{3+}/\text{Er}^{3+}$  upconversion excitation-emission scheme. Radiative transitions are color coded with dots in **A** above each emission band. **C** – Relative contribution of  ${}^4\text{G}_{11/2}$  (purple),  ${}^2\text{H}_{9/2}$  (blue),  ${}^2\text{H}_{11/2}/{}^4\text{S}_{3/2}$  (green) and  ${}^4\text{F}_{9/2} \rightarrow {}^4\text{I}_{15/2}$  (red) radiative transitions as a function of  $P_d$  and  $\text{Er}^{3+}$  doping.

The photon number,  $n$ , of  $\text{Er}^{3+}$ -RENPs showed a decreasing trend for all UC emission bands as  $\text{Er}^{3+}$  doping increased, with an unexpected jump of  $n$  values at 10 mol%  $\text{Er}^{3+}$  for certain emissions (Figure 8.11). The  $n$  values confirmed the three-photon excitation of the UV ( ${}^4\text{G}_{11/2}$ ) and blue ( ${}^2\text{H}_{9/2}$ ) emissions. On the other hand, the green ( ${}^2\text{H}_{11/2}/{}^4\text{S}_{3/2}$ ) emission of  $\text{Er}^{3+}$ -RENPs was clearly of two-photon order, and  $n > 2$  values for the red ( ${}^4\text{F}_{9/2}$ ) emission suggested that it could be populated via three- and two-photon processes. The higher-order population of the red ( ${}^4\text{F}_{9/2}$ ) energy state compared to that of the green ( ${}^2\text{H}_{11/2}/{}^4\text{S}_{3/2}$ ) could be anticipated from the previously proposed BET (back energy transfer)  ${}^4\text{G}_{11/2}(\text{Er}^{3+}) \rightarrow {}^2\text{F}_{5/2}(\text{Yb}^{3+})$  mechanism (Figure 8.12),<sup>[79]</sup> which is likely considering the host matrix of here presented RENPs is solely

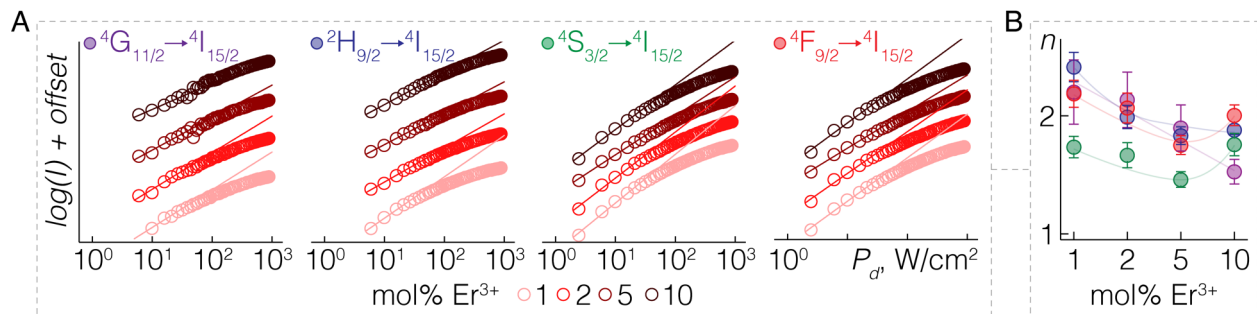
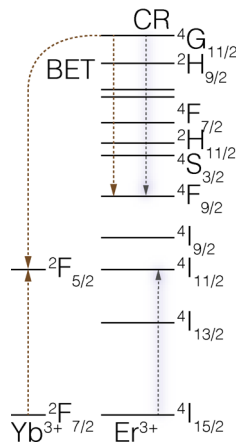


Figure 8.11. Power plot analysis of  $\text{LiYbF}_4:\text{Er}^{3+}/\text{LiYF}_4$  RENPs.

**A** – Intensity ( $I$ ) vs excitation power density ( $P_d$ ) log-log plots of UC emission of  $\text{LiYbF}_4: x \text{ mol}\% \text{Er}^{3+}/\text{LiYF}_4$  RENPs. **B** – Summary of the slope values,  $n$ , obtained from the linear fits in **A** at low  $P_d$  regime (2 – 20  $\text{W/cm}^2$ ).

comprised of  $\text{Yb}^{3+}$  sensitizer ions. In fact, it appeared that within 1 to 5 mol%  $\text{Er}^{3+}$ , excitation of  $^4\text{F}_{9/2}$  energy level gradually drifts towards a two-photon process evident from the decrease of  $n(^4\text{G}_{11/2})$  and  $n(^4\text{F}_{9/2})$ . Following the estimation proposed by Kaiser et al.,<sup>[245]</sup> the relative contribution of the three-photon excitation of  $^4\text{F}_{9/2}$  state was found to decrease roughly from 97 to 67%, moving from 1 to 5 mol%  $\text{Er}^{3+}$ , respectively. However, the sudden increase of  $n(^4\text{F}_{9/2})$  at 10 mol%  $\text{Er}^{3+}$  suggested that the three-photon excitation of this state by BET could be complemented by another process, possibly the  $^4\text{G}_{11/2} \rightarrow ^4\text{F}_{5/2} \cdot ^4\text{I}_{15/2} \rightarrow ^4\text{I}_{11/2}$  cross-relaxation (Figure 8.12), however more detailed examination is still necessary to ascertain this possibility.



**Figure 8.12. Possible  $\text{Er}^{3+}$   $^4\text{F}_{9/2}$  energy level excitation in  $\text{LiYbF}_4\text{:Er}^{3+}/\text{LiYF}_4$  RENPs.**

**Simplified  $\text{Er}^{3+}$  and  $\text{Yb}^{3+}$  energy level scheme visualizing BET and cross-relaxation (CR) processes that populate the  $^4\text{F}_{9/2}$  energy level at the expense of  $^4\text{G}_{11/2}$  excited state.**

Photoluminescence decay measurements demonstrated the decrease in the average lifetimes,  $\tau_d$ , of the  $\text{Er}^{3+}$  excited states, with near-linear dependency as a function of  $\text{Er}^{3+}$  concentration, confirming the growing influence of non-radiative depopulation, such as cross-relaxation, of the excited states at greater  $\text{Er}^{3+}$  doping (Figure 8.13). Average rise times,  $\tau_r$ , for the excitation of higher energy states also decreased with  $\text{Er}^{3+}$  concentration. Most notably,  $\tau_r$  of the red ( $^4\text{F}_{9/2}$ ) UC emission were considerably longer than the values observed for radiative transitions from other excited states. This, attests to the three-photon excitation of  $^4\text{F}_{9/2}$  excited state via BET, that first requires the three-photon population of  $^4\text{G}_{11/2}$  excited states; while  $\tau_d$  of the green ( $^2\text{H}_{11/2}/^4\text{S}_{3/2}$ ) emission being systematically longer than that of the red ( $^4\text{F}_{9/2}$ ) emission, speaks to the fact  $^4\text{F}_{9/2}$  energy level is intrinsically more affected to deactivation by cross-relaxation. Systematically lower  $\tau_d$  and  $\tau_r$  values of  $^4\text{G}_{11/2}$  and  $^2\text{H}_{9/2}$  excited states, indicate that in  $\text{Yb}^{3+}$ -based hosts these energy levels are populated as rapidly as they are deactivated, due to efficient energy exchange between  $\text{Yb}^{3+}$  and  $\text{Er}^{3+}$  which can happen directly at these higher laying energy levels or at the intermediate excited states that facilitate their population.

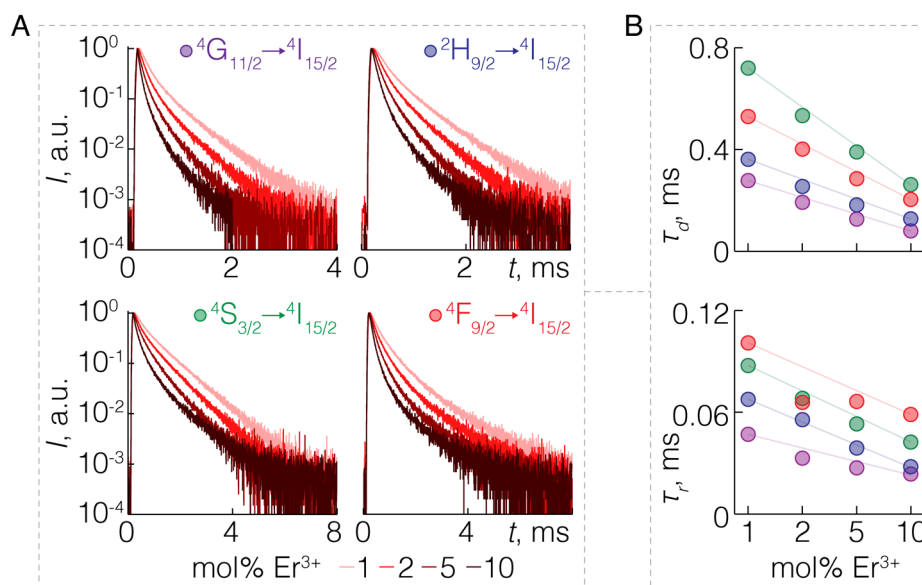


**Figure 8.13. Excited state lifetimes of LiYbF<sub>4</sub>:Er<sup>3+</sup>/LiYF<sub>4</sub> RENPs.**

**A** – Normalized emission decay profiles of different UC emissions of LiYbF<sub>4</sub>: x mol% Er<sup>3+</sup>/LiYF<sub>4</sub> RENPs. **B** – Summary of the average decay ( $\tau_d$ ) and rise time ( $\tau_r$ ) values obtained from the decay profiles in A.

In addition, *PLQY* of 5 mol% Er<sup>3+</sup>-doped RENPs was also measured (Figure 8.14). The *PLQY* of red (<sup>4</sup>F<sub>9/2</sub>) and green (<sup>2</sup>H<sub>11/2</sub>/<sup>4</sup>S<sub>3/2</sub>) UC emissions was at least few orders of magnitude higher than that of UV (<sup>4</sup>G<sub>11/2</sub>) and blue (<sup>2</sup>H<sub>9/2</sub>) emission. Also, the latter UC emission bands still exhibited *PLQY* increase at higher excitation  $P_d$ , while *PLQY* of red (<sup>4</sup>F<sub>9/2</sub>) and green (<sup>2</sup>H<sub>11/2</sub>/<sup>4</sup>S<sub>3/2</sub>) emissions reached saturation around 30 W/cm<sup>2</sup>, and showed random variation in the measured values due to experimental errors. The total *PLQY* at  $P_d \sim 90$  W/cm<sup>2</sup> was 0.78%, where the UV (<sup>4</sup>G<sub>11/2</sub>), blue (<sup>2</sup>H<sub>9/2</sub>), green (<sup>2</sup>H<sub>11/2</sub>/<sup>4</sup>S<sub>3/2</sub>) and red (<sup>4</sup>F<sub>9/2</sub>) emissions contributed 0.001, 0.014, 0.17 and 0.59%, respectively.

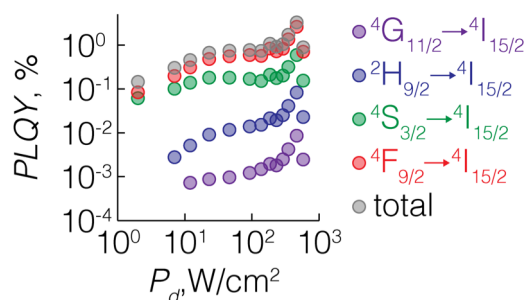


**Figure 8.14. *PLQY* of UC emission of LiYbF<sub>4</sub>:Er<sup>3+</sup>/LiYF<sub>4</sub> RENPs.**

*PLQY* of individual Er<sup>3+</sup> emission bands of LiYbF<sub>4</sub>: 5 mol% Er<sup>3+</sup>/LiYF<sub>4</sub> RENPs as a function of excitation  $P_d$ .

## 8.4 LiYbF<sub>4</sub>:Ho<sup>3+</sup>/LiYF<sub>4</sub>

The LiYbF<sub>4</sub>: x mol% Ho<sup>3+</sup>/LiYF<sub>4</sub> (x = 1, 2, 5) RENPs, under 960 nm excitation, showed multiple UC emissions across the visible spectral range, with the most intense ones centered around 485, 540, 650 and 750 nm (Figure 8.15A). These emission bands respectively correspond to the <sup>5</sup>F<sub>3</sub> → <sup>5</sup>I<sub>8</sub>, <sup>5</sup>S<sub>2</sub>/<sup>5</sup>F<sub>4</sub> → <sup>5</sup>I<sub>8</sub>, <sup>5</sup>F<sub>5</sub> → <sup>5</sup>I<sub>8</sub> and <sup>5</sup>S<sub>2</sub>/<sup>5</sup>F<sub>4</sub> → <sup>5</sup>I<sub>7</sub> radiative transitions (Figure 8.15A, B). For all Ho<sup>3+</sup>-doped RENPs, their emission was mainly composed of green/NIR (both stemming from <sup>5</sup>S<sub>2</sub>/<sup>5</sup>F<sub>4</sub> states) and red (<sup>5</sup>F<sub>5</sub>) upconversion bands. In addition to change in relative intensities of these bands with Ho<sup>3+</sup> doping and excitation  $P_d$ , an inversion point could be clearly discerned (Figure 8.15C). At first, increasing excitation  $P_d$  resulted in a growing contribution of emissions belonging to the <sup>5</sup>S<sub>2</sub>/<sup>5</sup>F<sub>4</sub> energy levels, however, it subsequently saturated making the red (<sup>5</sup>F<sub>5</sub>) emission more pronounced again.<sup>[246]</sup> The saturation point drifted to higher  $P_d$  values for higher Ho<sup>3+</sup> concentration, leading to a decrease in the relative difference between the green (<sup>5</sup>S<sub>2</sub>/<sup>5</sup>F<sub>4</sub>) and red (<sup>5</sup>F<sub>5</sub>) UC emission intensities.

The power plot analysis carried out on the Ho<sup>3+</sup>-RENPs indicated an increase in  $n(^5S_2/^5F_4)$  seen from the NIR emission and a decrease in  $n(^5F_3)$  of the blue band (centered at 485 nm) at higher Ho<sup>3+</sup> concentration (Figure 8.16). Similar to the case of Tm<sup>3+</sup>-RENPs, the increasing  $n(^5S_2/^5F_4)$  indicates lessened saturation of these state at greater Ho<sup>3+</sup> doping, as the excitation energy is shared between more activator ions. Green (<sup>5</sup>S<sub>2</sub>/<sup>5</sup>F<sub>4</sub>) and red (<sup>5</sup>F<sub>5</sub>) upconversion emissions also

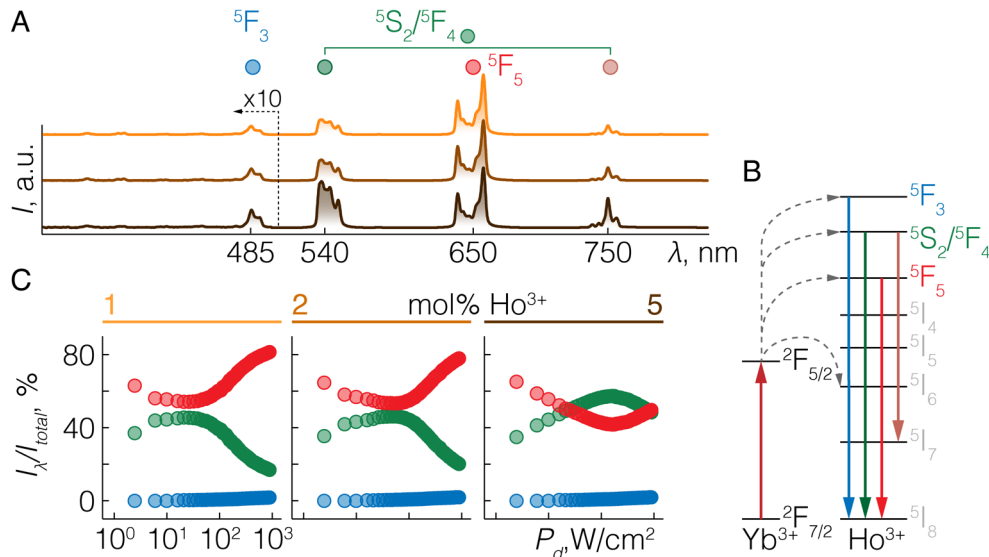
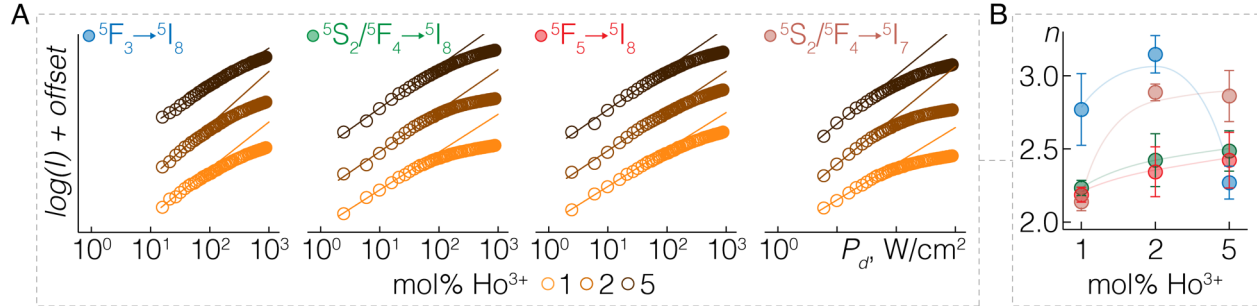


Figure 8.15. Spectral characterization of LiYbF<sub>4</sub>:Ho<sup>3+</sup>/LiYF<sub>4</sub> RENPs.

A – UC emission spectra of LiYbF<sub>4</sub>: x mol% Ho<sup>3+</sup>/LiYF<sub>4</sub> RENPs under 960 nm excitation.  $P_d \sim 200 \text{ W/cm}^2$ . Emission intensity of Ho<sup>3+</sup>-RENPs below 500 nm is magnified by 10 for clarity. B – Simplified Yb<sup>3+</sup>/Ho<sup>3+</sup> upconversion excitation-emission scheme. Radiative transitions are color coded with dots in A above each emission band. C – Relative contribution of <sup>5</sup>F<sub>3</sub> → <sup>5</sup>I<sub>8</sub> (blue), <sup>5</sup>S<sub>2</sub>/<sup>5</sup>F<sub>4</sub> → <sup>5</sup>I<sub>8</sub>+<sup>5</sup>I<sub>7</sub> (green) and <sup>5</sup>F<sub>5</sub> → <sup>5</sup>I<sub>8</sub> (red) radiative transitions as a function of  $P_d$  and Ho<sup>3+</sup> doping.

appeared to have a three-photon population component, having  $n > 2$  for each doping. Given the observed decrease in  $n(^5F_3)$  values, it can be presumed that the feeding of  $^5S_2/^5F_4$  excited state might stem from cross-relaxation processes depopulating the  $^5F_3$  and  $^5G_5$  energy levels (Figure 8.17), which would account for the three-photon component in the excitation of green and red upconversion.<sup>[247]</sup>



**Figure 8.16. Power plot analysis of  $\text{LiYbF}_4:\text{Ho}^{3+}/\text{LiYF}_4$  RENPs.**

**A** – Intensity ( $I$ ) vs excitation power density ( $P_d$ ) log-log plots of UC emission of  $\text{LiYbF}_4: x \text{ mol}\% \text{ Ho}^{3+}/\text{LiYF}_4$  RENPs. **B** – Summary of the slope values,  $n$ , obtained from the linear fits in **A** at low  $P_d$  regime ( $2 - 20 \text{ W/cm}^2$ ).

Average lifetime values,  $\tau_d$ , of  $^5F_3$  and  $^5S_2/^5F_4$  excited states were similar as measured from blue ( $^5F_3$ ), green and NIR ( $^5S_2/^5F_4$ ) UC emissions (Figure 8.18). While  $\tau_d$  of the  $^5F_5$  energy level was greater than that of others, it rapidly diminished with increasing  $\text{Ho}^{3+}$  concentration. The longest rise time,  $\tau_r$ , was also measured for the  $^5F_5$  state, indicating that this energy level can be quickly depleted and suffers less from excitation saturation than the  $^5S_2/^5F_4$  excited state. Furthermore,  $\tau_r$  values had a maximum point at 2 mol%  $\text{Ho}^{3+}$ . It is thus assumed that the  $\tau_r$  increase between 1 and 2 mol%  $\text{Ho}^{3+}$  is a result of reduced  $^5S_2/^5F_4$  excitation saturation due to increased number of activators that can receive energy from  $\text{Yb}^{3+}$ , and shorter rise times at even greater  $\text{Ho}^{3+}$  concentration is a consequence of cross-relaxation among  $\text{Ho}^{3+}$  themselves.

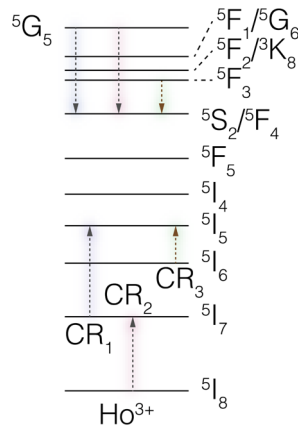


**Figure 8.17. Possible  $\text{Ho}^{3+} ^5S_2/^5F_4$  energy levels excitation in  $\text{LiYbF}_4:\text{Ho}^{3+}/\text{LiYF}_4$  RENPs.**

**Simplified  $\text{Ho}^{3+}$  energy level scheme visualizing cross-relaxation (CR) processes populating  $^5S_2/^5F_4$  energy levels, at the expense of higher laying excited states.**

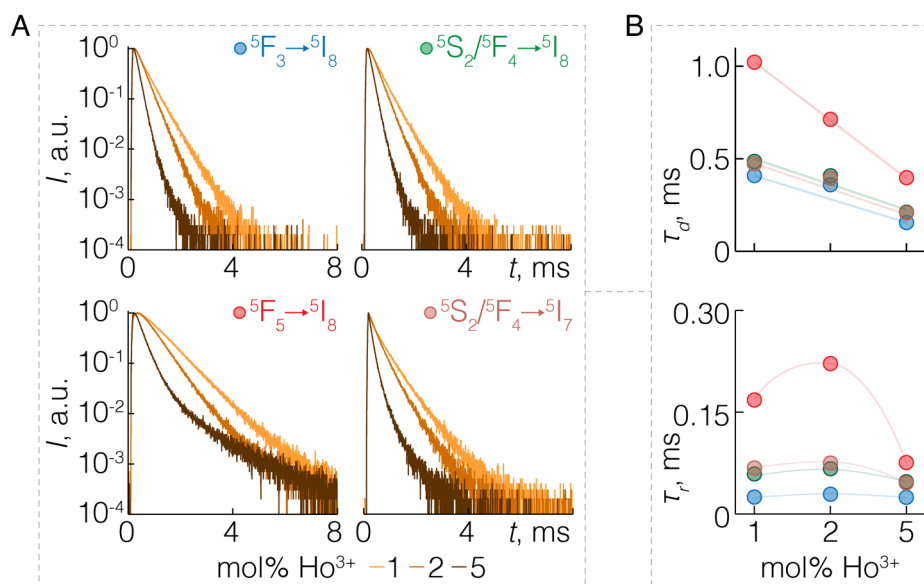


**Figure 8.18. Excited state lifetimes of LiYbF<sub>4</sub>:Ho<sup>3+</sup>/LiYF<sub>4</sub> RENPs.**

**A** – Normalized emission decay profiles of different UC emissions of LiYbF<sub>4</sub>: x mol% Ho<sup>3+</sup>/LiYF<sub>4</sub> RENPs. **B** – Summary of the average decay ( $\tau_d$ ) and rise time ( $\tau_r$ ) values obtained from the decay profiles in A.

The measured PLQY of 5 mol% Ho<sup>3+</sup>-doped RENPs displayed similar values for green (<sup>5</sup>S<sub>2</sub>/<sup>5</sup>F<sub>4</sub>) and red (<sup>5</sup>F<sub>5</sub>) UC emission bands across the whole excitation  $P_d$  range, while PLQY of blue (<sup>5</sup>F<sub>3</sub>) UC emission was few orders of magnitude lower. However, the PLQY of this emission band also increased more rapidly with the excitation  $P_d$ , owing to a higher-order excitation of <sup>5</sup>F<sub>3</sub> state. Overall, at  $P_d \sim 90$  W/cm<sup>2</sup> the net PLQY was 0.074%, with the <sup>5</sup>F<sub>3</sub> (blue), <sup>5</sup>S<sub>2</sub>/<sup>5</sup>F<sub>4</sub> (green+NIR) and <sup>5</sup>F<sub>5</sub> (red) energy levels, respectively contributing 0.0009, 0.039 and 0.035% (Figure 8.19).

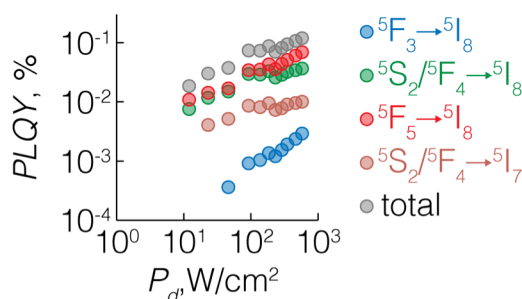


**Figure 8.19. PLQY of UC emission of LiYbF<sub>4</sub>:Ho<sup>3+</sup>/LiYF<sub>4</sub> RENPs.**

PLQY of individual Ho<sup>3+</sup> emission bands of LiYbF<sub>4</sub>: 5 mol% Ho<sup>3+</sup>/LiYF<sub>4</sub> RENPs as a function of excitation  $P_d$ .

## 8.5 Discussion

The library of LiYbF<sub>4</sub>:RE<sup>3+</sup>/LiYF<sub>4</sub> RENPs, where RE<sup>3+</sup> – Tm<sup>3+</sup>, Er<sup>3+</sup>, and Ho<sup>3+</sup>, was created to provide a more accurate picture of the spectral characteristics of LiYbF<sub>4</sub>-type RENPs, that eventually could be used in constructing the therapeutic layer of decoupled theranostic RENPs. These RENPs featured an Yb<sup>3+</sup>-based core, with an average separation between neighboring

RE<sup>3+</sup> of around 0.41 nm (see below) and a thicker-than-5 nm inert shell. This architecture ensures that the absorbed excitation energy is strictly confined to the core of the RENPs and absorption saturation among Yb<sup>3+</sup> is reached quickly. Introduction of activator ions allows Yb<sup>3+</sup> to relax from the excited state via non-radiative energy transfer, i.e. ETU, and even co-operative sensitization.<sup>[234]</sup> As was observed from Tm<sup>3+</sup>- or Ho<sup>3+</sup>-RENPs at low doping, excitation saturation also affects the lower lying excited states of these dopants, increasing the probability of higher state population via ETU. This leads to a greater contribution of higher-order UC emissions to the total photoluminescence spectrum of the activator ions, however, it is case-by-case specific. In contrast to Er<sup>3+</sup>- or Ho<sup>3+</sup>-RENPs where ETU from Yb<sup>3+</sup> is near-resonant, the Yb<sup>3+</sup> → Tm<sup>3+</sup> ETU processes are highly non-resonant, requiring absorption or emission of lattice phonons. The largest energy mismatch is present at the <sup>1</sup>D<sub>2</sub> excited state of Tm<sup>3+</sup>, thus to facilitate the four- and five-photon excitation of <sup>1</sup>D<sub>2</sub> and <sup>1</sup>I<sub>6</sub> energy levels, respectively, additional population pathways are needed. Increasing Tm<sup>3+</sup> doping leads to a reduced distance between the neighboring Tm<sup>3+</sup> and promotes energy transfer via cross-relaxation. In fact, for each activator studied, cross-relaxation processes became quickly apparent with increasing RE<sup>3+</sup> concentration, as witnessed from the linear decrease in the lifetimes of their excited states.<sup>[248]</sup> Thus for higher Tm<sup>3+</sup> doping, cross-relaxation plays an important role in distributing excitation energy from <sup>1</sup>G<sub>4</sub> to <sup>1</sup>D<sub>2</sub> states, while the latter then leads to a more efficient ETU excitation of the <sup>1</sup>I<sub>6</sub> energy level. Overall, higher doping influences UC emission of the RENPs by: i) exponentially increasing the number of available emissive centers, and ii) reducing the mean distance between them, which has an impact of several orders of magnitude on the non-resonant energy transfer (ET) rates for dipole-dipole (d-d), dipole-quadrupole (d-q), and quadrupole-quadrupole (q-q) interactions (Figure 8.20).<sup>[249,250]</sup>

Here, the number of dopants, #, and distance, *d*, between the RE<sup>3+</sup> ions in the LiYbF<sub>4</sub> RENPs was estimated considering the number of RE<sup>3+</sup> in each tetragonal unit cell of the crystal being *Z* = 4, and lattice parameters *a* = *b* = 5.1335 Å and *c* = 10.588 Å. Unit cell volume, *V<sub>cell</sub>* ~ 0.279 nm<sup>3</sup>. The morphology of LiYbF<sub>4</sub> RENPs can be approximated as a bi-pyramid with the width equal to the minor axis (*w*), and height – major axis (*h*) of RENPs. In turn, volume (*V<sub>RENPs</sub>*) of RENPs' core is expressed as *V<sub>RENPs</sub>* = 1/3·*w*<sup>2</sup>·*h*. Thus, the number of RE<sup>3+</sup> dopants per RENPs' core is # = *V<sub>RENPs</sub>*/*V<sub>cell</sub>*·*Z*·[RE<sup>3+</sup>], where [RE<sup>3+</sup>] represents the molar concentration of RE<sup>3+</sup> of interest in the RENPs. The average inter-ion distance is expressed as *d* = (*V<sub>cell</sub>*/*Z*·[RE<sup>3+</sup>])<sup>1/3</sup>.

Cross-relaxation represents an important aspect in color tuning of Yb<sup>3+</sup>-based RENPs, as can be also evidenced from the CIE color maps (Figure 8.21). In terms of observable color output

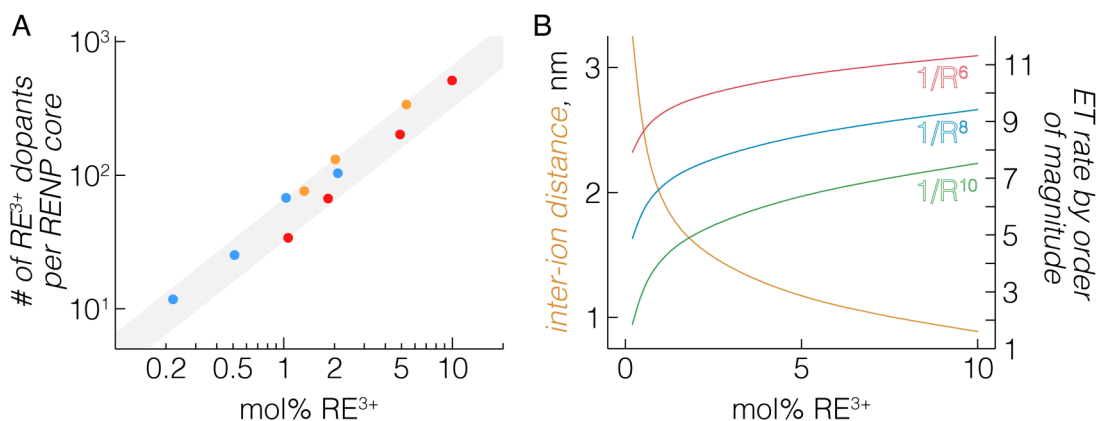


Figure 8.20. Number of RE<sup>3+</sup> consideration in LiYbF<sub>4</sub>:RE<sup>3+</sup>/LiYF<sub>4</sub> RENPs.

A – Log-log plot of # of RE<sup>3+</sup> activator ions per RENP core against mol% concentration of activator doping. Gray area indicates possible number of dopants for smallest and largest sized cores in this study. Colored points represent estimates of # of RE<sup>3+</sup> ions for each of the activator ion studied (blue – Tm<sup>3+</sup>, red – Er<sup>3+</sup>, and orange – Ho<sup>3+</sup>). B – Visualization of inter-ion distance change vs mol% concentration of RE<sup>3+</sup> doping in the LiYbF<sub>4</sub> matrix, as well as its influence, in measure of order of magnitude, on the inter-ion ET rates for d-d (1/R<sup>6</sup>), d-q (1/R<sup>8</sup>), and q-q (1/R<sup>10</sup>) interactions.

Tm<sup>3+</sup>-RENPs showed only minor change from light to deep blue photoluminescence upon increasing Tm<sup>3+</sup> concentration. Nonetheless, by varying Tm<sup>3+</sup> doping, RENPs with individually optimized UV, blue, or NIR UC emissions could be prepared for such tasks as photocleavable bond breaking,<sup>[107]</sup> optogenetic stimulation,<sup>[120]</sup> or NIR imaging,<sup>[251]</sup> respectively. Er<sup>3+</sup>-RENPs showed the least color variability with doping concentration, however, the perceived photoluminescence color could be varied from green to orange by increasing the excitation  $P_d$ ,

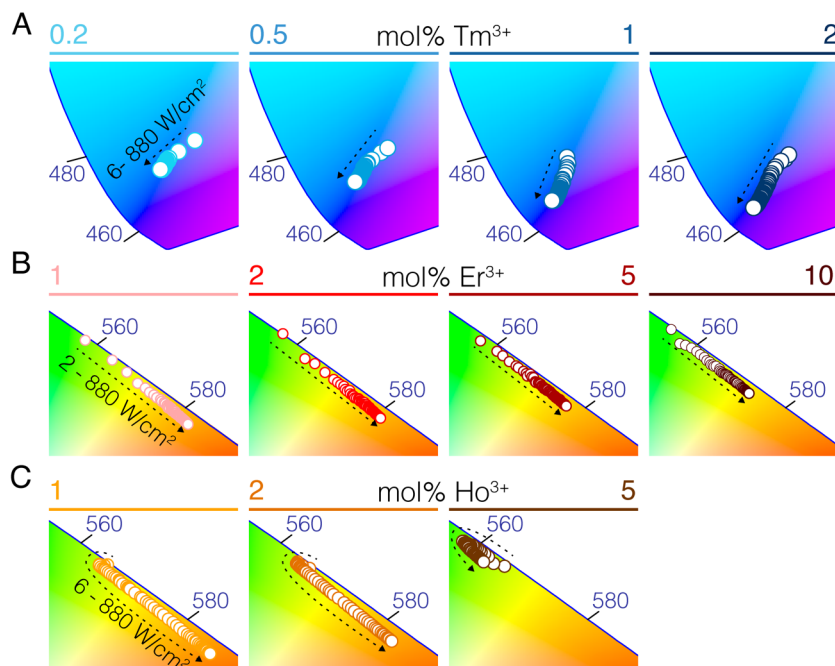


Figure 8.21. Perceived color of LiYbF<sub>4</sub>:RE<sup>3+</sup>/LiYF<sub>4</sub> RENPs.

CIE color coordinates for A – LiYbF<sub>4</sub>: x mol% Tm<sup>3+</sup>/LiYF<sub>4</sub>, B – LiYbF<sub>4</sub>: x mol% Er<sup>3+</sup>/LiYF<sub>4</sub>, and C – LiYbF<sub>4</sub>: x mol% Ho<sup>3+</sup>/LiYF<sub>4</sub>RENPs at different 960 nm laser excitation  $P_d$ .

and the dynamic range of this change was narrower at greater concentrations of  $\text{Er}^{3+}$ . Overall, these RENPs have predominantly red ( ${}^4\text{F}_{9/2}$ ) UC emission, which is sought after in PDT to excite PS in the vicinity of RENPs, like  $\text{Ce}_6$  in chapters 4 and 6.<sup>111,112,252</sup>  $\text{Ho}^{3+}$ -RENPs also showed intense red emission, however its *PLQY* was an order of magnitude lower than that of  $\text{Er}^{3+}$ -RENPs, making the latter a much better option for PDT. Nonetheless, the color invariability of 5 mol%  $\text{Ho}^{3+}$ -doped RENPs across a broad excitation  $P_d$  range could be interesting in lighting and security print applications requiring constant color output. Aside from the color of UC emission, the lifetimes of different excited states of  $\text{Tm}^{3+}$ -,  $\text{Er}^{3+}$ -, and  $\text{Ho}^{3+}$ -RENPs varied notably with doping concentration, which can be harnessed in multiplexing and sensing applications. Furthermore, the downshifting emission bands, further in the NIR, of these RENPs could be used for deep tissue imaging (Figure 8.22).

The *PLQY* measurements revealed that for  $\text{Er}^{3+}$ - and  $\text{Ho}^{3+}$ -doped RENPs  $\text{Na}^+$ -based systems remain unmatched in upconversion efficiency.<sup>[253,254]</sup> Yet the presence of high  $\text{Yb}^{3+}$  content (4-5 times more than if  $\text{Yb}^{3+}$  were dopants) allows  $\text{Yb}^{3+}$ -based systems to compete in terms of

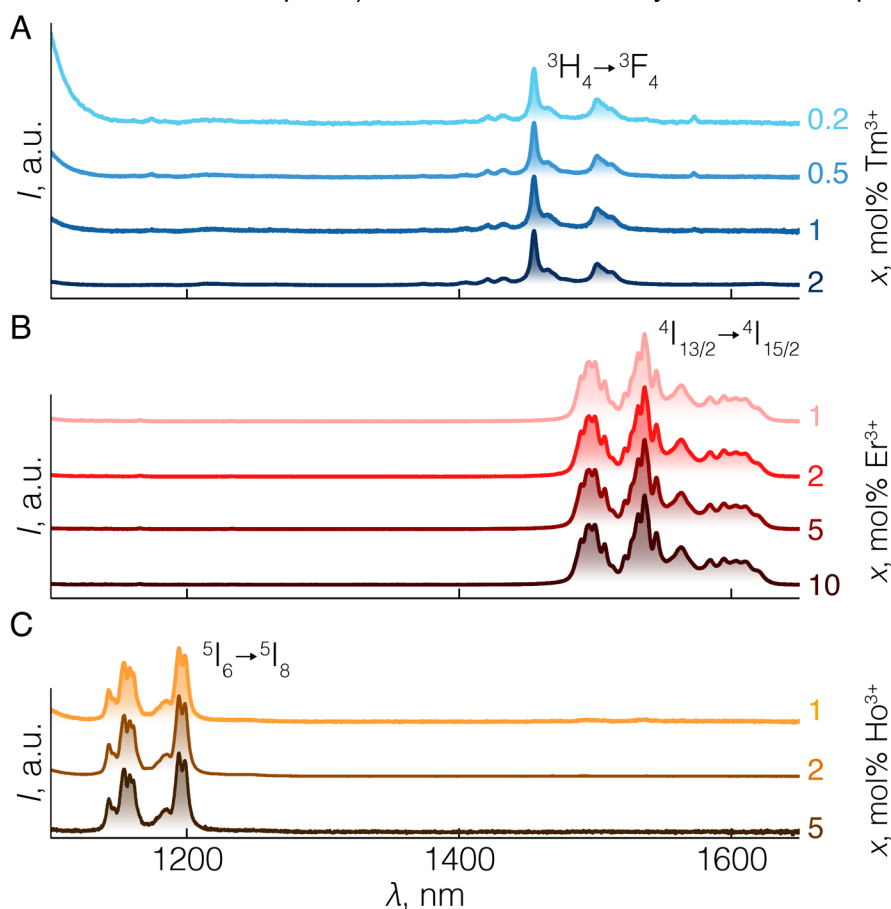


Figure 8.22. DS emission of  $\text{LiYbF}_4:\text{RE}^{3+}/\text{LiYF}_4$  RENPs.

Normalized DS emission spectra of  $\text{LiYbF}_4: x \text{ mol}\% \text{RE}^{3+}/\text{LiYF}_4$  RENPs under 960 nm excitation ( $\sim 30 \text{ W}/\text{cm}^2$ ). A –  $\text{Tm}^{3+}$ , B –  $\text{Er}^{3+}$ , C –  $\text{Ho}^{3+}$ .

brightness (product of *PLQY* and absorbance of RENPs). A more intriguing case is represented by  $\text{Tm}^{3+}$ -RENPs. Following the discussion of Zhang et al.,<sup>[255]</sup> the  $\text{Tm}^{3+}$  energy levels in  $\text{Li}^+$ -based hosts are blue-shifted compared to when  $\text{Tm}^{3+}$  is present in  $\text{NaYF}_4$  or  $\text{NaYbF}_4$  matrices. It is thus believed that this slight shift is the contributing factor for  $\text{Li}^+$ -based RENPs to generate higher order  $\text{Tm}^{3+}$  UC emission more efficiently, as it reduces energy mismatch between the non-resonant  $\text{Yb}^{3+} \rightarrow \text{Tm}^{3+}$  ETU. Still, as explored by Meijer et al.,<sup>[256]</sup> classic  $\text{LiYF}_4:\text{Tm}^{3+}$ ,  $\text{Yb}^{3+}$  RENPs feature orders of magnitude more efficient NIR emission ( $^3\text{H}_4 \rightarrow ^3\text{H}_6$ ) than UV or blue. Similar observations were reported by Kraft et al. for  $\text{NaYF}_4:\text{Tm}^{3+}$ ,  $\text{Yb}^{3+}$  RENPs.<sup>[257]</sup> Here, the *PLQY* of transitions stemming from the  $^1\text{I}_6$  (UV),  $^1\text{D}_2$  (UV/blue) and  $^1\text{G}_4$  (blue/red) energy levels was also one or two orders lower than that coming from  $^3\text{H}_4$  (NIR) excited state. However, *PLQY* of these emissions were either on par or greater than what was measured for much larger  $\text{LiYF}_4$ , as well as  $\text{NaYF}_4$  RENPs. Coupled with large  $\text{Yb}^{3+}$  content (hence high light absorption capacity), this makes  $\text{LiYbF}_4:\text{Tm}^{3+}/\text{LiYF}_4$  an overall brighter UV/blue light emitter and a more suitable candidate for high photon energy demanding applications. In addition, the total *PLQY* of  $\text{Tm}^{3+}$ -RENPs was close to few other studies on  $\text{LiYbF}_4:\text{Tm}^{3+}/\text{LiYF}_4$  RENPs, where either the same or greater values (possibly due to larger RNP size) were reported.<sup>[50,234,258]</sup>

$\text{LiYbF}_4:\text{RE}^{3+}/\text{LiYF}_4$  RENPs present an interesting formulation in the development of next generation upconversion probes, though to tap into their complete potential wider range of studies would be still necessary; especially, those complemented with theoretical modeling of excitation/emission dynamic in  $\text{Yb}^{3+}$ -based RENPs. It is also important to note that although RENPs might appear equal in composition and size, a multitude of factors can still affect their photoluminescence. When it comes to the shelling procedures particularly, reducing interlayer ion migration,<sup>[237]</sup> optimizing crystallization temperature,<sup>[259]</sup> removing hydroxyl groups,<sup>[253]</sup> and other factors all alter the upconversion efficiency of RENPs. Nonetheless, for the purposes of understanding how to create more efficient and fine-tuned multifunctional RENPs, herein presented optimization results are an invaluable first step towards the future development of decoupled theranostics  $\text{Li}^+$ -based RENPs.

## 9 SINGLE-BAND NANOTHERMOMETRY – Nd<sup>3+</sup>

---

The decoupled theranostic RENPs in chapter 6 were presented as nanothermometers operating by the intensity ratio between the Stark sub-level transitions of Nd<sup>3+</sup>, comprising the emission band around 1060 nm. Such single-band nanothermometry approach is particularly attractive to circumvent the uneven quenching of different emission bands of a nanothermometer, as emitted light passes through tissues with inhomogeneous absorption profile. Yet the number of Nd<sup>3+</sup> single-band nanothermometers, especially those that use 1060 nm DS emission for temperature sensing, is quite limited. Most of these studies also report on Nd<sup>3+</sup> single-band nanothermometry using RENPs with high size polydispersity or inherent lack of core/shell engineering.<sup>[144,225,260]</sup> Size polydispersity makes it impractical to use RENPs in a biomedical context, due to unpredictable behavior of differently sized RENPs in living objects; while shelling strategies are desirable to improve photoluminescence intensity of RENPs and endow them with additional functionalities. Moreover, to satisfy these requirements fine structure of Nd<sup>3+</sup> emission bands should be easy to resolve for a straightforward implementation of single-band nanothermometry. Li<sup>+</sup>-based RENPs are apt candidates to meet all of these conditions.

Optical nanothermometry in the NIR with Li<sup>+</sup>-based RENPs (LiYF<sub>4</sub>, LiLuF<sub>4</sub>) is a relatively new undertaking,<sup>[51,252]</sup> that requires additional exploration for a complete landscape of its peaks and valleys to emerge. Here, LiLuF<sub>4</sub>:Nd<sup>3+</sup> RENPs as NIR contrast agents and nanothermometers are investigated considering all three Nd<sup>3+</sup> DS emissions, covering BW-I and BW-II. These RENPs were synthesized following a modified first nuclei synthesis/stabilization protocol developed in chapter 7, which allowed to synthesize uniform RENPs of various Nd<sup>3+</sup> doping and carrying LiLuF<sub>4</sub> or LiYF<sub>4</sub> inert shell. Careful selection of integration ranges that define LIR thermometric parameters of LiLuF<sub>4</sub>:Nd<sup>3+</sup> RENPs resulted in more than doubling of relative thermal sensitivity as compared to that presented for the decoupled theranostics RENPs in chapter 6. Furthermore, appropriateness of these Nd<sup>3+</sup> doped RENPs for subcutaneous imaging and transient temperature measurements was evaluated.

*Herein results were published as: “Advancing neodymium single-band nanothermometry” A. Skripka, A. Morinvil, M. Matulionyte, T. Cheng and F. Vetrone, Nanoscale, 11 (23), 11322-11330, 2019.*

*Mr. Morinvil and Dr. Cheng have carried out the synthesis of various RENPs, their transfer to water, and TEM imaging and image analysis.*

## 9.1 RENP preparation and characterization

The  $\text{LiLuF}_4$ : x mol%  $\text{Nd}^{3+}/\text{LiLuF}_4$  and  $\text{LiLuF}_4$ : x mol%  $\text{Nd}^{3+}/\text{LiYF}_4$  core/shell RENPs (x = 1, 2.5, 5) were prepared via modified the FN synthesis/stabilization method as reported in chapter 7.<sup>[242]</sup> FN were synthesized via heat-up approach, where 1 mmol each of Li-TFA and Lu/Nd-TFA precursors were degassed and dissolved in a mixture of 5 mL each of OA and OM, and 10 mL ODE. Backfilled with Ar, the temperature was raised to 330 °C, and the mixture was allowed to react for 1 h. Afterwards, the mixture was cooled down to RT and the synthesized FN were transferred to Falcon centrifuge tubes (50 mL) for the subsequent stabilization step.

Core RENPs were then formed by the stabilization of FN in an excess of OA. FN (0.5 mmol, ~10 mL of stock solution) were mixed with 15 mL each of OA and ODE in a 100 mL three-neck round bottom flask. The solution was degassed at 110 °C under vacuum and magnetic stirring for 30 min. Then, backfilled with argon and the temperature was raised to 330 °C. After 1 h of reaction, the mixture was cooled to room temperature and a small portion (0.5 mL) of core RENPs was sampled for structural characterization.

Core/shell RENPs were prepared by hot-injection shelling of ~0.1 mmol of stabilized core RENPs, dispersed in equal parts of OA and ODE up to a total volume of 20 mL (Solution A). 0.25 mmol each of Li-TFA and Lu-TFA (or Y-TFA, Gd-TFA) in 10 mL each of OA and ODE constituted the shelling solution B. Both solutions were degassed under vacuum and magnetic stirring at 110 °C for 30 min. After degassing, the flask was backfilled with argon and the temperature was raised to 315 °C. After 1 h of reaction, the mixture was cooled to RT. Resultant core/shell RENPs were washed and re-dispersed in hexane for further structural and optical characterization. RENPs were transferred to water via ligand removal procedure.

Two sets of core/shell  $\text{Nd}^{3+}$ -RENPs were synthesized,  $\text{LiLuF}_4$ : $\text{Nd}^{3+}/\text{LiLuF}_4$  and  $\text{LiLuF}_4$ : $\text{Nd}^{3+}/\text{LiYF}_4$ , distinct by  $\text{Nd}^{3+}$  doping concentration and inert shell composition. Under the TEM, the well-defined bi-pyramidal morphology of RENPs could be observed (Figure 9.1). The sizes of the core and core/shell RENPs were determined by their major x minor axes.  $\text{LiLuF}_4$ : x mol%  $\text{Nd}^{3+}$  core-only RENPs were around 20 x 16 nm in size, while their  $\text{LiLuF}_4$ : $\text{Nd}^{3+}/\text{LiLuF}_4$  and  $\text{LiLuF}_4$ : $\text{Nd}^{3+}/\text{LiYF}_4$  core/shell counterparts were up to 34 x 27 nm, featuring at least 5 nm thick inert shell. Pure tetragonal (*I*41/a) phase of all  $\text{Nd}^{3+}$ -RENPs was confirmed by XRD (see Appendix I). Growth of  $\text{LiGdF}_4$  inert shell was also attempted, however proved to be unviable, due to lattice mismatch induced by compressive strain when grown over  $\text{LiLuF}_4$ .<sup>[261]</sup> Morphological changes and increase in the size of RENPs was observed, but a secondary population of NPs ascribable to pure  $\text{LiGdF}_4$  appeared (Figure 9.2).

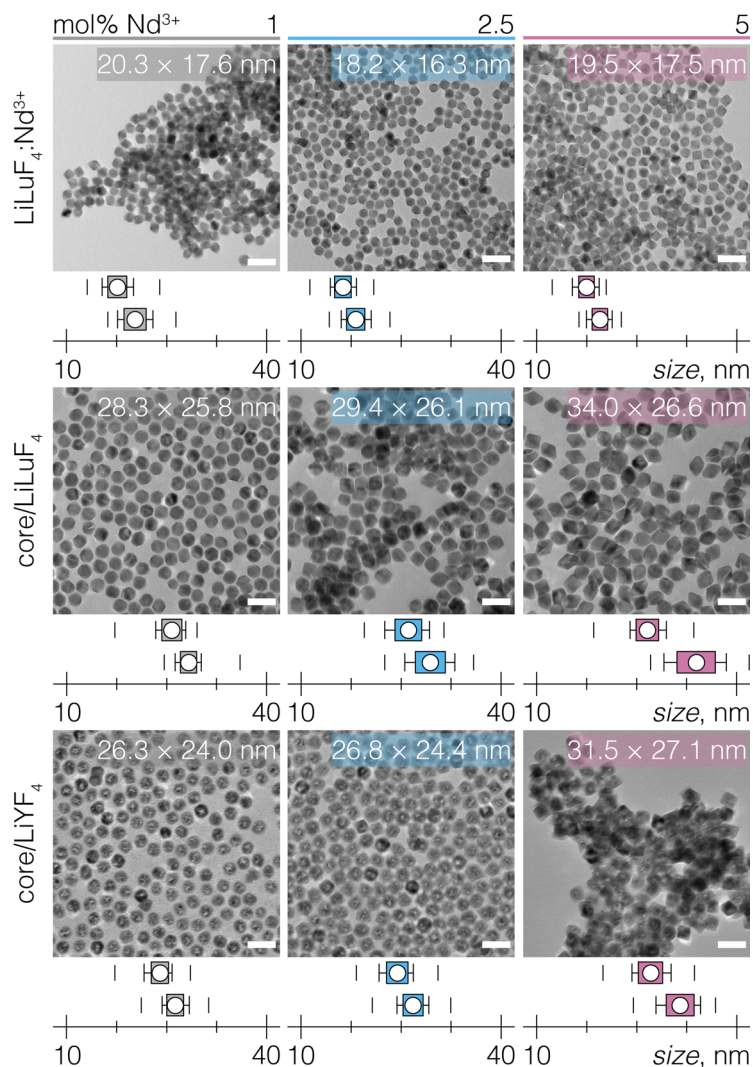


**Figure 9.1. Structural characterization of  $\text{LiLuF}_4:\text{Nd}^{3+}/\text{LiLuF}_4$  ( $\text{LiYF}_4$ ) RENPs.**

TEM images of  $\text{LiYbF}_4: x \text{ mol}\% \text{Nd}^{3+}/\text{LiLuF}_4$  ( $\text{LiYF}_4$ ) RENPs and their respective size distributions along major (bottom boxes) and minor axis (top boxes). Scale bar 50 nm. Box plots indicate: mean value (dot), SD (box outline), 5<sup>th</sup> and 95<sup>th</sup> percentiles (whiskers), and maximum/minimum values (dashes).

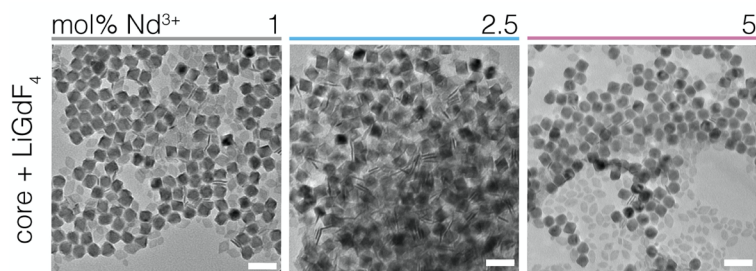


**Figure 9.2. Structural characterization of  $\text{LiLuF}_4:\text{Nd}^{3+} + \text{LiGdF}_4$  RENPs.**

TEM images of  $\text{LiLuF}_4: x \text{ mol}\% \text{Nd}^{3+}$  RENPs after attempted shelling with Li- and Gd-TFA.

Excited with 793 nm radiation, DS emission bands of  $\text{Nd}^{3+}$ -RENPs were present around 880, 1060 and 1320 nm, corresponding to the  ${}^4\text{F}_{3/2} \rightarrow {}^4\text{I}_{9/2}$ ,  ${}^4\text{I}_{11/2}$ , and  ${}^4\text{I}_{13/2}$  radiative transitions, respectively (Figure 9.3). Core/shell RENPs were brighter than their core-only counterparts,

owing to the presence of the passivating  $\text{LiLuF}_4$  (or  $\text{LiYF}_4$ ) shell. In terms of net photoluminescence intensity, only minor differences were observed for RENPs carrying the same shell but with varying  $\text{Nd}^{3+}$  concentration. Yet, RENPs shelled with  $\text{LiLuF}_4$  appeared generally brighter than those having the  $\text{LiYF}_4$  shell. Due to non-exact matching of the shell thicknesses between different core/shell RENPs ( $\text{LiYF}_4$  shells being systematically thinner), it was hard to definitively conclude that  $\text{LiLuF}_4$  shelling is superior to that of  $\text{LiYF}_4$ . Furthermore, absolute *PLQY* measurements, like in chapter 3, would be required to settle this question with accurate quantitative data. Overall,  $\text{LiLuF}_4$ : 2.5 mol%  $\text{Nd}^{3+}/\text{LiLuF}_4$  RENPs were selected as the representative sample for further imaging and thermometric studies. This sample provided considerable amount of  $\text{Nd}^{3+}$  for 793 nm excitation to be absorbed, relatively bright photoluminescence, and minimal cross-relaxation among  $\text{Nd}^{3+}$  that can result in undesired heating.<sup>[262]</sup> It is also worth noting that RENPs with higher  $\text{Lu}^{3+}$  concentration can bring additional advantage of X-ray imaging to these nanostructures.<sup>[263]</sup>

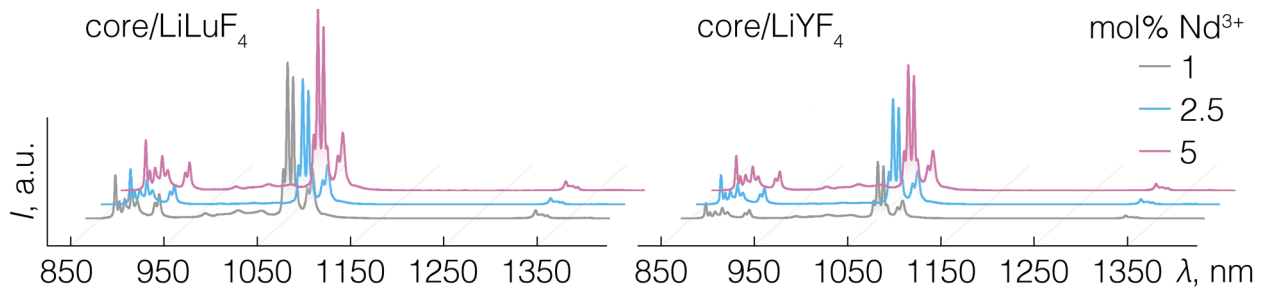


**Figure 9.3. Spectral characterization of  $\text{LiLuF}_4$ : $\text{Nd}^{3+}/\text{LiLuF}_4$  ( $\text{LiYF}_4$ ) RENPs.**

**DS emission spectra of  $\text{LiLuF}_4$ : x mol%  $\text{Nd}^{3+}/\text{LiLuF}_4$  (left) and  $\text{LiLuF}_4$ : x mol%  $\text{Nd}^{3+}/\text{LiLuF}_4$  (right) RENPs (x = 1, 2.5, 5) under 793 nm excitation. Excitation power density  $\sim 49 \text{ W/cm}^2$ .**

## 9.2 $\text{Nd}^{3+}$ single-band nanothermometry

Closer examination of the  $\text{LiLuF}_4$ : 2.5 mol%  $\text{Nd}^{3+}/\text{LiLuF}_4$  RENPs' photoluminescence spectra at two distinct temperatures (20 and 45 °C) allowed to distinguish spectral regions, which had most noticeable variation with temperature (Figure 9.4). For each of the  ${}^4\text{F}_{3/2} \rightarrow {}^4\text{I}_{9/2}$ ,  ${}^4\text{I}_{11/2}$ , and  ${}^4\text{I}_{13/2}$   $\text{Nd}^{3+}$  radiative transitions, several integration ranges within and between (peaks and valleys) their Stark components were defined, as candidates for LIR based temperature sensing. For the  ${}^4\text{F}_{3/2} \rightarrow {}^4\text{I}_{9/2}$  transition, three integration ranges were chosen:  $I_1$  (866.2-869.6 nm),  $I_2$  (883.2-884.2 nm), and  $I_3$  (912.5-913.7 nm). Here,  $I_1$  served as a common reference for  $I_2$  and  $I_3$ , thus two LIR thermometric parameters,  $\Delta$ , could be defined:  $\Delta_1 = I_1/I_2$  and  $\Delta_2 = I_1/I_3$ . In the case of the  ${}^4\text{F}_{3/2} \rightarrow {}^4\text{I}_{11/2}$  transition, two thermometric parameters  $\Delta_1 = I_1/I_3$  and  $\Delta_2 = I_2/I_3$  were defined, where the three integration ranges were:  $I_1$  (1045.3-1049.6 nm),  $I_2$  (1050.7-1055.9 nm), and  $I_3$  (1055.9-

1057.2 nm). The  $I_3$  served as the common reference. The  ${}^4F_{3/2} \rightarrow {}^4I_{13/2}$  transition also presented with the possibility of defining two integration ranges  $I_1$  (1316.7-1328.3 nm) and  $I_2$  (1328.4-1329.7 nm), constructing  $\Delta_1 = I_1/I_2$ . It must be noted that the temperature driven DS emission intensity changes between different Stark bands of the  $\text{Nd}^{3+} {}^4F_{3/2} \rightarrow {}^4I_J$  transitions stem from the thermal repopulation of the  ${}^4F_{3/2}$  ( $R_1$ ) and  ${}^4F_{3/2}$  ( $R_2$ ) Stark sub-levels, spectral shift and line broadening (see section 1.5.1 for more detail). Each of these phenomena can be individually used for optical nanothermometry, yet photoluminescence intensity change with temperature of here defined integration ranges stems from the cumulative influence of multiple factors.

In the physiological temperature range (20-45 °C), all the thermal parameters,  $\Delta$ , varied linearly with the temperature (Figure 9.5 A), validating the possibility to intermix different factors contributing to the  $\text{Nd}^{3+}$  temperature-driven photoluminescence intensity change. In fact, there is no universal method for temperature readout with  $\text{Nd}^{3+}$  based nanothermometers from the purely practical stand-point. The ratiometric approach is simple to realize yet lacks precision that can be achieved with more technically demanding band position or width measurements.

Although LIR based nanothermometry does provide a simple way to measure temperature, it has to be noted that adequate spectral resolution is always necessary to visualize fine Stark structure of  $\text{Nd}^{3+}$  radiative transitions for the chosen thermometric parameters  $\Delta$  to be used.

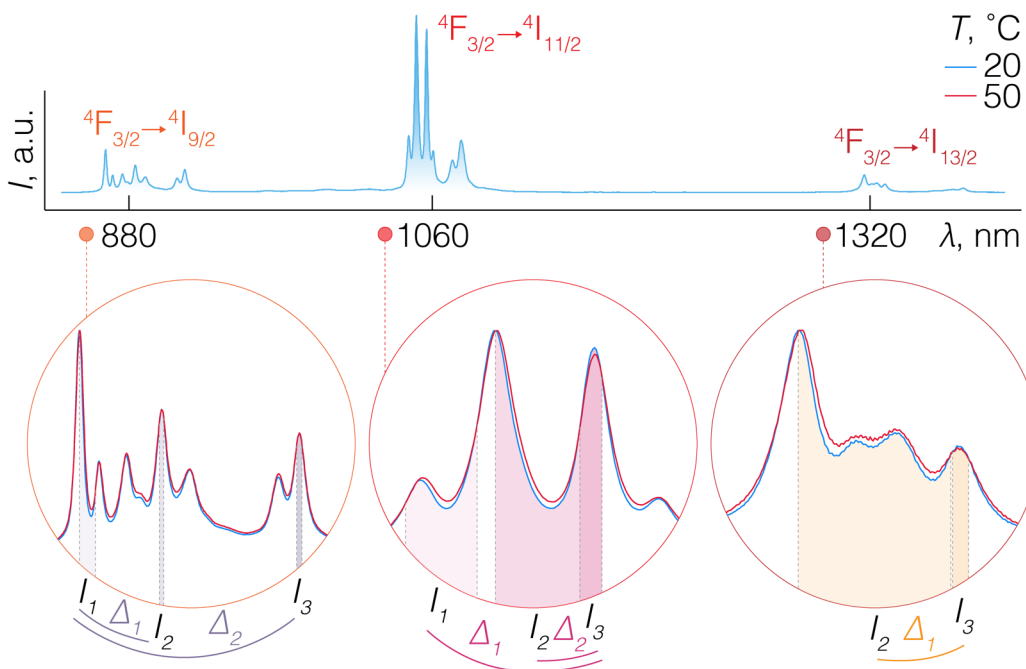
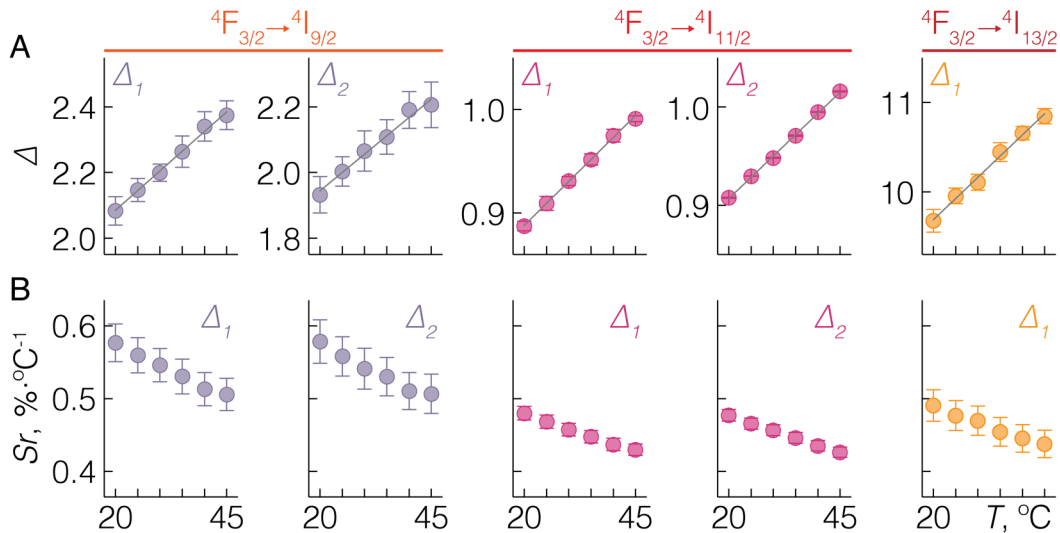


Figure 9.4. NIR nanothermometry with  $\text{LiLuF}_4:\text{Nd}^{3+}/\text{LiLuF}_4$  RENPs.

DS emission spectra of  $\text{LiLuF}_4: 2.5 \text{ mol}\% \text{Nd}^{3+}/\text{LiLuF}_4$  RENPs at 20 and 45 °C and blow-up view of individual  $\text{Nd}^{3+}$  emission bands corresponding to  ${}^4F_{3/2} \rightarrow {}^4I_{9/2}$ ,  ${}^4F_{3/2} \rightarrow {}^4I_{11/2}$ , and  ${}^4F_{3/2} \rightarrow {}^4I_{13/2}$  radiative transitions. Shaded areas represent integration ranges from which intensity values  $I_n$  and  $I_m$  ( $n, m = 1, 2, 3$ ) were calculated and by which different LIR thermometric parameters  $\Delta_k$  ( $k = 1$  or  $2$ ) were defined.



**Figure 9.5. Temperature sensing properties of LiLuF<sub>4</sub>:Nd<sup>3+</sup>/LiLuF<sub>4</sub> RENPs.**

**A** – Temperature dependence of the thermometric parameters,  $\Delta$ , defined for the  ${}^4F_{3/2} \rightarrow {}^4I_{9/2}$ ,  ${}^4F_{3/2} \rightarrow {}^4I_{11/2}$ , and  ${}^4F_{3/2} \rightarrow {}^4I_{13/2}$  radiative transitions of Nd<sup>3+</sup>, and their respective linear fits. **B** – Change of the corresponding relative thermal sensitivities,  $S_r$ , with temperature.

Relative thermal sensitivities,  $S_r$ , for each  $\Delta$  at 20 °C were calculated to be:  $\sim 0.58\ \% \cdot ^\circ\text{C}^{-1}$  for both  $\Delta_1$  and  $\Delta_2$  of the  ${}^4F_{3/2} \rightarrow {}^4I_{9/2}$  radiative transition,  $\sim 0.48\ \% \cdot ^\circ\text{C}^{-1}$  for both  $\Delta_1$  and  $\Delta_2$  of the  ${}^4F_{3/2} \rightarrow {}^4I_{11/2}$  one, and  $\sim 0.49\ \% \cdot ^\circ\text{C}^{-1}$  for  $\Delta_1$  of the  ${}^4F_{3/2} \rightarrow {}^4I_{13/2}$  radiative transition (Figure 9.5B). To the best of my knowledge, these values are thus far the highest reported among the proposed Nd<sup>3+</sup> single-band nanothermometers, and even rival with double-center nanothermometers, such as Nd<sup>3+</sup>/Yb<sup>3+</sup>.

It is interesting to note, that defining LIR purely based on the temperature dependent Boltzmann repopulation of the  $R_1$  and  $R_2$  Stark sub-levels of the  ${}^4F_{3/2}$  manifold, and disregarding contributions of peak shift and width change to the photoluminescence intensity, the attainable  $S_r$  would be governed entirely by the energy separation,  $\Delta E$ , between these levels:  $S_r = \Delta E/k_B \cdot T^2$ , where  $k_B$  is Boltzmann's constant. For the present RENPs the  $\Delta E$  can be estimated around  $55\ \text{cm}^{-1}$  (Figure 9.6), which is in line with that reported for LiYF<sub>4</sub>:Nd<sup>3+</sup>,<sup>[134]</sup> and provides a theoretically attainable  $S_r$  of only around  $0.09\ \% \cdot ^\circ\text{C}^{-1}$ . That said, for a well spectrally resolved DS emission of Nd<sup>3+</sup>, intermixing different factors that contribute to LIR change with temperature can be a viable strategy to significantly increase temperature sensitivity of Nd<sup>3+</sup>-doped RENPs.

$S_r$  of the thermometric parameters  $\Delta_2$  ( ${}^4F_{3/2} \rightarrow {}^4I_{11/2}$ ) was also investigated for RENPs of varying Nd<sup>3+</sup> doping concentration, and bearing different inert shells (LiLuF<sub>4</sub> or LiYF<sub>4</sub> shell). No clear tendency was observed for LiLuF<sub>4</sub>: x mol% Nd<sup>3+</sup>/LiLuF<sub>4</sub> RENPs (x = 1, 2.5, or 5), while in the case of LiLuF<sub>4</sub>: x mol% Nd<sup>3+</sup>/LiYF<sub>4</sub>,  $S_r$  appeared to decrease with increasing Nd<sup>3+</sup> concentration

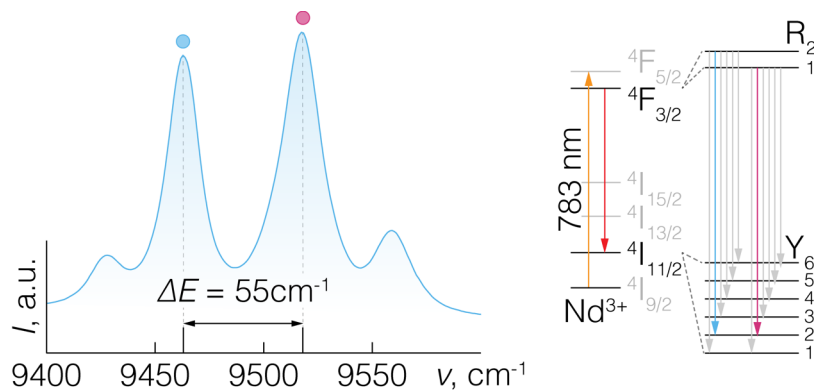


**Figure 9.6. Spectrum of LiLuF<sub>4</sub>:Nd<sup>3+</sup>/LiLuF<sub>4</sub> RENPs around 1060 nm and energy levels.**

**DS emission spectrum of LiLuF<sub>4</sub>: 2.5 mol% Nd<sup>3+</sup>/LiLuF<sub>4</sub> RENPs' <sup>4</sup>F<sub>3/2</sub> → <sup>4</sup>I<sub>11/2</sub> radiative transition and simplified energy level scheme of Nd<sup>3+</sup> with blown-up view of the inter Stark transitions between the <sup>4</sup>F<sub>3/2</sub> and <sup>4</sup>I<sub>11/2</sub> energy levels. From the peak positions of the most intense Stark bands, an energy gap  $\Delta E \sim 55 \text{ cm}^{-1}$  between the R<sub>2</sub> and R<sub>1</sub> sub-levels of <sup>4</sup>F<sub>3/2</sub> excited state can be estimated.**

(Figure 9.7). It has been previously shown that higher Nd<sup>3+</sup> doping (more than 10 mol%) can modify the  $S_r$  of different thermometric parameters in various hosts.<sup>[142]</sup> However, it is not expected for the current RENPs given that the Nd<sup>3+</sup> concentration varies only between 1 and 5 mol%. Thus, slight differences in  $S_r$  might be a consequence of RENPs' size and shape variation,<sup>[264]</sup> or more likely accrued as an experimental error. Overall, maximal  $S_r$  values remained within the 0.4-0.5 %·°C<sup>-1</sup> range, validating LIR based single-band nanothermometry for all studied RENPs.

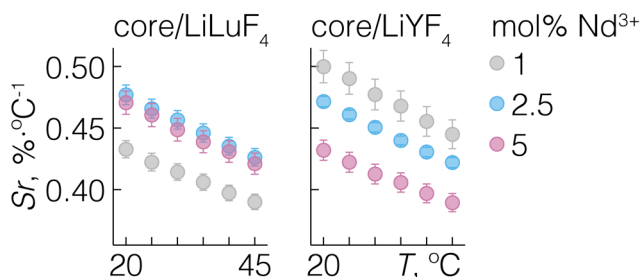


**Figure 9.7. Relative sensitivity of LiLuF<sub>4</sub>:Nd<sup>3+</sup>/LiLuF<sub>4</sub> (LiYF<sub>4</sub>) RENPs as nanothermometers.**

**$S_r$  values of thermometric parameter  $\Delta_2$  of the <sup>4</sup>F<sub>3/2</sub> → <sup>4</sup>I<sub>11/2</sub> radiative transition of LiLuF<sub>4</sub>: x mol% Nd<sup>3+</sup>/LiLuF<sub>4</sub> (left) and LiLuF<sub>4</sub>: x mol% Nd<sup>3+</sup>/LiYF<sub>4</sub> (right) RENPs.**

In addition to  $S_r$ , the temperature uncertainty,  $\delta T$ , of optical nanothermometers is one of the most important factors when considering their application. In contrast to the characterization of nanothermometers in chapter 5 and 6 (and also 10), here  $\delta T$  was estimated experimentally by consecutively measuring 200 spectra of RENPs at a fixed 28 °C temperature (Figure 9.8). The lowest  $\delta T$  was found to be 0.3 °C for  $\Delta_2$  (<sup>4</sup>F<sub>3/2</sub> → <sup>4</sup>I<sub>11/2</sub>). Unfortunately, high  $\delta T$  values for  $\Delta_1$  and  $\Delta_2$  of the <sup>4</sup>F<sub>3/2</sub> → <sup>4</sup>I<sub>9/2</sub> radiative transition are a result of low quantum efficiency in the shorter wavelength range of the employed NIR detector. Whereas, the low total DS emission intensity and with it associated high  $\delta T$  of the <sup>4</sup>F<sub>3/2</sub> → <sup>4</sup>I<sub>13/2</sub> radiative transition makes it impractical to use

for standalone single-band nanothermometry. Furthermore, repeatability,  $R$ , of different thermometric parameters  $\Delta$  was also measured and found to be: 98.1% for  $\Delta_1$  and 97.9% for  $\Delta_2$  of the  ${}^4F_{3/2} \rightarrow {}^4I_{9/2}$  radiative transition, 99.5% for  $\Delta_1$  and 99.8% for  $\Delta_2$  of the  ${}^4F_{3/2} \rightarrow {}^4I_{11/2}$  one, and 99.1% for  $\Delta_1$  of the  ${}^4F_{3/2} \rightarrow {}^4I_{13/2}$  radiative transitions (see Appendix IV).

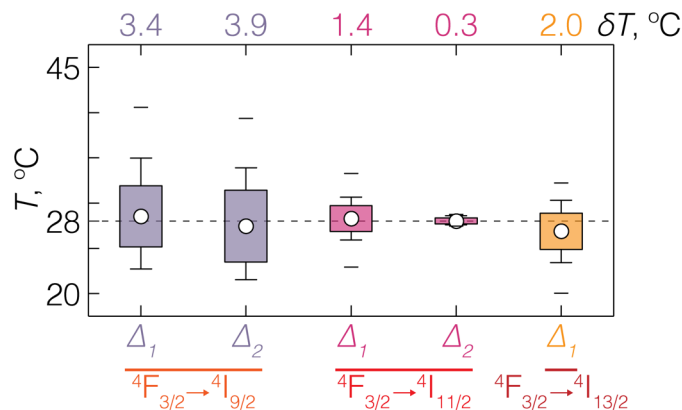


**Figure 9.8. Temperature uncertainty of  $\text{LiLuF}_4:\text{Nd}^{3+}/\text{LiLuF}_4$  RENPs as nanothermometers.**

Temperature uncertainty,  $\delta T$ , of  $\text{LiLuF}_4: 2.5 \text{ mol\% Nd}^{3+}/\text{LiLuF}_4$  RENPs determined for each thermometric parameter  $\Delta$  of the  ${}^4F_{3/2} \rightarrow {}^4I_{9/2}$ ,  ${}^4I_{11/2}$ , and  ${}^4I_{13/2}$  radiative transitions. Absolute temperature was measured from a set of 200 emission spectra at a fixed 28 °C temperature using a 5 mg/mL aqueous dispersion of RENPs.  $\delta T$  is defined as SD from the measured value. Box plots indicate: mean value (dot), SD (box outline), 5<sup>th</sup> and 95<sup>th</sup> percentiles (whiskers), and maximum/minimum values (dashes).

Given the above-mentioned characteristics of the different thermometric parameters  $\Delta$ , it can be seen that the thermometric parameter  $\Delta_2$  of the  ${}^4F_{3/2} \rightarrow {}^4I_{11/2}$  radiative transition around 1060 nm is best suited for  $\text{Nd}^{3+}$  single-band nanothermometry. Being the most intense and falling within BW-II, this  $\text{Nd}^{3+}$  emission band is more advantageous for subcutaneous temperature readout compared to the emission around 880 nm in the BW-I, which is prone to scattering and is more obscured by tissue autofluorescence. Also, the integration ranges defining the thermometric parameter  $\Delta_2$  ( ${}^4F_{3/2} \rightarrow {}^4I_{11/2}$ ) are spectrally adjacent and span extremely narrow spectral scale, which makes this parameter invariable to optical inhomogeneity of different tissues, thereby maintaining accurate temperature readout even under a tissue (see below). Also,  $\Delta$  of  ${}^4F_{3/2} \rightarrow {}^4I_{11/2}$  radiative transition is preferable to the other thermometric parameters of the  ${}^4F_{3/2} \rightarrow {}^4I_{9/2}$  and  ${}^4F_{3/2} \rightarrow {}^4I_{13/2}$  transitions, which have been demonstrated to lead to inaccurate temperature estimation resulting from self-absorption and solvent absorption effects, respectively (section 1.5.5).<sup>[173]</sup>

### 9.3 Ex vivo imaging and temperature sensing

To assess the applicability of studied RENPs as sub-cutaneous contrast agents and nanothermometers, two proof-of-concept experiments were carried out using pork fat as *ex vivo* model tissue.

Imaging capabilities of  $\text{LiLuF}_4: 2.5 \text{ mol\% Nd}^{3+}/\text{LiLuF}_4$  RENPs were tested by imaging a 2 mm wide and 0.2 mm thick glass capillary, filled with the RENPs, and placed at the back end of pork fat tissues of varying thickness,  $d$  (Figure 9.9). A 793 nm laser at a power density of  $0.5 \text{ W/cm}^2$  was used for through-tissue excitation, and a set of LP filters was used to selective reject DS emission signal stemming from the  ${}^4\text{F}_{3/2} \rightarrow {}^4\text{I}_{9/2}$  and  ${}^4\text{I}_{11/2}$  radiative transitions to the net photoluminescence of  $\text{Nd}^{3+}$ -RENPs. The intensity profiles across the width of the capillary were then studied from the acquired images. Each profile was fitted with a Lorentz function, where the full width at half maximum (FWHM) was used to assess the loss of spatial information. Increasing tissue thickness resulted in prominently increasing FWHM values irrespective of the LP filters utilized, setting clear constraints to the actual imaging that is possible with the herein employed imaging instrumentation. Nonetheless, for every tissue thickness studied, FWHM values of the capillary image were lower (by about 8–15%) when collecting only 1320 nm photoluminescence and blocking contribution from 880 and 1060 nm DS emission bands. These results indicate that although  ${}^4\text{F}_{3/2} \rightarrow {}^4\text{I}_{11/2}$  radiative transition around 1060 nm is most intense, imaging with  $\text{Nd}^{3+}$ -doped RENPs is best suited when accounting only for the 1320 nm emission,

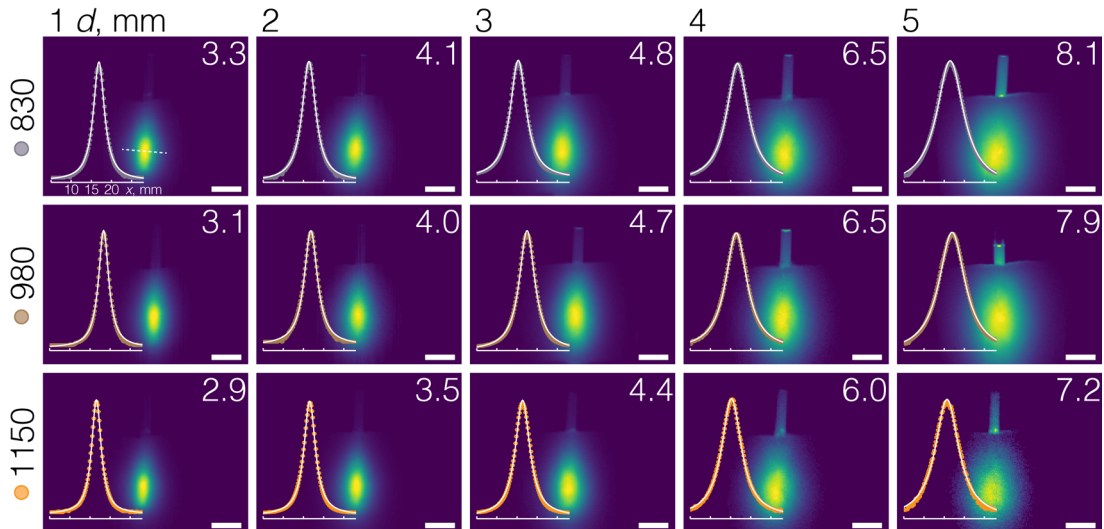
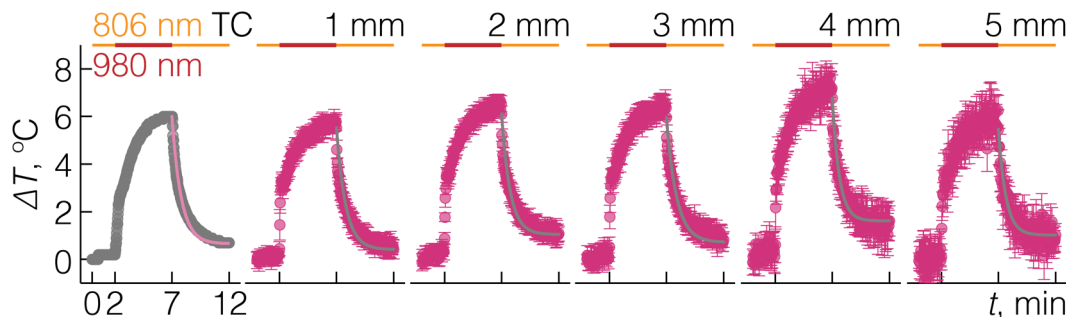


Figure 9.9. Subcutaneous imaging with  $\text{LiLuF}_4:\text{Nd}^{3+}/\text{LiLuF}_4$  RENPs *ex vivo*.

Imaging of  $\text{LiLuF}_4: 2.5 \text{ mol\% Nd}^{3+}/\text{LiLuF}_4$  RENPs in a glass capillary through pork fat tissue of varying thickness ( $d = 1\text{--}5 \text{ mm}$ ) RENPs were excited by 793 nm laser (power density on the tissue's surface  $0.5 \text{ W/cm}^2$ ), emission signal was filtered through LP830, LP980, or LP1150 nm filters and detected with an NIR camera. Intensity profiles (insets in each image, corresponding to the white line across the capillary (shown in the first image) were used to evaluate the FWHM (indicated in the top-right corner of each image) and its change with tissue thickness,  $d$ , and specific LP filter applied. Scale bars 5 mm.

as scattering for light of longer wavelengths is appreciably reduced. It is then possible to imagine a scenario where 1320 nm emission is first utilized to identify the target of interest, and 1060 nm band is subsequently used for temperature measurements.

To evaluate subcutaneous nanothermometry with present  $\text{Nd}^{3+}$ -RENPs, heating-cooling dynamics of RENPs dispersed in water were measured through pork fat tissues of varying thickness (Figure 9.10). Temperature of RENP water dispersion was monitored spectrally, utilizing RENPs as *in situ* thermometers, and via thermocouple (TC) that was placed inside the cuvette as a contact based reference. Similar to the proof-of-concept experiment in chapter 6,  $\text{Nd}^{3+}$ -RENPs were continuously excited with 793 nm laser and the DS emission around 1060 nm ( ${}^4\text{F}_{3/2} \rightarrow {}^4\text{I}_{11/2}$ ) with its  $\Delta_2$  thermometric parameter was used to determine thermal changes optically. Local heating was induced by 980 nm radiation, which was absorbed by water and converted to heat. During the first 2 min, only the 793 nm laser was ON followed by a 5 min ON period of the 980 nm laser, which was then turned OFF and the cooling of the dispersion was measured over the next 5 min with the 793 nm laser still being ON. Typical heating-cooling cycles were measured via the DS emission of RENPs for each of the pork tissue thickness studied. In each case, temperature dynamics measured optically closely resembled the one measured by the locally present TC.



**Figure 9.10.** Subcutaneous transient temperature measurement with  $\text{LiLuF}_4:\text{Nd}^{3+}/\text{LiLuF}_4$  RENPs.

Heating-cooling dynamics of 5 mg/mL aqueous colloid of  $\text{LiLuF}_4: 2.5 \text{ mol\% Nd}^{3+}/\text{LiLuF}_4$  RENPs measured directly with a TC and via optical nanothermometry ( $\Delta_2$  of the  ${}^4\text{F}_{3/2} \rightarrow {}^4\text{I}_{11/2}$  radiative transition) through varying thicknesses (1–5 mm) of pork fat. Heating was induced by 980 nm laser during the 5 min ON periods, power density was kept at  $\sim 37 \text{ W/cm}^2$ . The heat dissipation time constant,  $\tau$ , was estimated from the exponential decay fit of the cooling part.

With that in mind, the heat dissipation time constant,  $\tau$ , was determined by exponential fitting of the cooling curve, where the temperature difference,  $\Delta T$ , induced solely by 980 nm radiation was calculated between the OFF point of the 980 nm laser and the end of the cycle (Figure 9.11A, B). By tissue thickness of 4 mm, estimates of  $\tau$  began to deviate from that measured with the TC, while  $\Delta T$  values acquired significant error, all due to photoluminescence intensity extinction by the tissue. Subsequently, the temporal uncertainty,  $\delta t$ , of Nd<sup>3+</sup>-RENPs as single-band nanothermometers was calculated (Figure 9.11D). Although temperature uncertainty,  $\delta T$ , in the case of pork tissue blocking signal acquisition was not measured directly, it was extrapolated from that measured for  $\Delta_2$  ( ${}^4F_{3/2} \rightarrow {}^4I_{11/2}$ ) when no light obstruction was present (Figure 9.8). Taking into account an increase of spectral integration time by 2.5 times during the heating-cooling measurements and exponential signal attenuation by pork fat tissue ( $\exp[-0.465 \cdot d]$ ) determined from light propagation experiments (see Appendix V),  $\delta T$  would change from 0.19 to 1.23 °C with increasing tissue thickness from 1 to 5 mm, respectively. Accordingly, calculated  $\delta t$  values varied from  $(0.52 \pm 0.37)$  to  $(4.26 \pm 6.60)$  s. In the case of 3, 4, and particularly 5 mm tissue thickness,  $\delta t$  accrued significant estimation error, suggesting that its validity has to be taken cautiously. Altogether, it can be seen that transient temperature measurements via nanothermometry (with the present RENPs and measurement set-up) for relatively fast processes (on the order of tens of seconds)<sup>[150]</sup> would be most reliable at tissue depths of 1 to 2 mm. However, if the studied target exhibits slower thermal relaxation (on the order of hundreds of seconds, like in case of ischemia detection)<sup>[157]</sup> NIR nanothermometry approach can be extended to greater tissue depths. Finally, it is worth recognizing that spectral

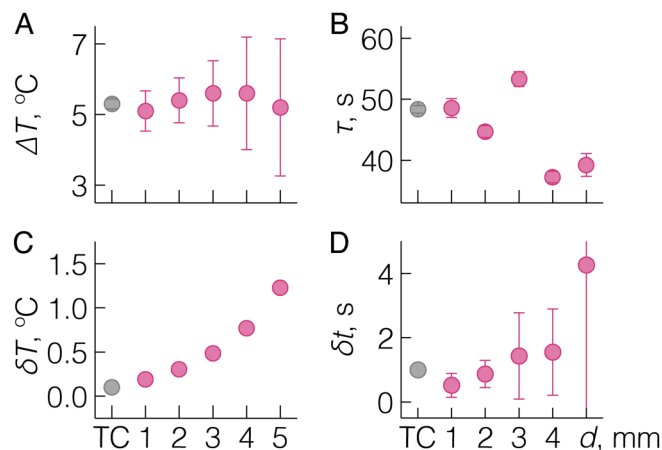


**Figure 9.11. Temperature sensing properties of LiLuF<sub>4</sub>:Nd<sup>3+</sup>/LiLuF<sub>4</sub> RENPs *ex vivo*.**

**A** –  $\Delta T$ , **B** –  $\tau$ , **C** –  $\delta T$ , and **D** –  $\delta t$  change with increasing thickness of pork fat tissue in the heating-cooling *ex vivo* experiment.  $\Delta T$  is temperature increase induced by the 980 nm laser and  $\tau$  is the relaxation time obtained from the single-exponential fit of the cooling curves (Figure 9.10). Grey points indicate the respective values obtained based on the TC measurement.

profile of  ${}^4F_{3/2} \rightarrow {}^4I_{11/2}$  radiative transition around 1060 nm did not show significant changes when passing through pork fat tissue of varying thickness (Figure 9.12). This attested to the proficiency of single-band nanothermometry to overcome faulty temperature readout due to photoluminescence spectra distortion by inhomogeneous tissue absorbance.

Taken together these results exemplify the validity of  $\text{Nd}^{3+}$  single-band nanothermometry in  $\text{Li}^+$ -based RENPs. Well defined, monodisperse in size, bright and sensitive optical nanothermometers could be constructed using  $\text{LiLuF}_4:\text{Nd}^{3+}$  formulation of RENPs, that are applicable for subcutaneous imaging and temperature sensing in the BW-II. Integration of these RENPs is particularly promising in decoupled theranostic RENPs, as seen in chapter 6. Yet, the possibility to move to the BW-III for single-band nanothermometry and take advantage of least light scattering for high contrast picture acquisition stills remains alluring and would require other optically active  $\text{RE}^{3+}$  than  $\text{Nd}^{3+}$ .

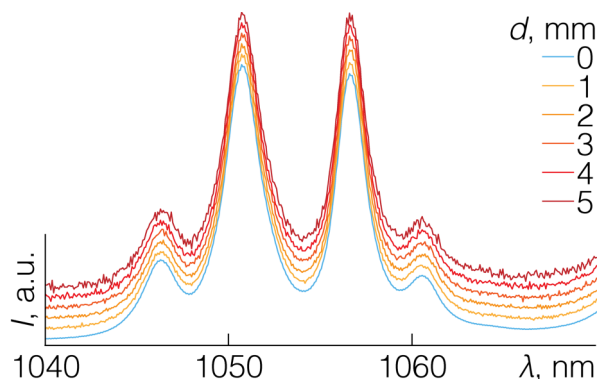


Figure 9.12. DS emission of  $\text{LiLuF}_4:\text{Nd}^{3+}/\text{LiLuF}_4$  RENPs *ex vivo*.

Normalized DS emission spectra of  $\text{LiLuF}_4: 2.5 \text{ mol\% Nd}^{3+}/\text{LiLuF}_4$  RENPs'  ${}^4F_{3/2} \rightarrow {}^4I_{11/2}$  radiative transition, collected before and after propagating through pork fat tissue of different thickness ( $d = 1\text{-}5 \text{ mm}$ ).

## 10 SINGLE-BAND NANOTHERMOMETRY – Er<sup>3+</sup>

---

As can be implied from chapters 6 and 9, single-band nanothermometry is a relatively simple and effective workaround to the tissue absorption induced distortion of RE<sup>3+</sup> photoluminescence spectra, and subsequent faulty temperature read-out. Yet, single-band nanothermometers based on Nd<sup>3+</sup> ions, are restricted to BW-I and BW-II. For the highest possible imaging contrast and accurate temperature mapping it would be beneficial to move NIR nanothermometry to BW-III. Like it was done in chapter 5, but relying on ratiometric single-band nanothermometry in BW-III, rather than DS emission bands spectrally distant from one another (i.e. Nd<sup>3+</sup> 1340 nm/Er<sup>3+</sup> 1550 nm). Literature on this topic is nonetheless scarce, as at the time only one report attempted on using Er<sup>3+</sup> DS emission around 1550 nm for single-band temperature sensing with powder RENPs, and the reported relative thermal sensitivity was far from being satisfactory.<sup>[210]</sup> Furthermore, thinking about the integration of such a Er<sup>3+</sup> single-band nanothermometers in the decoupled theranostics RENPs, for imaging and temperature sensing in BW-III, one has to consider intrinsic UC emission of Er<sup>3+</sup> and how to deliberately quench it. Left unchecked this would nullify the highlighted on-demand UC and DS emission response of decoupled theranostics RENPs.

Taking on this challenge, LiErF<sub>4</sub>:Ce<sup>3+</sup>/LiYF<sub>4</sub> RENPs were explored as candidates for NIR-to-NIR imaging and single-band nanothermometry in the BW-III. These RENPs were also synthesized following a modified first nuclei synthesis/stabilization protocol developed in chapter 7, obtaining a library of morphologically similar LiErF<sub>4</sub>: x mol% Ce<sup>3+</sup>/LiYF<sub>4</sub> RENPs with ease. As before Li<sup>+</sup>-based host was chosen to spectrally resolve the fine structure of Er<sup>3+</sup> DS emission around 1550 nm, which enabled to define spectrally adjacent integration areas for ratiometric nanothermometry. The purposeful Ce<sup>3+</sup> doping is explored as a mean to quench UC emission of these RENPs. Intriguingly, observed temperature response of RENPs depended on the vibrational modes of the solvent, as in chapter 5, as well as on the Ce<sup>3+</sup> doping. The combination of Er<sup>3+</sup> and Ce<sup>3+</sup> sets an important precedent, for the further advancement of the decoupled theranostics RENPs.

*This work was carried out jointly with Dr. Chanchal Hazra, who has conducted most of the RNP synthesis and photoluminescence thermometry measurements.*

*Herein results were published as: "Erbium Single-Band Nanothermometry in the Third Biological Imaging Window: Potential and Limitations" C. Hazra,\* A. Skripka,\* S. J. L. Ribeiro and F. Vetrone, Adv. Opt. Mater., 2020. \*equally contributing authors*

## 10.1 RENP preparation and characterization

The  $\text{LiErF}_4$ : x mol%  $\text{Ce}^{3+}/\text{LiYF}_4$  core/shell RENPs (x = 0, 1, 2, 3) were prepared via the modified FN synthesis/stabilization method as reported in chapter 7.<sup>[242]</sup> FN were synthesized via hot-injection approach, where 2.5 mmol each of Li-TFA and Er/Ce-TFA precursors were degassed and dissolved in a mixture of 3 mL each of OA and OM, and 6 mL ODE (solution B), and injected into the solution A containing 7 mL each of OA and OM, and 14 mL ODE at 330 °C. Injection rate was 1.5 mL/min. After 1 h of vigorous stirring, the mixture was cooled down to RT and the synthesized FN were transferred to Falcon centrifuge tubes (50 mL) for the subsequent stabilization step.

Core RENPs were then formed by the stabilization of FN in an excess of OA. FN (0.5 mmol, ~7 mL of stock solution) were mixed with 16.5 mL each of OA and ODE, and degassed at 125 °C under vacuum and magnetic stirring for 30 min. Then, the reaction flask was backfilled with argon and the temperature was raised to 330 °C. After 1 h of reaction, the mixture was cooled down to RT and a small portion (0.5 mL) of core RENPs was sampled for structural characterization.

Core/shell RENPs were prepared by hot-injection shelling of ~0.25 mmol of stabilized core RENPs, dispersed in equal parts of OA and ODE up to a total volume of 25 mL (Solution A). 0.75 mmol each of Li-TFA and Y-TFA in 7.5 mL each of OA and ODE constituted shelling solution B. Both solutions were degassed under vacuum and magnetic stirring at 125 °C for 30 min. After degassing, the flask was backfilled with argon and the temperature was raised to 320 °C. At this point, solution B was injected into solution A at a 0.5 mL/min injection rate. After 1 h of reaction time, the mixture was cooled down to RT. Resultant core/shell RENPs were washed and re-dispersed in hexane for further structural and optical characterization. RENPs were transferred to water via ligand exchange procedure, substituting OA for citrate.

A library of  $\text{LiErF}_4$ : x mol%  $\text{Ce}^{3+}/\text{LiYF}_4$  RENPs was synthesized, where  $\text{Ce}^{3+}$  doping varied from 0 (undoped RENPs) to 1, 2, and 3 mol%. Phase analysis of the core and core/shell RENPs was carried out by measuring their XRD spectra (see Appendix I), which matched well the reference diffraction pattern of tetragonal  $\text{LiErF}_4$  crystal. The shape and size of the RENPs, examined under TEM, indicated the formation of uniform and monodisperse RENPs of bi-pyramidal morphology with an average size along their major axis of approximately 21 and 37 nm for core and core/shell RENPs, respectively (Figure 10.1). The shell thickness for the core/shell RENPs varied between 7 and 9 nm, which was necessary to easily observe photoluminescence of

these RENPs.<sup>[59]</sup> Ce<sup>3+</sup> concentration in RENPs was determined by ICP-OES, and was 0, 1.1, 2.0, and 3.1 mol% for 0, 1, 2, and 3 mol% target values, respectively.

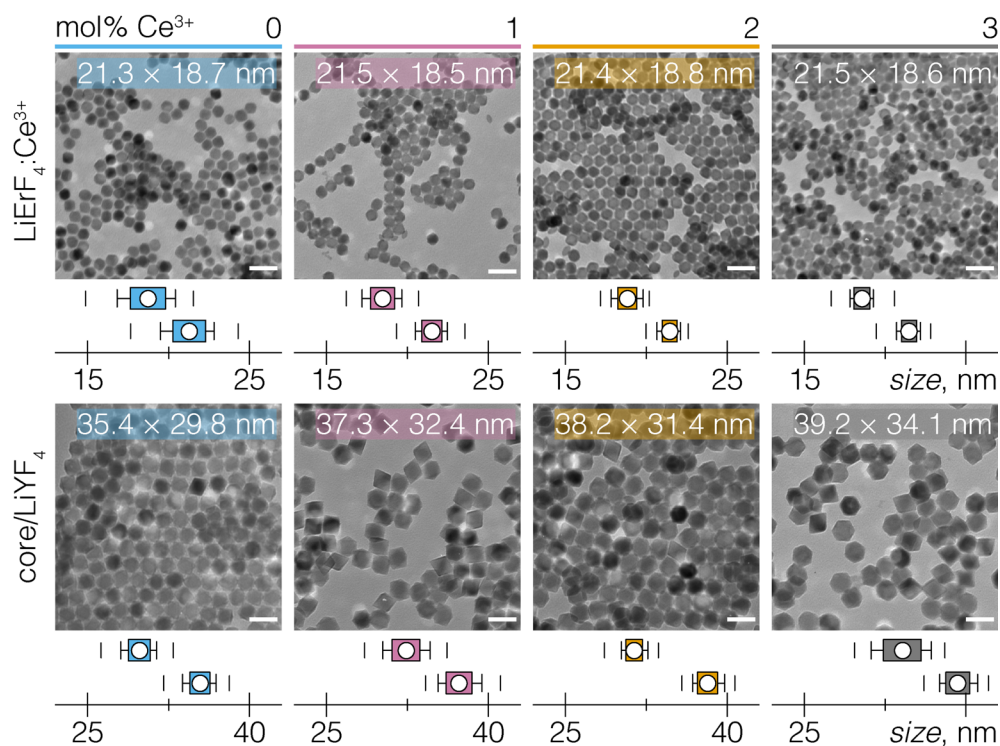


**Figure 10.1. Structural characterization of LiErF<sub>4</sub>:Ce<sup>3+</sup>/LiYF<sub>4</sub> RENPs.**

TEM images of LiErF<sub>4</sub>: x mol% Ce<sup>3+</sup>/LiYF<sub>4</sub> RENPs and their respective size distributions along major (bottom boxes) and minor axis (top boxes). Scale bar 50 nm. Box plots indicate: mean value (dot), SD (box outline), 5<sup>th</sup> and 95<sup>th</sup> percentiles (whiskers), and maximum/minimum values (dashes).

First the photoluminescence of undoped, LiErF<sub>4</sub>/LiYF<sub>4</sub>, RENPs was examined in hexane. Under 793 nm laser excitation LiErF<sub>4</sub>/LiYF<sub>4</sub> RENPs showed UC and DS emission bands in the visible and NIR spectral regions, respectively (Figure 10.2A). Excitation power density as high as 1kW/cm<sup>2</sup> was used in order to easily obtain UC emission from the RENPs. The Er<sup>3+</sup> UC emission was seen in the green (525/545 nm) and red (670 nm) regions, assigned to the <sup>2</sup>H<sub>11/2</sub>/<sup>4</sup>S<sub>3/2</sub> → <sup>4</sup>I<sub>15/2</sub> and <sup>4</sup>F<sub>9/2</sub> → <sup>4</sup>I<sub>15/2</sub> radiative transitions, respectively. Along with upconversion, the DS emission in the NIR was observed around 1550 nm, corresponding to the <sup>4</sup>I<sub>13/2</sub> → <sup>4</sup>I<sub>15/2</sub> radiative transition. To better understand the observed UC and DS processes, power plot studies were performed (Figure 10.2B). The obtained *n* values were 1.49, 1.49, and 0.77 for the green, red, and NIR emissions, respectively, which are in line with the two-photon order upconversion excitation and one-photon downshifting processes.

Based on the above results, the following excitation-emission scheme was proposed (Figure 10.2C). Note that in LiErF<sub>4</sub>/LiYF<sub>4</sub> RENPs Er<sup>3+</sup> simultaneously assume the role of excitation

sensitizers and emission activators. Under 793 nm irradiation,  $\text{Er}^{3+}$  are excited to  $^4\text{I}_{9/2}$  state via GSA, from which non-radiative decay processes (multi-phonon relaxation and cross-relaxation) populate the  $^4\text{I}_{11/2}$  and  $^4\text{I}_{13/2}$  excited states. Once in the  $^4\text{I}_{13/2}$  excited state, the  $\text{Er}^{3+}$  ions can either relax to  $^4\text{I}_{15/2}$  ground state by the radiative emission of NIR photons around 1550 nm (DS emission), or can be further excited to higher  $^2\text{H}_{11/2}/^4\text{S}_{3/2}$  states via ESA of 793 nm light. Additionally, excitation into these states can come from  $^4\text{I}_{9/2} \rightarrow ^4\text{I}_{13/2}; ^4\text{I}_{9/2} \rightarrow ^2\text{H}_{11/2}/^4\text{S}_{3/2}$  cross-relaxation.<sup>[265,266]</sup> From the  $^2\text{H}_{11/2}/^4\text{S}_{3/2}$ , excitation energy is either released as green light emission, or non-radiatively populates the red light emitting  $^4\text{F}_{9/2}$  excited state. Dominance of the red UC emission seems to indicate that the  $^2\text{H}_{11/2}/^4\text{S}_{3/2} \rightarrow ^4\text{F}_{9/2}; ^4\text{I}_{9/2} \rightarrow ^4\text{F}_{9/2}$  cross-relaxation is responsible for effective depopulation of the  $^2\text{H}_{11/2}/^4\text{S}_{3/2}$  excited states. Although, multi-phonon relaxation from  $^2\text{H}_{11/2}/^4\text{S}_{3/2}$  also leads to the greater population of red light emitting  $^4\text{F}_{9/2}$  energy level, the above mentioned cross-relaxation process is highly likely given fully  $\text{Er}^{3+}$ -based composition of RENPs.

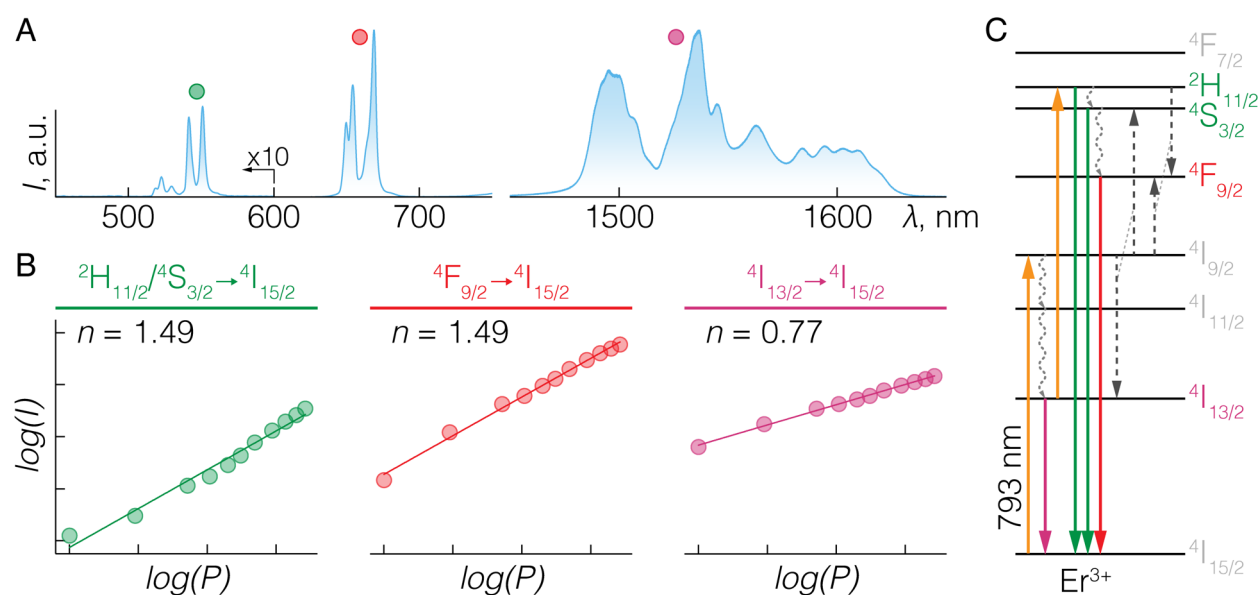
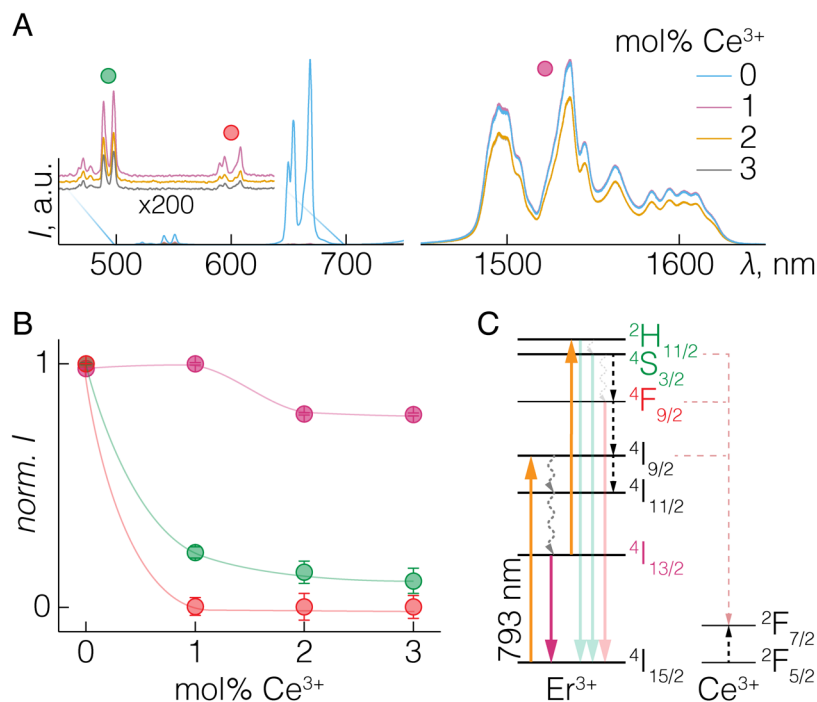


Figure 10.2. Spectral characterization of LiErF<sub>4</sub>/LiYF<sub>4</sub> RENPs

**A** – UC (left) and DS (right) emission spectrum of LiErF<sub>4</sub>/LiYF<sub>4</sub> RENPs in hexane under 793 nm excitation. Excitation power density  $\sim 1 \text{ kW/cm}^2$ . Intensities below 600 nm are multiplied by 10 for clarity. Radiative transitions are color coded with dots in A above each emission band. **B** – Intensity ( $I$ ) vs excitation power ( $P$ ) log-log plots for green ( $^2\text{H}_{11/2}/^4\text{S}_{3/2} \rightarrow ^4\text{I}_{15/2}$ ), red ( $^4\text{F}_{9/2} \rightarrow ^4\text{I}_{15/2}$ ), and NIR ( $^4\text{I}_{13/2} \rightarrow ^4\text{I}_{15/2}$ ) emissions. Slope values indicated in the top left corner were obtained from the linear fit of experimental points. **C** – Simplified excitation-emission scheme of LiErF<sub>4</sub>/LiYF<sub>4</sub> RENPs. Solid lines are radiative transitions, dashed lines are cross-relaxation processes, and wavy – non-radiative decay.

The inspiration for Ce<sup>3+</sup> doping came from a previously published report, which showed that the population of the NIR radiation emitting  $^4\text{I}_{13/2}$  energy level of  $\text{Er}^{3+}$  can be greatly enhanced by introducing Ce<sup>3+</sup>, while simultaneously quenching RENPs' UC emission.<sup>[89]</sup>

Photoluminescence spectra, under 793 nm excitation, of  $\text{LiErF}_4:\text{Ce}^{3+}/\text{LiYF}_4$  RENPs allowed to observe the effect  $\text{Ce}^{3+}$  doping had on the UC and DS emission of RENPs (Figure 10.3). Despite of near-negligible increase in DS emission intensity for 1 mol%  $\text{Ce}^{3+}$ -doped RENPs, higher 2 and 3 mol%  $\text{Ce}^{3+}$  doping led to marginal intensity quenching. These findings stand in contrast to the previously reported DS emission intensity enhancement by  $\text{Ce}^{3+}$  doping.<sup>[89,90,263]</sup> It is possible that due to the slightly different energy level positions, strong Stark sub-level splitting, and prominent cross-relaxation among  $\text{Er}^{3+}$ , the highly non-resonant  $^4I_{11/2}(\text{Er}^{3+}) \rightarrow ^2F_{7/2}(\text{Ce}^{3+})$  phonon-assisted energy transfer is less influential in  $\text{LiErF}_4$  than in Na-type ( $\text{NaYbF}_4:\text{Er}^{3+}, \text{Ce}^{3+}; \text{NaLuF}_4:\text{Gd}^{3+}, \text{Yb}^{3+}, \text{Er}^{3+}, \text{Ce}^{3+}$ ) RENPs. The energy difference between the  $^2F_{5/2}-^2F_{7/2}$  energy levels of  $\text{Ce}^{3+}$  is  $\sim 2200 \text{ cm}^{-1}$  (for the most intense inter-Stark  $Z_1 \rightarrow Y_2$  electronic transition)<sup>[267]</sup> which would require involvement of multiple lattice phonons to bridge the  $^4I_{11/2}-^4I_{13/2}$  energy gap ( $\sim 3650 \text{ cm}^{-1}$ )<sup>[268]</sup> of  $\text{Er}^{3+}$ . Meanwhile, subsequent decrease in DS emission intensity at higher  $\text{Ce}^{3+}$  doping has been tentatively attributed to the phonon-assisted energy transfer from the  $^4I_{13/2}$  excited state of  $\text{Er}^{3+}$  to  $\text{Ce}^{3+}$ ,<sup>[269]</sup> however more detail studies are needed to ascertain this phenomenon. On the other hand, in line with previous reports, UC emission



**Figure 10.3. Spectral characterization of  $\text{LiErF}_4:\text{Ce}^{3+}/\text{LiYF}_4$  RENPs**

**A** – UC (left) and DS (right) emission spectra of  $\text{LiErF}_4: x \text{ mol}\% \text{Ce}^{3+}/\text{LiYF}_4$  RENPs ( $x = 0, 1, 2, 3$ ) in hexane under 793 nm excitation. Excitation power density  $\sim 1 \text{ kW}/\text{cm}^2$ . Inset shows the 500-700 nm spectral range multiplied 200 times for clarity. Radiative transitions are color coded with dots in A above each emission band. **B** – Integrated green ( $^2H_{11/2}/^4S_{3/2} \rightarrow ^4I_{15/2}$ ), red ( $^4F_{9/2} \rightarrow ^4I_{15/2}$ ), and NIR ( $^4I_{13/2} \rightarrow ^4I_{15/2}$ ) emission intensities of  $\text{LiErF}_4:\text{Ce}^{3+}/\text{LiYF}_4$  RENPs as a function of  $\text{Ce}^{3+}$  doping. **C** – Simplified excitation-emission scheme for  $\text{LiErF}_4:\text{Ce}^{3+}/\text{LiYF}_4$  RENPs, depicting phonon-assisted energy transfer from higher excited states of  $\text{Er}^{3+}$  to  $\text{Ce}^{3+}$ , which subsequently leads to UC emission quenching.

from core/shell RENPs was quenched almost entirely with  $\text{Ce}^{3+}$  doping (Figure 10.3A, B). From the Dieke's diagram it can be seen that the energy difference between  $\text{Ce}^{3+}$  ground and excited states matches much better the energy gaps between  $^4\text{S}_{3/2}$ - $^4\text{F}_{9/2}$  ( $\sim 3100 \text{ cm}^{-1}$ ),  $^4\text{F}_{9/2}$ - $^4\text{I}_{9/2}$  ( $\sim 2880 \text{ cm}^{-1}$ ), and  $^4\text{I}_{9/2}$ - $^4\text{I}_{11/2}$  ( $\sim 2240 \text{ cm}^{-1}$ )  $\text{Er}^{3+}$  energy levels.<sup>[268]</sup> Thus, phonon-assisted energy transfer from these higher excited states of  $\text{Er}^{3+}$  to  $\text{Ce}^{3+}$  is more likely and can be reasonably expected (Figure 10.3C). This is further verified by a close look at the quenching of the green and red UC emission. Although net UC emission intensity is quenched in  $\text{Ce}^{3+}$ -doped RENPs, the  $^2\text{H}_{11/2}/^4\text{S}_{3/2} \rightarrow ^4\text{I}_{15/2}$  radiative transition becomes more pronounced than that of  $^4\text{F}_{9/2} \rightarrow ^4\text{I}_{15/2}$ . In turn, this attests to high probability of  $^4\text{F}_{9/2} (\text{Er}^{3+}) \rightarrow ^2\text{F}_{7/2} (\text{Ce}^{3+})$  phonon-assisted energy transfer, directly quenching the red UC emission. Although no substantial enhancement of NIR downshifting was observed, the possibility to selectively quench UC emission in these RENPs is extremely attractive to design decoupled theranostic RENPs. Introducing an upconversion-free  $\text{LiErF}_4:\text{Ce}^{3+}$  layer holds promise to move the NIR imaging into BW-III while preserving the  $\sim 800 \text{ nm}$  heating-free excitation of this layer.

## 10.2 $\text{Er}^{3+}$ nanothermometry

The potential of  $\text{LiErF}_4:\text{Ce}^{3+}/\text{LiYF}_4$  RENPs to act as nanothermometers was investigated in the physiological temperature range ( $20\text{-}45 \text{ }^\circ\text{C}$ ), simultaneously measuring their UC and DS emission spectra. As a representative case of temperature-induced spectral changes, the photoluminescence spectra of undoped  $\text{LiErF}_4/\text{LiYF}_4$  RENPs are shown at  $20$  and  $45 \text{ }^\circ\text{C}$  (Figure 10.4). Same changes accompanied the photoluminescence of  $\text{Ce}^{3+}$ -doped RENPs. Elevating the temperature from  $20$  to  $45 \text{ }^\circ\text{C}$ , an isothermal point around  $1580 \text{ nm}$  could be discerned in the intensity normalized DS emission spectra of RENPs. Inverse band shape change with temperature at this point was thus used to define discrete integration ranges within the NIR emission of  $^4\text{I}_{13/2} \rightarrow ^4\text{I}_{15/2}$  radiative transition of  $\text{Er}^{3+}$ , that could potentially serve for LIR

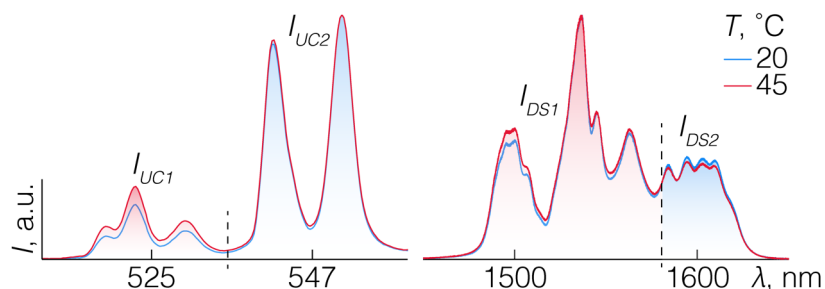
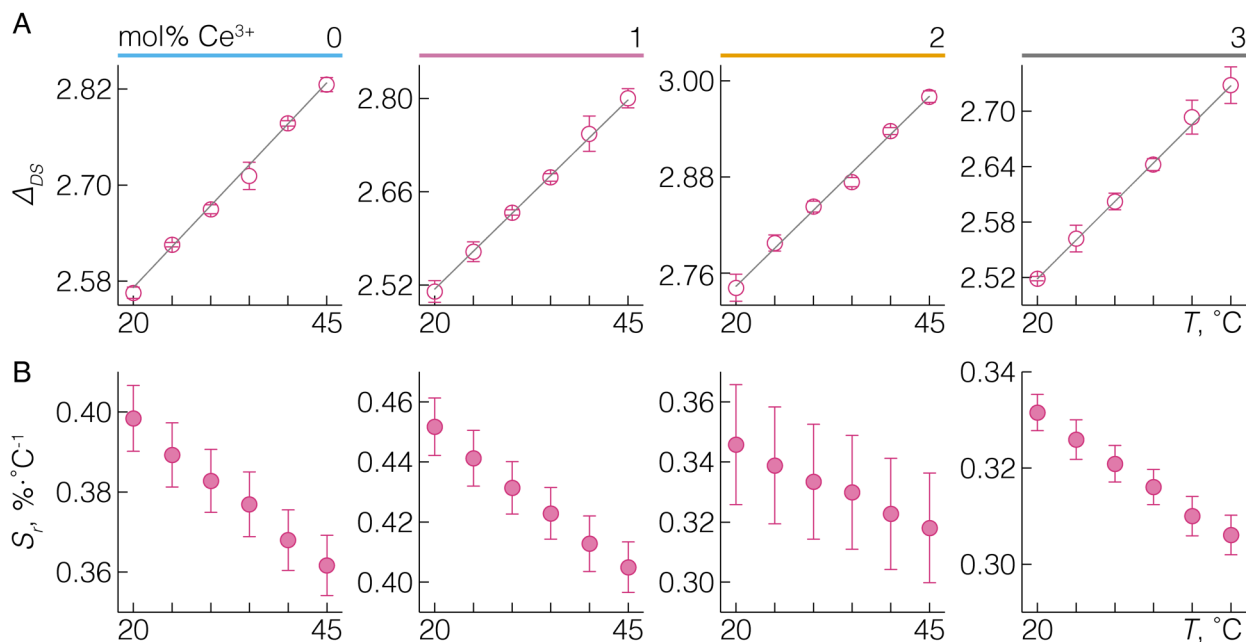


Figure 10.4. NIR nanothermometry with  $\text{LiErF}_4:\text{Ce}^{3+}/\text{LiYF}_4$  RENPs

Normalized UC (left) and DS (right) emission spectra of  $\text{LiErF}_4:\text{Ce}^{3+}/\text{LiYF}_4$  RENPs in water under  $793 \text{ nm}$  excitation at  $20$  and  $45 \text{ }^\circ\text{C}$ . Excitation power density  $\sim 1 \text{ kW/cm}^2$ . Integration ranges, further used to define thermometric parameters  $\Delta_{\text{UC}}$  and  $\Delta_{\text{DS}}$ , are delineated by the dashed line.

temperature sensing, namely  $I_{DS1}$  (1450-1580 nm) and  $I_{DS2}$  (1580-1650 nm). In the visible portion of RENPs' photoluminescence, the classic green UC emission temperature behavior between the thermally coupled  $^2H_{11/2}$  and  $^4S_{3/2}$  energy levels could be observed.<sup>48</sup> The intensity of  $^2H_{11/2} \rightarrow ^4I_{15/2}$  radiative transition ( $I_{UC1}$  514-535 nm) increased relative to the intensity of  $^4S_{3/2} \rightarrow ^4I_{15/2}$  one ( $I_{UC2}$  535-565 nm).

The LIR thermometric parameter  $\Delta_{DS} = I_{DS1}/I_{DS2}$  increased linearly with temperature, demonstrating that single-band ratiometric temperature sensing in BW-III with  $LiErF_4:Ce^{3+}/LiYF_4$  RENPs can be actually carried out (Figure 10.5A). The relative thermal sensitivity,  $S_r$ , for thermometric parameter  $\Delta_{DS}$  was estimated to be  $\sim 0.40\% \cdot ^\circ C^{-1}$  at 20  $^\circ C$  temperature for undoped  $LiErF_4/LiYF_4$  RENPs (Figure 10.5B). As with the DS emission intensity,  $S_r$  of single-band NIR nanothermometry increased at  $Ce^{3+}$  doping of 1 mol% to  $\sim 0.45\% \cdot ^\circ C^{-1}$ , and experienced subsequent decline to around  $0.33\% \cdot ^\circ C^{-1}$  for both 2 and 3 mol%  $Ce^{3+}$ -doped RENPs. It is worth noting that the  $S_r$  of  $LiErF_4: 1\text{ mol}\% Ce^{3+}/LiYF_4$  RENPs was on par with  $Nd^{3+}$ -based single band NIR nanothermometers in chapter 9.<sup>32</sup> The temperature measurement with DS emission of  $Er^{3+}$  for undoped and 1 mol%  $Ce^{3+}$ -doped RENPs had repeatability  $R > 99\%$  (see Appendix IV) and around 1.5  $^\circ C$  thermal uncertainty.



**Figure 10.5. Temperature sensing properties of  $LiErF_4:Ce^{3+}/LiYF_4$  RENPs via DS emission.**

**A** – Temperature dependence of the thermometric parameters,  $\Delta_{DS}$ , defined within the  $^4I_{13/2} \rightarrow ^4I_{15/2}$  radiative transitions, and their respective linear fits for  $LiErF_4: x\text{ mol}\% Ce^{3+}/LiYF_4$  RENPs. **B** – Change of the corresponding relative thermal sensitivities,  $S_r$ , with temperature.

On the other side of the optical spectrum, the thermometric parameter  $\Delta_{UC} = I_{UC1}/I_{UC2}$  also changed linearly in the measured temperature range and had a relative sensitivity  $S_r \sim 1.34\% \cdot ^\circ\text{C}^{-1}$  at 20  $^\circ\text{C}$  for  $\text{LiErF}_4/\text{LiYF}_4$  RENPs (Figure 10.6). This value was in line with nearly all  $\text{Er}^{3+}$  green UC emission based nanothermometers, as it solely depends on the energy gap between thermally coupled  $^2\text{H}_{11/2}$  and  $^4\text{S}_{3/2}$  excited states. Similar to the single-band temperature sensing in the NIR,  $S_r$  of upconversion nanothermometry appeared to increase for 1 mol%  $\text{Ce}^{3+}$  doped sample and then decrease at greater  $\text{Ce}^{3+}$  concentration. However, extremely quenched UC emission of the  $\text{Ce}^{3+}$ -doped RENPs makes determination of  $S_r$  too imprecise to appreciate if  $\text{Ce}^{3+}$  doping has any effect on the repopulation of thermally coupled  $^2\text{H}_{11/2}$  and  $^4\text{S}_{3/2}$  excited states. From these results, the optimum concentration of  $\text{Ce}^{3+}$  in RENPs was determined to be 1 mol%, and was further used along-side undoped  $\text{LiErF}_4/\text{LiYF}_4$  RENPs to better understand temperature dependence of  $\text{Er}^{3+}$  DS emission.

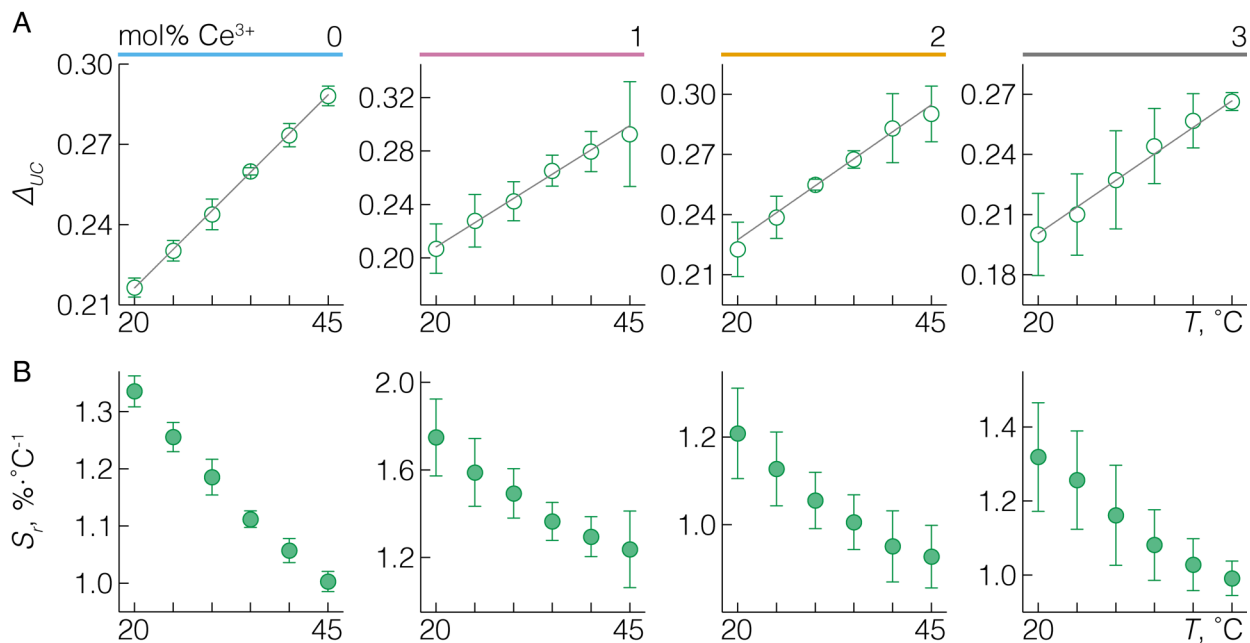


**Figure 10.6. Temperature sensing properties of  $\text{LiErF}_4:\text{Ce}^{3+}/\text{LiYF}_4$  RENPs via UC emission.**

**A** – Temperature dependence of the thermometric parameters,  $\Delta_{UC}$ , defined for green UC emission of  $\text{Er}^{3+}$ , and their respective linear fits for  $\text{LiErF}_4: x \text{ mol}\% \text{ Ce}^{3+}/\text{LiYF}_4$  RENPs. **B** – Change of the corresponding relative thermal sensitivities,  $S_r$ , with temperature.

### 10.3 Understanding thermal behavior of $\text{Er}^{3+}$ DS emission

As discussed in chapter 5, it is important to study the thermal behavior of optical nanothermometers, intended for biomedical research, in aqueous suspension, since it can be quite different in organic solvents or powder form. To understand the mechanisms responsible for the temperature dependent behavior of  $\text{Er}^{3+}$  DS emission, thermometric parameters,  $\Delta$ , and

corresponding relative thermal sensitivities,  $S_r$ , of undoped  $\text{LiErF}_4/\text{LiYF}_4$  RENPs were examined when RENPs were dispersed in hexane or heavy water (Figure 10.7). The  $^4I_{13/2}$  manifold of  $\text{Er}^{3+}$  under the influence of the crystal field splits into 7 Stark sub-levels ( $Y_i$ ,  $i = 1-7$ ). The energy difference between the bottom  $Y_{1-3}$  Stark sub-levels and the  $Y_{4-7}$  is on the order of  $\sim 74-166 \text{ cm}^{-1}$ , considering minimal ( $Y_3-Y_4$ ) and maximal ( $Y_1-Y_7$ ) energy difference.<sup>[270]</sup> Due to the thermal coupling of these two sets of Stark sub-levels, according to the Boltzmann distribution an expected thermal sensitivity for  $\text{Er}^{3+} \ ^4I_{13/2} \rightarrow \ ^4I_{15/2}$  radiative transition would be  $0.12-0.28 \text{ \%}\cdot\text{C}^{-1}$  at  $20 \text{ }^\circ\text{C}$ , which is very close to the experimentally measured  $S_r$  of  $\text{LiErF}_4/\text{LiYF}_4$  RENPs in hexane and heavy water (Figure 10.7B), as well as  $\text{Er}^{3+}$ -doped nanoparticles in powder form.<sup>[210]</sup> On the other hand, the temperature driven behavior of the green UC emission was invariant to the medium RENPs' were dispersed in (Figure 10.7D). It can be thus concluded that water plays an important role in the presented  $\text{LiErF}_4/\text{LiYF}_4$  RENPs single-band nanothermometers.

Just like in chapter 5,<sup>[152]</sup> OH stretching of the surrounding water molecules between  $3100-3700 \text{ cm}^{-1}$  (peaking at  $\sim 3400 \text{ cm}^{-1}$ ) can help to breach the  $\sim 3650 \text{ cm}^{-1}$  energy gap between  $^4I_{11/2}$ - $^4I_{13/2}$  excited states of  $\text{Er}^{3+}$  in a temperature-dependent manner. Elevating the temperature of the aqueous medium, the intramolecular hydrogen bonding of water molecules weakens and thus results in the OH groups vibrating at higher frequencies. The higher energy OH stretching comes to better match the energy gap between the  $^4I_{11/2}$ - $^4I_{13/2}$  energy levels of  $\text{Er}^{3+}$ , leading to

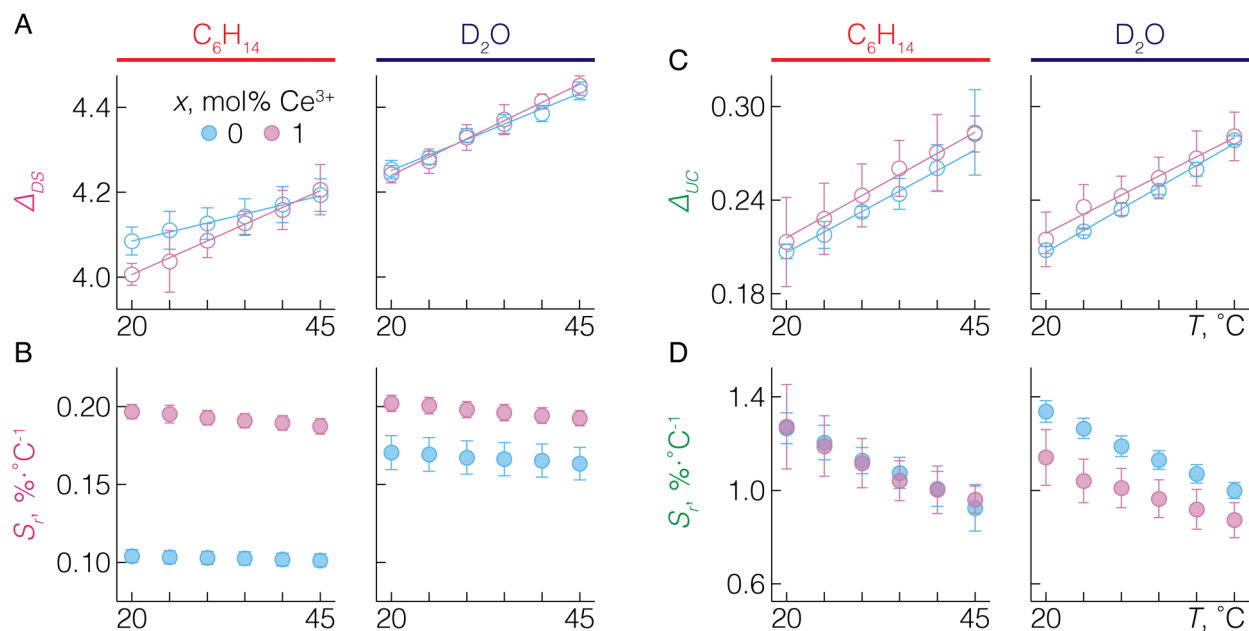


**Figure 10.7.** Temperature sensing properties of  $\text{LiErF}_4:\text{Ce}^{3+}/\text{LiYF}_4$  RENPs in hexane and heavy water.

**A, C** – Temperature dependence of the thermometric parameters  $\Delta_{UC}$  and  $\Delta_{DS}$ , respectively, for  $\text{LiErF}_4: x \text{ mol}\% \text{Ce}^{3+}/\text{LiYF}_4$  RENPs ( $x = 0$  and  $1$ ) dispersed in hexane ( $\text{C}_6\text{H}_{12}$ ) or heavy water ( $\text{D}_2\text{O}$ ). **B, D** – Corresponding thermal sensitivities,  $S_r$ .

increased population of NIR emitting  ${}^4I_{13/2}$  excited state. Thus, as the temperature of the aqueous dispersion increases, the EVET from the  ${}^4I_{11/2}$  excited state of  $\text{Er}^{3+}$  to water molecules becomes more prominent, leading to intensified  $\text{Er}^{3+}$  emission in the NIR. From the present single-band thermometric studies it appears that EVET based feeding of the  ${}^4I_{13/2}$  energy level is dominant towards the  $Y_{4-7}$  Stark sub-level set, thus increasing the thermal sensitivity of the  ${}^4I_{13/2} \rightarrow {}^4I_{15/2}$  emission in water. Meanwhile, the absence of high-energy vibrations in hexane and heavy water, makes  $\text{Er}^{3+}$  single-band nanothermometry in BW-III to solely depend on the Boltzmann determined repopulation of  ${}^4I_{13/2}$  Stark sub-levels.

Finally, in order to understand the effect of  $\text{Ce}^{3+}$  on the thermal sensitivity of  $\text{LiErF}_4:\text{Ce}^{3+}/\text{LiYF}_4$  RENPs, the temperature dependence of DS and UC emission of 1 mol%  $\text{Ce}^{3+}$ -doped RENPs was also studied in different media (Figure 10.7).  $S_r$  values determined from the  $\Delta_{DS}$  calibration curves were slightly higher ( $\sim 0.2\% \cdot ^\circ\text{C}^{-1}$ ) for  $\text{LiErF}_4: 1 \text{ mol}\% \text{ Ce}^{3+}/\text{LiYF}_4$  in hexane and heavy water, as compared to the undoped  $\text{LiErF}_4/\text{LiYF}_4$  RENPs, similar to previous observations in water (Figure 10.5). On the other hand, thermal sensing through UC emission remained unaffected by  $\text{Ce}^{3+}$  in both hexane and heavy water (Figure 10.7C, D). Based on the above observations, it is likely that the temperature-dependent  ${}^4I_{11/2} (\text{Er}^{3+}) \rightarrow {}^2F_{7/2} (\text{Ce}^{3+})$  phonon-assisted energy transfer (following the Miyakawa-Dexter model) additionally populates the

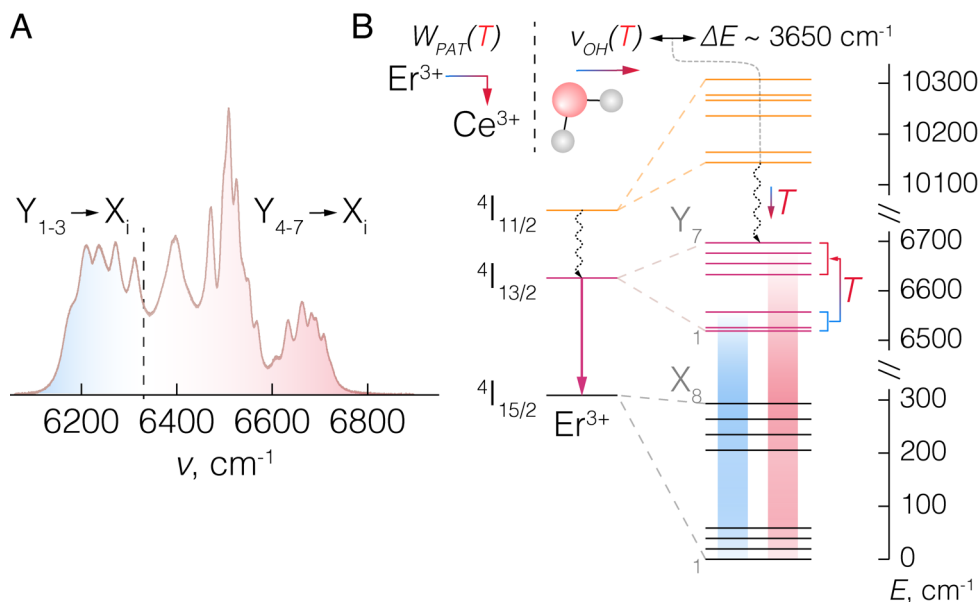


**Figure 10.8. Temperature dependence of  $\text{LiErF}_4:\text{Ce}^{3+}/\text{LiYF}_4$  RENPs' DS emission.**

**A** – High resolution spectrum of the  $\text{Er}^{3+} {}^4I_{13/2} \rightarrow {}^4I_{15/2}$  DS emission. The interband transitions between the Stark sub-levels of the  ${}^4I_{13/2}$  and  ${}^4I_{15/2}$  manifolds are approximately delineated as  ${}^4I_{13/2} (Y_{1-3})$  and  ${}^4I_{13/2} (Y_{4-7}) \rightarrow {}^4I_{15/2} (X_i)$ . **B** – Simplified  $\text{Er}^{3+}$  energy level diagram depicting Stark sub-levels of the first three  ${}^4I_J$  manifolds. Temperature dependent behavior of the  ${}^4I_{13/2} \rightarrow {}^4I_{15/2}$  DS emission of  $\text{LiErF}_4:\text{Ce}^{3+}/\text{LiYF}_4$  RENPs in water stems from the: i) Boltzmann governed repopulation of  $Y_{1-3}$  and  $Y_{4-7}$  Stark sets, ii) enhanced EVET from  $\text{Er}^{3+}$  to OH stretching ( $\nu_{\text{OH}}$ ) and iii)  $\text{Er}^{3+} \rightarrow \text{Ce}^{3+}$  phonon-assisted energy transfer ( $W_{\text{PAT}}$ ).

higher Stark sub-levels ( $Y_{4-7}$ ) of the  $^4I_{13/2}$  manifold, further enhancing thermal sensitivity of  $\text{LiErF}_4$ : 1 mol%  $\text{Ce}^{3+}/\text{LiYF}_4$  RENPs. The summary of the proposed temperature dependent mechanisms, responsible for thermal sensitivity of  $\text{LiErF}_4$ : 1 mol%  $\text{Ce}^{3+}/\text{LiYF}_4$  RENPs, is represented in Figure 10.8. As aqueous nanothermometers these RENPs depend not only on the Boltzmann statistics determined repopulation of Stark sub-levels of the  $^4I_{13/2}$  excited state, but also on the temperature dependent EVET to water molecules and phonon-assisted energy transfer between excited states of  $\text{Er}^{3+}$  and  $\text{Ce}^{3+}$ .

#### 10.4 Reliability of $\text{Er}^{3+}$ nanothermometry in BW-III

As previously pointed, it is important to study photoluminescence nanothermometers in an environment at least mimicking their destined application framework. RENPs intended for biomedical purposes have to be nominally scrutinized in water, as results obtained in their powder form or when dispersed in other type of solvents hold no guarantee of equivalence. However, it is even more so pertinent to appreciate the reliability of the photoluminescence nanothermometers, which can be affected by such factors as laser excitation power, self-absorption, or solvent (tissue) attenuation.<sup>[172, 173]</sup>

The reliability of temperature sensing, via the LIR thermometric parameter  $\Delta_{DS}$ , was evaluated at different excitation powers (100-900 mW) of the 793 nm laser. The  $\Delta_{DS}$  and corresponding temperature values, of the water dispersion containing  $\text{LiErF}_4/\text{LiYF}_4$  RENPs, were measured after several continuous 15 min laser irradiation intervals, increasing the excitation power by 200 mW each time. Temperature of the dispersion was also simultaneously measured with a thermocouple. Over the total irradiation time of 75 min, around 1 °C increase in the dispersion temperature was observed by both measurement methods (optical and thermocouple), as changes in the DS emission spectra of RENPs were only caused by the mild laser-induced water heating (Figure 10.9). The same observation was done when continuously exciting the RENPs with 960 nm laser light. However, in this case temperature of the solution increased by around 8 °C, due to strong water absorption.

The motivation for studying  $\text{LiErF}_4/\text{LiYF}_4$  RENPs as single-band nanothermometers arose from the need to overcome inhomogeneous light attenuation by tissues while moving imaging and thermal mapping to the highest contrast provided by the BW-III. Although at wavelengths beyond 1500 nm scattering and absorption by endogenous tissue components is greatly reduced, signal attenuation by water still remains an issue. To define the LIR thermometric parameter  $\Delta_{DS}$  relatively wide intensity integration ranges were used, which partially overlap with

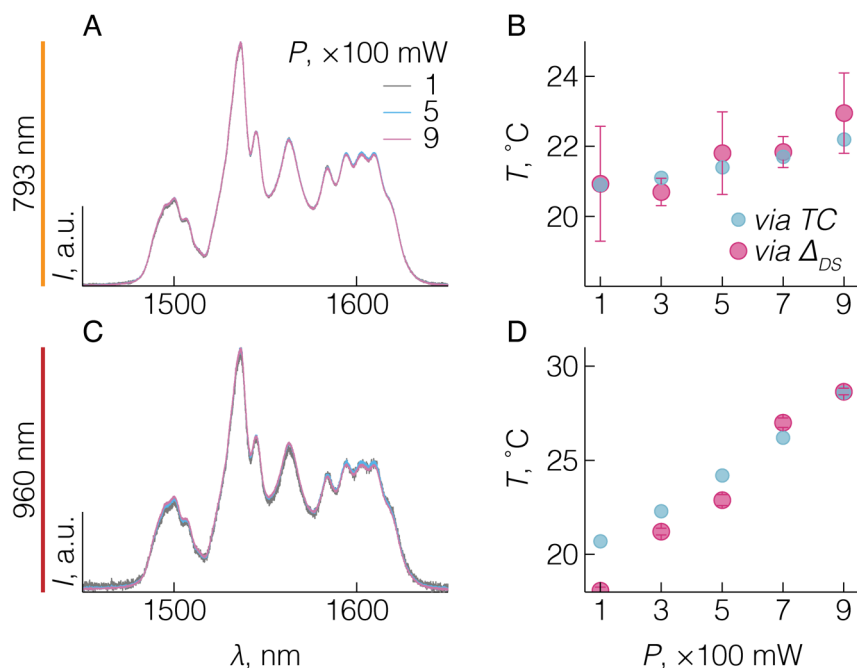


**Figure 10.9. Temperature sensing with LiErF<sub>4</sub>/LiYF<sub>4</sub> RENPs under different excitation power**

**A, C** – normalized DS emission spectra of LiErF<sub>4</sub>/LiYF<sub>4</sub> RENPs dispersed in water under 793 (A) or 960 nm (C) excitation of varying power density (100, 500, 900 mW). **B, D** – temperature of the dispersion measured optically via a LIR thermometric parameter  $\Delta_{DS}$  or via a thermocouple immersed into the dispersion, after excitation of RENPs at 793 (B) or 960 nm (D) wavelengths in the 100-900 mW range.

the water absorption band centered at around 1450 nm. As a result, this might lead to unreliable and hard to correct for temperature evaluation by subcutaneously collected photoluminescence. To check for the reliability of temperature sensing at varying signal acquisition “depth”,  $\Delta_{DS}$  was measured whilst collecting the DS emission of RENPs when allowed to propagate through different optical path lengths of water (~0.15 to 3.6 mm). Increasing the optical path length resulted in greater attenuation of the photoluminescence signal before it reached the detector, up to the point where emission in the 1450-1530 became entirely extinct (Figure 10.10A).

This spectral attenuation is subsequently followed by an apparent increase in the relative thermal sensitivity of the optical nanothermometer (Figure 10.10B) as the absolute values of  $\Delta_{DS}$  change drastically (Figure 10.11), similar to what has been brought to light by Shen et al.<sup>[172]</sup> The apparent increase in the  $S_r$  thus leads to incorrect subcutaneous temperature measurements, if not accounted for through *a priori* knowledge of water absorption properties at different temperatures. In an attempt to minimize this issue, the  $I_{DS1}$  and  $I_{DS2}$  integration ranges were narrowed to 1555-1573 and 1609-1650 nm, respectively, introducing thermometric parameter  $\Delta_{DS \text{ narrow}}$ . Although both similar  $S_r$  and apparent increase in  $S_r$  with optical path length was observed in this case too, the absolute thermal sensitivity,  $S_a$ , remained nearly unaffected in the 0.15-1.9 mm range (Figure 7C). This essentially means that the change of  $\Delta_{DS \text{ narrow}}$  per °C is

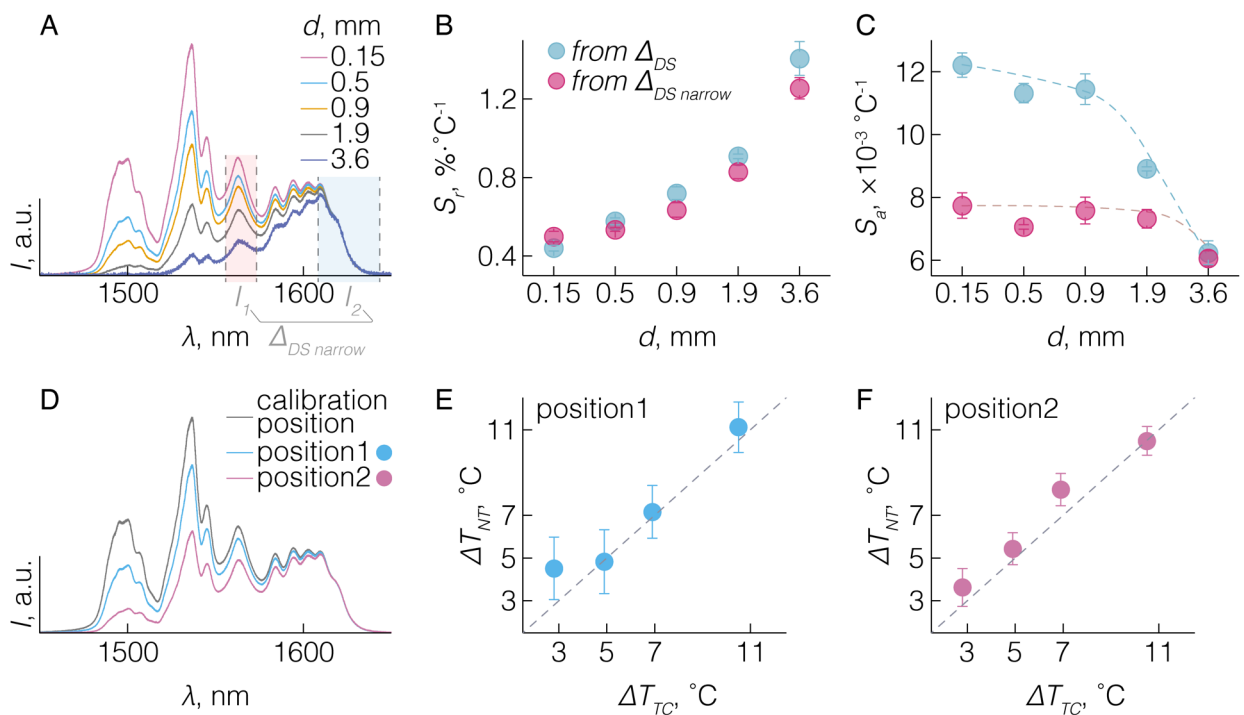


**Figure 10.10. Temperature sensing with LiErF<sub>4</sub>/LiYF<sub>4</sub> RENPs against water absorption**

**A** – normalized DS emission spectra of LiErF<sub>4</sub>/LiYF<sub>4</sub> RENPs in water acquiring the emission signal after it propagated through different optical path lengths of water. **B** – apparent change of  $S_p$  determined for  $\Delta_{DS}$  and  $\Delta_{DS\ narrow}$  (see **A** for integration ranges). **C** – change of absolute sensitivity  $S_a$  determined for  $\Delta_{DS}$  and  $\Delta_{DS\ narrow}$ . Lines are guides to the eye. **D** – normalized DS emission spectra of LiErF<sub>4</sub>/LiYF<sub>4</sub> RENPs in water when measured at the calibration position (grey) and at two arbitrary positions that lead to spectral distortions (blue, pink). **E, F** – relative temperature change determined optically with RENPs ( $\Delta T_{NT}$ ) at these two positions vs that measured with the thermocouple ( $\Delta T_{TC}$ ).

constant irrespective of water optical path length (“imaging depth”), allowing to still measure the relative temperature changes accurately. To demonstrate that, the temperature change at two arbitrary optical path length positions inside the cuvette (position1 < 1 mm, position2 > 1mm) was determined using the  $S_a$  value obtained prior (at ~0.1-0.2 mm optical path length position) to the spectral profile deformation by water absorption (Figure 10.10D). Although the absolute values of the temperature inside the cuvette could not be determined any more, the relative temperature changes via nanothermometry ( $\Delta T_{NT}$ ) perfectly correlated with those measured by thermocouple inside the cuvette ( $\Delta T_{TC}$ ) (Figure 10.10E, F). This clearly exemplifies the potential of Er<sup>3+</sup> single-band nanothermometry in the BW-III as a valuable addition to applications where transient temperature changes are measured subcutaneously, whilst directly circumventing signal attenuation by tissue absorption.

Taken together, a number of important points have been uncovered in this chapter. First, the possibility to provide decoupled theranostics RENPs with therapy-free (upconversion-free) imaging in the BW-III by introducing Ce<sup>3+</sup> to quench higher excited states of Er<sup>3+</sup>. As shown

here, and by other reports,  $\text{Ce}^{3+}$  doping can be used to deliberately knockout UC emission of  $\text{Er}^{3+}$ -RENPs. Second, the use of  $\text{Li}^+$ -based hosts allows to easily resolve the fine structure of  $\text{Er}^{3+}$  DS emission, making it straightforward to determine spectral areas that could be used to construct a single-band nanothermometers operating in the BW-III with high relative thermal sensitivity. Finally, thermometric behavior of  $\text{Er}^{3+}$  DS emission in water dispersed RENPs is governed more than just by repopulation of thermally coupled Stark sub-levels following Boltzmann statistics. The temperature-dependent EVET to water molecules and phonon-assisted energy transfer in the presence of  $\text{Ce}^{3+}$  play an important role in the thermal sensitivity of these RENPs. Definitely, more work still needs to be done to make these RENPs brighter, attain higher temperature sensitivities, and, most importantly, to test their performance *ex vivo* and *in vivo*. The latter point is required in order to decisively claim that promising  $\text{Er}^{3+}$  single-band nanothermometry allows to overcome faulty temperature readout due to uneven absorption of photoluminescence by tissues. Nonetheless, herein generated knowledge, combined with developments in chapters 7-9, constitute the much-needed guidelines on how to design 2<sup>nd</sup> generation decoupled theranostics RENPs, few examples of which are presented in the next chapter.

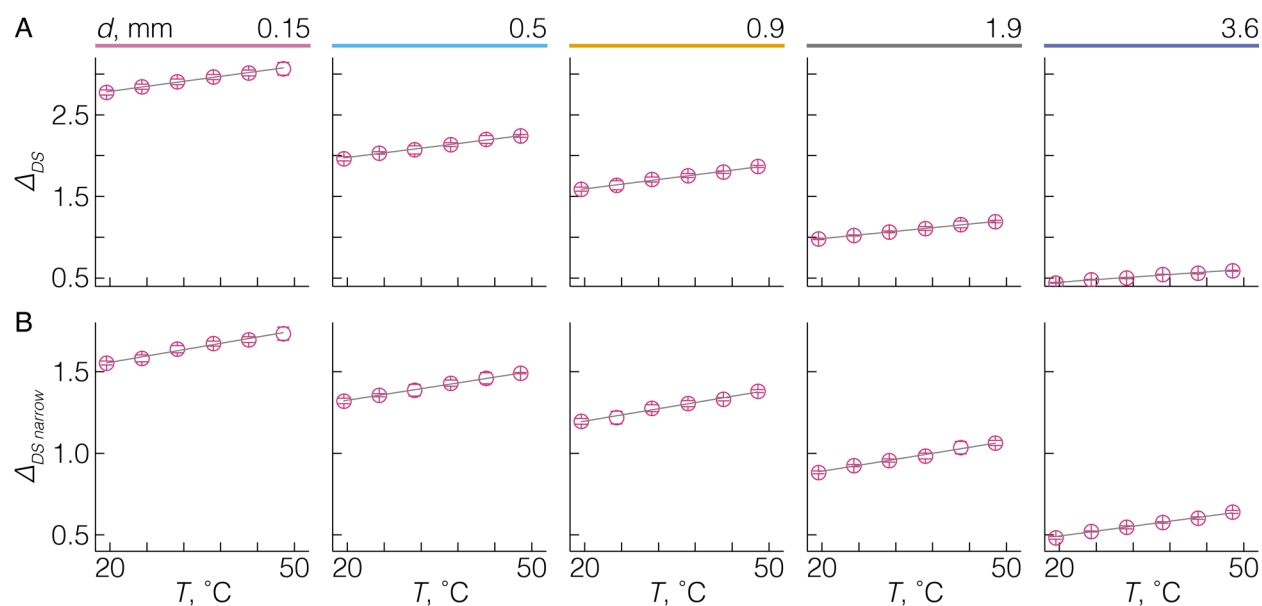


**Figure 10.11.  $\Delta_{DS}$  and  $\Delta_{DS\ narrow}$  of  $\text{LiErF}_4/\text{LiYF}_4$  RENPs against water absorption**

**Temperature dependence of the LIR thermometric parameters  $\Delta_{DS}$  (A) and  $\Delta_{DS\ narrow}$  (B) of  $\text{LiErF}_4/\text{LiYF}_4$  RENPs dispersed in water and measured after propagation through different optical path lengths ( $d$ ) of water.**

## 11 2<sup>nd</sup> GENERATION DECOUPLED THERANOSTICS RENPs

Different RENPs already presented in this thesis have been built from the ground-up starting with most simple singly-doped nanostructures, to multilayered RENPs with advanced functionalities, that were eventually “disintegrated” into separate parts and individually optimized. This meticulous process though does not end here, the lessons learned at each step were assemble together in two types of 2<sup>nd</sup> generation decoupled theranostics RENPs that are currently being studied on fundamental and *in vitro/in vivo* applicative levels.

First type of RENPs represented a significantly advanced type of decoupled theranostics RENPs conceived in chapter 6 (Figure 11.1). Following the newly developed FN synthesis/stabilization synthetic route, DS emission/nanothermometry, and UC emission optimization done in chapters 7, 8, and 9, respectively, LiLuF<sub>4</sub>:Nd<sup>3+</sup>/LiLuF<sub>4</sub>/LiYbF<sub>4</sub>:Er<sup>3+</sup>/LiYF<sub>4</sub> RENPs were made. Optically active, Nd<sup>3+</sup> and Yb<sup>3+</sup>/Er<sup>3+</sup>, layers of these RENPs were separated by an inert LiLuF<sub>4</sub> (idle-shell1) in order to prevent energy exchange between the aforementioned RE<sup>3+</sup> and obtain decoupled photoluminescence response under 800 and 980 nm excitation wavelengths. Idle-shell2, LiYF<sub>4</sub>, was grown as a final enclosure of the RENPs providing intense red UC emission from the LiYbF<sub>4</sub>:Er<sup>3+</sup> UC-shell. In contrast to decoupled theranostics RENPs in chapter 6, here DS emission (LiLuF<sub>4</sub>:Nd<sup>3+</sup> DS-core) and UC-emission (LiYbF<sub>4</sub>:Er<sup>3+</sup> UC-shell) layers were switched places. This provides a better protection of Nd<sup>3+</sup> from the solvent quenching, granting higher DS emission intensity in the BW-II for NIR imaging and nanothermometry; meanwhile, Er<sup>3+</sup> positioned closer to the surface increases the probability of energy exchange with coupled PS molecules for PDT. Intriguingly, while improving

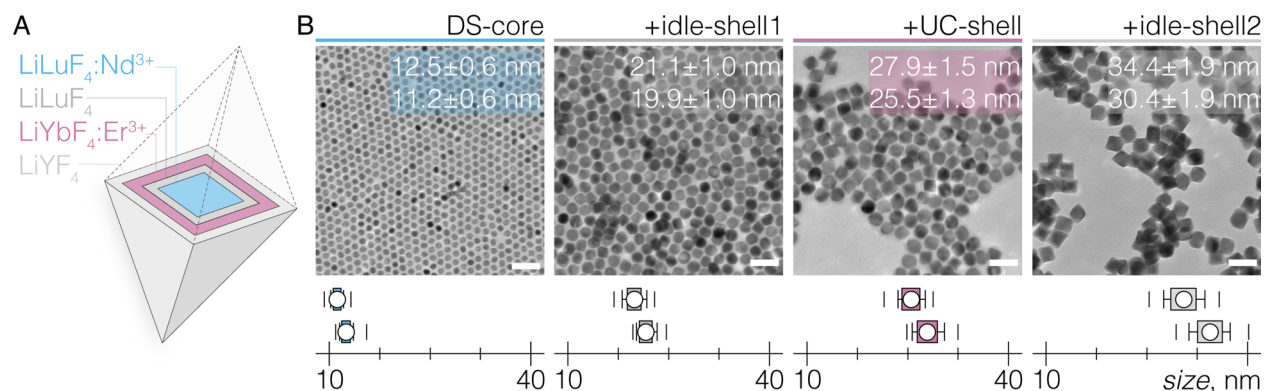


Figure 11.1. 2<sup>nd</sup> generation decoupled theranostics RENPs – example I.

A – Schematic representation of LiLuF<sub>4</sub>:Nd<sup>3+</sup>/LiLuF<sub>4</sub>/LiYbF<sub>4</sub>:Er<sup>3+</sup>/LiYF<sub>4</sub> RENPs. B – TEM images and size distributions of RENPs after addition of each functional layer. Scale bar 50 nm. Box plots indicate: mean value (dot), SD (box outline), 5<sup>th</sup> and 95<sup>th</sup> percentiles (whiskers), and maximum/minimum values (dashes). Upper and lower boxes represent the length of minor and major axes of the RENPs, respectively.

the spectral performance of these 2<sup>nd</sup> generation decoupled theranostic RENPs, their size was maintained around 34 x 30 nm, in comparison to 1<sup>st</sup> generation decoupled theranostic RENPs which were around 93 x 64 nm. Furthermore, Lu<sup>3+</sup> in the structure of these novel RENPs could be used for X-ray computer tomography imaging, adding one more diagnostic modality. Preliminary experiments with LiLuF<sub>4</sub>:Nd<sup>3+</sup>/LiLuF<sub>4</sub>/LiYbF<sub>4</sub>:Er<sup>3+</sup>/LiYF<sub>4</sub> RENPs confirmed their decoupled optical response when excited with distinct irradiation wavelengths. Also, after transfer to water via phospholipid coating, RENPs-Ce<sub>6</sub> complex was formed and effective indirect excitation of bound Ce<sub>6</sub> molecules was observed. Further experiments involve evaluation of singlet oxygen generation, therapy-free imaging in small animal models, and eradication of cancer cells via PDT *in vitro* and *in vivo*.

The second type of proposed 2<sup>nd</sup> generation decoupled theranostics RENPs, encompass controlled and robust synthesis via FN synthesis/stabilization, UC emission optimization, and a move of NIR imaging and nanothermometry to BW-III (chapter 10). Furthermore, these RENPs were designed in collaboration with the research group of Dr. Paras Prasad at University of Buffalo, NY, USA, drawing on their expertise of dye-sensitized RENPs. Dye-sensitization is increasingly becoming a mean by which low absorption cross-section of RE<sup>3+</sup> could be overcome. By introducing organic molecules on the surface of RENPs, orders of magnitude more of impinging NIR radiation can be absorbed by these molecules, and transferred to RE<sup>3+</sup> for DS and/or UC emission to take place. Subsequently LiYbF<sub>4</sub>:Er<sup>3+</sup>, Tm<sup>3+</sup>/LiYF<sub>4</sub>/LiYF<sub>4</sub>:Er<sup>3+</sup>, Yb<sup>3+</sup>, Ce<sup>3+</sup>/LiYbF<sub>4</sub>/LiYF<sub>4</sub>: Nd<sup>3+</sup>/Yb<sup>3+</sup> multilayered RENPs were sensitized and are currently studied as decoupled theranostic nanoplatform (Figure 11.2). Here, the LiYbF<sub>4</sub>:Er<sup>3+</sup>, Tm<sup>3+</sup> UC-core is intended for on-demand therapeutics under 980 nm excitation. Co-doping of Er<sup>3+</sup> and Tm<sup>3+</sup> allows to cover a wider range of optical spectrum and expand on the number of possible PS to be used for PDT once present at the surface of RENPs. As before, LiYF<sub>4</sub> idle-shell acts as a buffer layer that prohibits excitation of UC-core via energy migration from other optically active layers – sustaining decoupled optical response of RENPs. The LiYF<sub>4</sub>:Er<sup>3+</sup>, Yb<sup>3+</sup>, Ce<sup>3+</sup>/LiYbF<sub>4</sub>/LiYF<sub>4</sub>:Nd<sup>3+</sup>, Yb<sup>3+</sup> represent DS-shell, relay-shell, and sensitizing-shell, respectively, and are akin to RENPs presented in chapter 5. The LiYbF<sub>4</sub> relay-shell permits energy transfer between the DS- and sensitizing-shells, while separating Er<sup>3+</sup> and Nd<sup>3+</sup> from each other to avoid mutual quenching. Ce<sup>3+</sup> was co-doped in the DS-shell to deliberately quench UC emission of Er<sup>3+</sup>, granting therapy-free imaging and nanothermometry around 1550 nm in BW-III under 800 nm excitation. Opposite to most of the previously examined RENPs, the sensitizing-shell has been left un-passivated by an inert shell so that 800 nm harvesting organic molecules, indocyanine green (ICG), could be in near-direct contact with Nd<sup>3+</sup> to facilitate energy exchange

between the two species. Altogether, under 980 nm excitation all of RENP active layers could be excited, but UC emission is expected only from the UC-core, as that of  $\text{Er}^{3+}$  in DS-shell would be quenched by  $\text{Ce}^{3+}$  and also surface quenchers. On the other hand, 800 nm light would excite the bound to the surface ICG molecules, prompting the  $\text{ICG} \rightarrow \text{Nd}^{3+} \rightarrow \text{Yb}^{3+} \rightarrow \text{Er}^{3+}$  energy transfer cascade, with upconversion-free DS emission emerging as an end result. Notably, the size of these decoupled theranostic RENPs is just  $41.9 \times 35.8$  nm. Preliminary results have been particularly encouraging, as the expected spectral behavior under different excitation wavelengths could be seen, alongside significant enhancement of DS emission due to employed dye-sensitization approach. Further *in vitro* and *in vivo* studies are underway.

I like to think that this is just a taste of various sophisticated decoupled theranostics RENPs that could be developed. Granted widespread interest in these nanostructures, even more of precise, safe and effective decoupled theranostics RENPs will hopefully be design, and, most importantly, pushed over the brink of a materials science lab bench to real life application in biomedical research and maybe one day clinical use.

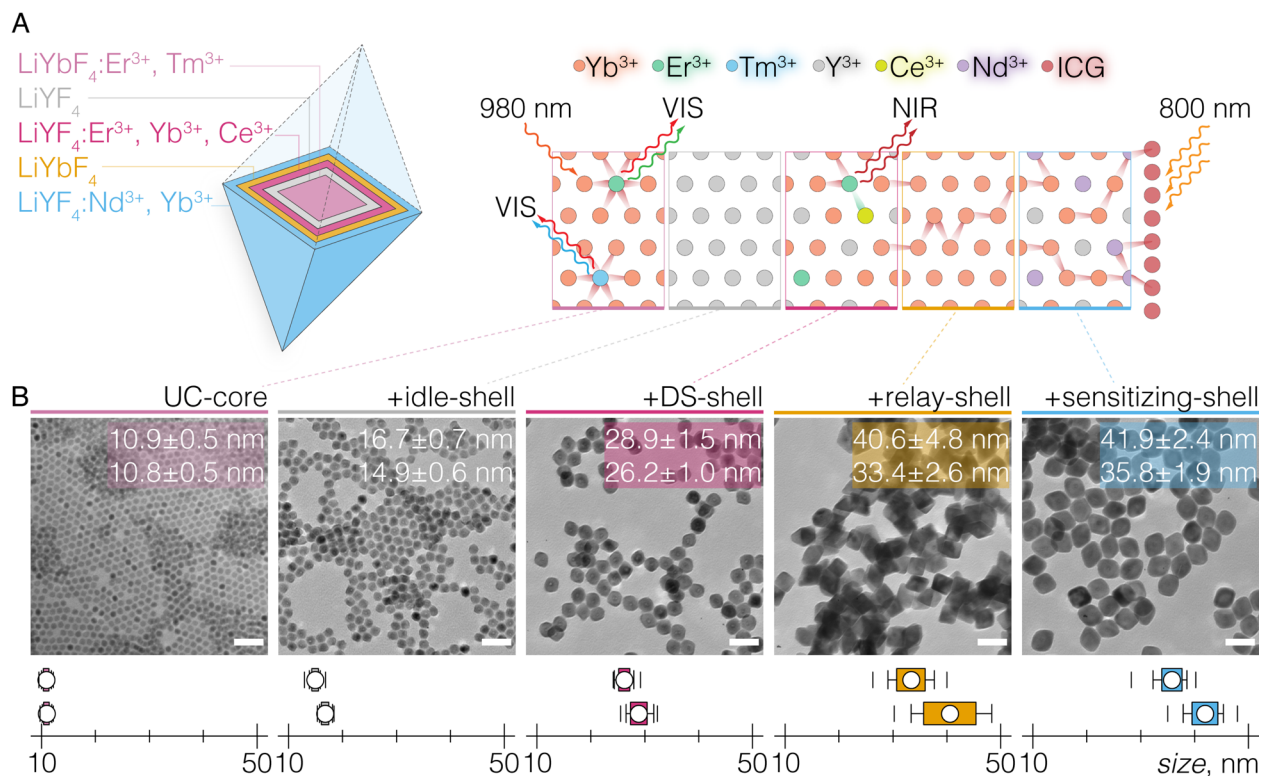


**Figure 11.2. 2<sup>nd</sup> generation decoupled theranostics RENPs – example II.**

**A** – Schematic representation of  $\text{LiYbF}_4:\text{Er}^{3+}, \text{Tm}^{3+}/\text{LiYF}_4/\text{LiYF}_4:\text{Er}^{3+}, \text{Yb}^{3+}, \text{Ce}^{3+}/\text{LiYbF}_4/\text{LiYF}_4:\text{Nd}^{3+}, \text{Yb}^{3+}$  RENPs. **B** – TEM images and size distributions of RENPs after addition of each functional layer. Scale bar 50 nm. Box plots indicate: mean value (dot), SD (box outline), 5<sup>th</sup> and 95<sup>th</sup> percentiles (whiskers), and maximum/minimum values (dashes). Upper and lower boxes represent the length of minor and major axes of the RENPs, respectively. In **A**, schematic visualization of selective  $\text{Er}^{3+}$  and  $\text{Tm}^{3+}$  UC emission (VIS) excitation via 980 nm radiation in the UC-core, and DS emission (NIR) excitation under 800 nm irradiation, dependent on the energy transfer cascade from ICG molecules to  $\text{Er}^{3+}$  in DS-shell.

## 12 GENERAL DISCUSSION AND CONCLUSIONS

---

Throughout the course of this thesis, concepts of nanomedicine, theranostics, and how those are intertwined with materials science research have been presented. It is focused on a particular kind of theranostic nano-agent – rare earth nanoparticles, or RENPs. RENPs constitute an intriguing proposition towards theranostics, as modular nanostructures that can be flexibly engineered to match the growing demands of safe and timely disease detection and eradication. Yet, it must be recognized that to attain these goals RENPs have to be thoroughly explored: their synthesis methods must be robust and reproducible, and their photophysical properties well-attuned towards diagnostic and therapeutic functions.

This thesis hinges on i) the rational design of RENPs: adjusting and exploring the  $RE^{3+}$  doping type, concentration, core/shell architectures, as well as advanced synthesis techniques and reporting on the photophysical properties of RENPs, which are all pertinent to their successful development and application in biomedicine; ii) promoting the integration of NIR nanothermometry in biological imaging windows (BW-II and BW-III) as a staple in advanced theranostic RENPs; iii) realization of a new theranostics approach – decoupled theranostics – as a means towards safer nanomedicines enacted by RENPs. Figure 12.1 visually summarizes the contents and outcomes of this thesis as they are outlined below.

The centerpiece of this thesis might as well be  $Nd^{3+}$ . RENPs doped with  $Nd^{3+}$  present the advantages of heating-free excitation in the BW-I around 800 nm, emission in BW-I and BW-II that can be used for deep-tissue imaging and nanothermometry, and the possibility to act as primary energy sensitizer ions promoting a wide gamut of radiative transitions spanning from UV to NIR. In that vein, the complete set of photophysical properties of singly  $Nd^{3+}$ -doped RENPs are first examined and presented in chapter 3. Optimal  $Nd^{3+}$  doping concentration has always been a point of contention in the RENPs' research community, with different studies claiming that either very low or very high  $Nd^{3+}$  doping levels result in brightest RENPs for deep-tissue imaging. Here, this dispute is hopefully reconciled. Results indicate that lower doping amounts of  $Nd^{3+}$  (5 mol%), where cross-relaxation among the  $Nd^{3+}$  is minimal, provide RENPs of highest *PLQY*. These  $Nd^{3+}$ -RENPs were also the brightest. Although the difference in brightness between low and high doping was less than between measured *PLQY*, it is recognized that low-doped  $Nd^{3+}$ -RENPs should be preferred in imaging and nanothermometry applications – avoiding undesired heating and faulty thermal readings.

Subsequently, multilayered Nd<sup>3+</sup>-doped RENPs are explored to promote simultaneous UC and DS emission excitation (chapter 4). By systematically studying 980 nm via Yb<sup>3+</sup> and 800 nm via Nd<sup>3+</sup> excitation routes, the spectral properties of these RENPs are compared. The 800 nm excitation endows the RENPs with the greater probability of higher order UC emission excitation within Er<sup>3+</sup> and Ho<sup>3+</sup>, and expands the available number of DS emission bands in the NIR, almost entirely covering all three BWs. These theranostic RENPs are then shown to have the ability to serve as i) energy donors to excited PS used in cancer treatment by PDT and as ii) NIR contrast agent for deep-tissue imaging. In chapter 5, the design of these RENPs is further improved to reduce inter-ion quenching for even brighter UC and DS emission, and, most importantly, these multilayered RENPs are studied as first of their kind optical nanothermometers working in the BW-III. Nanothermometry is achieved by employing Ho<sup>3+</sup>, Nd<sup>3+</sup>, and Er<sup>3+</sup> DS emission bands around 1180, 1340 and 1550 nm, respectively, to construct two LIR thermometric parameters,  $\Delta(\text{Ho}^{3+}/\text{Nd}^{3+})$  and  $\Delta(\text{Er}^{3+}/\text{Nd}^{3+})$ . As a result, RNP-based nanothermometers working in the BW-II and BW-III with approximately 1 %·°C<sup>-1</sup> relative thermal sensitivity are presented. Intriguingly, it was observed that temperature sensing properties in the BW-III of these RENPs stem from the interaction between the electronic states of RE<sup>3+</sup> and vibrational modes of water molecules. Energies of OH stretching modes are subject to thermal fluctuations and thus influence repopulation of RE<sup>3+</sup> excited states in a temperature-dependent manner. It becomes evident that RENPs as nanothermometers intended for biomedical use must be generally scrutinized in biologically relevant environments like water, and not only in organic solvents or powder form.

The above RENPs definitely qualify as theranostic nano-agents, they have the capacity to enact diagnostics (imaging and temperature sensing) and therapy (i.e. PDT) under a single wavelength excitation, simultaneously. But is there a better way to approach theranostics? It is worth considering situations where prompting therapeutic action could be premature and dangerous to the patient. Indeed, the corner stone of theranostics is the possibility to observe the theranostic nanoplatfrom as it reaches and when it reaches the target of interest, and even as it is being eliminated from the body. But for most of the theranostic agents this comes at the cost of simultaneous therapy, which might be harmful to surrounding healthy tissues or be expended before these agents come in contact with the actual malady. Chapter 6 presents the idea of decoupled theranostics RENPs, which take on the concept of orthogonal excitation – different excitation wavelengths prompt different RE<sup>3+</sup> photoluminescence. Just as before, these RENPs encompass both UC and DS emission, respectively used for therapy and diagnostics, however these modalities do not work at once, unless so desired. The Nd<sup>3+</sup> containing layer of

RENPs absorb 800 nm radiation and provide NIR emission in BW-I and BW-II for therapy-free imaging and nanothermometry, whereas Yb<sup>3+</sup>/Tm<sup>3+</sup> doped layer upconverts 980 nm excitation to UV-vis emission that can initiate PDT on-demand. These two layers are spatially separated by an intermediate idle-shell, so that no energy exchange between Nd<sup>3+</sup> and Yb<sup>3+</sup> could excite Tm<sup>3+</sup> UC emission and instigate therapy beforehand. *In vitro* studies in 2D and 3D cancer models helped to demonstrate that treatment with these decoupled theranostics RENPs is carried out only once 980 nm laser is switched ON, while under 800 nm excitation they act as purely diagnostic tools. The decoupled theranostics RENPs constituted a very important step forward in the development of advanced nanomedicines, however RENPs themselves still needed to be optimized from several vantage points. One of which required to make significantly smaller RENPs, but to do so without sacrificing their brightness.

A modified thermal decomposition synthesis method was developed to greatly reduce the size of the Li<sup>+</sup>-based RENPs, while implementing rational changes in their composition to be able to retain intense UC emission (chapter 7). Initially, RENPs as small as 5 nm could be made by introducing high amounts of OM in the reaction mixture, but these nanostructures proved to be too dim for therapy applications requiring high-energy photons, and prone to uncontrolled growth when shelled with an optically inactive layer intended to improve their brightness. It was discovered that LiYbF<sub>4</sub> RENPs in the presence of excess of OA tend to assume a more chemically stable form, that is accompanied by the increase in size of RENPs from 5 to around 10 nm. Once this stabilization step is carried out, shelling of RENPs can be accomplished with an utmost control, growing multilayered structures of desired size and shell thicknesses. Vivaly, small (~20 nm in size) LiYbF<sub>4</sub>:Tm<sup>3+</sup>/LiYF<sub>4</sub> RENPs generated as much, if not more, of UC emission in the UV region compared to the classic (~90 nm in size) LiYF<sub>4</sub>:Tm<sup>3+</sup>/Yb<sup>3+</sup> RENPs.

Following these developments an expansive library of LiYbF<sub>4</sub>:RE<sup>3+</sup>/LiYF<sub>4</sub> RENPs (RE<sup>3+</sup> – Tm<sup>3+</sup>, Er<sup>3+</sup>, Ho<sup>3+</sup>) was created and the photophysical characteristics of these RENPs were studied as a function of dopant type and doping concentration (chapter 8). Color-tuning via cross-relaxation of these RENPs was identified, and respective values of UC emission PLQY at different doping and excitation power densities were provided. Cross-relaxation was especially relevant in the case of Tm<sup>3+</sup>-RENPs. The energy exchange processes amongst Tm<sup>3+</sup>, at various doping amounts, led to the repopulation of excited states and dictated which of the high-order UC emissions, UV or blue, is the most dominant under NIR excitation. In the case of Er<sup>3+</sup>-RENPs only slight color tuning was observed upon different Er<sup>3+</sup> doping concentration, red UC emission of the <sup>4</sup>F<sub>9/2</sub> excited state being most intense in each case. Albeit being least efficient in photon

upconversion,  $\text{Ho}^{3+}$ -RENPs were found to have an inversion point between their green and red UC emission, at a specific excitation power density. In high  $\text{Ho}^{3+}$ -doped RENPs (5 mol%) this leads to almost constant color output irrespective of the excitation power density (Figure 8.15), which could be of interest in lighting and security print applications. This information is crucial to appreciate the capacity of RENPs to serve as theranostic agents by means of their UC emission, and how to best tune their spectral properties to match the intended application.

From the diagnostic standpoint, single-band nanothermometry with  $\text{Nd}^{3+}$ -doped RENPs in the BW-II, was studied in greater detail in chapter 9. Due to the  $\text{Li}^+$ -based host in which  $\text{Nd}^{3+}$  are doped, different  $\text{Nd}^{3+}$  radiative transitions could be well-resolved with ease. This allowed to carefully select the integration ranges for LIR thermometric parameters of greater thermal sensitivity and temperature readout accuracy, compared to the similar nanothermometry approach first presented in chapter 6. These RENPs were also studied using *ex vivo* tissue model, which helped to set clear limits on the possibility to use  $\text{Nd}^{3+}$ -single band nanothermometry for subcutaneous measurement of transient temperatures, which can be used to recognize healthy tissues from malignant ones. Importantly, single-band nanothermometry in the NIR allows to circumvent uneven attenuation of DS emission by tissues, better maintaining LIR thermal calibration despite inhomogeneous tissue optical properties. Nonetheless, the caveat of  $\text{Nd}^{3+}$ -based single-band nanothermometry is that it can only work as far as BW-II. To attain highest imaging contrast and precision in thermal mapping, single-band nanothermometers in BW-III must be developed. In chapter 10,  $\text{LiErF}_4:\text{Ce}^{3+}/\text{LiYF}_4$  RENPs are studied as such nanothermometers. In  $\text{Li}^+$ -based host  $\text{Er}^{3+}$  DS emission band around 1550 nm can be resolved well-enough to delineate two integration ranges for single-band nanothermometry in the BW-III. Just like in chapter 5, EVET between  $\text{Er}^{3+}$  and vibrational modes of water molecules proved to be key in thermal behavior of these nanothermometers, while their thermal sensitivity was close to that of  $\text{Nd}^{3+}$ -RENPs in chapter 9. The  $\text{Ce}^{3+}$  doping was introduced to deliberately quench UC emission of  $\text{Er}^{3+}$ , obtaining upconversion-free DS emission under 800 nm excitation. Introduction of  $\text{Ce}^{3+}$  exemplifies how these nanostructures could be integrated in the decoupled theranostics RENPs to move therapy-free imaging and nanothermometry to BW-III.

Finally, new concepts (2<sup>nd</sup> generation) of decoupled theranostics RENPs are proposed in chapter 11, that are designed based on all of the previously gained knowledge. With the aid of newly developed synthesis methods and optimized doping, much smaller and brighter decoupled theranostics RENPs, compared to their predecessors in chapter 6, could be

conceived. Also, alternative strategies, as dye-sensitization, are considered to obtain brighter DS emission and better deep-tissue imaging.

All in all, this thesis makes a strong case in favor of RENPs as theranostic agents of the future, highlighting their intrinsic virtues of upconversion and downshifting photoluminescence, and at the same time introducing new ways of approaching the design of theranostic RENPs in general. It is hard to predict the future of RENPs, but it is reasonable to assume that in biomedicine it is secured. Continuous flow of new ideas takes RENPs on unexplored journeys in the realm of biomedical research and application every day, stirring the scientific community in the direction previously unimagined. Yet, more exploration is needed to have a clearer vista on RENPs, particularly in regards to their photophysics, design, and synthesis strategies. As for every answered question there are many more that emerge, and only in complement between the fundamental and applicative research it is reasonable to expect for RENPs to become a staple in biomedical practice. The first steps in the direction of theranostic RENPs have been made more than a decade ago, and herein research and results hopefully contribute to push theranostic RENPs ever so closer to the final goal – from materials science benches to biomedical research laboratories and even patient beds.



## 13 BIBLIOGRAPHY

---

- (1) De M, Ghosh P S, Rotello V M. Applications of Nanoparticles in Biology. *Advanced Materials* **2008**, 20 (22), 4225–4241.
- (2) Ventola C L. Progress in Nanomedicine: Approved and Investigational Nanodrugs. *Pharmacy and Therapeutics* **2017**, 42 (12), 742.
- (3) Rastinehad A R, Anastos H, Wajswol E, Winoker J S, Sfakianos J P, Doppalapudi S K, Carrick M R, Knauer C J, Taouli B, Lewis S C, Tewari A K, Schwartz J A, Canfield S E, George A K, West J L, Halas N J. Gold Nanoshell-Localized Photothermal Ablation of Prostate Tumors in a Clinical Pilot Device Study. *Proceedings of the National Academy of Sciences* **2019**, 116 (37), 18590–18596.
- (4) Thakor A S, Jokerst J V, Ghanouni P, Campbell J L, Mittra E, Gambhir S S. Clinically Approved Nanoparticle Imaging Agents. *Journal of Nuclear Medicine* **2016**, 57 (12), 1833–1837.
- (5) Lammers T, Aime S, Hennink W E, Storm G, Kiessling F. Theranostic Nanomedicine. *Accounts of Chemical Research* **2011**, 44 (10), 1029–1038.
- (6) Lammers T, Storm G. Setting Standards to Promote Progress in Bio–Nano Science. *Nature Nanotechnology* **2019**, 14 (7), 626–626.
- (7) Wong X Y, Sena-Torralba A, Álvarez-Diduk R, Muthoosamy K, Merkoçi A. Nanomaterials for Nanotheranostics: Tuning Their Properties According to Disease Needs. *ACS Nano* **2020**, 14 (3), 2585–2627.
- (8) Kelkar S S, Reineke T M. Theranostics: Combining Imaging and Therapy. *Bioconjugate Chemistry* **2011**, 22 (10), 1879–1903.
- (9) Vankayala R, Hwang K C. Near-Infrared-Light-Activatable Nanomaterial-Mediated Phototheranostic Nanomedicines: An Emerging Paradigm for Cancer Treatment. *Advanced Materials* **2018**, 1706320.
- (10) Jacques S L. Optical Properties of Biological Tissues: A Review. *Physics in Medicine and Biology* **2013**, 58 (11), R37–R61.
- (11) Richards-Kortum R, Sevick-Muraca E. Quantitative Optical Spectroscopy for Tissue Diagnosis. *Annual Review of Physical Chemistry* **1996**, 47 (1), 555–606.
- (12) Weissleder R. A Clearer Vision for in Vivo Imaging. *Nature Biotechnology* **2001**, 19 (4), 316–317.
- (13) Smith A M, Mancini M C, Nie S. Second Window for in Vivo Imaging: Bioimaging. *Nature Nanotechnology* **2009**, 4 (11), 710–711.
- (14) Sordillo L A, Pu Y, Pratavieira S, Budansky Y, Alfano R R. Deep Optical Imaging of Tissue Using the Second and Third Near-Infrared Spectral Windows. *Journal of Biomedical Optics* **2014**, 19 (5), 056004.
- (15) Lim Y T, Kim S, Nakayama A, Stott N E, Bawendi M G, Frangioni J V. Selection of Quantum Dot Wavelengths for Biomedical Assays and Imaging. *Molecular Imaging* **2003**, 2 (1), 15353500200302163.
- (16) Tao Z, Hong G, Shinji C, Chen C, Diao S, Antaris A L, Zhang B, Zou Y, Dai H. Biological Imaging Using Nanoparticles of Small Organic Molecules with Fluorescence Emission at

- Wavelengths Longer than 1000 nm. *Angewandte Chemie International Edition* **2013**, *52* (49), 13002–13006.
- (17) Bruns O T, Bischof T S, Harris D K, Franke D, Shi Y, Riedemann L, Bartelt A, Jaworski F B, Carr J A, Rowlands C J, Wilson M W B, Chen O, Wei H, Hwang G W, Montana D M, Coropceanu I, Achorn O B, Kloepper J, Heeren J, So P T C, Fukumura D, Jensen K F, Jain R K, Bawendi M G. Next-Generation in Vivo Optical Imaging with Short-Wave Infrared Quantum Dots. *Nature Biomedical Engineering* **2017**, *1* (4), 0056.
  - (18) Hu J, Sanz-Rodríguez F, Rivero F, Rodríguez E M, Torres R A, Ortgies D H, Solé J G, Alfonso F, Jaque D. Gold Nanoshells: Contrast Agents for Cell Imaging by Cardiovascular Optical Coherence Tomography. *Nano Research* **2018**, *11* (2), 676–685.
  - (19) Marin R, Lifante J, Besteiro L V, Wang Z, Govorov A O, Rivero F, Alfonso F, Sanz-Rodríguez F, Jaque D. Plasmonic Copper Sulfide Nanoparticles Enable Dark Contrast in Optical Coherence Tomography. *Advanced Healthcare Materials* **2020**, *9* (5), 1901627.
  - (20) Ku G, Zhou M, Song S, Huang Q, Hazle J, Li C. Copper Sulfide Nanoparticles as a New Class of Photoacoustic Contrast Agent for Deep Tissue Imaging at 1064 nm. *ACS Nano* **2012**, *6* (8), 7489–7496.
  - (21) Hong G, Diao S, Chang J, Antaris A L, Chen C, Zhang B, Zhao S, Atochin D N, Huang P L, Andreasson K I, Kuo C J, Dai H. Through-Skull Fluorescence Imaging of the Brain in a New Near-Infrared Window. *Nature Photonics* **2014**, *8* (9), 723–730.
  - (22) Hong G, Lee J C, Robinson J T, Raaz U, Xie L, Huang N F, Cooke J P, Dai H. Multifunctional in Vivo Vascular Imaging Using Near-Infrared II Fluorescence. *Nature Medicine* **2012**, *18* (12), 1841–1846.
  - (23) Jansen E D, Pickett P M, Mackanos M A, Virostko J. Effect of Optical Tissue Clearing on Spatial Resolution and Sensitivity of Bioluminescence Imaging. *Journal of Biomedical Optics* **2006**, *11* (4), 041119.
  - (24) Wang T D, Van Dam J. Optical Biopsy: A New Frontier in Endoscopic Detection and Diagnosis. *Clinical Gastroenterology and Hepatology* **2004**, *2* (9), 744–753.
  - (25) Carr J A, Aellen M, Franke D, So P T C, Bruns O T, Bawendi M G. Absorption by Water Increases Fluorescence Image Contrast of Biological Tissue in the Shortwave Infrared. *Proceedings of the National Academy of Sciences* **2018**, *115* (37), 9080–9085.
  - (26) Tucker-Schwartz J M, Meyer T A, Patil C A, Duvall C L, Skala M C. In Vivo Photothermal Optical Coherence Tomography of Gold Nanorod Contrast Agents. *Biomedical Optics Express* **2012**, *3* (11), 2881.
  - (27) Huang X, El-Sayed I H, Qian W, El-Sayed M A. Cancer Cell Imaging and Photothermal Therapy in the Near-Infrared Region by Using Gold Nanorods. *Journal of the American Chemical Society* **2006**, *128* (6), 2115–2120.
  - (28) Skripka A, Valanciunaite J, Dauderis G, Poderys V, Kubiliute R, Rotomskis R. Two-Photon Excited Quantum Dots as Energy Donors for Photosensitizer Chlorin e6. *Journal of Biomedical Optics* **2013**, *18* (7), 078002.
  - (29) Dieke G H, Crosswhite H M, Crosswhite H, others. Spectra and Energy Levels of Rare Earth Ions in Crystals. **1968**.
  - (30) Bloembergen N. Solid State Infrared Quantum Counters. *Physical Review Letters* **1959**, *2* (3), 84–85.

- (31) Auzel F. Compteur Quantique Par Transfert d'énergie Entre Deux Ions de Terres Rares Dans Un Tungstate Mixte et Dans Un Verre. *Comptes rendus de l'Académie des Sciences* **1966**, 262, 1016–1019.
- (32) Ovsyakin V, Feofilov P. Cooperative Sensitization of Luminescence in Crystals Activated with Rare Earth Ions. *Soviet Journal of Experimental and Theoretical Physics Letters* **1966**, 4, 317.
- (33) Auzel F. Upconversion and Anti-Stokes Processes with f and d Ions in Solids. *Chemical Reviews* **2004**, 104 (1), 139–174.
- (34) Wang G, Qin W, Wang L, Wei G, Zhu P, Kim R. Intense Ultraviolet Upconversion Luminescence from Hexagonal NaYF<sub>4</sub>:Yb<sup>3+</sup>/Tm<sup>3+</sup> Microcrystals. *Optics Express* **2008**, 16 (16), 11907.
- (35) Joubert M-F. Photon Avalanche Upconversion in Rare Earth Laser Materials. *Optical Materials* **1999**, 11 (2–3), 181–203.
- (36) Liu Y, Lu Y, Yang X, Zheng X, Wen S, Wang F, Vidal X, Zhao J, Liu D, Zhou Z, Ma C, Zhou J, Piper J A, Xi P, Jin D. Amplified Stimulated Emission in Upconversion Nanoparticles for Super-Resolution Nanoscopy. *Nature* **2017**, 543 (7644), 229–233.
- (37) Levy E S, Tajon C A, Bischof T S, Iafrazi J, Fernandez-Bravo A, Garfield D J, Chamanzar M, Maharbiz M M, Sohal V S, Schuck P J, Cohen B E, Chan E M. Energy-Looping Nanoparticles: Harnessing Excited-State Absorption for Deep-Tissue Imaging. *ACS Nano* **2016**, 10 (9), 8423–8433.
- (38) Fernandez-Bravo A, Yao K, Barnard E S, Borys N J, Levy E S, Tian B, Tajon C A, Moretti L, Altoe M V, Aloni S, Beketayev K, Scotognella F, Cohen B E, Chan E M, Schuck P J. Continuous-Wave Upconverting Nanoparticle Microlasers. *Nature Nanotechnology* **2018**, 13 (7), 572–577.
- (39) Pollnau M, Gamelin D R, Lüthi S R, Güdel H U, Hehlen M P. Power Dependence of Upconversion Luminescence in Lanthanide and Transition-Metal-Ion Systems. *Physical Review B* **2000**, 61 (5), 3337–3346.
- (40) Chen G, Qiu H, Prasad P N, Chen X. Upconversion Nanoparticles: Design, Nanochemistry, and Applications in Theranostics. *Chemical Reviews* **2014**, 114 (10), 5161–5214.
- (41) Yi G-S, Chow G-M. Colloidal LaF<sub>3</sub>:Yb,Er, LaF<sub>3</sub>:Yb,Ho and LaF<sub>3</sub>:Yb,Tm Nanocrystals with Multicolor Upconversion Fluorescence. *Journal of Materials Chemistry* **2005**, 15 (41), 4460.
- (42) Mai H-X, Zhang Y-W, Si R, Yan Z-G, Sun L, You L-P, Yan C-H. High-Quality Sodium Rare-Earth Fluoride Nanocrystals: Controlled Synthesis and Optical Properties. *Journal of the American Chemical Society* **2006**, 128 (19), 6426–6436.
- (43) Du Y-P, Zhang Y-W, Sun L-D, Yan C-H. Optically Active Uniform Potassium and Lithium Rare Earth Fluoride Nanocrystals Derived from Metal Trifluoroacetate Precursors. *Dalton Transactions* **2009**, No. 40, 8574.
- (44) Pedroni M, Piccinelli F, Passuello T, Polizzi S, Ueda J, Haro-González P, Martinez Maestro L, Jaque D, García-Solé J, Bettinelli M, Speghini A. Water (H<sub>2</sub>O and D<sub>2</sub>O) Dispersible NIR-to-NIR Upconverting Yb<sup>3+</sup>/Tm<sup>3+</sup> Doped MF<sub>2</sub> (M = Ca, Sr) Colloids: Influence of the Host Crystal. *Crystal Growth & Design* **2013**, 13 (11), 4906–4913.

- (45) Wang J, Deng R, MacDonald M A, Chen B, Yuan J, Wang F, Chi D, Andy Hor T S, Zhang P, Liu G, Han Y, Liu X. Enhancing Multiphoton Upconversion through Energy Clustering at Sublattice Level. *Nature Materials* **2014**, 13 (2), 157–162.
- (46) Zhuo Z, Liu Y, Liu D, Huang P, Jiang F, Chen X, Hong M. Manipulating Energy Transfer in Lanthanide-Doped Single Nanoparticles for Highly Enhanced Upconverting Luminescence. *Chemical Science* **2017**, 8 (7), 5050–5056.
- (47) Wong H-T, Vetrone F, Naccache R, Chan H L W, Hao J, Capobianco J A. Water Dispersible Ultra-Small Multifunctional KGdF<sub>4</sub>:Tm<sup>3+</sup>, Yb<sup>3+</sup> Nanoparticles with near-Infrared to near-Infrared Upconversion. *Journal of Materials Chemistry* **2011**, 21 (41), 16589.
- (48) Krämer K W, Biner D, Frei G, Güdel H U, Hehlen M P, Lüthi S R. Hexagonal Sodium Yttrium Fluoride Based Green and Blue Emitting Upconversion Phosphors. *Chemistry of Materials* **2004**, 16 (7), 1244–1251.
- (49) Mahalingam V, Vetrone F, Naccache R, Speghini A, Capobianco J A. Colloidal Tm<sup>3+</sup>/Yb<sup>3+</sup>-Doped LiYF<sub>4</sub> Nanocrystals: Multiple Luminescence Spanning the UV to NIR Regions via Low-Energy Excitation. *Advanced Materials* **2009**, 21 (40), 4025–4028.
- (50) Huang P, Zheng W, Zhou S, Tu D, Chen Z, Zhu H, Li R, Ma E, Huang M, Chen X. Lanthanide-Doped LiLuF<sub>4</sub> Upconversion Nanoprobes for the Detection of Disease Biomarkers. *Angewandte Chemie International Edition* **2014**, 53 (5), 1252–1257.
- (51) Huang P, Zheng W, Tu D, Shang X, Zhang M, Li R, Xu J, Liu Y, Chen X. Unraveling the Electronic Structures of Neodymium in LiLuF<sub>4</sub> Nanocrystals for Ratiometric Temperature Sensing. *Advanced Science* **2019**, 6 (10), 1802282.
- (52) Zhao C, Kong X, Liu X, Tu L, Wu F, Zhang Y, Liu K, Zeng Q, Zhang H. Li<sup>+</sup> Ion Doping: An Approach for Improving the Crystallinity and Upconversion Emissions of NaYF<sub>4</sub>:Yb<sup>3+</sup>, Tm<sup>3+</sup> Nanoparticles. *Nanoscale* **2013**, 5 (17), 8084.
- (53) Alivisatos A P. Semiconductor Clusters, Nanocrystals, and Quantum Dots. *Science* **1996**, 271 (5251), 933–937.
- (54) Tian B, Fernandez-Bravo A, Najafiaghdam H, Torquato N A, Altoe M V P, Teitelboim A, Tajon C A, Tian Y, Borys N J, Barnard E S, Anwar M, Chan E M, Schuck P J, Cohen B E. Low Irradiance Multiphoton Imaging with Alloyed Lanthanide Nanocrystals. *Nature Communications* **2018**, 9 (1), 3082.
- (55) Schietinger S, Menezes L de S, Lauritzen B, Benson O. Observation of Size Dependence in Multicolor Upconversion in Single Yb<sup>3+</sup>, Er<sup>3+</sup> Codoped NaYF<sub>4</sub> Nanocrystals. *Nano Letters* **2009**, 9 (6), 2477–2481.
- (56) Vetrone F, Naccache R, Mahalingam V, Morgan C G, Capobianco J A. The Active-Core/Active-Shell Approach: A Strategy to Enhance the Upconversion Luminescence in Lanthanide-Doped Nanoparticles. *Advanced Functional Materials* **2009**, 19 (18), 2924–2929.
- (57) Zhong Y, Tian G, Gu Z, Yang Y, Gu L, Zhao Y, Ma Y, Yao J. Elimination of Photon Quenching by a Transition Layer to Fabricate a Quenching-Shield Sandwich Structure for 800 nm Excited Upconversion Luminescence of Nd<sup>3+</sup>-Sensitized Nanoparticles. *Advanced Materials* **2014**, 26 (18), 2831–2837.
- (58) Wang F, Wang J, Liu X. Direct Evidence of a Surface Quenching Effect on Size-Dependent Luminescence of Upconversion Nanoparticles. *Angewandte Chemie International Edition* **2010**, 49 (41), 7456–7460.

- (59) Su Q, Han S, Xie X, Zhu H, Chen H, Chen C-K, Liu R-S, Chen X, Wang F, Liu X. The Effect of Surface Coating on Energy Migration-Mediated Upconversion. *Journal of the American Chemical Society* **2012**, 134 (51), 20849–20857.
- (60) Johnson N J J, He S, Diao S, Chan E M, Dai H, Almutairi A. Direct Evidence for Coupled Surface and Concentration Quenching Dynamics in Lanthanide-Doped Nanocrystals. *Journal of the American Chemical Society* **2017**, 139 (8), 3275–3282.
- (61) Rabouw F T, Prins P T, Villanueva-Delgado P, Castelijns M, Geitenbeek R G, Meijerink A. Quenching Pathways in NaYF<sub>4</sub>:Er<sup>3+</sup>, Yb<sup>3+</sup> Upconversion Nanocrystals. *ACS Nano* **2018**, 12 (5), 4812–4823
- (62) Kong W, Sun T, Chen B, Chen X, Ai F, Zhu X, Li M, Zhang W, Zhu G, Wang F. A General Strategy for Ligand Exchange on Upconversion Nanoparticles. *Inorganic Chemistry* **2017**, 56 (2), 872–877.
- (63) Chen Z, Chen H, Hu H, Yu M, Li F, Zhang Q, Zhou Z, Yi T, Huang C. Versatile Synthesis Strategy for Carboxylic Acid-functionalized Upconverting Nanophosphors as Biological Labels. *Journal of the American Chemical Society* **2008**, 130 (10), 3023–3029.
- (64) Bogdan N, Vetrone F, Ozin G A, Capobianco J A. Synthesis of Ligand-Free Colloidally Stable Water Dispersible Brightly Luminescent Lanthanide-Doped Upconverting Nanoparticles. *Nano Letters* **2011**, 11 (2), 835–840.
- (65) Sivakumar S, Diamente P R, van Veggel F C J M. Silica-Coated Ln<sup>3+</sup>-Doped LaF<sub>3</sub> Nanoparticles as Robust Down- and Upconverting Biolabels. *Chemistry - A European Journal* **2006**, 12 (22), 5878–5884.
- (66) Jiang G, Pichaandi J, Johnson N J J, Burke R D, van Veggel F C J M. An Effective Polymer Cross-Linking Strategy To Obtain Stable Dispersions of Upconverting NaYF<sub>4</sub> Nanoparticles in Buffers and Biological Growth Media for Biolabeling Applications. *Langmuir* **2012**, 28 (6), 3239–3247.
- (67) Wang L, Yan R, Huo Z, Wang L, Zeng J, Bao J, Wang X, Peng Q, Li Y. Fluorescence Resonant Energy Transfer Biosensor Based on Upconversion-Luminescent Nanoparticles. *Angewandte Chemie International Edition* **2005**, 44 (37), 6054–6057.
- (68) Xiong L, Chen Z, Tian Q, Cao T, Xu C, Li F. High Contrast Upconversion Luminescence Targeted Imaging in Vivo Using Peptide-Labeled Nanophosphors. *Analytical Chemistry* **2009**, 81 (21), 8687–8694.
- (69) Wang X, Valiev R R, Ohulchanskyy T Y, Ågren H, Yang C, Chen G. Dye-Sensitized Lanthanide-Doped Upconversion Nanoparticles. *Chemical Society Reviews* **2017**, 46 (14), 4150–4167.
- (70) Mendez-Gonzalez D, Lopez-Cabarcos E, Rubio-Retama J, Laurenti M. Sensors and Bioassays Powered by Upconverting Materials. *Advances in Colloid and Interface Science* **2017**, 249, 66–87.
- (71) Karimi M, Sahandi Zangabad P, Baghaee-Ravari S, Ghazadeh M, Mirshekari H, Hamblin M R. Smart Nanostructures for Cargo Delivery: Uncaging and Activating by Light. *Journal of the American Chemical Society* **2017**, 139 (13), 4584–4610.
- (72) Wang M, Hou Z, Al Kheraif A A, Xing B, Lin J. Mini Review of TiO<sub>2</sub>-Based Multifunctional Nanocomposites for Near-Infrared Light-Responsive Phototherapy. *Advanced Healthcare Materials* **2018**, 7 (20) 1800351.

- (73) Lv R, Yang P, Hu B, Xu J, Shang W, Tian J. In Situ Growth Strategy to Integrate Up-Conversion Nanoparticles with Ultrasmall CuS for Photothermal Theranostics. *ACS Nano* **2017**, *11* (1), 1064–1072.
- (74) Heer S, Kömpe K, Güdel H-U, Haase M. Highly Efficient Multicolour Upconversion Emission in Transparent Colloids of Lanthanide-Doped NaYF<sub>4</sub> Nanocrystals. *Advanced Materials* **2004**, *16* (23–24), 2102–2105.
- (75) Xie X, Gao N, Deng R, Sun Q, Xu Q-H, Liu X. Mechanistic Investigation of Photon Upconversion in Nd<sup>3+</sup>-Sensitized Core–Shell Nanoparticles. *Journal of the American Chemical Society* **2013**, *135* (34), 12608–12611.
- (76) Wang Y-F, Liu G-Y, Sun L-D, Xiao J-W, Zhou J-C, Yan C-H. Nd<sup>3+</sup>-Sensitized Upconversion Nanophosphors: Efficient *In Vivo* Bioimaging Probes with Minimized Heating Effect. *ACS Nano* **2013**, *7* (8), 7200–7206.
- (77) Cheng X, Ge H, Wei Y, Zhang K, Su W, Zhou J, Yin L, Zhan Q, Jing S, Huang L. Design for Brighter Photon Upconversion Emissions via Energy Level Overlap of Lanthanide Ions. *ACS Nano* **2018**, *12* (11), 10992–10999.
- (78) Chen Q, Xie X, Huang B, Liang L, Han S, Yi Z, Wang Y, Li Y, Fan D, Huang L, Liu X. Confining Excitation Energy in Er<sup>3+</sup>-Sensitized Upconversion Nanocrystals through Tm<sup>3+</sup>-Mediated Transient Energy Trapping. *Angewandte Chemie International Edition* **2017**, *56* (26), 7605–7609.
- (79) Fischer S, Bronstein N D, Swabeck J K, Chan E M, Alivisatos A P. Precise Tuning of Surface Quenching for Luminescence Enhancement in Core–Shell Lanthanide-Doped Nanocrystals. *Nano Letters* **2016**, *16* (11), 7241–7247.
- (80) Würth C, Fischer S, Grauel B, Alivisatos A P, Resch-Genger U. Quantum Yields, Surface Quenching, and Passivation Efficiency for Ultrasmall Core/Shell Upconverting Nanoparticles. *Journal of the American Chemical Society* **2018**, *140* (14), 4922–4928.
- (81) Stouwdam J W, van Veggel F C J M. Near-Infrared Emission of Redispersible Er<sup>3+</sup>, Nd<sup>3+</sup>, and Ho<sup>3+</sup> Doped LaF<sub>3</sub> Nanoparticles. *Nano Letters* **2002**, *2* (7), 733–737.
- (82) Stouwdam J W, Hebbink G A, Huskens J, van Veggel F C J M. Lanthanide-Doped Nanoparticles with Excellent Luminescent Properties in Organic Media. *Chemistry of Materials* **2003**, *15* (24), 4604–4616.
- (83) Yu X-F, Chen L-D, Li M, Xie M-Y, Zhou L, Li Y, Wang Q-Q. Highly Efficient Fluorescence of NdF<sub>3</sub>/SiO<sub>2</sub> Core/Shell Nanoparticles and the Applications for *In Vivo* NIR Detection. *Advanced Materials* **2008**, *20* (21), 4118–4123.
- (84) Villa I, Vedda A, Cantarelli I X, Pedroni M, Piccinelli F, Bettinelli M, Speghini A, Quintanilla M, Vetrone F, Rocha U, Jacinto C, Carrasco E, Rodríguez F S, Juarranz Á, del Rosal B, Ortgies D H, Gonzalez P H, Solé J G, García D J. 1.3 nm Emitting SrF<sub>2</sub>:Nd<sup>3+</sup> Nanoparticles for High Contrast *In Vivo* Imaging in the Second Biological Window. *Nano Research* **2015**, *8* (2), 649–665.
- (85) Krasnovsky A A, Kovalev Yu V. Spectral and Kinetic Parameters of Phosphorescence of Triplet Chlorophyll a in the Photosynthetic Apparatus of Plants. *Biochemistry Moscow* **2014**, *79* (4), 349–361.
- (86) Soga K, Tokuzen K, Tsuji K, Yamano T, Hyodo H, Kishimoto H. NIR Bioimaging: Development of Liposome-Encapsulated, Rare-Earth-Doped Y<sub>2</sub>O<sub>3</sub> Nanoparticles as Fluorescent Probes. *European Journal of Inorganic Chemistry* **2010**, *2010* (18), 2673–2677.

- (87) Zhong Y, Dai H. A Mini-Review on Rare-Earth Down-Conversion Nanoparticles for NIR-II Imaging of Biological Systems. *Nano Research* **2020**, 1-14.
- (88) Naczynski D J, Tan M C, Zevon M, Wall B, Kohl J, Kulesa A, Chen S, Roth C M, Riman R E, Moghe P V. Rare-Earth-Doped Biological Composites as in Vivo Shortwave Infrared Reporters. *Nature Communications* **2013**, 4 (1), 1-10.
- (89) Zhong Y, Ma Z, Zhu S, Yue J, Zhang M, Antaris A L, Yuan J, Cui R, Wan H, Zhou Y, Wang W, Huang N F, Luo J, Hu Z, Dai H. Boosting the Down-Shifting Luminescence of Rare-Earth Nanocrystals for Biological Imaging beyond 1500 nm. *Nature Communications* **2017**, 8 (1), 1-7.
- (90) Zhong Y, Ma Z, Wang F, Wang X, Yang Y, Liu Y, Zhao X, Li J, Du H, Zhang M, Cui Q, Zhu S, Sun Q, Wan H, Tian Y, Liu Q, Wang W, Garcia K C, Dai H. In Vivo Molecular Imaging for Immunotherapy Using Ultra-Bright Near-Infrared-IIb Rare-Earth Nanoparticles. *Nature Biotechnology* **2019**, 37 (11), 1322-1331.
- (91) Ortgies D H, Tan M, Ximendes E C, del Rosal B, Hu J, Xu L, Wang X, Martín Rodríguez E, Jacinto C, Fernandez N, Chen G, Jaque D. Lifetime-Encoded Infrared-Emitting Nanoparticles for in Vivo Multiplexed Imaging. *ACS Nano* **2018**, 12 (5), 4362-4368.
- (92) He S, Johnson N J J, Nguyen Huu V A, Cory E, Huang Y, Sah R L, Jokerst J V, Almutairi A. Simultaneous Enhancement of Photoluminescence, MRI Relaxivity, and CT Contrast by Tuning the Interfacial Layer of Lanthanide Heteroepitaxial Nanoparticles. *Nano Letters* **2017**, 17 (8), 4873-4880.
- (93) Rieffel J, Chen F, Kim J, Chen G, Shao W, Shao S, Chitgupi U, Hernandez R, Graves S A, Nickles R J, Prasad P N, Kim C, Cai W, Lovell J F. Hexamodal Imaging with Porphyrin-Phospholipid-Coated Upconversion Nanoparticles. *Advanced Materials* **2015**, 27 (10), 1785-1790.
- (94) Tsai E S, Himmelstoß S F, Wiesholler L M, Hirsch T, Hall E A. Upconversion Nanoparticles for Sensing PH. *Analyst* **2019**, 144 (18), 5547-5557.
- (95) Liu Q, Peng J, Sun L, Li F. High-Efficiency Upconversion Luminescent Sensing and Bioimaging of Hg(II) by Chromophoric Ruthenium Complex-Assembled Nanophosphors. *ACS Nano* **2011**, 5 (10), 8040-8048.
- (96) Kong M, Gu Y, Liu Y, Shi Y, Wu N, Feng W, Li F. Luminescence Lifetime-Based In Vivo Detection with Responsive Rare Earth-Dye Nanocomposite. *Small* **2019**, 15 (46), 1904487.
- (97) Jesu Raj J G, Quintanilla M, Mahmoud K A, Ng A, Vetrone F, Zourob M. Sensitive Detection of SsDNA Using an LRET-Based Upconverting Nanohybrid Material. *ACS Applied Materials & Interfaces* **2015**, 7 (33), 18257-18265.
- (98) Liu J, Zhang R, Shang C, Zhang Y, Feng Y, Pan L, Xu B, Hyeon T, Bu W, Shi J, Du J. Near-Infrared Voltage Nanosensors Enable Real-Time Imaging of Neuronal Activities in Mice and Zebrafish. *Journal of the American Chemical Society* **2020**, 142 (17), 7858-7867.
- (99) DaCosta M V, Doughan S, Han Y, Krull U J. Lanthanide Upconversion Nanoparticles and Applications in Bioassays and Bioimaging: A Review. *Analytica Chimica Acta* **2014**, 832, 1-33.
- (100) Guo S, Xie X, Huang L, Huang W. Sensitive Water Probing through Nonlinear Photon Upconversion of Lanthanide-Doped Nanoparticles. *ACS Applied Materials and Interfaces* **2016**, 8 (1), 847-853.

- (101) Wisser M D, Chea M, Lin Y, Wu D M, Mao W L, Salleo A, Dionne J A. Strain-Induced Modification of Optical Selection Rules in Lanthanide-Based Upconverting Nanoparticles. *Nano Letters* **2015**, *15* (3), 1891–1897.
- (102) Lay A, Sheppard O H, Siefe C, McLellan C A, Mehlenbacher R D, Fischer S, Goodman M B, Dionne J A. Optically Robust and Biocompatible Mechanosensitive Upconverting Nanoparticles. *ACS Central Science* **2019**, *5* (7), 1211–1222.
- (103) Yang Y, Velmurugan B, Liu X, Xing B. NIR Photoresponsive Crosslinked Upconverting Nanocarriers Toward Selective Intracellular Drug Release. *Small* **2013**, *9* (17), 2937–2944.
- (104) Liu J, Bu W, Pan L, Shi J. NIR-Triggered Anticancer Drug Delivery by Upconverting Nanoparticles with Integrated Azobenzene-Modified Mesoporous Silica. *Angewandte Chemie International Edition* **2013**, *52* (16), 4375–4379.
- (105) Dong J, Zink J I. Light or Heat? The Origin of Cargo Release from Nanoimpeller Particles Containing Upconversion Nanocrystals under IR Irradiation. *Small* **2015**, *11* (33), 4165–4172.
- (106) Yan B, Boyer J-C, Habault D, Branda N R, Zhao Y. Near Infrared Light Triggered Release of Biomacromolecules from Hydrogels Loaded with Upconversion Nanoparticles. *Journal of the American Chemical Society* **2012**, *134* (40), 16558–16561.
- (107) Jalani G, Naccache R, Rosenzweig D H, Haglund L, Vetrone F, Cerruti M. Photocleavable Hydrogel-Coated Upconverting Nanoparticles: A Multifunctional Theranostic Platform for NIR Imaging and On-Demand Macromolecular Delivery. *Journal of the American Chemical Society* **2016**, *138* (3), 1078–1083.
- (108) Chu H, Zhao J, Mi Y, Di Z, Li L. NIR-Light-Mediated Spatially Selective Triggering of Anti-Tumor Immunity via Upconversion Nanoparticle-Based Immunodevices. *Nature Communications* **2019**, *10* (1), 2839.
- (109) Wang D, Xue B, Kong X, Tu L, Liu X, Zhang Y, Chang Y, Luo Y, Zhao H, Zhang H. 808 Nm Driven Nd<sup>3+</sup>-Sensitized Upconversion Nanostructures for Photodynamic Therapy and Simultaneous Fluorescence Imaging. *Nanoscale* **2015**, *7* (1), 190–197.
- (110) Idris N M, Gnanasammandhan M K, Zhang J, Ho P C, Mahendran R, Zhang Y. In Vivo Photodynamic Therapy Using Upconversion Nanoparticles as Remote-Controlled Nanotransducers. *Nature Medicine* **2012**, *18* (10), 1580–1585.
- (111) Skripka A, Marin R, Benayas A, Canton P, Hemmer E, Vetrone F. Covering the Optical Spectrum through Collective Rare-Earth Doping of NaGdF<sub>4</sub> Nanoparticles: 806 and 980 nm Excitation Routes. *Physical Chemistry Chemical Physics* **2017**, *19* (19), 11825–11834.
- (112) He S, Johnson N J J, Nguyen Huu V A, Huang Y, Almutairi A. Leveraging Spectral Matching between Photosensitizers and Upconversion Nanoparticles for 808 Nm-Activated Photodynamic Therapy. *Chemistry of Materials* **2018**, *30* (12), 3991–4000.
- (113) Hamblin M R. Upconversion in Photodynamic Therapy: Plumbing the Depths. *Dalton Transactions* **2018**, *47* (26), 8571–8580.
- (114) Liu Y, Meng X, Bu W. Upconversion-Based Photodynamic Cancer Therapy. *Coordination Chemistry Reviews* **2019**, *379*, 82–98.
- (115) Hou Z, Deng K, Li C, Deng X, Lian H, Cheng Z, Jin D, Lin J. 808 Nm Light-Triggered and Hyaluronic Acid-Targeted Dual-Photosensitizers Nanoplatform by Fully Utilizing Nd<sup>3+</sup>-Sensitized Upconversion Emission with Enhanced Anti-Tumor Efficacy. *Biomaterials* **2016**, *101*, 32–46.

- (116) Zhang J Y, Chen S, Wang P, Jiang D J, Ban D X, Zhong N Z, Jiang G C, Li H, Hu Z, Xiao J R, Zhang Z G, Cao W W. NaYbF<sub>4</sub> Nanoparticles as near Infrared Light Excited Inorganic Photosensitizers for Deep Penetration in Photodynamic Therapy. *Nanoscale* **2017**, 9 (8), 2706–2710.
- (117) Mironova K E, Khochenkov D A, Generalova A N, Rocheva V V, Sholina N V, Nechaev A V, Semchishen V A, Deyev S M, Zvyagin A V, Khaydukov E V. Ultraviolet Phototoxicity of Upconversion Nanoparticles Illuminated with Near-Infrared Light. *Nanoscale* **2017**, 9 (39), 14921–14928.
- (118) Rocha U, Upendra Kumar K, Jacinto C, Ramiro J, Caamaño A J, García Solé J, Jaque D. Nd<sup>3+</sup> Doped LaF<sub>3</sub> Nanoparticles as Self-Monitored Photo-Thermal Agents. *Applied Physics Letters* **2014**, 104 (5), 053703.
- (119) All A H, Zeng X, Teh D B L, Yi Z, Prasad A, Ishizuka T, Thakor N, Hiromu Y, Liu X. Expanding the Toolbox of Upconversion Nanoparticles for In Vivo Optogenetics and Neuromodulation. *Advanced Materials* **2019**, 31 (41), 1803474.
- (120) Chen S, Weitemier A Z, Zeng X, He L, Wang X, Tao Y, Huang A J Y, Hashimoto-dani Y, Kano M, Iwasaki H, Parajuli L K, Okabe S, Teh D B L, All A H, Tsutsui-Kimura I, Tanaka K F, Liu X, McHugh T J. Near-Infrared Deep Brain Stimulation via Upconversion Nanoparticle-Mediated Optogenetics. *Science* **2018**, 359 (6376), 679–684.
- (121) Ma Y, Bao J, Zhang Y, Li Z, Zhou X, Wan C, Huang L, Zhao Y, Han G, Xue T. Mammalian Near-Infrared Image Vision through Injectable and Self-Powered Retinal Nanoantennae. *Cell* **2019**, 177 (2), 243–255.
- (122) Sengupta P, Garrity P. Sensing Temperature. *Current Biology* **2013**, 23 (8), R304–R307.
- (123) Evans S S, Repasky E A, Fisher D T. Fever and the Thermal Regulation of Immunity: The Immune System Feels the Heat. *Nature Reviews Immunology* **2015**, 15 (6), 335–349.
- (124) Day E S, Morton J G, West J L. Nanoparticles for Thermal Cancer Therapy. *Journal of Biomechanical Engineering* **2009**, 131 (7), 074001.
- (125) Li S, Zhang K, Yang J-M, Lin L, Yang H. Single Quantum Dots as Local Temperature Markers. *Nano Letters* **2007**, 7 (10), 3102–3105.
- (126) Löw P, Kim B, Takama N, Bergaud C. High-Spatial-Resolution Surface-Temperature Mapping Using Fluorescent Thermometry. *Small* **2008**, 4 (7), 908–914.
- (127) Deepankumar K, Nadarajan S P, Bae D-H, Baek K-H, Choi K-Y, Yun H. Temperature Sensing Using Red Fluorescent Protein. *Biotechnology and Bioprocess Engineering* **2015**, 20 (1), 67–72.
- (128) Uchiyama S, Kawai N, de Silva A P, Iwai K. Fluorescent Polymeric AND Logic Gate with Temperature and PH as Inputs. *Journal of the American Chemical Society* **2004**, 126 (10), 3032–3033.
- (129) Gota C, Okabe K, Funatsu T, Harada Y, Uchiyama S. Hydrophilic Fluorescent Nanogel Thermometer for Intracellular Thermometry. *Journal of the American Chemical Society* **2009**, 131 (8), 2766–2767.
- (130) Brites C D S, Balabhadra S, Carlos L D. Lanthanide-Based Thermometers: At the Cutting-Edge of Luminescence Thermometry. *Advanced Optical Materials* **2019**, 7 (5), 1801239.
- (131) Miller M P, Wright J C. Multiphonon and Energy Transfer Relaxation in Charge Compensated Crystals. *The Journal of Chemical Physics* **1979**, 71 (1), 324–338.

- (132) Dramićanin M D. Sensing Temperature via Downshifting Emissions of Lanthanide-Doped Metal Oxides and Salts. A Review. *Methods and Applications in Fluorescence* **2016**, 4 (4), 042001.
- (133) Baffou G, Kreuzer M P, Kulzer F, Quidant R. Temperature Mapping near Plasmonic Nanostructures Using Fluorescence Polarization Anisotropy. *Optics Express* **2009**, 17 (5), 3291.
- (134) Sardar D K, Yow R M. Inter-Stark Energy Levels and Effects of Temperature on Sharp Emission Lines of Nd<sup>3+</sup> in LiYF<sub>4</sub>. *Physica Status Solidi (a)* **1999**, 173 (2), 521–534.
- (135) Brites C D S, Lima P P, Silva N J O, Millán A, Amaral V S, Palacio F, Carlos L D. Thermometry at the Nanoscale. *Nanoscale* **2012**, 4 (16), 4799.
- (136) Brites C D S, Millán A, Carlos L D. Lanthanides in Luminescent Thermometry. In *Handbook on the Physics and Chemistry of Rare Earths*; Elsevier, 2016; Vol. 49, pp 339–427.
- (137) Quintanilla M, Liz-Marzán L M. Guiding Rules for Selecting a Nanothermometer. *Nano Today* **2018**, 19, 126–145.
- (138) Jaque D, Vetrone F. Luminescence Nanothermometry. *Nanoscale* **2012**, 4 (15), 4301.
- (139) Wang X, Wolfbeis O S, Meier R J. Luminescent Probes and Sensors for Temperature. *Chemical Society Reviews* **2013**, 42 (19), 7834.
- (140) Rai V K. Temperature Sensors and Optical Sensors. *Applied Physics B* **2007**, 88 (2), 297–303.
- (141) Vetrone F, Naccache R, Zamarrón A, Juarranz de la Fuente A, Sanz-Rodríguez F, Martínez Maestro L, Martín Rodríguez E, Jaque D, García Solé J, Capobianco J A. Temperature Sensing Using Fluorescent Nanothermometers. *ACS Nano* **2010**, 4 (6), 3254–3258.
- (142) Wawrzynczyk D, Bednarkiewicz A, Nyk M, Strek W, Samoc M. Neodymium(III) Doped Fluoride Nanoparticles as Non-Contact Optical Temperature Sensors. *Nanoscale* **2012**, 4 (22), 6959.
- (143) Kolesnikov I E, Golyeva E V, Kurochkin M A, Lähderanta E, Mikhailov M D. Nd<sup>3+</sup>-Doped YVO<sub>4</sub> Nanoparticles for Luminescence Nanothermometry in the First and Second Biological Windows. *Sensors and Actuators B: Chemical* **2016**, 235, 287–293.
- (144) Quintanilla M, Zhang Y, Liz-Marzán L M. Subtissue Plasmonic Heating Monitored with CaF<sub>2</sub>:Nd<sup>3+</sup>, Y<sup>3+</sup> Nanothermometers in the Second Biological Window. *Chemistry of Materials* **2018**, 30 (8), 2819–2828.
- (145) Balabhadra S, Debasu M L, Brites C D S, Rocha J, Carlos L D. Implementing Luminescence Thermometry at 1.3 μm Using (GdNd)<sub>2</sub>O<sub>3</sub> Nanoparticles. *Journal of Luminescence* **2016**, 180, 25–30.
- (146) Skripka A, Morinvil A, Matulionyte M, Cheng T, Vetrone F. Advancing Neodymium Single-Band Nanothermometry. *Nanoscale* **2019**, 11 (23), 11322–11330.
- (147) Souza A S, Nunes L A O, Silva I G N, Oliveira F A M, da Luz L L, Brito H F, Felinto M C F C, Ferreira R A S, Júnior S A, Carlos L D, Malta O L. Highly-Sensitive Eu<sup>3+</sup> Ratiometric Thermometers Based on Excited State Absorption with Predictable Calibration. *Nanoscale* **2016**, 8 (9), 5327–5333.

- (148) Marciniak L, Bednarkiewicz A, Elzbieciak K. NIR–NIR Photon Avalanche Based Luminescent Thermometry with Nd<sup>3+</sup> Doped Nanoparticles. *Journal of Materials Chemistry C* **2018**, 6 (28), 7568–7575.
- (149) Marciniak L, Bednarkiewicz A, Stefanski M, Tomala R, Hreniak D, Strek W. Near Infrared Absorbing near Infrared Emitting Highly-Sensitive Luminescent Nanothermometer Based on Nd<sup>3+</sup> to Yb<sup>3+</sup> Energy Transfer. *Physical Chemistry Chemical Physics* **2015**, 17 (37), 24315–24321.
- (150) Ximendes E C, Santos W Q, Rocha U, Kagola U K, Sanz-Rodríguez F, Fernández N, Gouveia-Neto A da S, Bravo D, Domingo A M, del Rosal B, Brites C D S, Carlos L D, Jaque D, Jacinto C. Unveiling in Vivo Subcutaneous Thermal Dynamics by Infrared Luminescent Nanothermometers. *Nano Letters* **2016**, 16 (3), 1695–1703.
- (151) Cortelletti P, Skripka A, Facciotti C, Pedroni M, Caputo G, Pinna N, Quintanilla M, Benayas A, Vetrone F, Speghini A. Tuning the Sensitivity of Lanthanide-Activated NIR Nanothermometers in the Biological Windows. *Nanoscale* **2018**, 10 (5), 2568–2576.
- (152) Skripka A, Benayas A, Marin R, Canton P, Hemmer E, Vetrone F. Double Rare-Earth Nanothermometer in Aqueous Media: Opening the Third Optical Transparency Window to Temperature Sensing. *Nanoscale* **2017**, 9 (9), 3079–3085.
- (153) Martínez E D, Brites C D S, Carlos L D, García-Flores A F, Urbano R R, Rettori C. Electrochromic Switch Devices Mixing Small- and Large-Sized Upconverting Nanocrystals. *Advanced Functional Materials* **2019**, 29 (8), 1807758.
- (154) Zhou J, Wen S, Liao J, Clarke C, Tawfik S A, Ren W, Mi C, Wang F, Jin D. Activation of the Surface Dark-Layer to Enhance Upconversion in a Thermal Field. *Nature Photonics* **2018**, 12 (3), 154–158.
- (155) Mi C, Zhou J, Wang F, Lin G, Jin D. Ultrasensitive Ratiometric Nanothermometer with Large Dynamic Range and Photostability. *Chemistry of Materials* **2019**, 31 (22), 9480–9487.
- (156) Ximendes E C, Rocha U, Sales T O, Fernández N, Sanz-Rodríguez F, Martín I R, Jacinto C, Jaque D. In Vivo Subcutaneous Thermal Video Recording by Supersensitive Infrared Nanothermometers. *Advanced Functional Materials* **2017**, 27 (38), 1702249.
- (157) Ximendes E C, Rocha U, del Rosal B, Vaquero A, Sanz-Rodríguez F, Monge L, Ren F, Vetrone F, Ma D, García-Solé J, Jacinto C, Jaque D, Fernández N. In Vivo Ischemia Detection by Luminescent Nanothermometers. *Advanced Healthcare Materials* **2017**, 6 (4), 1601195.
- (158) Santos H D A, Ximendes E C, Iglesias-de la Cruz M del C, Chaves-Coira I, del Rosal B, Jacinto C, Monge L, Rubia-Rodríguez I, Ortega D, Mateos S, GarcíaSolé J, Jaque D, Fernández N. In Vivo Early Tumor Detection and Diagnosis by Infrared Luminescence Transient Nanothermometry. *Advanced Functional Materials* **2018**, 1803924.
- (159) del Rosal B, Ruiz D, Chaves-Coira I, Juárez B H, Monge L, Hong G, Fernández N, Jaque D. In Vivo Contactless Brain Nanothermometry. *Advanced Functional Materials* **2018**, 1806088.
- (160) Rocha U, Jacinto da Silva C, Ferreira Silva W, Guedes I, Benayas A, Martínez Maestro L, Acosta Elías M, Bovero E, van Veggel F C J M, García Solé J A, Jaque D. Subtissue Thermal Sensing Based on Neodymium-Doped LaF<sub>3</sub> Nanoparticles. *ACS Nano* **2013**, 7 (2), 1188–1199.

- (161) Rocha U, Hu J, Rodríguez E M, Vanetsev A S, Rähn M, Sammelselg V, Orlovskii Y V, Solé J G, Jaque D, Ortgies D H. Subtissue Imaging and Thermal Monitoring of Gold Nanorods through Joined Encapsulation with Nd-Doped Infrared-Emitting Nanoparticles. *Small* **2016**, *12* (39), 5394–5400.
- (162) Zhu X, Feng W, Chang J, Tan Y-W, Li J, Chen M, Sun Y, Li F. Temperature-Feedback Upconversion Nanocomposite for Accurate Photothermal Therapy at Facile Temperature. *Nature Communications* **2016**, *7*, 10437.
- (163) Quintanilla M, García I, de Lázaro I, García-Alvarez R, Henriksen-Lacey M, Vranic S, Kostarelos K, Liz-Marzán L M. Thermal Monitoring during Photothermia: Hybrid Probes for Simultaneous Plasmonic Heating and Near-Infrared Optical Nanothermometry. *Theranostics* **2019**, *9* (24), 7298–7312.
- (164) Brites C D S, Xie X, Debasu M L, Qin X, Chen R, Huang W, Rocha J, Liu X, Carlos L D. Instantaneous Ballistic Velocity of Suspended Brownian Nanocrystals Measured by Upconversion Nanothermometry. *Nature Nanotechnology* **2016**, *11* (10), 851–856.
- (165) Brites C D S, Fuertes M C, Angelomé P C, Martínez E D, Lima P P, Soler-Illia G J A A, Carlos L D. Tethering Luminescent Thermometry and Plasmonics: Light Manipulation to Assess Real-Time Thermal Flow in Nanoarchitectures. *Nano Letters* **2017**, *17* (8), 4746–4752.
- (166) Miandashti A R, Kordesch M, Richardson H H. Time Resolved Temperature Measurement of Single Gold Structures via Luminescence Thermometry. *MRS Advances* **2018**, *3* (14), 747–751.
- (167) Savchuk O A, Carvajal J J, Brites C D S, Carlos L D, Aguilo M, Diaz F. Upconversion Thermometry: A New Tool to Measure the Thermal Resistance of Nanoparticles. *Nanoscale* **2018**, *10* (14), 6602–6610.
- (168) Bastos A R N, Brites C D S, Rojas-Gutierrez P A, DeWolf C, Ferreira R A S, Capobianco J A, Carlos L D. Thermal Properties of Lipid Bilayers Determined Using Upconversion Nanothermometry. *Advanced Functional Materials* **2019**, *29* (48), 1905474.
- (169) Hartman T, Geitenbeek R G, Whiting G T, Weckhuysen B M. Operando Monitoring of Temperature and Active Species at the Single Catalyst Particle Level. *Nature Catalysis* **2019**, *2* (11), 986–996.
- (170) Balabhadra S, Debasu M L, Brites C D S, Ferreira R A S, Carlos L D. Upconverting Nanoparticles Working As Primary Thermometers In Different Media. *The Journal of Physical Chemistry C* **2017**, *121* (25), 13962-13968.
- (171) Qiu X, Zhou Q, Zhu X, Wu Z, Feng W, Li F. Ratiometric Upconversion Nanothermometry with Dual Emission at the Same Wavelength Decoded via a Time-Resolved Technique. *Nature Communications* **2020**, *11* (1), 4.
- (172) Shen Y, Lifante J, Fernández N, Jaque D, Ximendes E. *In Vivo* Spectral Distortions of Infrared Luminescent Nanothermometers Compromise Their Reliability. *ACS Nano* **2020**, *14* (4), 4122–4133.
- (173) Labrador-Páez L, Pedroni M, Speghini A, García-Solé J, Haro-González P, Jaque D. Reliability of Rare-Earth-Doped Infrared Luminescent Nanothermometers. *Nanoscale* **2018**, *10* (47), 22319-22328.
- (174) Pickel A D, Teitelboim A, Chan E M, Borys N J, Schuck P J, Dames C. Apparent Self-Heating of Individual Upconverting Nanoparticle Thermometers. *Nature Communications* **2018**, *9* (1), 1-12.

- (175) Boyer J-C, Vetrone F, Cuccia L A, Capobianco J A. Synthesis of Colloidal Upconverting NaYF<sub>4</sub> Nanocrystals Doped with Er<sup>3+</sup>, Yb<sup>3+</sup> and Tm<sup>3+</sup>, Yb<sup>3+</sup> via Thermal Decomposition of Lanthanide Trifluoroacetate Precursors. *Journal of the American Chemical Society* **2006**, 128 (23), 7444–7445.
- (176) Dubertret B. In Vivo Imaging of Quantum Dots Encapsulated in Phospholipid Micelles. *Science* **2002**, 298 (5599), 1759–1762.
- (177) Skripka A, Dapkute D, Valanciunaite J, Karabanovas V, Rotomskis R. Impact of Quantum Dot Surface on Complex Formation with Chlorin e<sub>6</sub> and Photodynamic Therapy. *Nanomaterials* **2018**, 9 (1), 9.
- (178) May P S, Berry M. Tutorial on the Acquisition, Analysis, and Interpretation of Upconversion Luminescence Data. *Methods and Applications of Fluorescence* **2019**, 7 (2), 023001.
- (179) Chen G, Ohulchanskyy T Y, Liu S, Law W-C, Wu F, Swihart M T, Ågren H, Prasad P N. Core/Shell NaGdF<sub>4</sub>:Nd<sup>3+</sup>/NaGdF<sub>4</sub> Nanocrystals with Efficient Near-Infrared to Near-Infrared Downconversion Photoluminescence for Bioimaging Applications. *ACS Nano* **2012**, 6 (4), 2969–2977.
- (180) Marciniak L, Pilch A, Arabasz S, Jin D, Bednarkiewicz A. Heterogeneously Nd<sup>3+</sup> Doped Single Nanoparticles for NIR-Induced Heat Conversion, Luminescence, and Thermometry. *Nanoscale* **2017**, 9 (24), 8288–8297.
- (181) Jiang X, Cao C, Feng W, Li F. Nd<sup>3+</sup>-Doped LiYF<sub>4</sub> Nanocrystals for Bio-Imaging in the Second near-Infrared Window. *Journal of Materials Chemistry B* **2016**, 4 (1), 87–95.
- (182) Qin Q-S, Zhang P-Z, Sun L-D, Shi S, Chen N-X, Dong H, Zheng X-Y, Li L-M, Yan C-H. Ultralow-Power near-Infrared Excited Neodymium-Doped Nanoparticles for Long-Term in Vivo Bioimaging. *Nanoscale* **2017**, 9 (14), 4660–4664.
- (183) Asawa C K, Robinson M. Temperature-Dependent Concentration Quenching of Fluorescence by Cross Relaxation of Nd<sup>3+</sup> in LaF<sub>3</sub>. *Physical Review* **1966**, 141 (1), 251–258.
- (184) del Rosal B, Pérez-Delgado A, Misiak M, Bednarkiewicz A, Vanetsev A S, Orlovskii Y, Jovanović D J, Dramićanin M D, Rocha U, Upendra Kumar K, Jacinto C, Navarro E, Martín Rodríguez E, Pedroni M, Speghini A, Hirata G A, Martín I R, Jaque D. Neodymium-Doped Nanoparticles for Infrared Fluorescence Bioimaging: The Role of the Host. *Journal of Applied Physics* **2015**, 118 (14), 143104.
- (185) Shi R, Ling X, Li X, Zhang L, Lu M, Xie X, Huang L, Huang W. Tuning Hexagonal NaYbF<sub>4</sub> Nanocrystals down to Sub-10 nm for Enhanced Photon Upconversion. *Nanoscale* **2017**, 9 (36), 13739–13746.
- (186) Pilch-Wrobel A, Czaban B, Wawrzyńczyk D, Bednarkiewicz A. Quantum Yield Measurements of Yb, Ho Co-Doped Upconverting Nanomaterials: The Impact of Methods, Reference Materials and Concentration. *Journal of Luminescence* **2018**, 198, 482–487.
- (187) Kushida T, Marcos H M, Geusic J E. Laser Transition Cross Section and Fluorescence Branching Ratio for Nd<sup>3+</sup> in Yttrium Aluminum Garnet. *Physical Review* **1968**, 167 (2), 289–291.
- (188) Strohhöfer C. Optical Properties of Ion Beam Modified Waveguide Materials Doped with Erbium and Silver. PhD Thesis, 2001.

- (189) Jayakumar M, Kumara gnanasammandhan, Idris N M, Huang K, Zhang Y. A Paradigm Shift in the Excitation Wavelength of Upconversion Nanoparticles. *Nanoscale* **2014**, 6 (15), 8441–8443.
- (190) Naccache R, Vetrone F, Mahalingam V, Cuccia L A, Capobianco J A. Controlled Synthesis and Water Dispersibility of Hexagonal Phase NaGdF<sub>4</sub>:Ho<sup>3+</sup>/Yb<sup>3+</sup> Nanoparticles. *Chemistry of Materials* **2009**, 21 (4), 717–723.
- (191) Riedener T, Egger P, Hulliger J, Güdel H U. Upconversion Mechanisms in Er<sup>3+</sup>-Doped Ba<sub>2</sub>YCl<sub>7</sub>. *Physical Review B* **1997**, 56 (4), 1800–1808.
- (192) Chan E M, Han G, Goldberg J D, Gargas D J, Ostrowski A D, Schuck P J, Cohen B E, Milliron D J. Combinatorial Discovery of Lanthanide-Doped Nanocrystals with Spectrally Pure Upconverted Emission. *Nano Letters* **2012**, 12 (7), 3839–3845.
- (193) Jagosich F H, Gomes L, Tarelho L V G, Courrol L C, Ranieri I M. Deactivation Effects of the Lowest Excited States of Er<sup>3+</sup> and Ho<sup>3+</sup> Introduced by Nd<sup>3+</sup> Ions in LiYF<sub>4</sub> Crystals. *Journal of Applied Physics* **2002**, 91 (2), 624–632.
- (194) Kumar G A, Chen C W, Ballato J, Riman R E. Optical Characterization of Infrared Emitting Rare-Earth-Doped Fluoride Nanocrystals and Their Transparent Nanocomposites. *Chemistry of Materials* **2007**, 19 (6), 1523–1528.
- (195) Dai S, Yu C, Zhou G, Zhang J, Wang G. Effect of OH<sup>-</sup> Content on Emission Properties in Er<sup>3+</sup>-Doped Tellurite Glasses. *Journal of Non-Crystalline Solids* **2008**, 354 (12–13), 1357–1360.
- (196) Valanciunaite J, Skripka A, Streckyte G, Rotomskis R. Complex of Water-Soluble CdSe/ZnS Quantum Dots and Chlorin e<sub>6</sub>: Interaction and FRET. *Laser Applications in Life Sciences* **2010**, 7376, 737607.
- (197) Frolov A A, Zenkevich E I, Gurinovich G P, Kochubeyev G A. Chlorin e<sub>6</sub>-Liposome Interaction. Investigation by the Methods of Fluorescence Spectroscopy and Inductive Resonance Energy Transfer. *Journal of Photochemistry and Photobiology B: Biology* **1990**, 7 (1), 43–56.
- (198) Mojzisova H, Bonneau S, Vever-Bizet C, Brault D. The PH-Dependent Distribution of the Photosensitizer Chlorin E6 among Plasma Proteins and Membranes: A Physico-Chemical Approach. *Biochimica et Biophysica Acta (BBA) - Biomembranes* **2007**, 1768 (2), 366–374.
- (199) Przybylska D, Grzyb T. Synthesis and Up-Conversion of Core/Shell SrF<sub>2</sub>:Yb<sup>3+</sup>,Er<sup>3+</sup>@SrF<sub>2</sub>:Yb<sup>3+</sup>,Nd<sup>3+</sup> Nanoparticles under 808, 975, and 1532 nm Excitation Wavelengths. *Journal of Alloys and Compounds* **2020**, 831, 154797.
- (200) Hesse J, Klier D T, Sgarzi M, Nsubuga A, Bauer C, Grenzer J, Hübner R, Wislicenus M, Joshi T, Kumke M U, Stephan H. Rapid Synthesis of Sub-10 Nm Hexagonal NaYF<sub>4</sub>-Based Upconverting Nanoparticles Using Thermanol<sup>®</sup> 66. *ChemistryOpen* **2018**, 7 (2), 159–168.
- (201) Liao J, Jin D, Chen C, Li Y, Zhou J. Helix Shape Power-Dependent Properties of Single Upconversion Nanoparticles. *Journal of Physical Chemistry Letters* **2020**, 11(8), 2883–2890.
- (202) Wiesholler L M, Frenzel F, Grauel B, Würth C, Resch-Genger U, Hirsch T. Yb, Nd, Er-Doped Upconversion Nanoparticles: 980 nm versus 808 nm Excitation. *Nanoscale* **2019**, 11 (28), 13440–13449.
- (203) Carrasco E, del Rosal B, Sanz-Rodríguez F, de la Fuente Á J, Gonzalez P H, Rocha U, Kumar K U, Jacinto C, Solé J G, Jaque D. Intratumoral Thermal Reading During Photo-

- Thermal Therapy by Multifunctional Fluorescent Nanoparticles. *Advanced Functional Materials* **2015**, 25 (4), 615–626.
- (204) Benayas A, del Rosal B, Pérez-Delgado A, Santacruz-Gómez K, Jaque D, Hirata G A, Vetrone F. Nd:YAG Near-Infrared Luminescent Nanothermometers. *Advanced Optical Materials* **2015**, 3 (5), 687–694.
- (205) Lian X, Zhao D, Cui Y, Yang Y, Qian G. A near Infrared Luminescent Metal–Organic Framework for Temperature Sensing in the Physiological Range. *Chemical Communications* **2015**, 51 (100), 17676–17679.
- (206) Rocha U, Jacinto C, Kumar K U, López F J, Bravo D, Solé J G, Jaque D. Real-Time Deep-Tissue Thermal Sensing with Sub-Degree Resolution by Thermally Improved Nd<sup>3+</sup>:LaF<sub>3</sub> Multifunctional Nanoparticles. *Journal of Luminescence* **2016**, 175, 149–157.
- (207) Marciniak L, Bednarkiewicz A, Kowalska D, Strek W. A New Generation of Highly Sensitive Luminescent Thermometers Operating in the Optical Window of Biological Tissues. *Journal of Materials Chemistry C* **2016**, 4 (24), 5559–5563.
- (208) Marciniak L, Prorok K, Francés-Soriano L, Pérez-Prieto J, Bednarkiewicz A. A Broadening Temperature Sensitivity Range with a Core–Shell YbEr@YbNd Double Ratiometric Optical Nanothermometer. *Nanoscale* **2016**, 8 (9), 5037–5042.
- (209) Cerón E N, Ortgies D H, del Rosal B, Ren F, Benayas A, Vetrone F, Ma D, Sanz-Rodríguez F, Solé J G, Jaque D, Rodríguez E M. Hybrid Nanostructures for High-Sensitivity Luminescence Nanothermometry in the Second Biological Window. *Advanced Materials* **2015**, 27 (32), 4781–4787.
- (210) Savchuk O A, Carvajal J J, Haro-Gonzalez P, Aguiló M, Díaz F. Luminescent Nanothermometry Using Short-Wavelength Infrared Light. *Journal of Alloys and Compounds* **2018**, 746, 710–719.
- (211) Wortmann L, Suyari S, Ube T, Kamimura M, Soga K. Tuning the Thermal Sensitivity of  $\beta$ -NaYF<sub>4</sub>:Yb<sup>3+</sup>, Ho<sup>3+</sup>, Er<sup>3+</sup> Nanothermometers for Optimal Temperature Sensing in OTN-NIR (NIR II/III) Biological Window. *Journal of Luminescence* **2018**, 198, 236–242.
- (212) Jia M, Fu Z, Liu G, Sun Z, Li P, Zhang A, Lin F, Hou B, Chen G. NIR-II/III Luminescence Ratiometric Nanothermometry with Phonon-Tuned Sensitivity. *Advanced Optical Materials* **2020**, 8 (6), 1901173.
- (213) Miyakawa T, Dexter D L. Phonon Sidebands, Multiphonon Relaxation of Excited States, and Phonon-Assisted Energy Transfer between Ions in Solids. *Physical Review B* **1970**, 1 (7), 2961–2969.
- (214) Martín-Rodríguez R, Meijerink A. Infrared to Near-Infrared and Visible Upconversion Mechanisms in LiYF<sub>4</sub>:Yb<sup>3+</sup>, Ho<sup>3+</sup>. *Journal of Luminescence* **2014**, 147, 147–154.
- (215) Rubin J, Brenier A, Moncorge R, Pedrini C. Er<sup>3+</sup> → Ho<sup>3+</sup> Energy Transfer Mechanisms at Room Temperature in YLiF<sub>4</sub> Single Crystals. *Journal de Physique* **1987**, 48 (10), 1761–1777.
- (216) Walrafen G E. Raman Spectral Studies of the Effects of Temperature on Water Structure. *The Journal of Chemical Physics* **1967**, 47 (1), 114–126.
- (217) Nilsson A, Pettersson L G M. The Structural Origin of Anomalous Properties of Liquid Water. *Nature Communications* **2015**, 6 (1), 1–11.

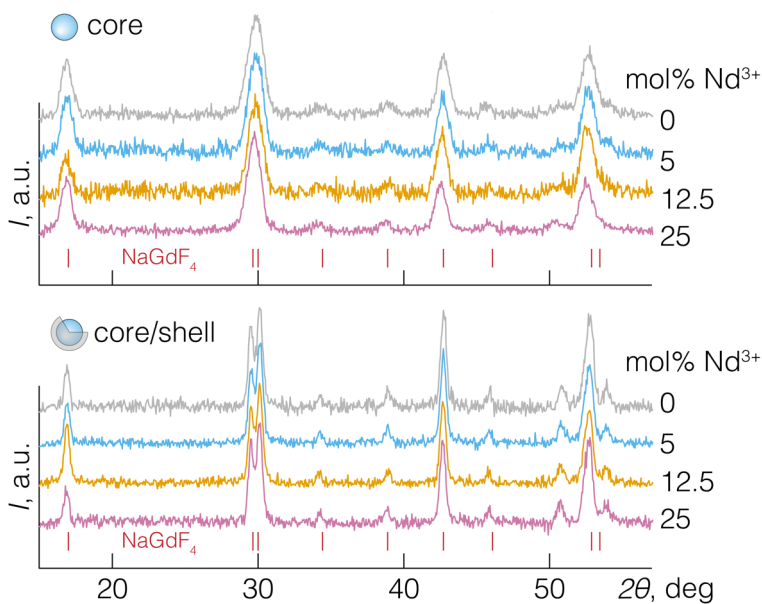
- (218) Segtnan V H, Šašić š., Isaksson T, Ozaki Y. Studies on the Structure of Water Using Two-Dimensional Near-Infrared Correlation Spectroscopy and Principal Component Analysis. *Analytical Chemistry* **2001**, 73 (13), 3153–3161.
- (219) Cooper G, Hausman R. The Molecular Composition of Cells. *The Cell: A Molecular Approach* **2000**, 43–72.
- (220) Wen H, Zhu H, Chen X, Hung T F, Wang B, Zhu G, Yu S F, Wang F. Upconverting Near-Infrared Light through Energy Management in Core-Shell-Shell Nanoparticles. *Angewandte Chemie* **2013**, 125 (50), 13661–13665.
- (221) Lai J, Zhang Y, Pasquale N, Lee K-B. An Upconversion Nanoparticle with Orthogonal Emissions Using Dual NIR Excitations for Controlled Two-Way Photoswitching. *Angewandte Chemie International Edition* **2014**, 53 (52), 14419–14423.
- (222) Zhou B, Yan L, Tao L, Song N, Wu M, Wang T, Zhang Q. Enabling Photon Upconversion and Precise Control of Donor-Acceptor Interaction through Interfacial Energy Transfer. *Advanced Science* **2018**, 5 (3), 1700667.
- (223) Marin R, Labrador-Paéz L, Skripka A, Haro-González P, Benayas A, Canton P, Jaque D, Vetrone F. Upconverting Nanoparticle to Quantum Dot Förster Resonance Energy Transfer: Increasing the Efficiency through Donor Design. *ACS Photonics* **2018**, 5 (6), 2261-2270.
- (224) Dong N-N, Pedroni M, Piccinelli F, Conti G, Sbarbati A, Ramírez-Hernández J E, Maestro L M, Iglesias-de la Cruz M C, Sanz-Rodríguez F, Juarranz A, Chen F, Vetrone F, Capobianco J A, Solé J G, Bettinelli M, Jaque D, Speghini A. NIR-to-NIR Two-Photon Excited CaF<sub>2</sub>:Tm<sup>3+</sup>, Yb<sup>3+</sup> Nanoparticles: Multifunctional Nanoprobes for Highly Penetrating Fluorescence Bio-Imaging. *ACS Nano* **2011**, 5 (11), 8665–8671.
- (225) Savchuk OI, Carvajal J J, De la Cruz L G, Haro-González P, Aguiló M, Díaz F. Luminescence Thermometry and Imaging in the Second Biological Window at High Penetration Depth with Nd:KGd(WO<sub>4</sub>)<sub>2</sub> Nanoparticles. *Journal of Materials Chemistry C* **2016**, 4 (31), 7397–7405.
- (226) Auzel F, Malta O L. A Scalar Crystal Field Strength Parameter for Rare-Earth Ions : Meaning and Usefulness. *Journal de Physique* **1983**, 44 (2), 201–206.
- (227) Fillmore C M, Kuperwasser C. Human Breast Cancer Cell Lines Contain Stem-like Cells That Self-Renew, Give Rise to Phenotypically Diverse Progeny and Survive Chemotherapy. *Breast Cancer Research* **2008**, 10 (2), R25.
- (228) Flors C. Imaging the Production of Singlet Oxygen in Vivo Using a New Fluorescent Sensor, Singlet Oxygen Sensor Green®. *Journal of Experimental Botany* **2006**, 57 (8), 1725–1734.
- (229) Gollmer A, Arnbjerg J, Blaikie F H, Pedersen B W, Breitenbach T, Daasbjerg K, Glasius M, Ogilby P R. Singlet Oxygen Sensor Green®: Photochemical Behavior in Solution and in a Mammalian Cell: Photochemistry and Photobiology. *Photochemistry and Photobiology* **2011**, 87 (3), 671–679.
- (230) Jarockyte G, Dapkute D, Karabanovas V, Daugmaudis J V, Ivanauskas F, Rotomskis R. 3D Cellular Spheroids as Tools for Understanding Carboxylated Quantum Dot Behavior in Tumors. *Biochimica et Biophysica Acta (BBA) - General Subjects* **2018**, 1862 (4), 914–923.
- (231) Hoshyar N, Gray S, Han H, Bao G. The Effect of Nanoparticle Size on *in Vivo* Pharmacokinetics and Cellular Interaction. *Nanomedicine* **2016**, 11 (6), 673–692.

- (232) Chithrani B D, Chan W C W. Elucidating the Mechanism of Cellular Uptake and Removal of Protein-Coated Gold Nanoparticles of Different Sizes and Shapes. *Nano Letters* **2007**, 7 (6), 1542–1550.
- (233) Hong A-R, Kim S Y, Cho S-H, Lee K, Jang H S. Facile Synthesis of Multicolor Tunable Ultrasmall LiYF<sub>4</sub>:Yb,Tm,Er/LiGdF<sub>4</sub> Core/Shell Upconversion Nanophosphors with Sub-10 nm Size. *Dyes and Pigments* **2017**, 139, 831–838.
- (234) Zou Q, Huang P, Zheng W, You W, Li R, Tu D, Xu J, Chen X. Cooperative and Non-Cooperative Sensitization Upconversion in Lanthanide-Doped LiYbF<sub>4</sub> Nanoparticles. *Nanoscale* **2017**, 9 (19), 6521–6528.
- (235) Kale V, Lastusaari M, Hölsä J, Soukka T. Intense UV Upconversion through Highly Sensitized NaRF<sub>4</sub>:Tm (R:Y,Yb) Crystals. *RSC Advances* **2015**, 5 (45), 35858–35865.
- (236) Wen S, Zhou J, Zheng K, Bednarkiewicz A, Liu X, Jin D. Advances in Highly Doped Upconversion Nanoparticles. *Nature Communications* **2018**, 9 (1), 1-12.
- (237) Hudry D, Busko D, Popescu R, Gerthsen D, Abeykoon A M M, Kübel C, Bergfeldt T, Richards B S. Direct Evidence of Significant Cation Intermixing in Upconverting Core@Shell Nanocrystals: Toward a New Crystallochemical Model. *Chemistry of Materials* **2017**, 29 (21), 9238–9246.
- (238) Razgoniaeva N, Yang M, Garrett P, Kholmicheva N, Moroz P, Eckard H, Royo Romero L, Porotnikov D, Khon D, Zamkov M. Just Add Ligands: Self-Sustained Size Focusing of Colloidal Semiconductor Nanocrystals. *Chemistry of Materials* **2018**, 30 (4), 1391–1398.
- (239) Wang F, Han Y, Lim C S, Lu Y, Wang J, Xu J, Chen H, Zhang C, Hong M, Liu X. Simultaneous Phase and Size Control of Upconversion Nanocrystals through Lanthanide Doping. *Nature* **2010**, 463 (7284), 1061–1065.
- (240) Huang X. Tuning the Size and Upconversion Luminescence of NaYbF<sub>4</sub>:Er<sup>3+</sup>/Tm<sup>3+</sup> Nanoparticles through Y<sup>3+</sup> or Gd<sup>3+</sup> Doping. *Optical Materials Express* **2016**, 6 (7), 2165.
- (241) Damasco J A, Chen G, Shao W, Ågren H, Huang H, Song W, Lovell J F, Prasad P N. Size-Tunable and Monodisperse Tm<sup>3+</sup>/Gd<sup>3+</sup>-Doped Hexagonal NaYbF<sub>4</sub> Nanoparticles with Engineered Efficient Near Infrared-to-Near Infrared Upconversion for In Vivo Imaging. *ACS Applied Materials & Interfaces* **2014**, 6 (16), 13884–13893.
- (242) Cheng T, Marin R, Skripka A, Vetrone F. Small and Bright Lithium-Based Upconverting Nanoparticles. *Journal of the American Chemical Society* **2018**, 140 (40), 12890–12899.
- (243) Chen B, Kong W, Wang N, Zhu G, Wang F. Oleylamine-Mediated Synthesis of Small NaYbF<sub>4</sub> Nanoparticles with Tunable Size. *Chemistry of Materials* **2019**, 31 (13), 4779–4786.
- (244) Marin R, Sponchia G, Zucchetta E, Riello P, Enrichi F, De Portu G, Benedetti A. Monitoring the *t* → *m* Martensitic Phase Transformation by Photoluminescence Emission in Eu<sup>3+</sup>-Doped Zirconia Powders. *Journal of the American Ceramic Society* **2013**, 96 (8), 2628–2635.
- (245) Kaiser M, Würth C, Kraft M, Soukka T, Resch-Genger U. Explaining the Influence of Dopant Concentration and Excitation Power Density on the Luminescence and Brightness of β-NaYF<sub>4</sub>:Yb<sup>3+</sup>,Er<sup>3+</sup> Nanoparticles: Measurements and Simulations. *Nano Research*. **2019**, 12(8), 1871-1879.
- (246) Chen B, Liu Y, Xiao Y, Chen X, Li Y, Li M, Qiao X, Fan X, Wang F. Amplifying Excitation-Power Sensitivity of Photon Upconversion in a NaYbF<sub>4</sub>:Ho Nanostructure for Direct

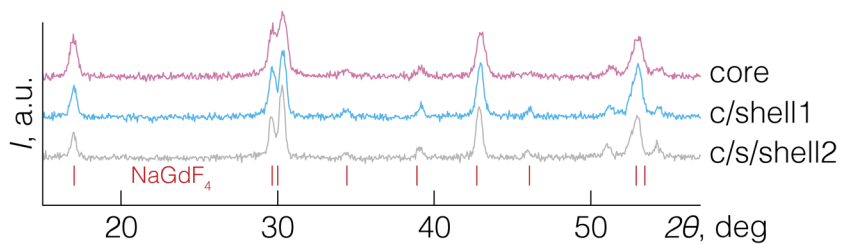
- Visualization of Electromagnetic Hotspots. *The Journal of Physical Chemistry Letters* **2016**, 7 (23), 4916–4921.
- (247) Pilch A, Wawrzyńczyk D, Kurnatowska M, Czaban B, Samoć M, Strek W, Bednarkiewicz A. The Concentration Dependent Up-Conversion Luminescence of Ho<sup>3+</sup> and Yb<sup>3+</sup> Co-Doped β-NaYF<sub>4</sub>. *Journal of Luminescence* **2017**, 182, 114–122.
- (248) Fong F K, Diestler D J. Many-Body Processes in Nonradiative Energy Transfer between Ions in Crystals. *The Journal of Chemical Physics* **1972**, 56 (6), 2875–2880.
- (249) Malta O L. Mechanisms of Non-Radiative Energy Transfer Involving Lanthanide Ions Revisited. *Journal of Non-Crystalline Solids* **2008**, 354 (42–44), 4770–4776.
- (250) Carneiro Neto A N, Moura R T, Malta O L. On the Mechanisms of Non-Radiative Energy Transfer between Lanthanide Ions: Centrosymmetric Systems. *Journal of Luminescence* **2019**, 210, 342–347.
- (251) Chen G, Shen J, Ohulchanskyy T Y, Patel N J, Kutikov A, Li Z, Song J, Pandey R K, Ågren H, Prasad P N, Han G. (α-NaYbF<sub>4</sub>:Tm<sup>3+</sup>)/CaF<sub>2</sub> Core/Shell Nanoparticles with Efficient Near-Infrared to Near-Infrared Upconversion for High-Contrast Deep Tissue Bioimaging. *ACS Nano* **2012**, 6 (9), 8280–8287.
- (252) Skripka A, Karabanovas V, Jarockyte G, Marin R, Tam V, Cerruti M, Rotomskis R, Vetrone F. Decoupling Theranostics with Rare Earth Doped Nanoparticles. *Advanced Functional Materials* **2019**, 29 (12), 1807105.
- (253) Homann C, Krukewitt L, Frenzel F, Grauel B, Würth C, Resch-Genger U, Haase M. NaYF<sub>4</sub>:Yb,Er/NaYF<sub>4</sub> Core/Shell Nanocrystals with High Upconversion Luminescence Quantum Yield. *Angewandte Chemie International Edition* **2018**, 57 (28), 8765–8769.
- (254) Pilch A, Würth C, Kaiser M, Wawrzyńczyk D, Kurnatowska M, Arabasz S, Prorok K, Samoć M, Strek W, Resch-Genger U, Bednarkiewicz A. Shaping Luminescent Properties of Yb<sup>3+</sup> and Ho<sup>3+</sup> Co-Doped Upconverting Core-Shell β-NaYF<sub>4</sub> Nanoparticles by Dopant Distribution and Spacing. *Small* **2017**, 13 (47), 1701635.
- (255) Zhang X, Wang M, Ding J, Gao D, Shi Y, Song X. The Novel Upconversion Properties of LiYbF<sub>4</sub>:Er Microcrystals Compared to the Na Counterpart. *CrystEngComm* **2012**, 14 (24), 8357.
- (256) Meijer M S, Rojas-Gutierrez P A, Busko D, Howard I A, Frenzel F, Würth C, Resch-Genger U, Richards B S, Turshatov A, Capobianco J A, Bonnet S. Absolute Upconversion Quantum Yields of Blue-Emitting LiYF<sub>4</sub>:Yb<sup>3+</sup>,Tm<sup>3+</sup> Upconverting Nanoparticles. *Physical Chemistry Chemical Physics* **2018**, 20 (35), 22556–22562.
- (257) Kraft M, Würth C, Palo E, Soukka T, Resch-Genger U. Colour-Optimized Quantum Yields of Yb, Tm Co-Doped Upconversion Nanocrystals. *Methods and Applications in Fluorescence* **2019**, 7 (2), 024001.
- (258) Zheng W, Huang P, Gong Z, Tu D, Xu J, Zou Q, Li R, You W, Bünzli J-C G, Chen X. Near-Infrared-Triggered Photon Upconversion Tuning in All-Inorganic Cesium Lead Halide Perovskite Quantum Dots. *Nature Communications* **2018**, 9 (1), 3462.
- (259) Liu L, Li X, Fan Y, Wang C, El-Toni A M, Alhoshan M S, Zhao D, Zhang F. Elemental Migration in Core/Shell Structured Lanthanide Doped Nanoparticles. *Chemistry of Materials* **2019**, 31 (15), 5608–5615.

- (260) Kolesnikov I E, Golyeva E V, Kalinichev A A, Kurochkin M A, Lähderanta E, Mikhailov M D. Nd<sup>3+</sup> Single Doped YVO<sub>4</sub> Nanoparticles for Sub-Tissue Heating and Thermal Sensing in the Second Biological Window. *Sensors and Actuators B: Chemical* **2017**, 243, 338–345.
- (261) Johnson N J J, van Veggel F C J M. Lanthanide-Based Heteroepitaxial Core–Shell Nanostructures: Compressive *versus* Tensile Strain Asymmetry. *ACS Nano* **2014**, 8 (10), 10517–10527.
- (262) Bednarkiewicz A, Wawrzynczyk D, Nyk M, Strek W. Optically Stimulated Heating Using Nd<sup>3+</sup> Doped NaYF<sub>4</sub> Colloidal Near Infrared Nanophosphors. *Applied Physics B* **2011**, 103 (4), 847–852.
- (263) Li Y, Zeng S, Hao J. Non-Invasive Optical Guided Tumor Metastasis/Vessel Imaging by Using Lanthanide Nanoprobe with Enhanced Down-Shifting Emission beyond 1500 nm. *ACS Nano* **2019**, 13 (1), 248–259.
- (264) Marciniak L, Prorok K, Bednarkiewicz A. Size Dependent Sensitivity of Yb<sup>3+</sup>,Er<sup>3+</sup> up-Converting Luminescent Nano-Thermometers. *Journal of Materials Chemistry C* **2017**, 5 (31), 7890–7897.
- (265) Pominova D V, Ryabova A V, Romanishkin I D, Kuznetsov S V, Ovsyannikova A A, Voronov V V, Loschenov V B. Influence of Y–Gd Ratio on Phase Formation and Spectroscopic Properties of NaGd<sub>0.8-x</sub>Y<sub>x</sub>Yb<sub>0.17</sub>Er<sub>0.03</sub>F<sub>4</sub> Solid Solutions. *Laser Physics Letters* **2019**, 16 (3), 035604.
- (266) Ivanova T Yu, Man'shina A A, Povolotskiy A V. Cross-Relaxation Processes and Structural Modifications in Ga–Ge–S:Er<sup>3+</sup> Chalcogenide Glasses. *Journal of Non-Crystalline Solids* **2005**, 351 (16–17), 1403–1409.
- (267) Wells J-P R, Horvath S P, Reid M F. Temperature Dependent Infrared Absorption, Crystal-Field and Intensity Analysis of Ce<sup>3+</sup> Doped LiYF<sub>4</sub>. *Optical Materials* **2015**, 47, 30–33.
- (268) Brown M R, Roots K G, Shand W A. Energy Levels of Er<sup>3+</sup> in LiYF<sub>4</sub>. *Journal of Physics C: Solid State Physics*. **1969**, 2 (4), 593–602.
- (269) Zhai X, Li J, Liu S, Liu X, Zhao D, Wang F, Zhang D, Qin G, Qin W. Enhancement of 153 Mm Emission Band in NaYF<sub>4</sub>:Er<sup>3+</sup>, Yb<sup>3+</sup>, Ce<sup>3+</sup> Nanocrystals for Polymer-Based Optical Waveguide Amplifiers. *Optical Materials Express* **2013**, 3 (2), 270.
- (270) Karayianis N. Theoretical Energy Levels and g Values for the <sup>4</sup>I Terms of Nd<sup>3+</sup> and Er<sup>3+</sup> in LiYF<sub>4</sub>. *Journal of Physics and Chemistry of Solids* **1971**, 32 (10), 2385–2391.

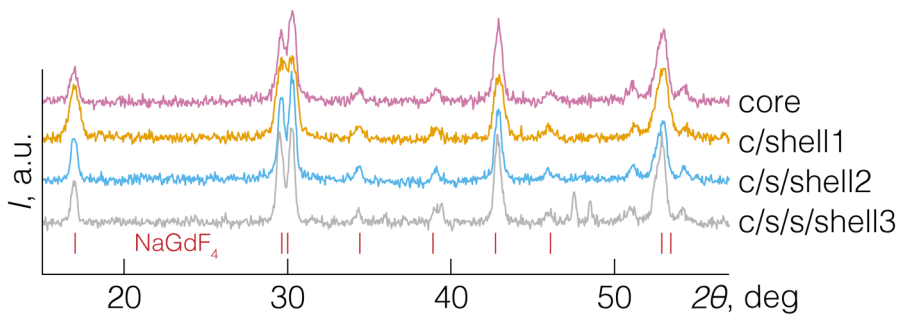
## Appendix I – XRD data



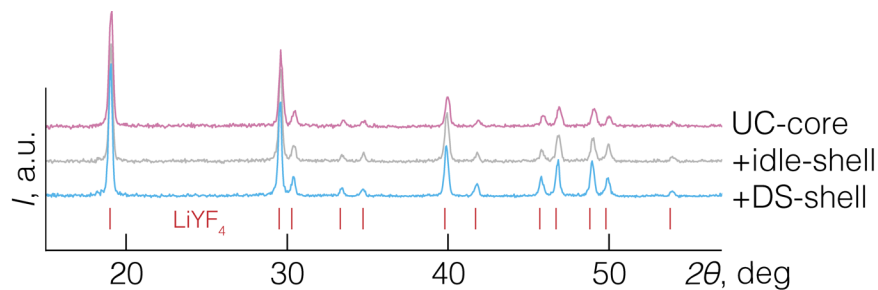
XRD patterns of core (top) and core/shell (bottom)  $\text{NaGdF}_4$ :  $x$  mol%  $\text{Nd}^{3+}/\text{NaGdF}_4$  RENPs ( $x = 0, 5, 12.5, 25$ ) of chapter 3. Reference pattern of pure  $\text{NaGdF}_4$  (PDF# 00-027-0699) is also shown.



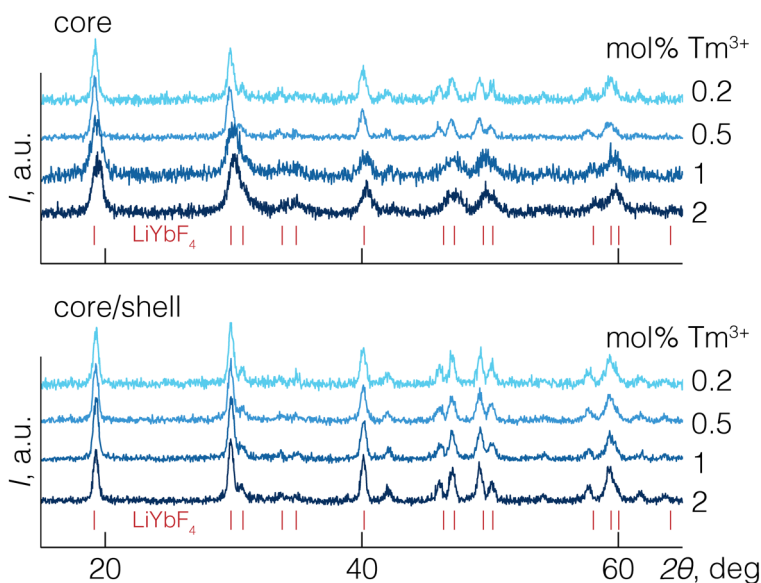
XRD patterns of core-only, core/shell1 (c/shell1) and core/shell1/shell2 (c/s/shell2) RENPs of chapter 4. Reference pattern of pure  $\text{NaGdF}_4$  (PDF# 00-027-0699) is also shown.



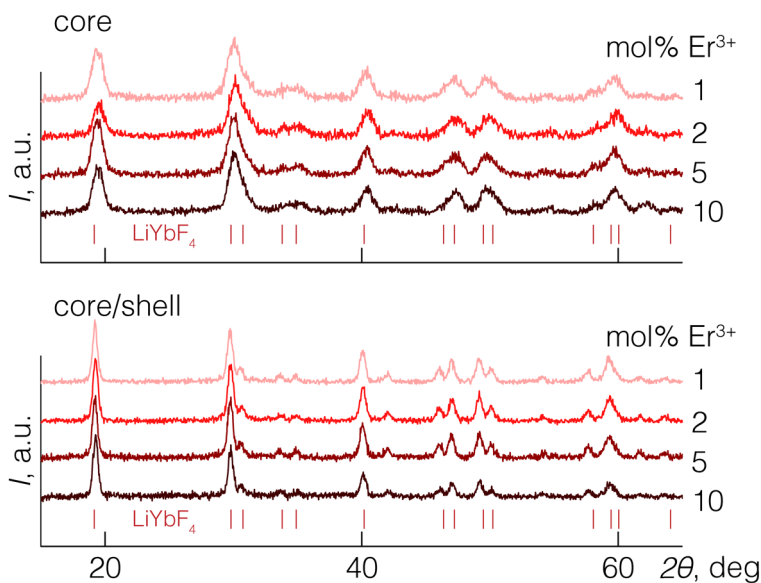
XRD patterns of core-only, core/shell1 (c/shell1), core/shell1/shell2 (c/s/shell2) and core/shell1/shell2/shell3 (c/s/s/shell3) RENPs of chapter 5. Reference pattern of pure  $\text{NaGdF}_4$  (PDF# 00-027-0699) is also shown.



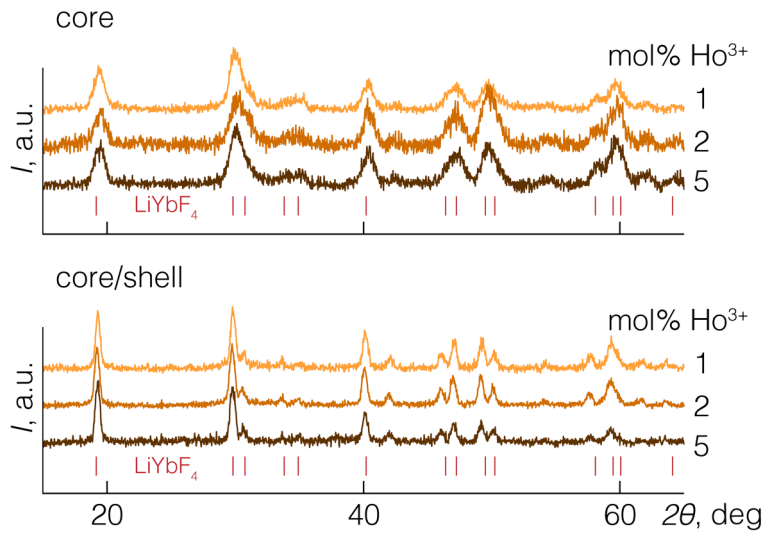
XRD patterns of UC-core, UC-core/idle-shell and UC-core/idle-shell/DS-shell RENPs of chapter 6. Reference pattern of pure  $\text{LiYF}_4$  (PDF# 00-017-0874) is also shown.



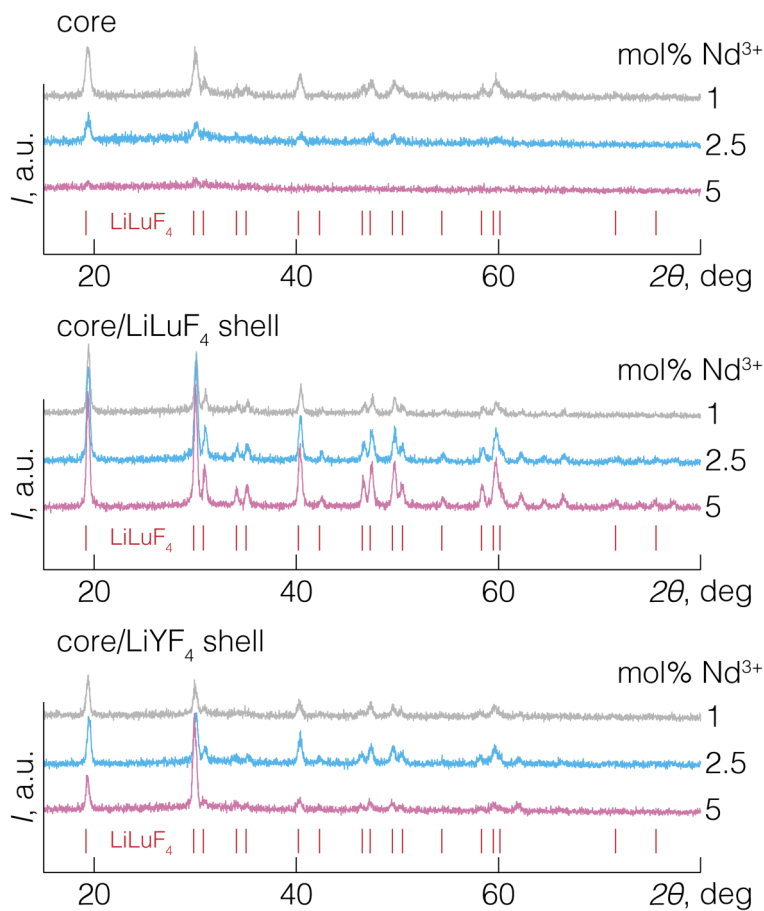
XRD patterns of core (top) and core/shell (bottom)  $\text{LiYbF}_4: x \text{ mol\% Tm}^{3+}/\text{LiYF}_4$  RENPs ( $x = 0.2, 0.5, 1, 2$ ) of chapter 8. Reference pattern of pure  $\text{LiYbF}_4$  (PDF# 00-023-0371) is also shown.



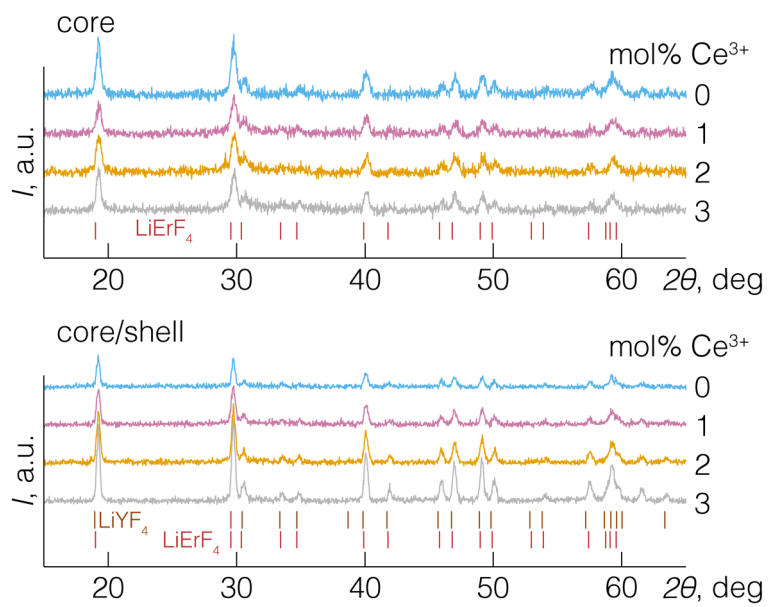
XRD patterns of core (top) and core/shell (bottom)  $\text{LiYbF}_4: x \text{ mol\% Er}^{3+}/\text{LiYF}_4$  RENPs ( $x = 1, 2, 5, 10$ ) of chapter 8. Reference pattern of pure  $\text{LiYbF}_4$  (PDF# 00-023-0371) is also shown.



XRD patterns of core (top) and core/shell (bottom)  $\text{LiYbF}_4$ :  $x$  mol%  $\text{Ho}^{3+}/\text{LiYF}_4$  RENPs ( $x = 1, 2, 5$ ) of chapter 8. Reference pattern of pure  $\text{LiYbF}_4$  (PDF# 00-023-0371) is also shown.

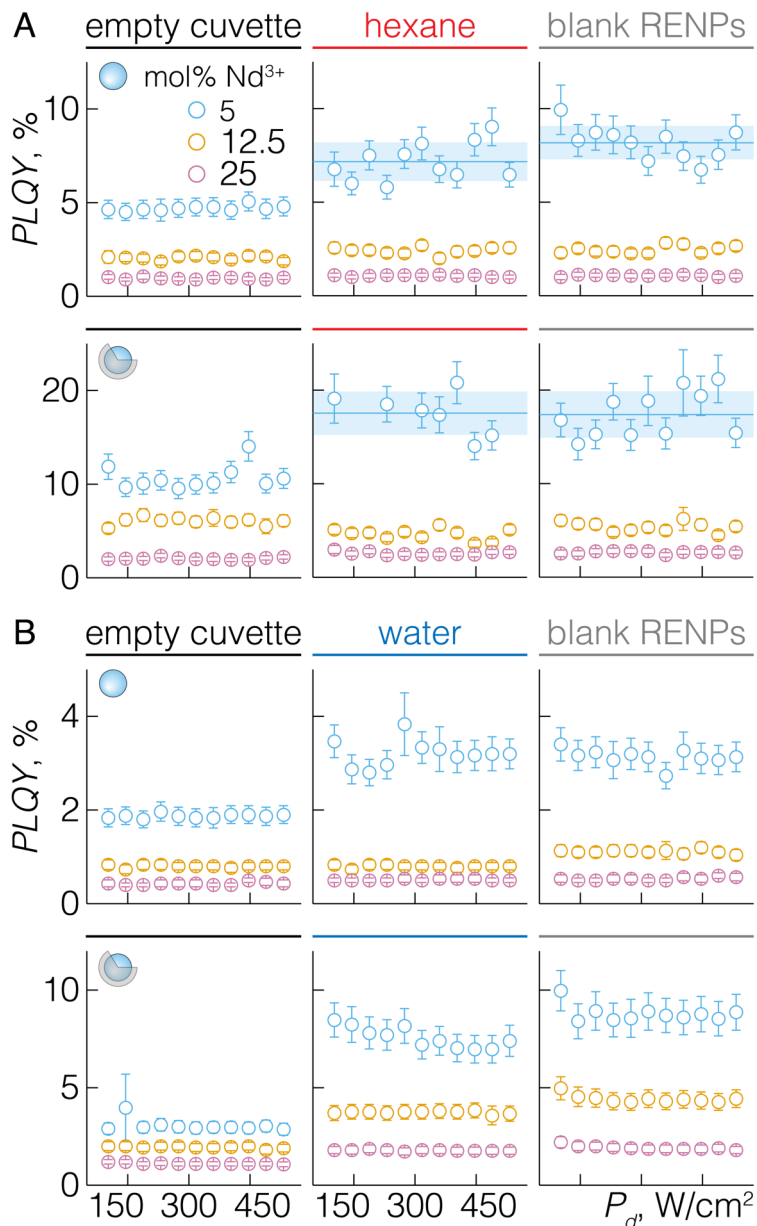


XRD patterns of core (top), core/ $\text{LiLuF}_4$  shell (middle) and core/ $\text{LiYF}_4$  shell (bottom)  $\text{LiLuF}_4$ :  $x$  mol%  $\text{Nd}^{3+}/\text{LiLuF}_4$  ( $\text{LiYF}_4$ ) RENPs ( $x = 1, 2.5, 5$ ) of chapter 9. Reference pattern of pure  $\text{LiLuF}_4$  (PDF# 00-027-1251) is also shown.



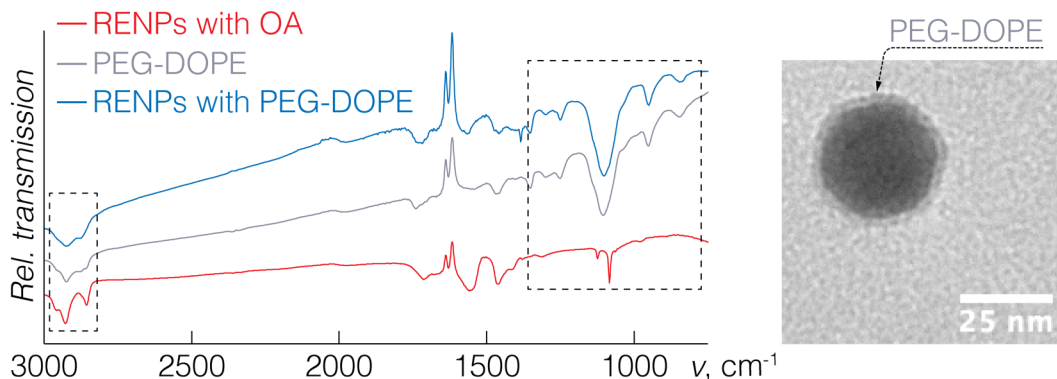
**XRD patterns of core (top) and core/shell (bottom) LiErF<sub>4</sub>: x mol% Ce<sup>3+</sup>/LiYF<sub>4</sub> RENPs (x = 0, 1, 2, 3) of chapter 10. Reference patterns of pure LiErF<sub>4</sub> (PDF# 00-051-1618) and pure LiYF<sub>4</sub> (PDF# 00-017-0874) are also shown.**

## Appendix II – PLQY data

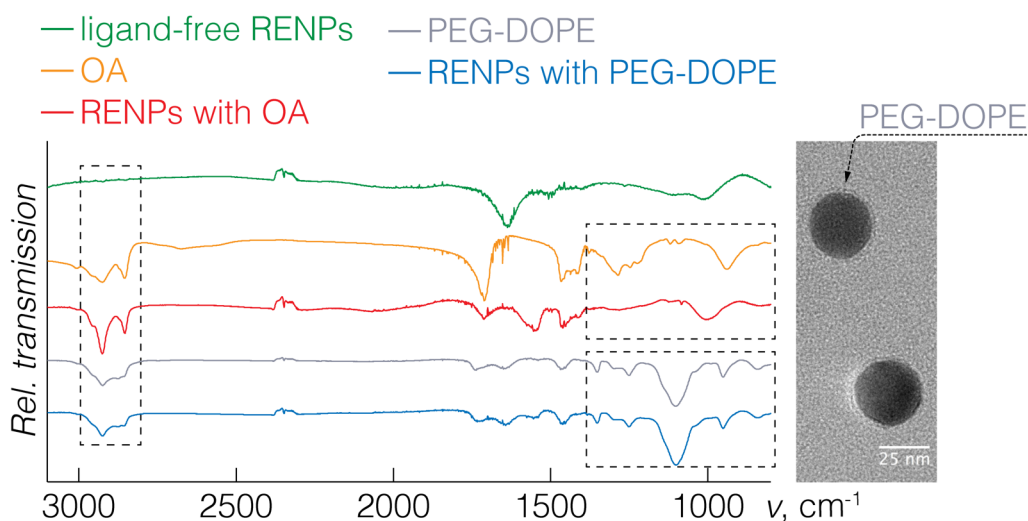


**PLQY of core (top) and (bottom) core/shell NaGdF<sub>4</sub>: x mol% Nd<sup>3+</sup>/NaGdF<sub>4</sub> RENPs (x = 5, 12.5 and 25), of chapter 3, dispersed in hexane (A) or in water (B) under 804 nm laser excitation of varying power density ( $P_d$ ). PLQY was measured using an empty cuvette, cuvette filled with hexane (or water), or cuvette filled with undoped (blank) RENPs dispersed in hexane (or water) as references. Solid lines and shaded areas for certain 5 mol% Nd<sup>3+</sup>-doped RENPs represent average PLQY and standard deviation, respectively.**

## Appendix III – FTIR data

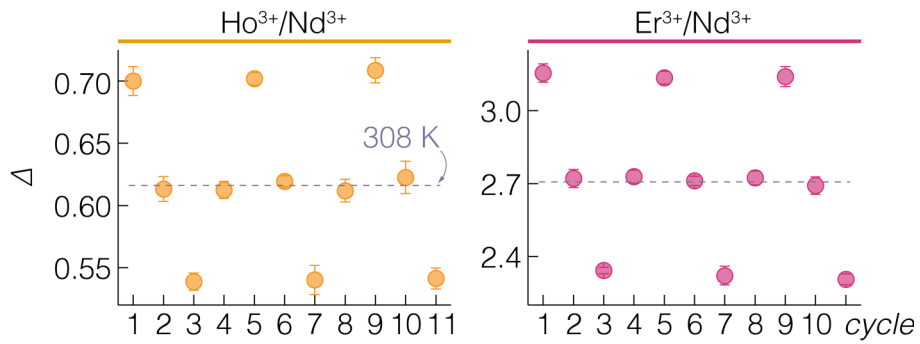


FTIR spectra of as-synthesized OA coated RENPs, pure PEG-DOPE phospholipids, and RENPs coated with PEG-DOPE phospholipids in chapter 4; as well as TEM image of PEG-DOPE coated RENPs with the layer of PEG-DOPE visible as halo around the RENPs. In FTIR spectra, the aliphatic C-H<sub>2</sub> stretching in the 2900-2850  $\text{cm}^{-1}$  region and vibrations characteristic to phosphate group ( $\text{PO}_4$ ) in the 1350-850  $\text{cm}^{-1}$  region are attributed to phospholipids.

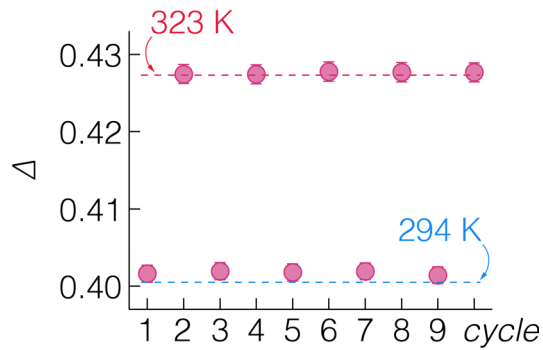


FTIR spectra of ligand-free RENPs, pure OA, OA coated RENPs, pure PEG-DOPE phospholipids, and RENPs coated with PEG-DOPE phospholipids in chapter 5; as well as TEM image of PEG-DOPE coated RENPs with the layer of PEG-DOPE visible as halo around the RENPs. In FTIR spectra, the aliphatic C-H<sub>2</sub> stretching in the 2900-2850  $\text{cm}^{-1}$  region and vibrations characteristic to phosphate group ( $\text{PO}_4$ ) in the 1350-850  $\text{cm}^{-1}$  region are attributed to phospholipids.

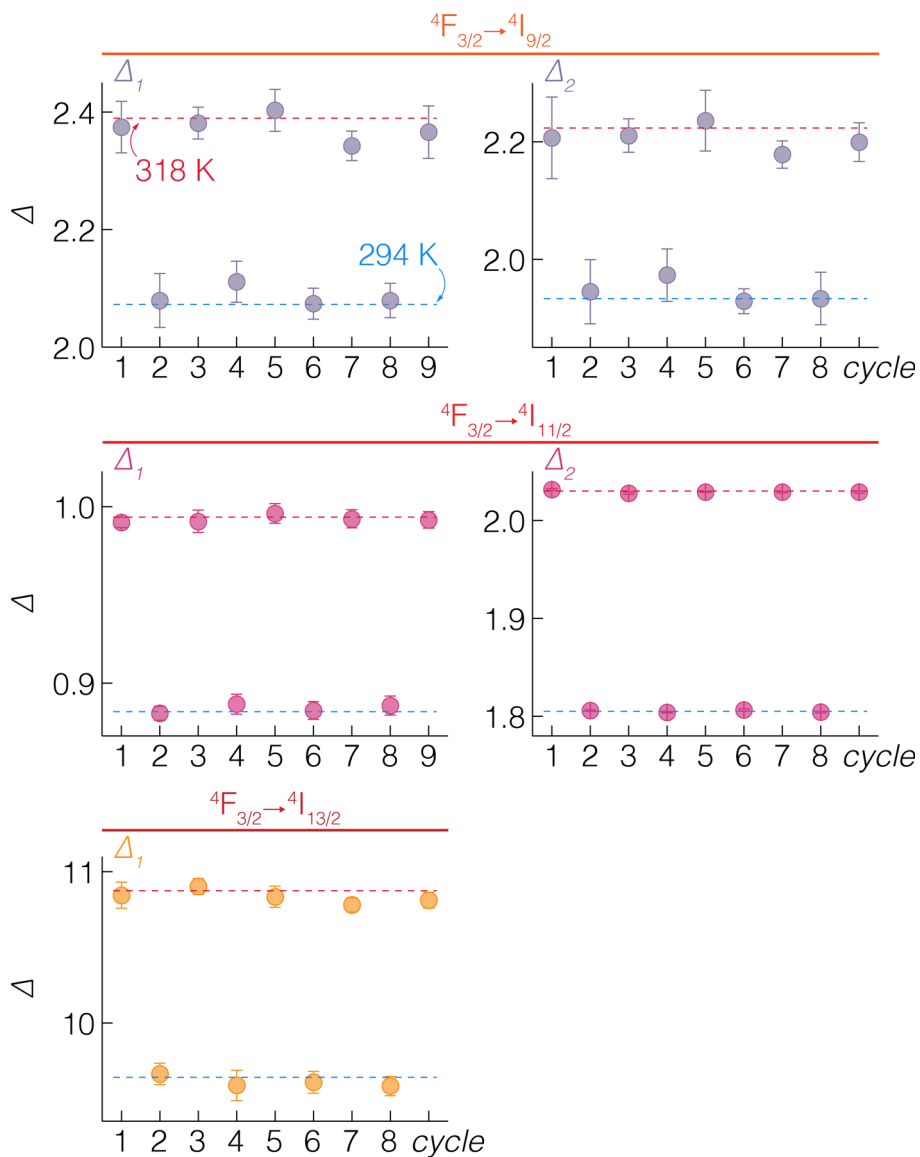
## Appendix IV – Temperature repeatability data



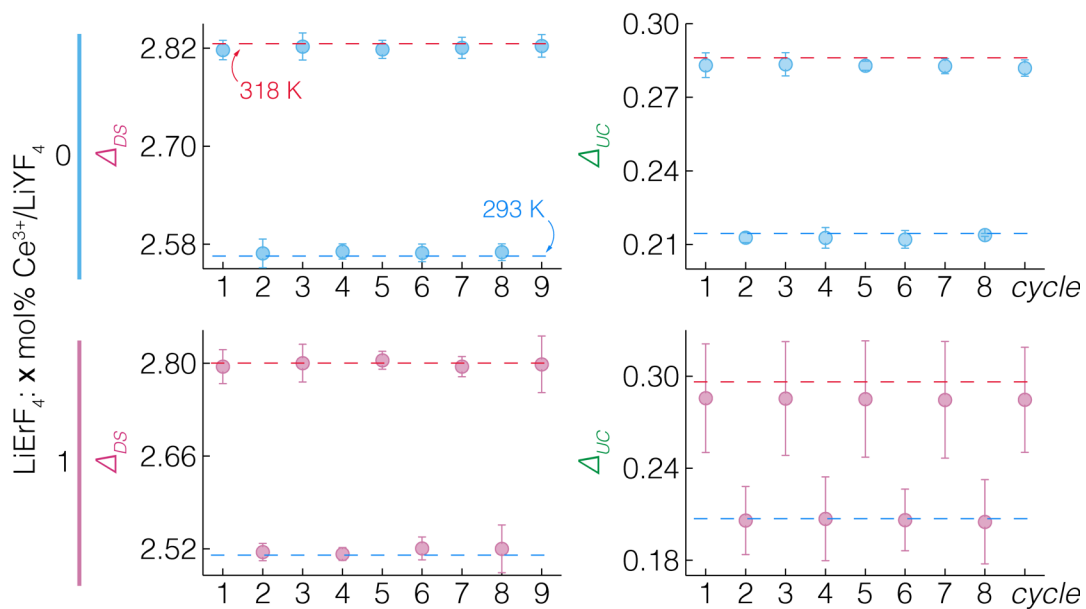
Repeatability parameter,  $R$ , for the different thermometric parameters of RENPs in chapter 5, evaluated from measuring temperature following multiple heating-cooling cycles. Left –  $\Delta(\text{Ho}^{3+}/\text{Nd}^{3+})$ , right –  $\Delta(\text{Ho}^{3+}/\text{Nd}^{3+})$ , corresponding  $R$  values are 98.9% and 99.2%.



Repeatability parameter,  $R$ , for the thermometric parameter of RENPs in chapter 6, evaluated from measuring temperature following multiple heating-cooling cycles.  $R$  value is 99.6%.



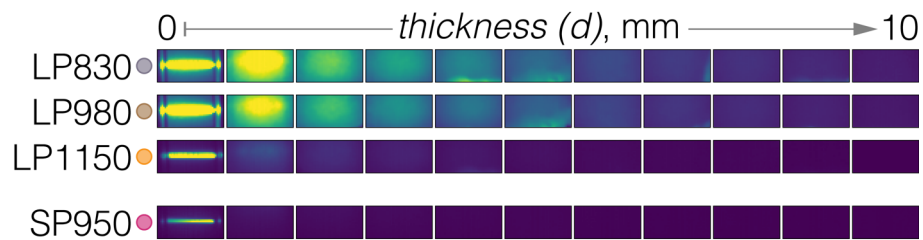
Repeatability parameter,  $R$ , for the different thermometric parameters of RENPs in chapter 9, evaluated from measuring temperature following multiple heating-cooling cycles. Top –  $\Delta_1$  ( $R = 98.1\%$ ) and  $\Delta_2$  ( $R = 97.9\%$ ) of the  ${}^4F_{3/2} \rightarrow {}^4I_{9/2}$  emission, middle –  $\Delta_1$  ( $R = 99.5\%$ ) and  $\Delta_2$  ( $R = 99.8\%$ ) of the  ${}^4F_{3/2} \rightarrow {}^4I_{11/2}$  emission, bottom –  $\Delta_1$  ( $R = 99.1\%$ ) of the  ${}^4F_{3/2} \rightarrow {}^4I_{13/2}$  emission.



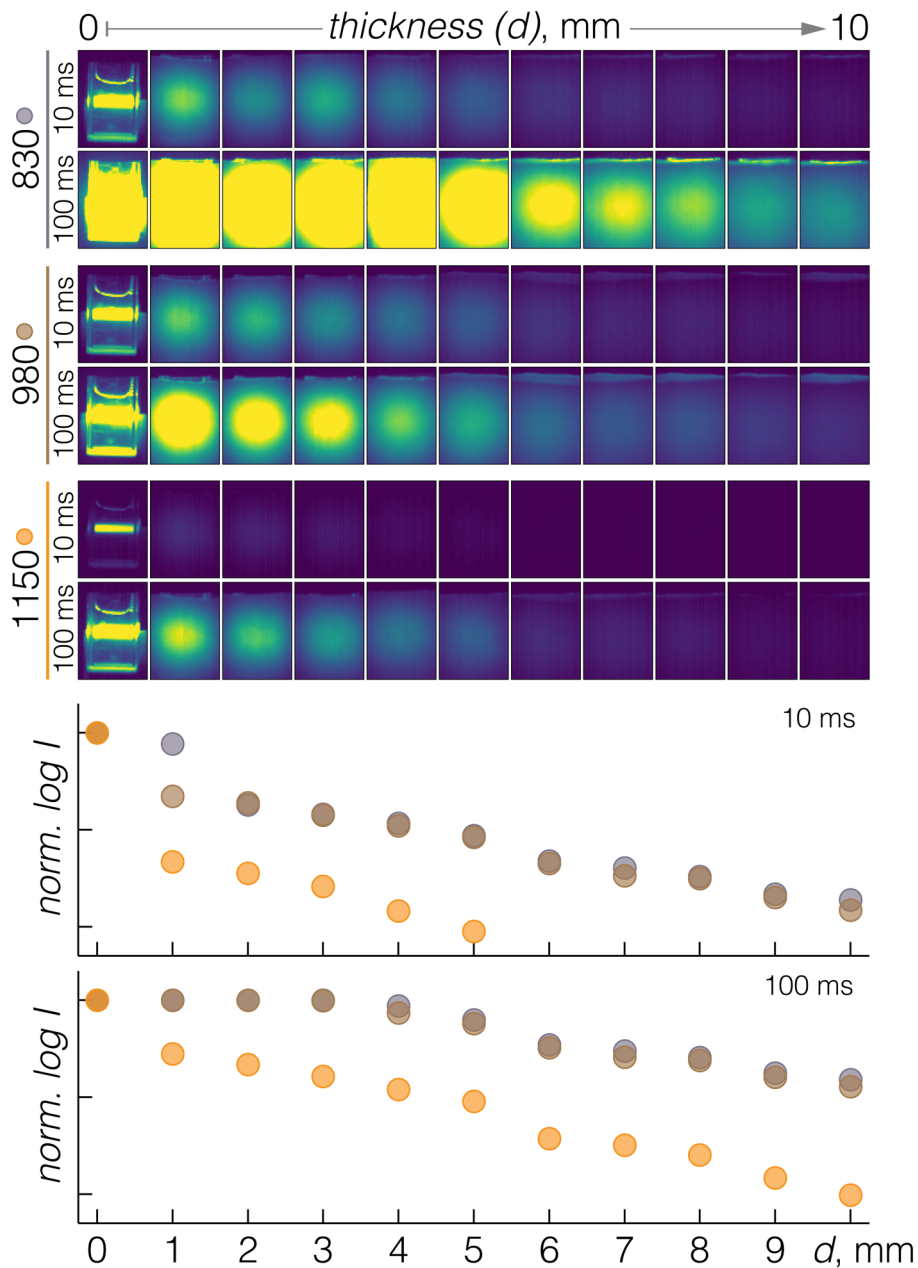
Repeatability parameter,  $R$ , for the DS emission (left) and UC emission (right) thermometric parameters of RENPs in chapter 10, evaluated from measuring temperature following multiple heating-cooling cycles. Top –  $\Delta_{DS}$  ( $R = 99.7\%$ ) and  $\Delta_{UC}$  ( $R = 98.8\%$ ) for  $\text{LiErF}_4/\text{LiYF}_4$  RENPs, bottom –  $\Delta_{DS}$  ( $R = 99.6\%$ ) and  $\Delta_{UC}$  ( $R = 97.2\%$ ) for  $\text{LiErF}_4: 1 \text{ mol\% Ce}^{3+}/\text{LiYF}_4$  RENPs.

## Appendix V – Additional NIR images

---



NIR imaging of the RENP of chapter 6 in water dispersion through pork fat tissue of increasing thickness. RENPs were excited at 806 nm laser excitation and DS emission was collected utilizing various LP optical filters (cut-off wavelength of each is indicated on the left to the images). Excited with 980 nm light NIR UC emission of  $Tm^{3+}$  was also observed using short-pass (SP) 950 nm filter.



NIR imaging of the RENP of chapter 9 in water dispersion through pork fat tissue of increasing thickness. RENPs were excited at 793 nm laser excitation and DS emission was collected utilizing various LP optical filters (cut-off wavelength of each is indicated on the left to the images). Images were acquired with 10 and 100 ms of exposure time. Emission intensity (normalized to the initial value at 0 mm) is also plotted against increasing tissue thickness. Experimental data points are color coded with the LP filters used to collect the NIR signal. From intensity vs tissue thickness data, exponential signal attenuation by pork fat tissue following  $\exp[-0.465 \cdot d]$  form could be determined.

## Appendix VI – deconvolution of Tm<sup>3+</sup> emission band at 790 nm

---

Spectra of UC emission of Tm<sup>3+</sup>-RENPs around 790 nm ( $y_{obs,i}$ ) were fitted point by point via linear combination of the spectral profiles of the ( $y_i$ ) of  ${}^3\text{H}_4 \rightarrow {}^3\text{H}_6$  ( $Q_i$ ) and  ${}^1\text{G}_4 \rightarrow {}^3\text{H}_5$  ( $U_i$ ) transitions (see figure below). Given that the  ${}^3\text{H}_4$  excited state quickly saturates for 0.2 mol% Tm<sup>3+</sup>-doped RENPs at higher power density ( $P_d$ ), its 790 nm emission at  $P_d > 2\text{ k W/cm}^2$  was considered as the closest representation of pristine  ${}^1\text{G}_4 \rightarrow {}^3\text{H}_5$  radiative transition. In contrast, 2 mol% Tm<sup>3+</sup>-doped RENPs prominently featured 790 nm PL from the  ${}^3\text{H}_4 \rightarrow {}^3\text{H}_6$  radiative transition, which for purity was measured at  $P_d < 5\text{ W/cm}^2$ . The mathematical procedure then relies on the minimization of a squared residual function  $S$ :

$$S = \sum_i (y_{obs,i} - y_i)^2 = \sum_i [y_{obs,i} - (aQ_i + bU_i)]^2$$

$a$  and  $b$  are weighing coefficients that account for the contribution of each radiative transition.

Imposing the first order derivative of this function, calculated with respect to the weighing coefficients, to be equal to zero minimizes  $S$ :

$$\frac{\partial S}{\partial a} = \frac{\partial S}{\partial b} = 0$$

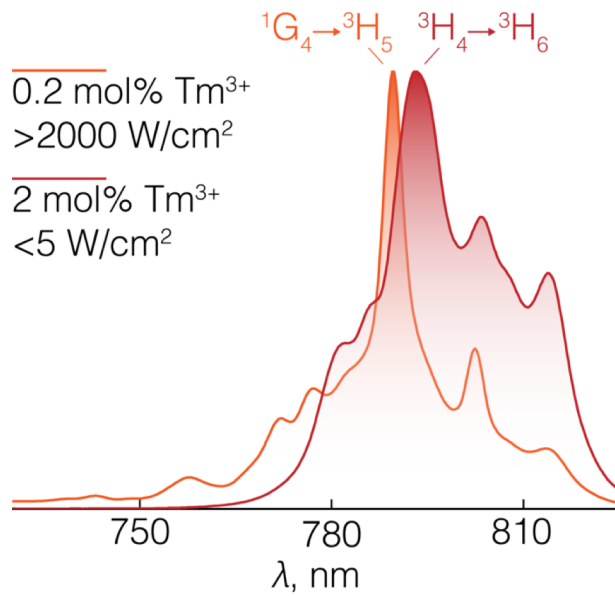
This leads to the homogeneous system:

$$\begin{pmatrix} \sum_i Q_i^2 & \sum_i Q_i U_i \\ \sum_i U_i Q_i & \sum_i U_i^2 \end{pmatrix} \begin{pmatrix} a \\ b \end{pmatrix} = \begin{pmatrix} \sum_i Q_i y_{obs,i} \\ \sum_i U_i y_{obs,i} \end{pmatrix}$$

And, rearranged:

$$\begin{pmatrix} a \\ b \end{pmatrix} = \begin{pmatrix} \sum_i Q_i^2 & \sum_i Q_i U_i \\ \sum_i U_i Q_i & \sum_i U_i^2 \end{pmatrix}^{-1} \begin{pmatrix} \sum_i Q_i y_{obs,i} \\ \sum_i U_i y_{obs,i} \end{pmatrix}$$

By solving this system, the values  $a$  and  $b$  are obtained, thus the relative contribution to the total Tm<sup>3+</sup> PL at 790 nm from the two radiative transitions can be extracted.



Emission profiles used for spectral deconvolution of the UC emission band around 790 nm measured for 0.2 mol% and 2 mol%  $Tm^{3+}$ -RENPs under high and low  $P_d$  of 960 nm laser excitation, respectively. The former RENPs represent the  $1G_4 \rightarrow 3H_5$  radiative transition while the latter represents the  $3H_4 \rightarrow 3H_6$  one.